

RESOLVED CHEMICAL EVOLUTION: STELLAR BUILDUP AND GASEOUS
REJUVENATION IN THE LOCAL UNIVERSE

By

Zachary J. Pace

A dissertation submitted in partial fulfillment of
the requirements for the degree of

Doctor of Philosophy
(Astronomy)

at the

UNIVERSITY OF WISCONSIN-MADISON

2020

Date of final oral examination: 13 August 2020

The dissertation is approved by the following members of the Final Oral Committee:

Christy Tremonti, Associate Professor, Astronomy

Matthew Bershady, Professor, Astronomy

Keith Bechtol, Assistant Professor, Physics

Robert Benjamin, Professor, Astronomy, University of Wisconsin-Whitewater

Aleksandar Diamond-Stanic, Assistant Professor, Physics and Astronomy, Bates College

Abstract

Fuck you I'm smart

Acknowledgments

Thanks to my parents, who let me drag the old telescope out of the driveway, and then didn't laugh at me when I decided I wanted to take pictures of the sky for a living; to Joe and Grandma Sue, who demand a one-sentence answer but get a ten-minute diatribe;

To my advisor, Christy, and to the other UW faculty who gave me the tools

To Brianna, whose unwavering support has made the last 2 years much more fun than would have been otherwise possible;

To my late grandparents Zelson & Pace; particularly to my grandfather Sidney Zelson, an academic who always told a joke; to his father, Louis Zelson, also a UW-Madison Ph.D;

To the Monday night trivia crowd (Chris, Greg, Nick, Arthur, Kendall, Bri, DK, and Catherine; with recent additions Erik, Rachel, Andrew, and Anthony; and occasional guest stars Melissa, Logan, Aaron, and Ben): thanks for the hangouts, knocking off early with me, and not letting me always guess Russia; and to the Sunday soccer crew: thanks for getting me on my feet & moving;

To my grad school officemates Nick, Corey, Arthur, Ben, Catherine, and most of all Jacqueline & Diego: thanks for answering my basic questions about other fields, listening to my complaints about my code being too slow, and telling me to go sail when I wasn't getting anything done anyway; and to my housemates past & present

To my fellow students and friends, many named already, but especially DK, Diego, Julie, Jacqueline, Catherine, Kendall, and Matt: the community we have built together in

adversity and success alike has gotten me through the most challenging moments;

To the people of the Ho-Chunk Nation, whose lands encompass the space where I have lived and studied

Contents

Abstract	i
Acknowledgments	ii
Contents	iv
List of Tables	viii
List of Figures	x
1 Introduction	1
1.1 Problems in galaxy chemical evolution	2
1.1.1 Chemical evolution: the theoretical & the practical	4
1.1.2 Inflows: where are they, and what are their effects?	5
1.1.3 How to measure a galaxy's stellar mass	7
1.1.4 The growth of resolved spectroscopic surveys	8
1.2 Contents of this dissertation	8
References	9
2 PCA spectral fitting & stellar mass-to-light ratio estimates	15
Abstract	16
2.1 Introduction	17
2.2 Data	22
2.3 The Composite Stellar Population Library	25

2.3.1	SFHs and stellar population properties	26
2.3.1.1	SFH families: the delayed- τ model	27
2.3.1.2	Stellar composition & velocities, attenuation, and uncertain stellar evolution	34
2.3.2	D _n 4000-H δ_A comparison of training library to MaNGA spaxels . .	40
2.3.3	Why not use CMLRs?	41
2.4	Parameter Estimation in the PCA Framework	47
2.4.1	The PCA system	47
2.4.2	Validating number of PCs retained: eigenvalues and the scree plot .	51
2.4.2.1	Computational concerns	52
2.4.3	Developing a physical intuition for principal components	55
2.4.4	The observational spectral covariance matrix	56
2.4.5	Fitting the observations with eigenspectra	60
2.4.6	Towards optimal flagging and masking of Balmer emission-lines .	63
2.4.6.1	Tension between flagged-and-replaced spectra and their fits? .	65
2.4.6.2	Evaluating Balmer-masking with synthetic observations of PCA best-fits	66
2.4.6.3	Flag-and-replace stellar models	68
2.4.7	Estimating PC coefficients and uncertainties for observed spectra .	70
2.4.7.1	Effects of sky residuals	72
2.4.8	Quantity estimates	74
2.4.8.1	Validating number of models against reliability of quantity estimates	77
2.4.8.2	What limits our ability to infer quantities of interest?	77
2.4.9	Data-quality and masking	79

2.4.10	Tests on held-out, synthetic data	81
2.5	Resolved stellar mass-to-light ratios: Discussion and Conclusion	94
2.5.1	Remaining spectral-fitting systematics and degeneracies	95
2.5.2	Public Data and Future Work	98
A	The MaNGA Instrumental Line-Spread Function	99
B	Constructing synthetic observations using held-out test data	100
C	Statement of Work	102
	References	102
3	Applications of PCA-based stellar mass estimates	109
	Abstract	110
3.1	Introduction	111
3.2	Data	114
3.3	Resolved stellar-mass surface densities: comparison to results from dynamics	116
3.4	A catalog of aperture-corrected total galaxy stellar masses	122
3.4.1	Tests of aperture-correction against resolved photometry	129
3.4.2	Integrated masses: comparison to NASA-Sloan Atlas & JHU-MPA Catalog	132
3.4.3	Are stellar masses derived from galaxy-coadded spectroscopy reliable?	133
3.5	Discussion and Conclusions	142
3.5.1	Galaxy total stellar-mass: aperture-correction and luminosity-weighting	144
3.5.2	Public Data	146
A	Statement of Work	146
	References	147

4 Gaseous Inflows & Steep Metallicity Profiles	151
Abstract	152
4.1 Introduction	153
4.2 Data	157
4.3 Abundance calibrations and radial decrements	159
4.3.1 Radial decrement definition	161
4.3.2 Sample & Data quality	162
4.4 Abundance decrement trends	165
4.4.1 Decrement vs. gradients	165
4.4.2 Radial metallicity trends and HI	167
4.5 Inflow model: does it explain the metallicities?	174
4.5.1 Total H I, dust, and extended UV disks in the accretion-dilution model	180
4.6 Discussion and Conclusions	183
References	187
5 Discussion, Summary, and Conclusions	192

List of Tables

2.1	Selected parameters for ten sample SFHs	33
2.2	Population synthesis inputs of this work, compared to previous	43
2.3	Color–mass-to-light ratio relation linear fits	46
2.4	PCA method notation	48
2.5	Locations of figures & summary statistics for mock observations & real MaNGA data.	83
2.6	Statistics of $\Delta \log \Upsilon_i^*$ for mock observations, separated by mean SNR and $g - r$ color	86
2.7	Statistics of $\sigma_{\log \Upsilon_i^*}$ for mock observations, separated by mean SNR and $g - r$ color	86
2.8	Statistics of $\sigma_{\log \Upsilon_i^*}$ for real MaNGA observations, separated by mean SNR and $g - r$ color	90
2.9	Statistics of $\frac{\Delta \log \Upsilon_i^*}{\sigma_{\log \Upsilon_i^*}}$ for mock observations, separated by mean SNR and $g - r$ color	90
2.10	Statistics of $\Delta \log \Upsilon_i^*$ for mock observations, separated by mean SNR and known stellar metallicity	93
2.11	Statistics of $\Delta \log \Upsilon_i^*$ for mock observations, separated by mean SNR and τ_V	93
3.1	The effects of disk scale height assumptions	118

3.2	Linear first between stacking-induced mass deficit and dust & SFR	141
3.3	The twenty galaxies with the largest difference between M^* and M_{LW}^*	142
4.1	Correlation coefficients & p-values between $\Delta(O/H)^*$, $\tilde{\sigma}(O/H)^*$, and $\frac{M_{\text{HI}}}{M^*}$, separated by total galaxy stellar-mass.	173
4.2	A segment of the machine-readable table aggregating total galaxy stellar masses, chemical variations, and HI masses/upper-limits (where available) .	186

List of Figures

1.1	A cartoon of the multiphase gas flows around galaxies	11
1.2	Simulations and reported observations ($z \sim 2.5$) of multi-filament inflows . .	12
1.3	A graphical representation of a gas-regulator or “bathtub” model of chemical evolution	13
1.4	A graphical overview of the components of stellar population synthesis. . .	14
2.1	Median spaxel signal-to-noise ratios	25
2.2	Distributions of stellar population synthesis inputs	27
2.3	Distributions of absorption indices in training data	28
2.4	Distributions of derived SFH properties in training data	29
2.5	Ten sample SFHs	34
2.6	Distribution of the log mass-weighted mean stellar age for training data . .	35
2.7	Comparison of SDSS nebular metallicity distribution with training data stellar metallicity distribution	37
2.8	D_n4000 - $H\delta_A$ comparison between training data, MaNGA DAP values, and a set of expanded models	42
2.9	Color–mass-to-light ratio relations ($g - r$ to i -band) for the training data .	44
2.10	Color–mass-to-light ratio relations ($g - i$ vs i -band) for the training data .	45
2.11	Principal component system	50

2.12 Scree plot, and variance explained	53
2.13 Fractional reconstruction residual for validation data	54
2.14 Principal component amplitudes versus SFH properties of interest	57
2.15 Spectrophotometric covariance matrix	59
2.16 Sample noise spectra drawn from MaNGA and BOSS spectrophotometric covariance	60
2.17 Effects of strong Balmer emission on fits to highest four Balmer absorption features	66
2.18 Effects of Balmer-masking strategies	67
2.19 Balmer fit residuals using two masking strategies	69
2.20 MaNGA spaxel diagnostic figure from PC fits	73
2.21 Effects of imperfect sky subtraction on PC down-projection	75
2.22 Number of models' effect on reliability of parameter estimate	78
2.23 Parameter reliability assuming imperfect PC down-projection	80
2.24 Reliability of $\log \Upsilon_i^*$ versus color and signal-to-noise	85
2.25 $\sigma_{\log \Upsilon_i^*}$ versus color and signal-to-noise in fits to mock data	87
2.26 $\sigma_{\log \Upsilon_i^*}$ versus color and signal-to-noise for observations	87
2.27 As Figure 2.25, except with distributions of $\frac{\Delta \log \Upsilon_i^*}{\sigma_{\log \Upsilon_i^*}}$	89
2.28 As Figure 2.24, except binning with respect to known [Z]	91
2.29 As Figure 2.24, except binning with respect to known τ_V	92
2.30 Maps of <i>i</i> -band stellar mass-to-light ratio for three early-type galaxies	96
2.31 As Figure 2.30, but a selection of four late-type galaxies	97
2.32 Full diagnostic figure for synthetic data based on the test galaxy 8566-12705	101

3.1	Comparison between PCA-measured stellar mass surface density and DiskMass measured dynamical mass surface densities	119
3.2	The flux fraction assumed outside the MaNGa IFU	124
3.3	The difference between the “ring” and “CMLR” aperture corrections	126
3.4	The difference in total stellar mass induced by aperture-correction method	128
3.5	Spectroscopic-photometric aperture curve of growth	130
3.6	Comparison between NSA catalog and PCA-derived total stellar masses	134
3.7	Mass deficit induced by luminosity-weighted stacking	136
3.8	The relationship between mass deficit and unequal dust attenuation across the IFU	137
3.9	The relationship between mass deficit and axis ratio	138
3.10	The relationship between star-formation rate and stacking-induced mass deficit	140
3.11	The twenty galaxies with the largest difference between M^* and M_{LW}^*	143
4.1	The radial binning scheme described above, applied to four MaNGA galaxies with decreasing disk aspect-ratios. Pixels are colored according to their use in radial bins: light green indicates radial bin 0 ($0.0 - 0.5 R_e$), and lavender indicates radial bin 1 ($1.25 - 1.75 R_e$). Pixels colored white indicate locations not included in any bin, due to either radial coordinate or azimuthal angle away from the major axis. These restrictions are applied in addition to those on data-quality (see Section 4.3.2). Contours are in units of R_e , and are labeled at the outer boundary of bin 0, as well as the inner & outer boundaries of bin 1. The spatial resolution element (FWHM) is visualized as an orange circle in the bottom-right panel: as inclination increases, the PSF samples an increasing diversity of galaxy radii along the minor axis.	163

4.2	The correlations between total galaxy stellar mass, radial abundance decrement, and $\frac{M_{\text{HI}}}{M^*}$, overlaid with transformed literature values.	166
4.3	The correlation between radial metallicity decrement and $\frac{M_{\text{HI}}}{M^*}$, separated by total galaxy stellar mass.	169
4.4	As Figure 4.3, but relating dispersion of gas-phase metallicity at fixed radius with the strength of metallicity decrement.	171
4.5	As Figures 4.3 & 4.4, but relating dispersion of gas-phase metallicity at fixed radius and $\frac{M_{\text{HI}}}{M^*} \log \frac{M_{\text{HI}}}{M^*}$	172
4.6	Two-component decompositions of stellar mass bins' distributions by their scatter of their metallicity distribution at fixed radius.	177
4.7	A toy model of inflow's diluting effects on local metallicity and the mass increase of the associated gas reservoir.	179

Chapter 1

Introduction

Galaxies are the most immediately visible large structures in the universe, broadly containing some combination of stars, stellar remnants, gas, and dark matter. Though the relative abundances of baryons and dark matter are thought to have been set almost immediately after the Big Bang, the proportions of gas, stars, and stellar remnants in a single galaxy are deeply informative about the individual. In other words, galaxies' properties can be inferred largely from the light emitted by stars and gas. With this information, observers may discern a galaxy's history and fate.

The process of galaxy evolution can be envisaged as the transformation of cold gas into stars, and the subsequent recycling of the stars' ejecta (rich in elements heavier than Helium—"metals") back into the a galaxy's ambient gaseous reservoir. This process begins after the initial collapse of a dark matter halo, with the progenitors of more massive dark matter halos (corresponding to denser regions in the early universe) collapsing, accreting baryons, and forming stars first. Each subsequent generation of stars builds upon the metal ejecta of generations before. Consequently, the dark matter halos most depleted in their supply of cold, neutral gas have a larger proportion of heavy elements. Metal content is described in two major ways: the first, common in stellar astrophysics, quantifies a mass

fraction of all metals (and is notated Z). The chemistry of the interstellar medium (ISM) is described by the abundance of oxygen, by number, in relation to hydrogen on a logarithmic scale (notated $12 + \log(\text{O/H})$). The chemistry of the interstellar medium is sensitive to the total star-formation that has occurred throughout a galaxy’s lifetime, and is of the most pertinence to this dissertation.

1.1 Problems in galaxy chemical evolution

Early theories of galaxy formation relied upon the idea that a single cloud of primordial gas formed a single galaxy (Eggen et al. 1962). Therefore, the gas fraction ($f_g = \frac{M_{\text{gas}}}{M_{\text{gas}} + M_*}$) should be a simple and reliable indicator of evolutionary state, giving information about the galaxy’s past star-formation and its potential to form stars in the future (Tinsley 1980; Pei & Fall 1995). In this theory, a galaxy was a “closed box” which neither gained nor lost gas, but simply transformed its original gas reservoir into stars until the gas ran out.

Today we know that the actual picture is more complicated: galaxies form hierarchically and from the “inside-out” (Wang et al. 2011; Bovy et al. 2016)—meaning that galaxy centers collapsed and formed stars earlier in cosmic time, and disks formed as gas built up around the bulge. Feedback from supernovae gives rise to gas and metal transport within galaxies, as well as more wholesale expulsion of gas from the disk (“galactic winds” Veilleux et al. 2005). In simulations, bursty star-formation drives brief, “gusty” outflows that eject much of the interstellar medium from the galaxy disk, briefly suppressing further star formation and enriching the circum-galactic medium (CGM, Muratov et al. 2015). This idea is also borne out by case-studies of, e.g., NGC891, which exhibits an HI disk in profile preferentially “puffed-up” in regions with the most vigorous star formation (Oosterloo et al. 2007). However, it is not clear whether this gas eventually rains back down onto

the disk (a “galactic fountain”), or simply remains in the halo. Figure 1.1 shows the gas flows thought to impact galaxies’ ongoing chemical evolution.

It is likely that gas not only flows out of galaxies, but also in. The simplest reason is to allow star-formation to proceed for many Gyr. For the Milky Way’s current star-formation rate (SFR) to continue unabated for the past 8 Gyr without also exhausting the Galaxy’s gaseous reservoir, additional gas must have been introduced at a similar rate ($1.5 \text{ M}_\odot \text{yr}^{-1}$). This is also true of statistical samples of galaxies all the way back to the peak of the cosmic star-formation rate density (Tacconi et al. 2013). Even continued star-formation alone seems to demand consistent refueling. Exacerbating matters further is star-formation’s self-regulating effects: the winds from massive stars and the mechanical impacts from the ensuing supernovae drive cold gas out of the disk at rates greater than the SFR (Chisholm et al. 2018; Roberts-Borsani et al. 2020). The impact of star-formation on surrounding cold gas is much greater than simple depletion, and bolster the indirect arguments for continual infusions of new gas.

There are also chemical signatures of gaseous refueling: the distributions of metal abundances in Milky Way G-dwarf stars were long known to be inconsistent with the closed-box model of chemical evolution (van den Bergh 1962), though the accepted resolution was much later to come: the “G-dwarf problem” can be solved by allowing galaxies to accrete gas from other sources (Fraternali et al. 2007). Indeed, observations of the Milky Way and other galaxies indicate that dwarf companions do contribute gas to their larger, nearby siblings (Martínez-Delgado et al. 2010). The chemical abundances of this gas seems to be seeded by the original parent halo: Schaefer et al. (2019) demonstrated the likely pre-enrichment of gas in low-mass satellites in higher-mass halos: in other words, low-mass galaxies have their metallicities “seeded” by gas accreted from the more massive galaxies in whose halos they reside. A simple “re-budgeting” of gas between galaxies does not

accomplish the wholesale rejuvenation that will continually sustain star formation.

The supply of gas that galaxies can exchange with their neighbors is just a drop in the bucket compared to the gas residing outside galaxies. Simulations suggest that galaxies will accrete pristine gas in “cold flows” along filaments between galaxies, the “cosmic web” (Silk & Mamon 2012; Sancisi et al. 2008; Cresci et al. 2010). Recent observations of distant systems near the peak of the cosmic star formation rate density show gas kinematics suggestive of accretion from the cosmic web’s gas reservoirs. Figure 1.2 shows a simulated multi-filament inflow beside two Lyman-alpha emitter systems observed with the Keck Cosmic Web Imager integral-field unit (Martin et al. 2019). Those systems, at $z \sim 2.5$, are very different from the galaxies present in the local universe; but conceptually demonstrate that the gas in extragalactic filaments could be captured by galaxies and transformed into stars.

1.1.1 Chemical evolution: the theoretical & the practical

Though the co-evolution of gas fraction, metallicity, and stellar mass reflects a complex interplay between accretion, star formation, supernova- & AGN-driven outflows, and galaxy-galaxy interactions, several robust, empirical relationships emerge: galaxies with higher gas fractions tend to have lower masses (de Blok et al. 1996), form rotationally-supported disks (McGaugh & de Blok 1997), and lie on the “star-forming main sequence” (SFMS), a linear correlation between stellar mass and star-formation rate (SFR) (Brinchmann et al. 2004). Additionally, a positive correlation is observed between galaxy mass and metal content (the mass-metallicity relation, or MZR) (Tremonti et al. 2004). When combined, these trends imply that galaxies’ SFRs “self-regulate”, and so the process of galaxy-wide chemical enrichment is gradual (Davé et al. 2012; Fu et al. 2013). Thus, even though the closed-box model of chemical evolution is not true in detail, gas fraction remains

an illustrative property.

Galaxies' self-regulatory mechanisms bring about a sort of equilibrium. Yes, galaxies do evolve—but they do so slowly in comparison to the lifetimes of individual star-forming regions. Figure 1.3 shows a cartoon of a chemical evolution model which treats instantaneous star-formation and evolving metallicity as quantities governed by a gas reservoir (this model and others like it have been termed “gas-regulator models”—[Lilly et al. 2013; Davé et al. 2012](#)). In such models, the availability (or not) of gas drives star formation forward. The gaseous reservoir is depleted by the material residing in long-lived stars, as well as by the gaseous outflows which the massive, short-lived stars expel (“feedback”). Those same feedback mechanisms return metals to the reservoir, relocate them to other reservoirs, or banish them to the halo. Finally, the reservoir is rejuvenated by gas either originating from other reservoirs (in which case it has been processed through the star-formation and is metal-enriched) or from low-metallicity sources such as the cosmic web.

1.1.2 Inflows: where are they, and what are their effects?

Measurements of the gas and metals *lost* by star-forming galaxies due to feedback have become more possible with time ([Telford et al. 2019; Chisholm et al. 2018; Belfiore et al. 2019](#)). The exact parameters of inflows in samples of galaxies remain elusive, though. The Milky Way’s high-velocity clouds (HVCs) have long been considered signatures of the Galaxy’s gas exchange with its environment: HVCs are gas clouds characterized by extreme velocities relative to the Milky Way disk, as well as relatively low metallicities (generally less than $0.5 Z_{\odot}$), both of which suggest that they originated elsewhere and are now being accreted. HVCs may have analogs in the extragalactic context, but radio instrumentation has not reached the combination of resolution and sensitivity required to

map them in relation to galaxies' ambient gas supply. Furthermore, though simulations indicate that the filaments of the cosmic web supply rejuvenating gas flows, the structures are orders of magnitude larger in size than galaxies and the medium much more diffuse and thus observationally inaccessible. It is worth repeating, though, that inflows are at least a buttress of current galaxy chemical evolution theories, if not a keystone. They must be understood and characterized, not merely inferred.

In order to deeply understand galaxies' self-regulation, we must measure their star-forming gaseous reservoirs. This is most straightforwardly accomplished using radio (21cm HI) observations. Indeed, radio follow-up of optical surveys is commonplace; however, it is very infrequently complete in either scope, resolution, or depth. All three are required to spot and statistically characterize inflows. Simply put, interferometric surveys have yet to be realized due to their inherent immense time commitment. For example, the highest-resolution configuration on the Very Large Array (A-array, which has beam size 2") requires 5.5 hours on source to reach an RMS noise of 0.2 mJy ($N = 2.08 \times 10^{21} \text{ cm}^{-2}$, or $\Sigma \sim 16 \text{ M}_\odot \text{pc}^{-2}$) with a velocity resolution of 40 km s^{-1} . This is many times larger than the on-source time of the latest resolved spectroscopic surveys. There have been attempts to circumvent radio observations by using the optical attenuation (modulated by metallicity and an assumed dust-to-metal ratio) as a proxy for gas content (Brinchmann et al. 2013; Carton et al. 2017; Barrera-Ballesteros et al. 2020), but the uncertainties, systematics, and degeneracies involved have not been fully quantified. In particular, low-metallicity inflows likely have very different dust content (Kahre et al. 2018). For the purposes of locating gaseous inflows, it is therefore most prudent to fall back on global estimates of gas content, such as single-dish HI surveys, whose samples are larger and more statistically complete.

1.1.3 How to measure a galaxy's stellar mass

A galaxy's mass in stars serves as a proxy for its evolutionary stage: as a general rule, the higher a galaxy's stellar mass, the earlier the progenitor dark matter halo collapsed, and the more evolved the system is at the present day. Measuring stellar mass is fraught with uncertainties, though, which emerge largely due to the variable brightnesses & colors of different-age & -mass stars. If every star's mass-to-light ratio was the same, then a precise measurement of total flux would yield a precise measurement of mass. Complicating the matter is the relative rarity of high-mass stars: if high-mass stars were the most abundant by number, a stellar population's luminosity would better reflect its mass. Thus, it can be observationally difficult to reliably disentangle the true balance between a galaxy's old and young stellar populations, when the most visible constituents are the youngest and brightest.

Other factors also influence the light that reaches us from stellar populations. Figure 1.4 (reproduced from [Conroy \(2013\)](#)) illustrates the inputs to stellar population synthesis (SPS), starting at models of individual stars & their birth abundance by number, including their modulation by foreground dust, and culminating in a model of the spectral energy distribution (SED) of a composite stellar population (CSP, the weighted sum of many fixed-metallicity, coeval stellar populations). This process has many observational degeneracies, most importantly between stellar age, stellar metallicity, and foreground dust attenuation. Increasing any one of the three reddens a spectrum, but it is difficult to distinguish which of the three is responsible, and therefore, what the exact past SFH is.

Some early attempts to disentangle stellar populations of different ages in the extragalactic context revolved around relations between optical colors and stellar mass-to-light ratios (see [Bell & de Jong 2001; Bell et al. 2003](#)), calibrated by assuming a star-

formation history, a stellar initial mass function (IMF, the proportion of stars of various ages arising from one instantaneous burst of star-formation), and a set of spectral-energy distributions for stars at different evolutionary stages. These relations yield adequate order-of-magnitude estimates, but their precision belies the systematics & observational degeneracies at play. Star-formation histories with nearly-identical broadband colors can be very different indeed, having a diversity of metallicity, dominance & era of enhanced star-formation episodes, and foreground dust attenuation. With high-precision spectroscopic surveys, many (though not all) of these difficulties can be overcome. By precisely measuring a galaxy's stellar mass, one measures part of the denominator of gas fraction (or equivalently, further constrains the balance between young & old stars), and quantifies a galaxy's evolutionary state.

1.1.4 The growth of resolved spectroscopic surveys

1.2 Contents of this dissertation

The aim of this dissertation is to track the buildup of stellar mass and metals in the gas phase across a large sample of galaxies with resolved spectroscopic measurements, and relate those to the availability & ongoing consumption of star-forming gas. Chapter 2 endeavors to measure the stellar content of galaxies at kiloparsec scales. This is accomplished by quantifying the degeneracies in spectroscopic observations using a low-dimensional spectroscopic basis set generated with principal component analysis (PCA). The result is a catalog of resolved stellar mass maps for approximately 4700 galaxies. Chapter 3 compares the resolved mass estimates from Chapter 2 to measurements of galaxy dynamical masses obtained by studying the vertical kinematics of face-on disk galaxies; and aggregates & aperture-corrects the maps of resolved stellar mass into a

catalog of total galaxy stellar masses, also addressing the effects of resolution mismatch on estimates of stellar mass. This dissertation’s final chapter, Chapter 4, turns to galaxies’ gas-phase chemical abundances, and relates resolved chemistry to a galaxy’s total gas content. We identify a correlation between a strongly-varying radial oxygen abundance profile, increased metallicity scatter at fixed radius, and enhanced HI content; and attempt to explain the extreme metallicities and gas content with atomic-rich, low-metallicity inflows from galaxies’ environments. The intuitive model produces qualitative agreement with analytic models of chemical evolution in the presence of inflows; and may permit selection of probable inflow hosts for high-resolution radio follow-up. Together, these three works expand the existing breadth of measurements of galaxy chemical evolution, and provide a path towards statistical characterization of galaxies’ transformation through time.

References

- Barrera-Ballesteros, J. K., Utomo, D., Bolatto, A. D., et al. 2020, MNRAS, 492, 2651
- Belfiore, F., Vincenzo, F., Maiolino, R., & Matteucci, F. 2019, MNRAS, 487, 456
- Bell, E. F., & de Jong, R. S. 2001, ApJ, 550, 212
- Bell, E. F., McIntosh, D. H., Katz, N., & Weinberg, M. D. 2003, ApJS, 149, 289
- Bovy, J., Rix, H.-W., Schlafly, E. F., et al. 2016, ApJ, 823, 30
- Brinchmann, J., Charlot, S., Kauffmann, G., et al. 2013, MNRAS, 432, 2112
- Brinchmann, J., Charlot, S., White, S. D. M., et al. 2004, MNRAS, 351, 1151
- Carton, D., Brinchmann, J., Shirazi, M., et al. 2017, MNRAS, 468, 2140
- Chisholm, J., Tremonti, C., & Leitherer, C. 2018, MNRAS, 481, 1690
- Conroy, C. 2013, ARA&A, 51, 393
- Cresci, G., Mannucci, F., Maiolino, R., et al. 2010, Nature, 467, 811
- Davé, R., Finlator, K., & Oppenheimer, B. D. 2012, MNRAS, 421, 98
- de Blok, W. J. G., McGaugh, S. S., & van der Hulst, J. M. 1996, MNRAS, 283, 18
- Eggen, O. J., Lynden-Bell, D., & Sandage, A. R. 1962, ApJ, 136, 748

- Frernali, F., Oosterloo, T., Binney, J. J., & Sancisi, R. 2007, *Astrophysics and Space Science Proceedings*, 3, 271
- Fu, J., Kauffmann, G., Huang, M.-l., et al. 2013, *MNRAS*, 434, 1531
- Kahre, L., Walterbos, R. A., Kim, H., et al. 2018, *ApJ*, 855, 133
- Lilly, S. J., Carollo, C. M., Pipino, A., Renzini, A., & Peng, Y. 2013, *ApJ*, 772, 119
- Martin, D. C., O'Sullivan, D., Matuszewski, M., et al. 2019, *Nature Astronomy*, 3, 822
- Martínez-Delgado, D., Gabany, R. J., Crawford, K., et al. 2010, *AJ*, 140, 962
- McGaugh, S. S., & de Blok, W. J. G. 1997, *ApJ*, 481, 689
- Muratov, A. L., Kereš, D., Faucher-Giguère, C.-A., et al. 2015, *MNRAS*, 454, 2691
- Oosterloo, T., Frernali, F., & Sancisi, R. 2007, *AJ*, 134, 1019
- Pei, Y. C., & Fall, S. M. 1995, *ApJ*, 454, 69
- Roberts-Borsani, G. W., Saintonge, A., Masters, K. L., & Stark, D. V. 2020, *MNRAS*, 493, 3081
- Sancisi, R., Frernali, F., Oosterloo, T., & van der Hulst, T. 2008, *A&A Rev.*, 15, 189
- Schaefer, A. L., Tremonti, C., Pace, Z., et al. 2019, *ApJ*, 884, 156
- Silk, J., & Mamon, G. A. 2012, *Research in Astronomy and Astrophysics*, 12, 917
- Tacconi, L. J., Neri, R., Genzel, R., et al. 2013, *ApJ*, 768, 74
- Telford, O. G., Werk, J. K., Dalcanton, J. J., & Williams, B. F. 2019, *ApJ*, 877, 120
- Tinsley, B. M. 1980, *Fund. Cosmic Phys.*, 5, 287
- Tremonti, C. A., Heckman, T. M., Kauffmann, G., et al. 2004, *ApJ*, 613, 898
- Tumlinson, J., Peeples, M. S., & Werk, J. K. 2017, *ARA&A*, 55, 389
- van den Bergh, S. 1962, *AJ*, 67, 486
- Veilleux, S., Cecil, G., & Bland-Hawthorn, J. 2005, *ARA&A*, 43, 769
- Wang, J., Kauffmann, G., Overzier, R., et al. 2011, *MNRAS*, 412, 1081

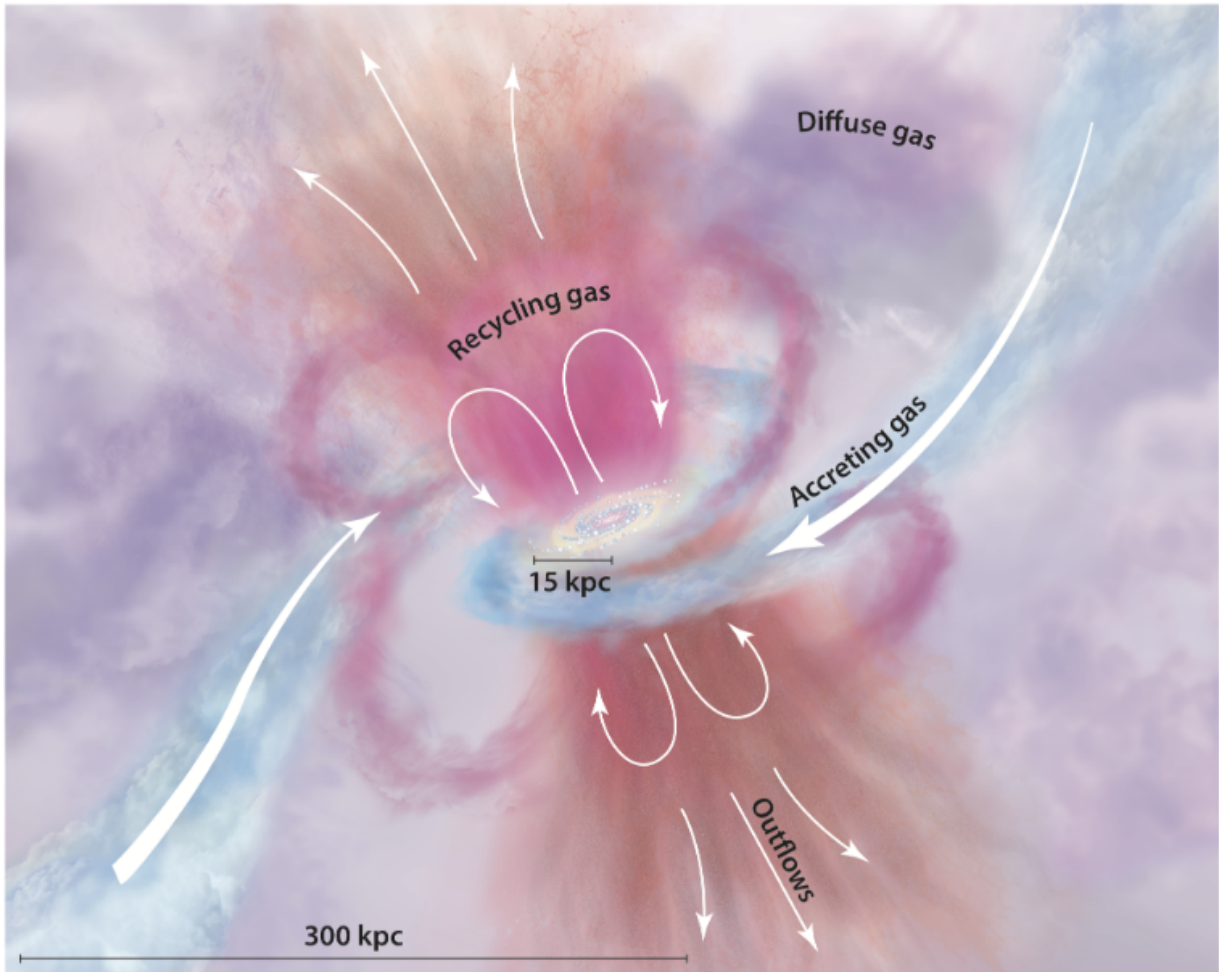


Figure 1.1 : A cartoon representation of the multiphase gas flows present near a star-forming galaxy, reproduced from [Tumlinson et al. \(2017\)](#). Gas, some combination of metal-enriched and pristine, forms stars; and the mechanical & radiation feedback from the most massive stars drives outflows into the halo while further metal-enriching the ambient gas.

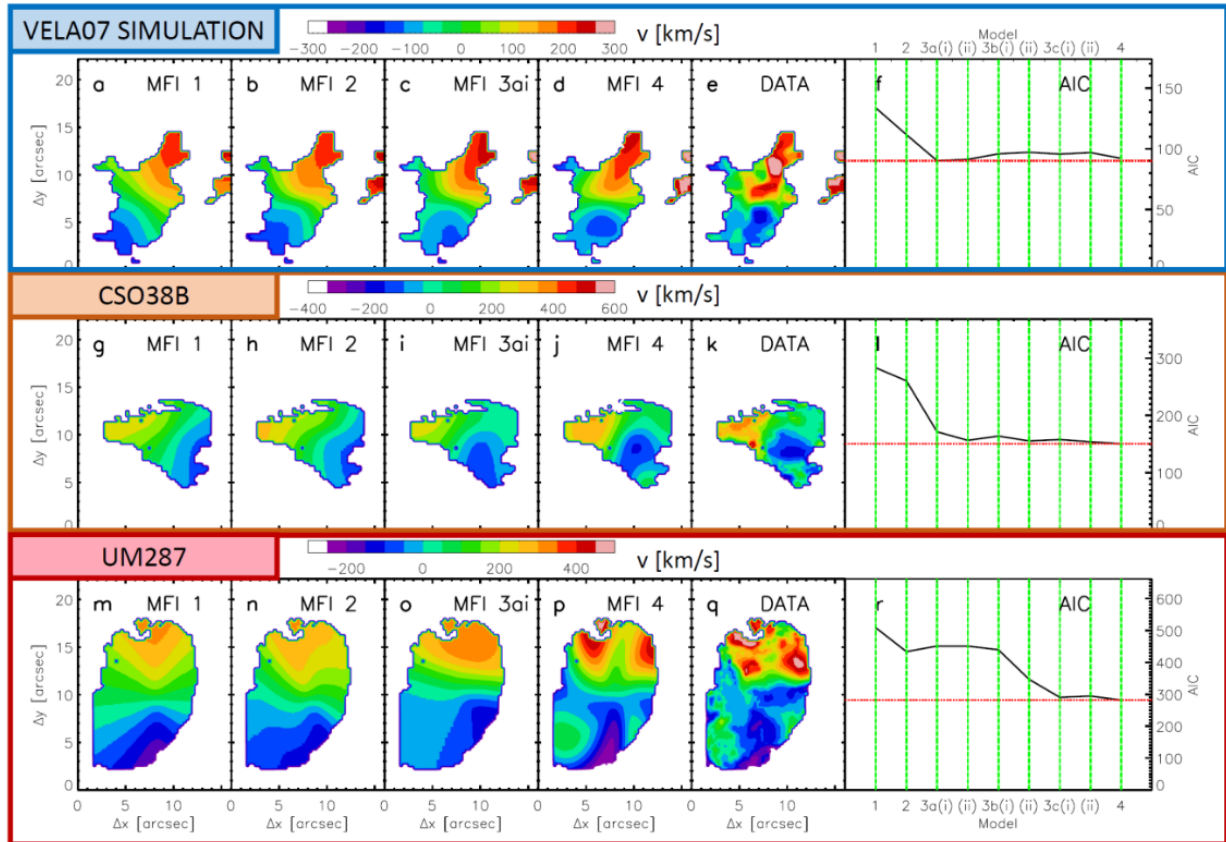


Figure 1.2 : Velocity maps of a simulated multi-component inflow impacting a star-forming disk (top row); and of two observed Lyman-alpha emitters (bottom two rows). Each system is fit by four models (left-most four columns in each row): Model 1 is a simple Keplerian disk in an NFW dark matter profile; Model 2 adds an isotropic radial collapse; Model 3ai replaces the radial collapse with a single collimated inflow; and Model 4 replaces the single inflow with a three-mode inflow, also adding azimuthal flows away from each source filament. The measured velocity map is shown in the second-from-right panel. The right-most panel shows the Akaike Information Criterion (AIC) for each model: this model diagnostic penalizes complex models. Despite these penalties, accretion from multiple sources is favored.

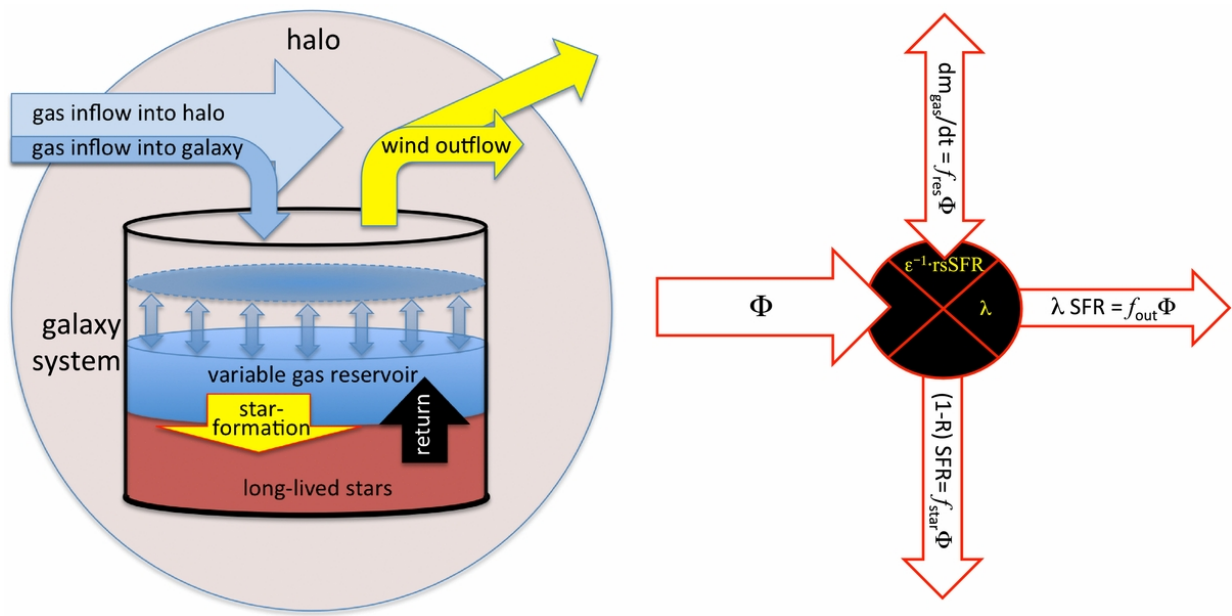


Figure 1.3 : A graphical representation of a gas-regulator or “bathtub” model of chemical evolution, reproduced from [Lilly et al. \(2013\)](#). Gas is introduced at a rate Φ , and its exhaustion by star-formation & winds, as well as its proportional return to the halo and disk, are dictated by the balance between Φ , λ , ϵ , and R , the parameters governing the gaseous inflow rate, the power of winds, the star-formation efficiency, and the mass fraction of old stars which do not produce appreciable quantities of metals.

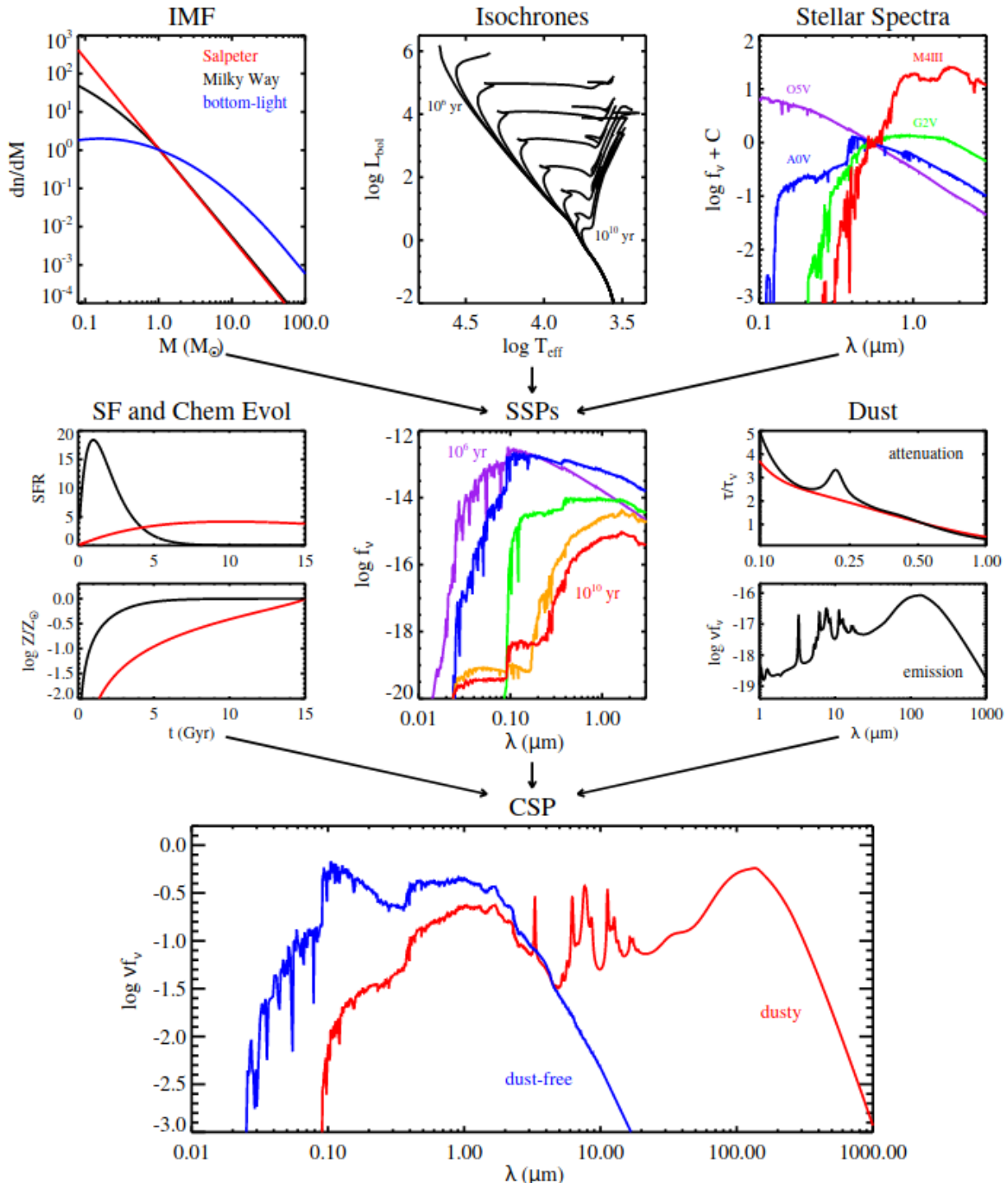


Figure 1.4 : A graphical overview of the components of stellar population synthesis, reproduced from Conroy (2013). Three example stellar initial mass functions (IMFs) are shown in the upper left panel, several stellar isochrones ($10^6 - 10^{10}$ yr) are shown in the top center panel, and four individual stellar spectra are shown in the top right panel. These three components are combined to form simple stellar populations (SSPs, center panel), which are themselves modulated by a star-formation history (SFH, middle left panel). After

Chapter 2

Resolved and Integrated Stellar Masses in the SDSS-IV/MaNGA Survey, Paper I: PCA spectral fitting & stellar mass-to-light ratio estimates

*A version of this chapter has previously appeared
in the Astrophysical Journal
Pace, et al. 2019, ApJ, 883, 82
and is notated P19a throughout this dissertation*

Abstract

We present a method of fitting optical spectra of galaxies using a basis set of six vectors obtained from principal component analysis (PCA) of a library of synthetic spectra of 40000 star formation histories (SFHs). Using this library, we provide estimates of resolved effective stellar mass-to-light ratio (Υ^*) for thousands of galaxies from the SDSS-IV/MaNGA integral-field spectroscopic survey. Using a testing framework built on additional synthetic SFHs, we show that the estimates of $\log \Upsilon_i^*$ are reliable (as are their uncertainties) at a variety of signal-to-noise ratios, stellar metallicities, and dust attenuation conditions. Finally, we describe the future release of the resolved stellar mass-to-light ratios as a SDSS-IV/MaNGA Value-Added Catalog (VAC) and provide a link to the software used to conduct this analysis¹

¹The software can be found at <https://github.com/zpace/pcay>, and the VAC (including a full datamodel and link to the latests data) at https://www.sdss.org/dr16/data_access/value-added-catalogs/?vac_id=manga-pca-vac.

2.1 Introduction

A galaxy's stellar mass is one of its most important physical properties, reflecting its current evolutionary state and future pathway. On the whole, more massive systems tend to possess older stellar populations (Gallazzi et al. 2005, 2006) with very little current star formation (Kauffmann et al. 2003; Balogh et al. 2004; Baldry et al. 2006), a small gas mass fraction (McGaugh & de Blok 1997), higher gas-phase metallicity (Tremonti et al. 2004), and stellar populations enhanced in α -elements relative to iron (Thomas et al. 2004, 2005). Fundamentally, a galaxy's stellar mass indicates the total mass of the dark matter halo in which it is embedded (Yang et al. 2003; Behroozi et al. 2013; Somerville et al. 2018): the higher the mass of the dark matter halo, the more evolved the galaxy tends to be, and the lesser the galaxy's capacity for future star formation.

Traditionally, two methods have been used to estimate galaxy stellar mass: kinematics and stellar population analysis. By measuring the average motions of stars, the dynamical mass (a distinct but related property which includes both baryonic and dark matter), can be determined. The DiskMass Survey (DMS, Bershady et al. 2010) used measurements of the vertical stellar and gas velocity field and stellar velocity dispersion σ_z^* , in concert with inferred values of disk scale height h_z to estimate the azimuthally-averaged dynamical mass surface density Σ^{dyn} of 30 local, low-inclination disk galaxies within several radial bins (Martinsson et al. 2013). However, dynamical measurements are subject to systematics related to the vertical distribution and scale height of stars, how the vertical velocity is measured (Aniyan et al. 2016, 2018), and the typical assumption of a constant stellar mass-to-light ratio used in Jeans-based estimates (Bernardi et al. 2017).

The second method of stellar mass estimation relies on comparing photometry or

spectroscopy of galaxies to stellar population synthesis (SPS) models. SPS weds theoretical stellar isochrones to theoretical model atmospheres or observed libraries of stellar spectra, under the constraint of the stellar initial mass function (IMF), in order to obtain an estimate of the mass-to-light ratio, and therefore, the mass. Tinsley (1972, 1973) defined the fundamentals of this method, combining the analytic expressions for the stellar IMF, star formation rates (SFR), and theory of chemical enrichment. Bell & de Jong (2001) and Bell et al. (2003) later took existing stellar models and described empirical relationships between optical colors and stellar mass-to-light ratios. Other approaches infer a star formation history (SFH) from broadband, multi-wavelength spectral energy distributions (SEDs): in such a case, the starlight itself can be observed in many bands (Shapley et al. 2005), or its indirect consequences can also be considered, such as infrared dust emission that arises after stars form (Dale et al. 2001). Software libraries such as MagPhys (da Cunha et al. 2008; da Cunha & Charlot 2011), Cigale (Burgarella et al. 2005; Giovannoli et al. 2011; Serra et al. 2011), and Prospector (Leja et al. 2017) take this approach, often (but not always) after adopting a family of SFHs. In short, estimates of stellar mass-to-light are generally made by finding the combination of simple stellar populations (SSPs; i.e., stars of a single age and metallicity) that produces the best match to an observed galaxy spectrum or photometry.

Simple SFH scenarios, such as Bell et al. (2003), produce almost-linear relationships (often referred to as color-mass-to-light relations, or CMLRs) between optical color and the logarithm of stellar mass-to-light ratio. This can be a convenient first tool, but there are significant systematics associated with stellar IMF, metallicity, and attenuation by dust (see Section 2.3.3). Often, different CMLRs produce extremely contradictory mass-to-light estimates (McGaugh & Schombert 2014). We demonstrate below that inferring stellar mass-to-light ratio from optical spectra offers some improvements over CMLRs.

Additionally, certain spectroscopic features—such as the strength of the 4000Å break (D_n4000 : [Bruzual A. 1983](#); [Balogh et al. 1999, 2000](#)), equivalent width of the H δ absorption line (H δ_A : [Worley & Ottaviani 1997](#)), and several other atomic and molecular indices (e.g. CN, Mgb, NaD: [Worley et al. 1994](#))—have been used to estimate mean stellar age, metallicity, activity of recent starbursts, and stellar mass-to-light ([Kauffmann et al. 2003](#); [Gallazzi et al. 2005](#); [Sil’chenko 2006](#); [Wild et al. 2007](#)). Spectral indices are akin to optical colors in that they are a lower-dimensional view on a galaxy’s spectrum, but a view designed to effectively capture an informative phase of stellar evolution.

The advent of large spectroscopic surveys with good spectrophotometric calibration has enabled more widespread use of full-spectral fitting: spectra spanning a large fraction of the visible wavelength range offer a much more detailed view on a galaxy’s SED, albeit within a smaller overall wavelength range than techniques which simultaneously examine UV, optical, infrared, and radio domains. Many software libraries exist for performing such analysis, including such as FIREFLY ([Wilkinson et al. 2015](#)), STECKMAP ([Ocvirk et al. 2006](#)), VESPA ([Tojeiro et al. 2007](#)), pPXF ([Cappellari & Emsellem 2004](#)), STARLIGHT ([Cid Fernandes et al. 2005](#)), and Pipe3D ([Sánchez et al. 2016a,b](#)). Very recent developments include techniques which simultaneously consider spectroscopic and photometric measurements ([Chevallard & Charlot 2016](#); [Thomas et al. 2017](#); [Fossati et al. 2018](#)).

The reliability of the resulting spectral fits is hampered by four main factors. First, certain phases of stellar evolution, such as the thermally-pulsating asymptotic giant branch (TP-AGB) stage, are still poorly understood, and this causes troublesome systematics ([Maraston et al. 2006](#); [Marigo et al. 2008](#)). Second, due to the degeneracy between stellar population age and metallicity, it is difficult to map spectral features uniquely to a combination of stellar populations. Modern spectroscopic surveys alleviate this somewhat with the inclusion of the NIR CaII triplet ([Terlevich et al. 1989](#); [Vazdekis et al. 2003](#)), a

feature that is sensitive to Calcium abundance (and secondarily, overall metal abundance) in stars older than 2 Gyr (Usher et al. 2018), as well as other spectral indices (Spinello et al. 2012, 2014), but care is still required. Third, the process of stellar population-synthesis relies on fully-populating the parameter space of temperature, surface gravity, metal abundance, and $[\alpha/\text{Fe}]$ (usually combining multiple stellar libraries, interpolating across un-sampled regions of parameter space, or patching with theoretical libraries). Fourth, it is unclear how to best recover the information contained in spectra: some approaches continue to model spectra as the sum of simple mono-age, mono-abundance SSPs; but it is possible that the resulting numerical freedom may produce un-physical results.

This work’s spectral-fitting technique follows Chen et al. (2012, hereafter C12): in C12, principal component analysis (PCA) was performed on a “training library” of synthetic optical spectra (the synthetic spectra were themselves produced using a stochastically-generated family of SFHs), yielding a set of orthogonal “principal component” (PC) vectors. PCA is a method of finding structure in a high-dimensional point process (Jolliffe 1986), which has been applied in the field of astronomy to such problems as spectral-fitting (Budavári et al. 2009), photometric redshifts (Cabanac et al. 2002), and classification of quasars (Yip et al. 2004; Suzuki 2006). PCA transforms data in many dimensions into fewer dimensions in a way that minimizes information loss. If a spectrum containing measurements of flux at l wavelengths is interpreted as a single data point in l -dimensional space, a group of n spectra forms a cloud of n points. PCA finds the q vectors (also called “eigenvectors”, “eigenspectra”, or “PCs”) that are best able to mimic the full, l -dimensional data. Equivalently, PCA finds a vector space in which the covariance matrix is diagonalized for those n spectra.

In the PCA-based spectral-fitting paradigm, a set of 4–10 eigenspectra were used as a reduced basis set for fitting observed spectra at low-to-moderate signal-to-noise. That is,

the best representation was found for each observed spectrum in terms of the eigenspectra. The goodness-of-fit was evaluated in PC space for each model spectrum in the training library: this was used as a weight in constructing a posterior PDF for stellar mass-to-light ratio. In this paradigm, the “samples” of the PDF are simply the full set of CSP models, which have known stellar mass-to-light ratio. In other words, the training library both defines the eigenspectra and provides samples for a quantity of interest. This process can be carried out on thousands of observed spectra (using tens of thousands of models) simultaneously, and is Bayesian-like because the training library acts as a prior on the “allowed” values of, for example, stellar mass-to-light ratio. Tinker et al. (2017) utilized the stellar mass-to-light ratio estimates from C12 to measure the intrinsic scatter of stellar mass at a fixed halo mass for high-mass BOSS galaxies, finding that PCA-based estimates of stellar mass correlated with total halo mass *better* than photometric mass estimates, a result suggesting that the PCA estimates are more accurate.

Though this work uses a method very similar to C12, we also integrate new model spectra generated with modern isochrones and stellar atmospheres. We apply this method to galaxy spectra from SDSS-IV/MaNGA (Mapping Nearby Galaxies at Apache Point Observatory, Bundy et al. 2015), an integral-field spectroscopic (IFS) survey of 10,000 nearby galaxies ($z \lesssim 0.15$). The MaNGA survey is designed to enhance the current understanding of galaxy growth and self-regulation by observing galaxies with a wide variety of stellar masses, specific star formation rates, and environments. We produce resolved maps of stellar mass-to-light ratio for a significant fraction of the 6779 galaxies included in MaNGA Product Launch 8 (MPL-8).

The structure of this paper is as follows: in Section 2.2, we discuss the MaNGA IFS data; in Section 2.3, we detail the procedural generation of star-formation histories and their optical spectra (the “training data”), a D_n4000 – $H\delta_A$ comparison between the model

library & actual observations, and why CMLRs do not recover sufficient detail about the underlying stellar mass-to-light ratio; in Section 2.4, we review the underlying mathematics of PCA, present its application to parameter estimation—concentrating, in particular, on why we might expect improvement over traditional methods in the case of IFS data—and examine the reliability of the resulting estimates of stellar mass-to-light ratio in relation to degenerate parameters like metallicity and attenuation; and in Section 2.5, we provide example maps of stellar mass-to-light ratio for a selection of four late-type galaxies and three early-type galaxies, discussing possible future improvements to the spectral library, and outlining a future release of resolved stellar mass-to-light ratio maps. To complement this work’s investigation of random errors in PCA-based estimates of stellar mass-to-light ratio, in Pace et al. (2019, hereafter MaNGA-PCA Paper II), we compare resolved maps of stellar mass surface density (derived from stellar mass-to-light ratio estimates made in this work) to estimates of dynamical mass surface density from the DiskMass Survey, in a view on the systematics of PCA-derived stellar mass-to-light ratios; and construct aperture-corrected, total stellar masses for a large sample of MaNGA galaxies.

2.2 Data

This work employs IFS data from the MaNGA survey, part of SDSS-IV (Blanton et al. 2017). MaNGA is the most extensive IFS survey undertaken to date, targeting 10,000 galaxies in the local universe ($0.01 < z < 0.15$), with observations set to complete in early 2020 (Bundy et al. 2015). MaNGA’s instrument is built around the SDSS 2.5-meter telescope at Apache Point Observatory (Gunn et al. 2006) and the SDSS-BOSS spectrograph (Smee et al. 2013; Dawson et al. 2013), which has a wavelength range of 3600 to 10300 Å and spectral resolution $R \sim 2000$. The BOSS spectrograph is coupled to close-packed fiber hexabundles (also called integral-field units, or IFUs) with between 19 and

127 fibers subtending 2" apiece on the sky (Drory et al. 2015). The IFUs are secured to the focal plane with a plugplate (York et al. 2000), and are exposed simultaneously. Flux-calibration is accomplished with 12 seven-fiber “mini-bundles” which observe standard stars simultaneous to science observations (Yan et al. 2016b), and sky-subtraction uses 92 single fibers spread across the three-degree focal plane.

MaNGA observations use only dark time, and require three sets of exposures, which are accumulated until a specified threshold signal-to-noise is achieved (Yan et al. 2016a). Additionally, all constituents of each set of exposures must be taken under similar conditions. A three-point dither pattern is used to increase the spatial sampling such that 99% of the area within the IFU is exposed to within 1.2% of the mean exposure time (Law et al. 2015). This also accomplishes a more uniform sampling of the plane of the sky than non-dithered observations, and gives a closer match to the fiber point-spread function: a typical fiber-convolved point-spread function has FWHM of 2.5" (Law et al. 2015).

The MaNGA survey primarily targets galaxies from the NASA-Sloan Atlas v1_0_1 (NSA, Blanton et al. 2011). The survey’s science goals guide the specific target choices made: in particular, two-thirds of targets (the “Primary+ sample”) are covered to 1.5 effective radii (R_e), and one-third (the “Secondary sample”) are covered to 2.5 R_e . MaNGA targets are selected uniformly in SDSS *i*-band absolute magnitude (Fukugita et al. 1996; Doi et al. 2010), which will result in an approximately-flat distribution in the log of stellar mass (Wake et al. 2017). Further, within a prescribed redshift range corresponding to a given absolute magnitude, the MaNGA sample is selected to be volume-limited. Absolute magnitudes have been calculated using K-corrections computed with the `kcorrect v4_2` software package (Blanton & Roweis 2007), assuming a Chabrier (2003) stellar initial mass function and Bruzual & Charlot (2003) SSPs, and are tabulated in the DRPALL catalog file.

The MaNGA Data Reduction Pipeline (DRP: Law et al. 2016) reduces individual

integrations into both row-stacked spectra (RSS), which behave like collections of single-fiber pointings; and rectified data-cubes (CUBE), which are constructed from the RSS with a modified Shepard’s algorithm to produce a spatially-uniform grid on the plane of the sky with spaxels measuring 0.5 arcsecond on a side. This work uses CUBE products with logarithmically-uniform wavelength spacing ($d \log \lambda = 10^{-4}$, $d \ln \lambda \approx 2.3 \times 10^{-4}$)², also called LOGCUBE products. LOGCUBE products are then analyzed further, using the MaNGA Data Analysis Pipeline (DAP: [Westfall et al. 2019](#)), which produces resolved measurements (referred to as “MAPS”) of stellar and gas line-of-sight velocity, the stellar continuum, gaseous emission fluxes, and spectral indices.

The 1773 galaxies analyzed in this study are drawn randomly from MaNGA Product Launch 8 (MPL-8), an internally-released set of both reduced and analyzed observations numbering 6779 galaxies observed between March 2014 and July 2018. MPL-8’s reduced products number nearly 2100 more than SDSS DR15 ([Aguado et al. 2019](#)), which was released in December 2018.

This study uses both DRP-LOGCUBE and DAP-MAPS products. The DAP-MAPS products (at this time released only within the SDSS collaboration) are not spatially-binned for the stellar continuum fit (see [Westfall et al. 2019](#)) (i.e., this work uses the “SPX” products). We apply no sample cuts. The distribution of the median spectral signal-to-noise ratio of all MaNGA spaxels is shown in Figure 2.1: spectral channels flagged at the MaNGA-DRP stage as either having low or no IFU coverage, or with known unreliable measurement, have had their inverse-variance weight set to zero (spaxels with such issues affecting their spectra form the low-SNR tail of the distribution).

²In this work, the notation \log denotes a base-10 logarithm, and \ln denotes a base- e logarithm.

2.3 The Composite Stellar Population Library

In order to generate the eigenvectors composing the principal component space, we first generate training data using theoretical models of SFHs. Training spectra are generated by passing a piecewise-continuous star formation history (according to a randomized prescription described below) through a stellar population synthesis library, after assuming a stellar initial mass function (IMF), a set of isochrones, and a stellar library. In this case, the `fortran` code **Flexible Stellar Population Synthesis** (**FSPS**) (Conroy et al. 2009, 2010; Conroy & Gunn 2010) and its `python` bindings (Foreman-Mackey et al. 2014) were used. Padova 2008 (Marigo et al. 2008) isochrones were adopted.

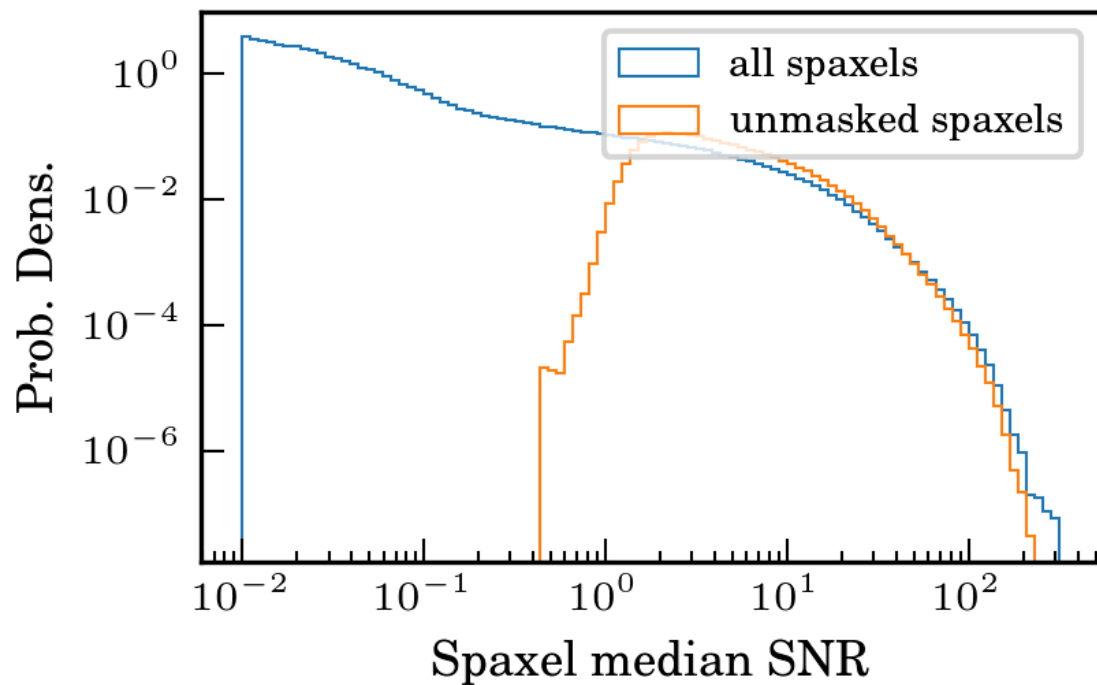


Figure 2.1 : The distributions of median spectral signal-to-noise ratio for all MaNGA spaxels (blue) and those spaxels for which none of the MaNGA DRP data-quality flags indicate potential problems with the estimates obtained in this work (orange)—see Section 2.4.9 for descriptions of data-quality diagnostics, and how channel-specific quality flags inform reliability of mass-to-light ratio estimates.

The unpublished C3K library of theoretical stellar spectra (Conroy, in prep.) was used for the population synthesis: the library is based on the Kurucz frameworks (routines and line lists)edit2, and the native resolution is $R = 10,000$ from 1500Å to 1.1 μ m. Though most similar studies employ empirical stellar libraries (e.g. MILES or E-MILES: [Vazdekis et al. 2010, 2016](#)), there is at this time no widely-used library which closely matches the MaNGA wavelength range and resolution while covering the full stellar age and metallicity range expected in MaNGA. The latest E-MILES stellar population models, for instance, match MaNGA resolution and wavelength range, but have few stars younger than 0.1 Gyr at solar metallicity and above (see [Vazdekis et al. 2016](#), Figures 5 and 6).

2.3.1 SFHs and stellar population properties

In order for the PCA model to emulate observed galaxy spectra, it must first be “trained” to recognize what they can look like (that is, PCA “learns” which wavelengths tend to vary together, and how strongly). By generating a plausible library of SFHs and their associated spectra, we provide the initial guidelines informing how real, observed spectra are fit. Since any fit to an observed spectrum must fall within the circumscribed domain of the training data, it is important to make that training data permissive enough to encompass physical reality. With too restrictive a training set, fits would suffer from additional systematic bias. As such, our SFH template parameters are intended to have weakly informative priors ([Simpson et al. 2014; Gelman & Hennig 2015](#)) which encompass the areas of parameter space that are physically allowable and in line with previous studies (to this point, see the below description of the mass weighted mean stellar age distribution, Figure 2.6), while allowing only a relatively small proportion of more complex models (e.g., those involving bursts or a transition in SFH behavior).

Distributions of most parameters provided to **FSPS**, selected resulting stellar absorp-

tion indices, and other derived parameters of interest are respectively shown in Figures 2.2, 2.3, and 2.4, in addition to the full-text descriptions provided below.

2.3.1.1 SFH families: the delayed- τ model

C12 based the adopted family of SFHs on a tau (declining exponential) model:

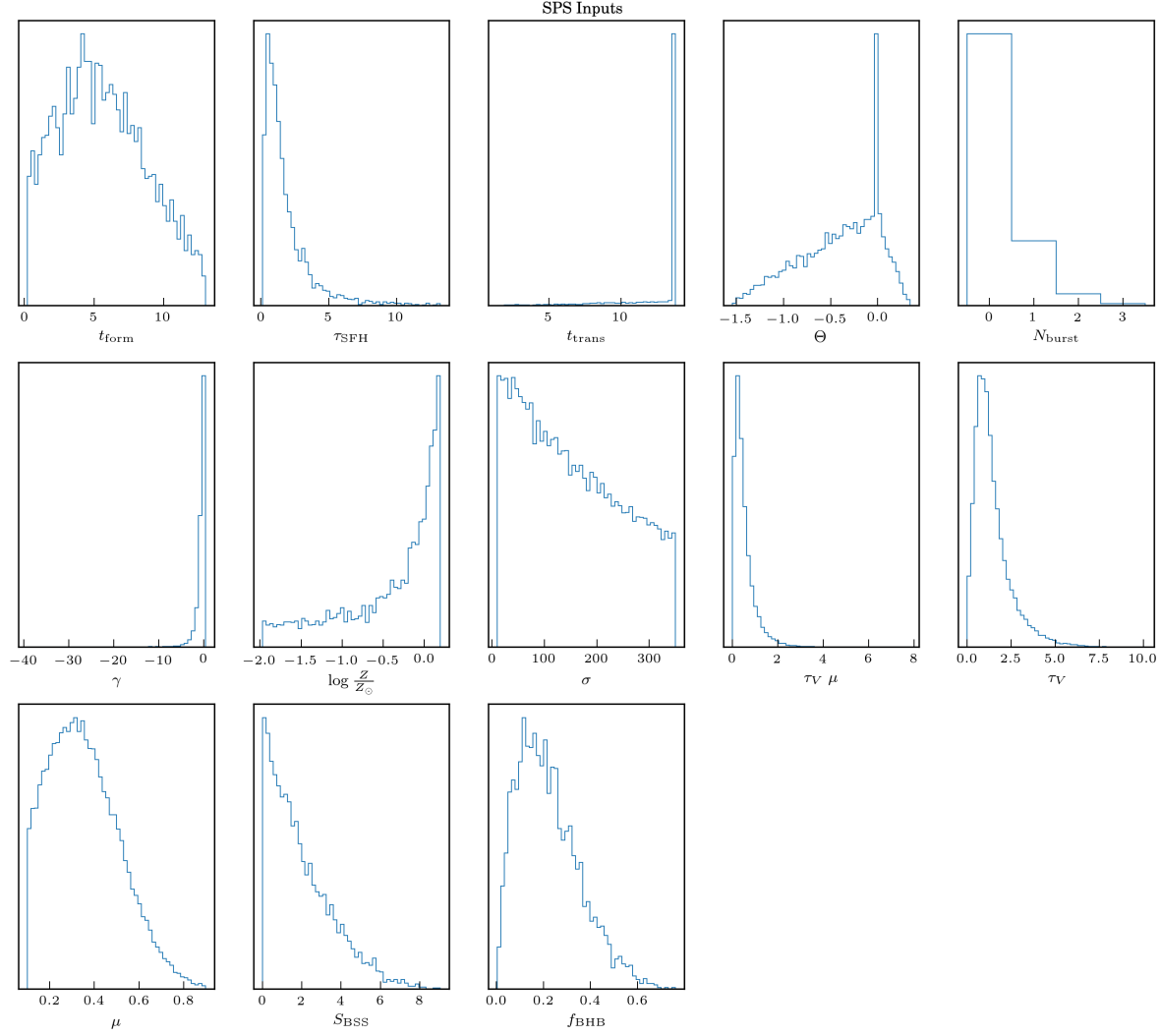


Figure 2.2 : The distributions of the inputs provided to FSPS described in more detail in Section 2.3.1.1, left to right and top to bottom: formation time, e-folding time, transition time, transition strength, transition slope, number of bursts, stellar metallicity, stellar velocity dispersion, attenuation, specific frequency of blue straggler stars, and fraction of blue horizontal branch stars. There is no covariance between these parameters.

additionally, one or more stochastic bursts were permitted, and a fraction of SFHs cut off rapidly, in order to emulate post-starburst galaxies at high redshifts (Kriek et al. 2006, 2009). However, merely allowing a *cutoff* in the SFH does a poor job at reproducing the more vigorously-star-forming outer regions of disk galaxies, which do have older stars, but whose SFHs are shown in both observations and cosmological simulations to rise through the present day (Pacifici et al. 2012, 2013). Simha et al. (2014) found that a more flexible delayed- τ model (also referred to as “lin-exp”) plus stochastic bursts and an

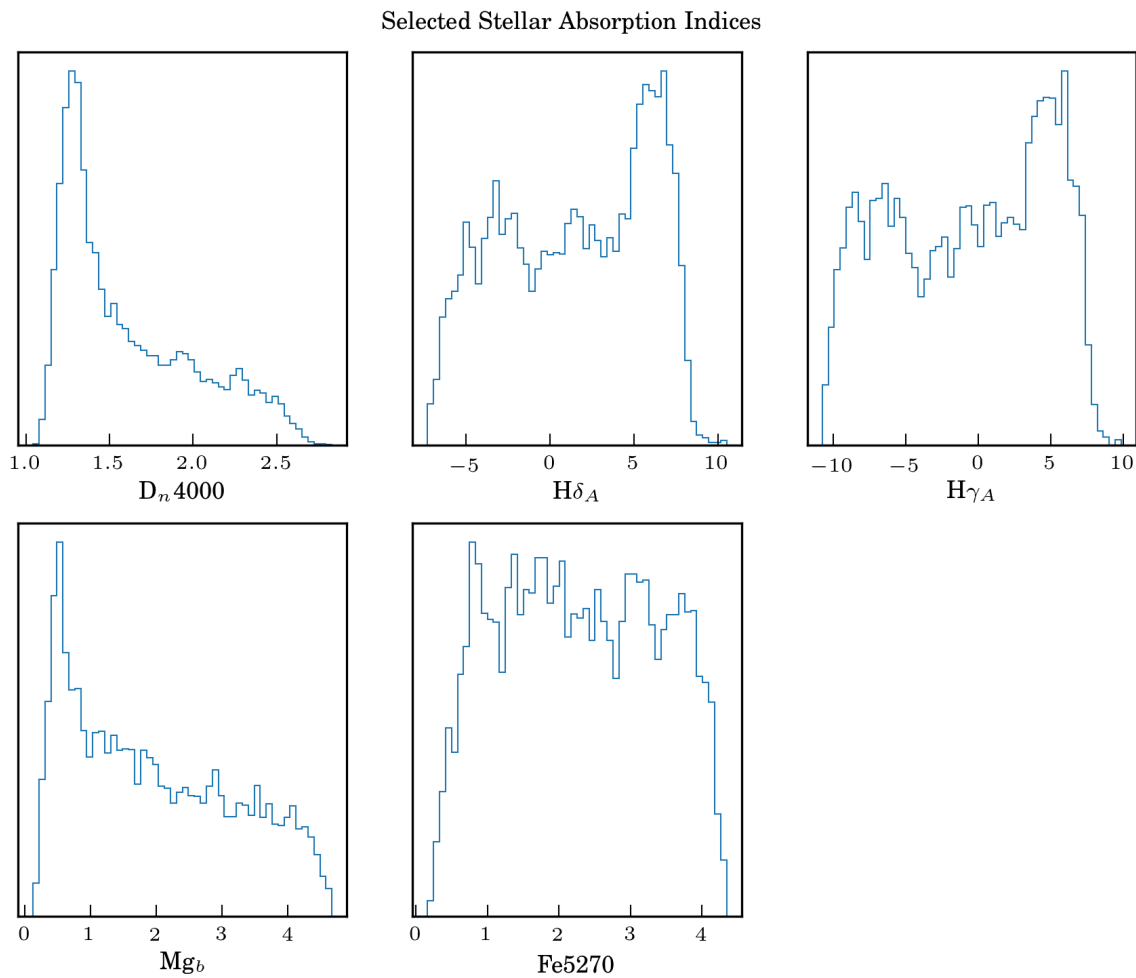


Figure 2.3 : The distributions of five absorption indices in our synthetic training data: D_n4000 , $H\delta_A$, $H\gamma_A$, Mg_b , and $Fe5270$.

optional subsequent ramp up (rejuvenation) or down (cutoff) effectively decouples late from early star-formation, and provides a better fit to photometric data. As such, we adopt this slightly more complicated framework.

The most basic delayed- τ model is parametrized by a starting time (before which the SFH is identically zero) and an e -folding timescale (which sets the shape of the SFH). Each

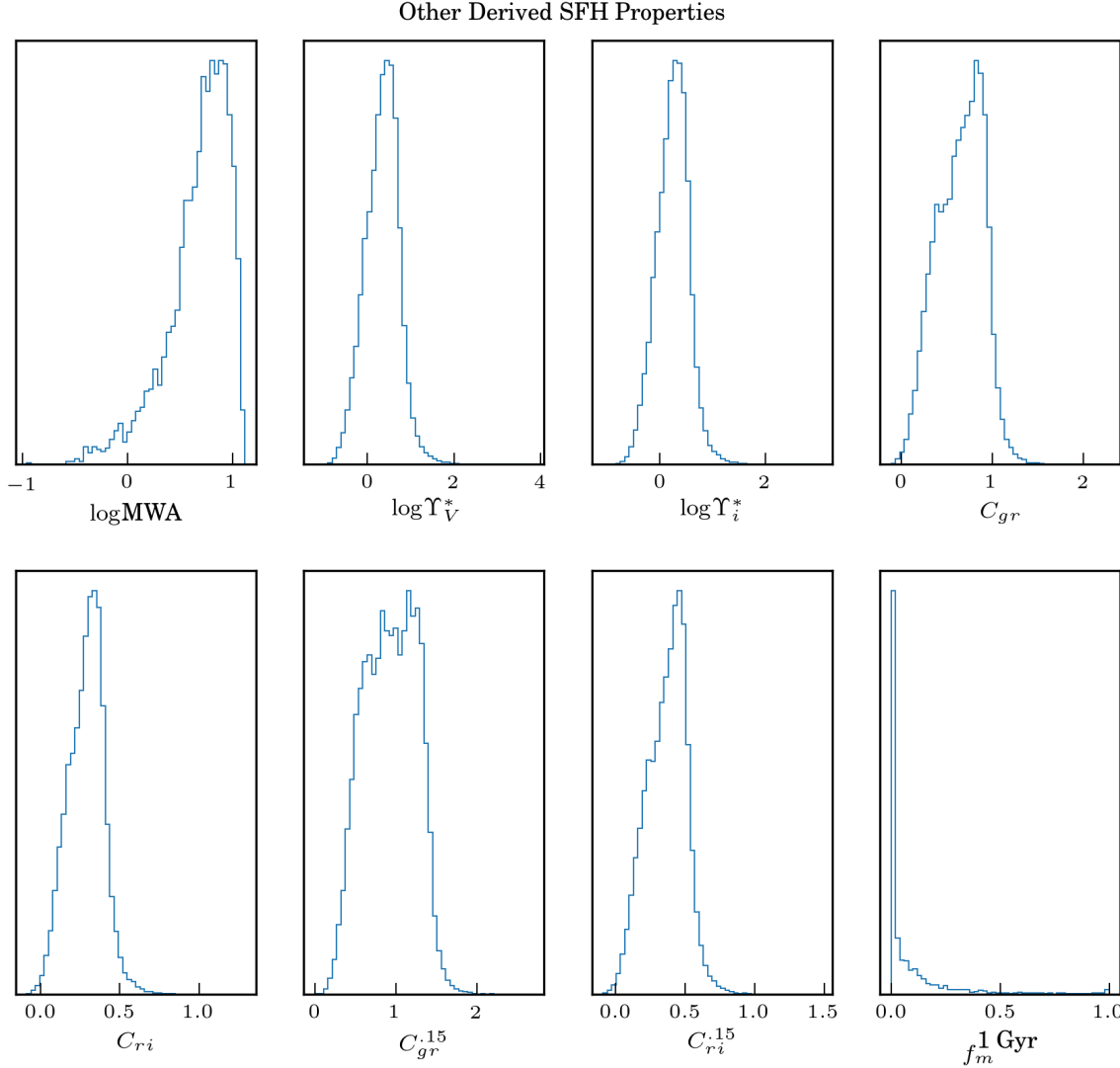


Figure 2.4 : The distributions of eight derived parameters which are secondarily obtained from the SPS, using the distributions of inputs shown in Figure 2.2: mass-weighted stellar age, stellar mass-to-light ratios in V & i bands, rest-frame $g - r$ and $r - i$ color, the same colors at redshift of 0.15, and fraction of stellar mass formed in the past 1 Gyr.

are drawn from a smooth distribution:

- *Formation time* (t_{form}), drawn from a normal distribution with mean of 5 Gyr and width of 4 Gyr, and which truncates below 0.2 Gyr and above 13.0 Gyr. This broad distribution is similar to the uniform distribution adopted in C12.
- *e-folding timescale of the continuous component* (EFTU), which has a log-normal distribution centered at $\log \frac{\mu}{\text{Gyr}} = 0.4$ and with $\log \frac{\sigma}{\text{Gyr}} = 0.4$. The distribution truncates below 0.1 Gyr and above 15 Gyr. Since the peak of the $te^{-t/\tau}$ has its peak at an interval τ after formation, this broad distribution of e-folding times allows SFHs that form quickly, as well as those that continue to rise until the present day.

The prevalence, duration, and strength of merger-induced bursts have been investigated in Tree-SPH and N-body sticky-particles simulations (Di Matteo et al. 2008). Though such simulations lack the resolution to model gas cooling to molecular-cloud temperatures, they are useful simply as order-of-magnitude guidance. Di Matteo et al. (2008) also found that most merger-driven bursts last several 10^8 years, with the vast majority lasting less than 1 Gyr, which informs the upper-limit for burst duration shown below. Gallazzi & Bell (2009) conclude that recent bursts are necessary to reproduce the full space of stellar absorption features, simultaneously warning that *overestimating* the number of bursts could result in systematically-low mass-to-light ratios for galaxies dominated by a continuous SFH.

We express the strength of a burst in terms relative to the peak of the underlying lin-exp model: that factor is simply added to the latent SFR at all times in the range $[t_{burst}, t_{burst} + dt_{burst}]$. Finally, we note that we do not model stochastic, short-timescale (several to tens of Myr) variations in SFR, primarily due to computational concerns. Conceivably, for sufficiently young (< 1 Gyr) stellar populations, anomalously-steady

models (i.e., SFHs that are *too smooth*) could induce a negative systematic in stellar mass-to-light ratio (effecting an additional, intrinsic scatter in the SFH parameter space). The bursts are generated according to the following randomized prescription:

- *Number of bursts* (n_{bursts} , an integer) giving the number of starbursts. The value is generated by a Poisson distribution with a mean and variance $\frac{0.5 \times (t_0 - \min(\{t_t\}, t_{form}))}{t_0}$.

That is, if a SFH were to initiate immediately at $t = 0$ Gyr and not be cut off, the average number of bursts would be 0.5. Functionally, most SFHs experience zero stochastic bursts, and the mean number of bursts per SFH is 0.256.

- *Burst amplitudes* (A , a list with n_{bursts} elements). Individual values in A are distributed log-normally between 0.1 and 10, and indicate the addition of A times the maximum value of the pure delayed- τ model during the times when the burst is active.
- *Burst times* (t_{burst} , a list), whose length is the same as A , and whose elements are uniformly distributed between t_{form} and t_0 (or t_t , if there is a cutoff).
- *Burst duration* (dt_{burst} , a list) which specifies the duration for each burst, uniformly distributed between 0.05 and 1 Gyr.

The delayed- τ model with bursts is further modulated by conservative allowances for a cutoff/rejuvenation at late times:

- *Transition probability* (p_t), a 25% chance of either a rejuvenation or a cutoff in the SFH at time t_t , under the assumption that most SFHs are smoothly-varying.
- *Transition time* (t_t), after which star formation may occasionally (as dictated by p_t) cut off or revive. This may occur with equal probability after $t_{form} + EFTU/4$ until

the present day (at the smallest allowable value, such a SFH functions like a brief starburst which could last as little as 25 Myr). If p_t dictates there is no burst, t_t is set to the age of the universe, and thus never impacts the SPS.

- *Transition strength* θ , specifying an “angle” in time-SFR space, such that $\theta = 0$ corresponds to a SFR held constant after t_t and $\theta = \frac{\pi}{2}$ corresponds to an immediate cutoff in the SFH. θ is distributed according to a triangular distribution rising from zero in the domain $\frac{\pi}{2} < \theta \leq 0$, and falling back to zero in the domain $0 < \theta \leq \frac{\pi}{6}$. If p_t dictates there is no burst, θ is set to zero, but does not impact the SPS because t_t is set to the age of the universe.
- *Cutoff slope* is an arctan-re-parametrization of θ , scaled in units of the maximum of a pure delayed- τ model Φ_{max} per Gyr. Therefore, $\gamma = 0$ corresponds to a perfectly constant SFR after t_t , and $\gamma = -1.0$ to a reduction in the SFR by Φ in 1 Gyr.

These specific parameter distributions were chosen to produce the best match to the joint distribution of moderate- and high-signal-to-noise MaNGA spectra in $D_n4000-H\delta_A$ space (see Section 2.3.2). Compared with C12, t_{form} is peaked more strongly at intermediate times, and EFTU is permitted to be less than 1 Gyr (and indeed, $\sim 40\%$ are). Additionally, starbursts occur on average less frequently in this work, but with stronger amplitude, since C12 considered spatially-unresolved spectra (whose bursts have been “spatially-averaged” to a greater probability, but lower mean strength). A sample of ten SFHs, drawn randomly from this prescription, is shown in Figure 2.5.

Previous analyses of SDSS central spectroscopy have derived distributions of mass-weighted mean stellar age (MWA) for galaxies in the nearby universe: for example, Gallazzi et al. (2005), following Kauffmann et al. (2003), reports a distribution of mass-weighted mean stellar age (MWA) derived from fits to high signal-to-noise spectra. The Gallazzi

[et al. \(2005\)](#) MWA distribution strongly resembles the distribution from this work’s model library (Figure 2.6). This work’s model library has a more probable low-MWA tail, and a significantly younger mode. As the galaxy disks sampled by MaNGA have a diversity of ages (both young and old) compared to the central regions sampled in SDSS-I spectroscopy, this is a positive characteristic. The model MWA distribution from this work also bears similarity to the MWA distribution derived from integrating the [Madau & Dickinson \(2014\)](#) cosmic star formation rate density: [Madau & Dickinson \(2014\)](#) report a young-age tail, which this work’s prior easily encompasses, but has a mode at nearly 10Gyr (about twice as old as the mode of this work’s model libraries). No value judgment is made here regarding a particular MWA distribution; that said, noting MWA distributions’ changes in shape resulting from manipulating the CSP inputs has proven informative in constructing a flexible training library.

Line color	t_f	EFTU	t_t	θ
C0 (Tableau Blue)	9.14	1.40	12.13	-1.36
C1 (Tableau Orange)	1.01	2.38	5.78	-1.43
C2 (Tableau Green)	5.71	1.27	13.01	0.13
C3 (Tableau Red)	3.02	1.29	5.25	-0.70
C4 (Tableau Purple)	0.96	5.18	7.10	-0.04
C5 (Tableau Brown)	4.71	0.50	12.90	0.13
C6 (Tableau Pink)	1.78	2.61	-	-
C7 (Tableau Gray)	8.09	2.10	10.37	-0.92
C8 (Tableau Olive)	7.00	3.39	13.25	-0.59
C9 (Tableau Cyan)	8.85	3.88	-	-

Table 2.1 : Selected CSP parameters for the SFHs shown in Figure 2.5. For each CSP, we list the line color, the formation time t_f , the e-folding time of the continuous component (EFTU), the transition time t_t , and the transition strength θ . Models with no transition behavior have the t_t and θ columns left blank.

2.3.1.2 Stellar composition & velocities, attenuation, and uncertain stellar evolution

Since the star-forming ISM is known to enrich with heavy elements as successive generations of stars form, it is most correct to consider both a metallicity history and a star formation history. Though gaseous emission captures the current enrichment state, it is subject to significant differences in interpretation, including concepts as fundamental as the zeropoint (Stasińska 2007). Certain stellar absorption indices, particularly those targeting magnesium (Barbuy et al. 1992), reflect the average enrichment state of the stars. However, the Mg-based indices in particular are not reliable at low metallicity (Maraston et al. 2003). In addition, there is some evidence that when trying to fit a population

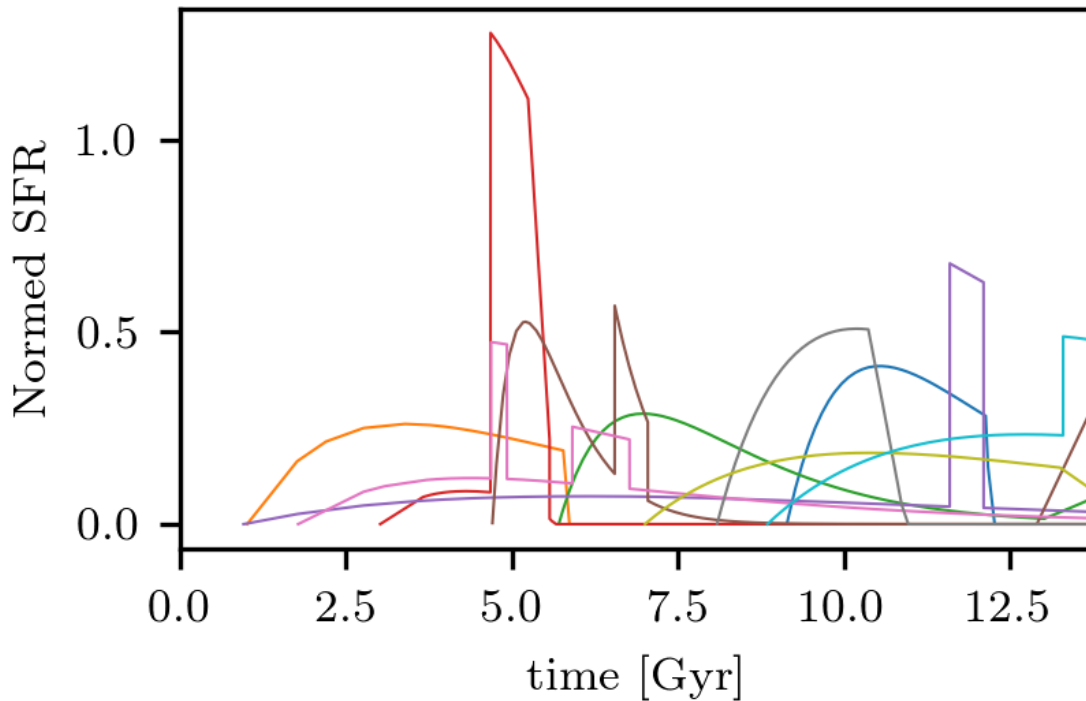


Figure 2.5 : Ten sample SFHs generated using the random prescription given in Section 2.3.

with known-evolving metallicity using a single, non-evolving stellar metallicity, absorption index-based estimates of stellar mass-to-light ratio suffer from smaller biases than do color-based estimates. This is because stellar mass-to-light ratio varies in the $D_n4000 - H\delta_A$ plane in a very similar way, when fixed- and evolving-metallicity populations are compared (see [Gallazzi & Bell 2009](#), Section 5). Finally, in order to properly consider a SFH with an evolving metallicity, additional parameters must be introduced to capture inflows, outflows, and feedback ([Matteucci 2016](#)). Section 2.3.2 briefly outlines a comparison made between spectral indices such as D_n4000 and $H\delta_A$ measured in the models and in the observations, and supports the assertion that non-evolving metallicities suffice for our purposes.

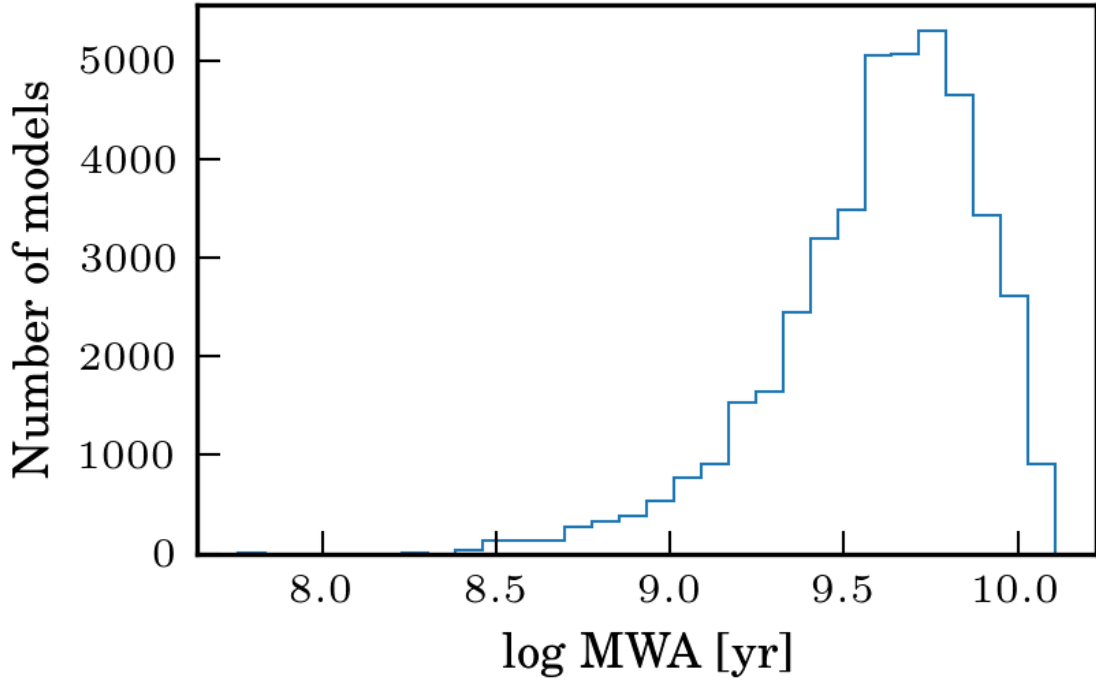


Figure 2.6 : The distribution of the log of mass-weighted mean stellar age for all of the template SFHs. As in [Gallazzi et al. \(2008\)](#), the distribution has a broad peak around $\log \text{MWA} \sim 9.8$. Unlike [Gallazzi et al. \(2008\)](#), though, the distribution extends with significant power below $\log \text{MWA} \sim 9.0$, meaning that more recent star-formation is permitted.

With these considerations in mind, we do not implement any chemical evolution prescription, instead adopting SFHs with non-evolving stellar metallicities. Each SFH model is assigned a single metallicity $[Z]$, constant through time, which has an 80% chance to be drawn from a metallicity distribution that is linearly-uniform, and a 20% chance to be drawn from a metallicity distribution that is logarithmically-uniform. This allows a small, but well-populated low-metallicity tail. Figure 2.7 compares the gas-phase oxygen abundance from the SDSS MPA-JHU catalog (Tremonti et al. 2004) to the adopted metallicity prior, after a zeropoint normalization (Asplund et al. 2009). These distributions should be (and are) roughly similar, since the chemical composition of the gas reflects how baryons are cycled through stars and enriched successively by several generations of star-formation.

Two uncertain phases of stellar evolution, blue horizontal branch (BHB) and blue straggler stars (BSS), are also modulated in prevalence: while they can affect stellar mass-to-light ratio estimates by ~ 0.1 dex for the intermediate-age populations found in galaxy disks (Conroy et al. 2009), there are precious few precise enough measurements of either of their abundances to inform this work’s CSP library. Adopting smooth and permissive priors for these less-well-constrained parameters avoids unjustified restrictions on the resulting spectral fits. In reality, we are in most cases unable to further constrain these parameters based on our fits to spectra (see Section 2.4 and Appendix B), but we also lack the observational constraints from stellar-evolution to choose one value in particular.

While BHB stars are likely more common at low metallicity, it is inadvisable to neglect them for other cases Conroy et al. (2009). As such, we draw their fraction by number (f_{BHB}) from a beta-distribution with shape parameters $\alpha = 2$ and $\beta = 7$: this distribution is restricted to lie between zero and one, and represents a plausible range of BHB incidence rates. Specific BSS frequency (S_{BSS} , defined with respect to *all* horizontal branch stars)

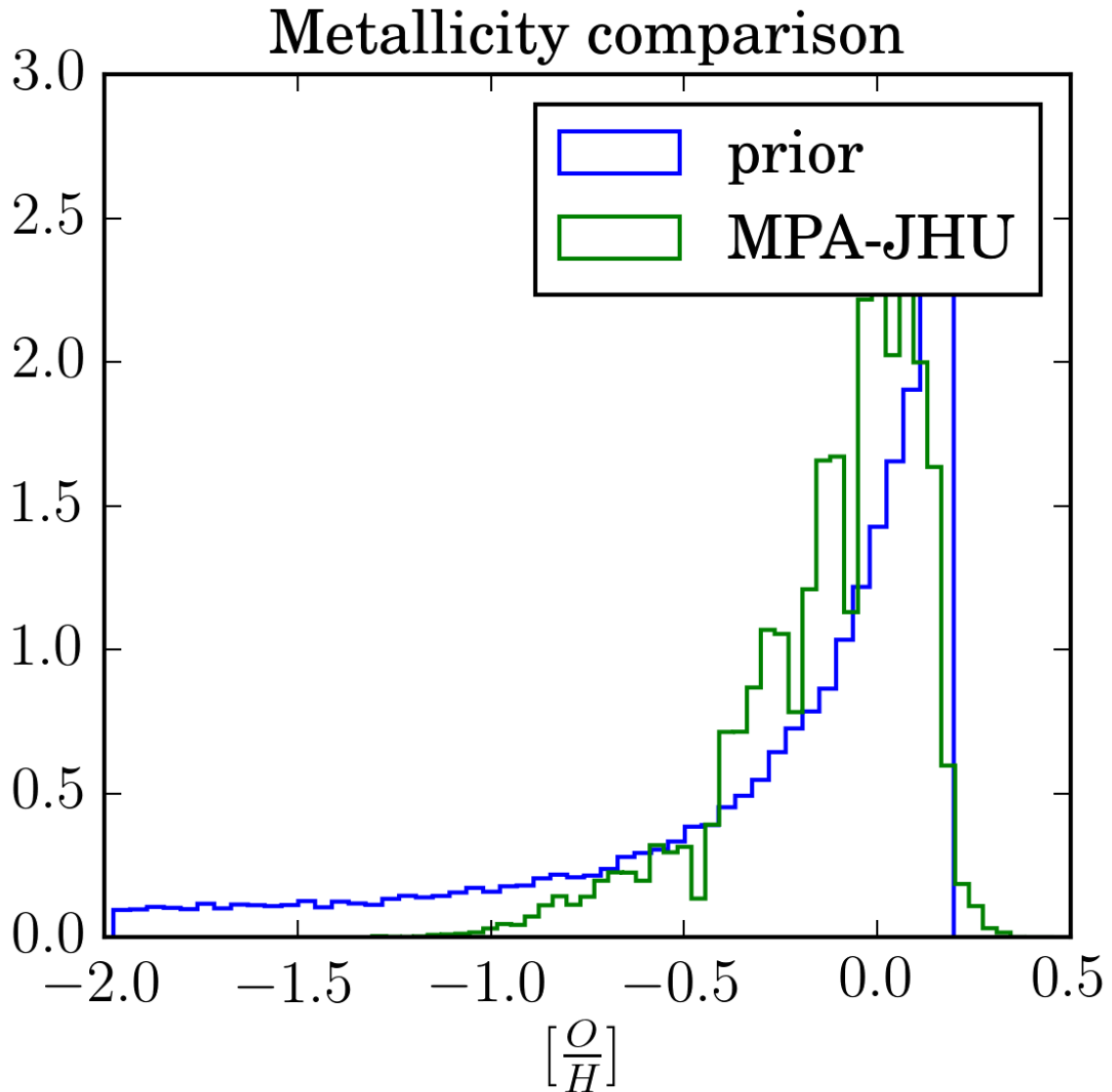


Figure 2.7 : Comparison of the solar-normalized oxygen abundance ($[\frac{O}{H}]$) inferred from SDSS nebular emission (*green*) with the adopted metallicity prior. An offset of approximately -.29 dex is applied to re-scale the SFH library's metallicity range ($[Z]$, based on mass) to the number-abundance of oxygen from the SDSS data, since the two adopt different values of solar metallicity and oxygen abundance.

is known to vary somewhat with environment, but is not constrained well in an absolute sense by observations (Santucci et al. 2015). The binary mass-transfer pathway for BSS formation (Gosnell et al. 2014) implies that any factors (e.g., environment or metallicity) affecting star formation could also manifest in the BSS population. Furthermore, Piotto et al. (2004) noted that BSS frequency is lower in clusters than in the field, in a way not explained by the expected increased collision rates in clusters. As such, we adopt a broad distribution, 10 times the value of a draw from a beta distribution with shape parameters $\alpha = 1$ and $\beta = 4$ —which allows the full range of 0.0–0.5 adopted by Conroy et al. (2009), is more permissive at the high end than the estimates of Dorman et al. (1995), and peaks at approximately 0.2.

Attenuation of the starlight is accomplished using a two-component dust model (Charlot & Fall 2000). In this model, all stars are attenuated by diffuse dust with a V-band optical depth $\tau_V\mu$ and power-law slope of -0.7 (as in Chevallard & Charlot 2016; da Cunha et al. 2008); while stars younger than 10 Myr are further attenuated by the dense ISM with optical depth $\tau_V(1 - \mu)$ and power-law slope of -1.3. Therefore, a young stellar population will in total experience an optical depth of τ_V , discounting effects resulting from different dust law slopes. In our schema, $\tau_V\mu$ and μ are randomized directly (rather than τ_V and μ individually), because all stellar populations experience $\tau_V\mu$, meaning that it is a more effective parameter most of the time:

- The *product* $\tau_V\mu$ is drawn from a normal distribution with mean 0.4 and standard deviation 0.2, truncated at 0 and 1.2.
- *Fractional optical depth of the diffuse ISM* (μ), drawn from a normal distribution with mean of 0.3 and standard deviation of 0.2, truncated at 0.1 and 0.9.
- *Optical depth of young birth clouds* (τ_V), the quotient $\frac{\tau_V\mu}{\mu}$.

These distributions were chosen such that their means correspond roughly to the “standard” values given in Charlot & Fall (2000), with significant latitude to allow for both unobscured and highly-obscured stellar populations. The overall distribution has a similar mode to, but is broader (i.e., more permissive at the high end) than the attenuation distribution for star-forming galaxies found in Brinchmann et al. (2004) by fitting emission lines with photoionization models.

Stellar velocity dispersion (σ) is also varied, and is drawn from a truncated exponential distribution with lower-limit of 10 km s^{-1} , upper-limit of 350 km s^{-1} , and e-folding scale of 350 km s^{-1} . This is intended to populate both the low- σ stellar disk and the high- σ bulge. This does not include the wavelength- and redshift-varying contribution of the instrumental line-spread function (LSF), which is accounted for separately (see Appendix A).

Each SFH is initialized with several different sets of dust properties (τ_V and μ) and velocity dispersion (σ), for computational reasons. In addition to easing the processing load, this ensures a complete population of the parameter space at significantly lower computational cost (in total, 4000 CSPs were generated, each of which has 10 combinations of attenuation and velocity dispersion.) Subsampling in velocity dispersion and attenuation becomes important to ensure that enough models fit the data well enough to perform good parameter inference: in Appendix B, we use additional synthetic data (i.e., “held-out data” generated identically to the training spectra but not included in PCA training) to test the reliability of our stellar mass-to-light estimates against mock galaxies with known physical properties; and in Section 2.3.2, we compare the distribution of all of the training data in D_n4000 and $H\delta_A$ to empirical measurements of the same indices from many thousands of spectra reported in the MaNGA DAP, demonstrating that other than one small, well-known systematic affecting $H\delta_A$ at moderate D_n4000 , the training models are distributed very similarly to empirical measurements of D_n4000 and $H\delta_A$ in observed spectra.

For each model, the SFH is stored (as it is used explicitly by FSPS), along with the strengths of several spectral absorption indices³, the mass-weighted age, and V - & i -band mass-to-light ratios (Υ_V^* & Υ_i^*)⁴.

2.3.2 D_n4000 - $H\delta_A$ comparison of training library to MaNGA spaxels

We evaluated the correspondence between the suite of synthetic models and the real MaNGA data by comparing the distribution of the D_n4000 and $H\delta_A$ absorption indices measured by the MaNGA DAP to those from the full suite of SFH models (the “training data”) used in this work (Figure 2.8). We observe an offset in $H\delta_A$ between synthetic models and observations at fixed D_n4000 greater than 1.5, consistent with previous work (see Kauffmann et al. 2003, Figure 2). This effect has been attributed to stellar models, and the offset observed (which grows with D_n4000 , but remains less than 0.8 Å) is well within the locus of previous measurements. Some degree of this offset may be attributable to α -enhancement, which cannot be manipulated in the set of stellar atmospheres adopted for this work. It is likely that such a mismatch exists at all values of D_n4000 , but becomes apparent only at $D_n4000 > 1.5$ —that is, at ages of several Gyr (where CSPs with e-folding timescales shorter than 1 Gyr begin to have similar spectra to SSPs).

³All stellar absorption indices are computed on spectra with velocity dispersion of $\sigma = 65 \text{ km s}^{-1}$, approximately equal to the difference in resolution between full-resolution model spectra and MaNGA data. This is preferable to employing correction factors which are not guaranteed to work for stellar populations younger than 3 Gyr (Kuntschner 2004).

⁴*Effective* mass-to-light ratios are used, since they include only light that reaches the observer. In other words, these effective mass-to-light ratios are affected by dust. All subsequent references to mass-to-light ratio use this same abbreviation. For the purposes of estimating stellar mass, though, this convention suffices, because the bandpass flux which is multiplied by the mass-to-light ratio and the distance modulus *also* is attenuated by dust, so the two dust contributions cancel.

Furthermore, though Maraston et al. (2009) finds that superimposing approximately 3% (by mass) of low-metallicity stars onto synthetic continuous stellar populations can resolve a color mismatch between synthetic CSP models and luminous red galaxies (LRGs), we find no evidence for a similar improvement in the case of D_n4000 and $H\delta_A$ (in Figure 2.8, we show the case where the mass fraction is 3%). We observe, though we do not show, that as the mass fraction of the SSP increases, the value of $H\delta_A$ actually *decreases* at fixed D_n4000 . That said, Maraston et al. (2009) note that a potential astrophysical reason for the bluer-than-anticipated colors in metal-poor galaxies is an especially strong blue horizontal branch, which is manipulated separately in our population synthesis. Finally, since the fraction of MaNGA spaxels that lie in the centers of massive LRGs is low, any effect of mixed-metallicity populations may be subdominant to others which pertain to more star-forming systems.

An attempt to replace $H\delta_A$ with the sum of $H\delta_A$ and $H\gamma_A$ in lieu of just $H\delta_A$, since a deficiency in $H\gamma_A$ has been noted to function opposite to a deficiency in $H\delta_A$. In reality, the match is not greatly improved.

2.3.3 Why not use CMLRs?

Bell et al. (2003) produced conversions between various optical colors and mass-to-light ratio, and we will re-evaluate this approach here. Table 2.2 compares the inputs to the stellar population synthesis modelling used to derive the Bell et al. (2003) CMLRs, to the inputs used in this work. Salient differences include this work’s modest allowances for starbursts, inclusion of attenuation—previously argued to be unimportant, due to the slope of the reddening vector being very similar to the CMLR (Bell & de Jong 2001; Bell et al. 2003)—, and use of the Kroupa (2001) IMF.

Using the training data described above, we use a least-squares fit to find the optimal

CMLR for i -band stellar mass-to-light ratio and both $g - r$ and $g - i$ colors—the latter being provided as a point of comparison to the GAMA survey (Taylor et al. 2011)—and then examine the mean absolute deviation between the predicted and actual values of $\log \Upsilon_i^*$ (Figures 2.9 and 2.10). As Figures 2.9 and 2.10 illustrate, our models follow a well-defined CMLR, but with a scatter of at 0.05–0.1 dex about the best-fit: scatter is lowest at modest

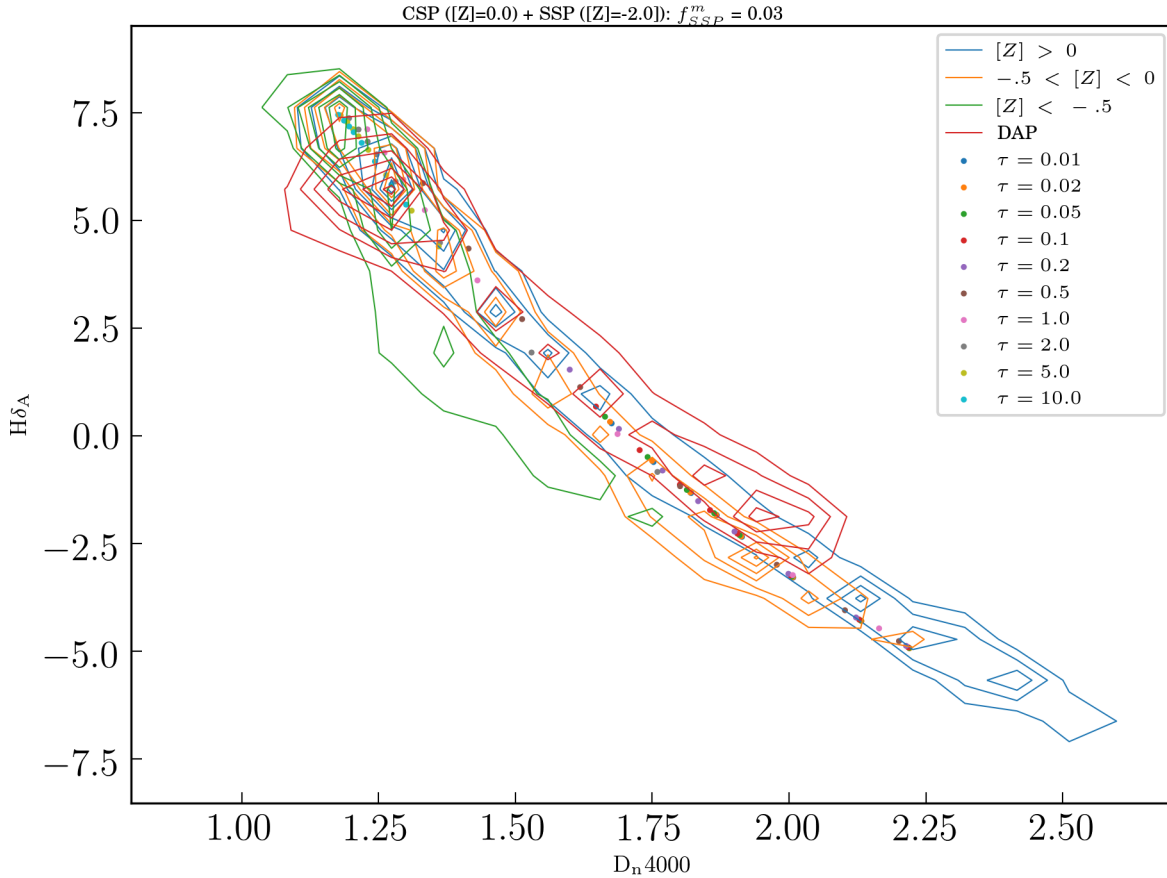


Figure 2.8 : The distribution of the training models in D_n4000 - $H\delta_A$ space (separated by stellar metallicity: super-solar metallicity in blue contours, slightly sub-solar in orange contours, and very sub-solar in green contours); plus data points for individual models with composite metallicities. Each point signifies a delayed-tau model with time constant denoted by the color of point (but forming at a variety of times post-Big-Bang). The continuous portion of the model is fixed at solar metallicity. Added to this CSP is a SSP which forms instantaneously at the same time as the CSP begins to form stars, with a contribution to the current stellar mass of 3%. The SSP has an extremely low metallicity ($[Z] = -2$).

values of stellar attenuation and sub-solar metallicities (the $g - i$ CMLR is slightly better in this respect). Furthermore, the CMLRs rely upon nearly perfect photometry, which in reality rarely improves to sub-0.02 levels at kiloparsec sampling scales for large surveys. That is, depending on the precise choice of CMLR, observational effects can very easily add further uncertainties of ~ 0.05 dex. The differences between the Bell et al. (2003), Taylor et al. (2011), and this work's CMLRs are not insubstantial: Bell et al. (2003) CMLRs have uniformly smaller slope, meaning that they will produce mass estimates that are higher (lower) for blue (red) colors. In contrast, stellar mass-to-light ratios from the Taylor et al. (2011) CMLR will be uniformly lower than this work's, by 0.15–0.4 dex. This highlights the impact of the specific SFH family chosen, the stellar models, and even the choice of attenuation (see below).

Input	Bell et al. (2003)	Taylor et al. (2011)	This Work
Stellar models	PÉGASE (Fioc & Rocca-Volmerange 1997)	Bruzual & Charlot (2003)	Conroy et al. (in prep.)
Stellar IMF	“Diet” Salpeter (1955)—also see Bell & de Jong (2001)	Chabrier (2003)	Kroupa (2001)
SFHs	delayed- τ	τ -model, grid-sampled	Composite: delayed- τ , burst(s), cutoff, rejuvenation
Attenuation	None	Uniform screen	Two-component (Charlot & Fall 2000)

Table 2.2 : SPS inputs, compared between Bell et al. (2003), Taylor et al. (2011), and this work.

Overall, one should note that the scatter about the CMLR is not entirely random. This means that even before systematics related to stellar model atmospheres and our fiducial SFH family, the functional lower-limit on stellar mass-to-light ratio uncertainty is about 0.1 dex. Especially in the case of vigorous recent star-formation, stellar metallicity is associated with pronounced departures from the “mean” CMLR (the large number of blue, low-metallicity models at higher-than-predicted mass-to-light ratios is one noticeable example). Figures 2.9 and 2.10 show that while CSPs in the most common regions of parameter space have their stellar mass-to-light ratios described well by the best-fit CMLR,

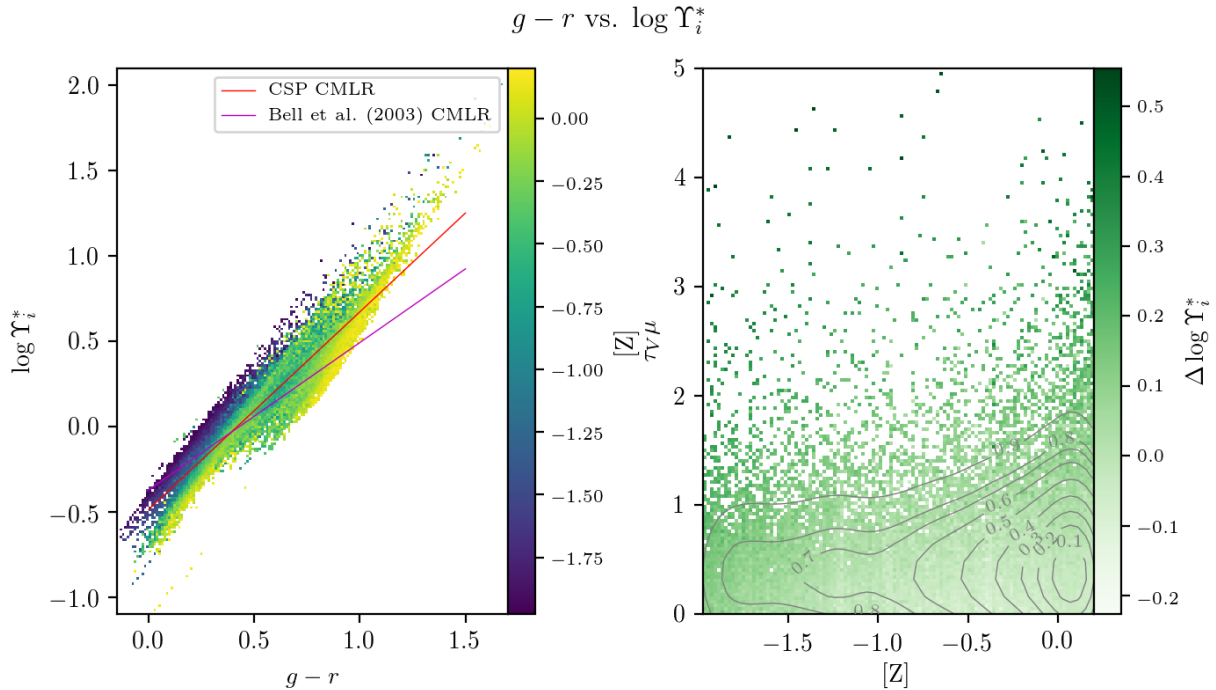


Figure 2.9 : Left-hand panel: effective i -band stellar mass-to-light ratios (in solar units) for model spectra generated above, plotted against rest-frame $g - r$ color, and colored by stellar metallicity; in *red*, the CMLR obtained from a least-squares fit to the CSP library; in *magenta*, the CMLR from Bell et al. (2003), after a -0.15 dex Salpeter-to-Kroupa IMF correction. Right-hand panel: a visualization of the typical difference between a SFH’s true stellar mass-to-light ratio and the mean CMLR at that color: each image pixel is colored according to the median of the CMLR deviation for all CSPs in that small $[Z]-\tau_{V\mu}$ bin (or white, if there are none). Overlaid in red contours is shown the approximate fraction of models within a given contour (derived from a two-dimensional kernel density estimation).

departures from the median case can cause troublesome systematics: for instance, at low metallicity, $\Delta \log \Upsilon_i^*$ can reach values of 0.2–0.3 dex, even at low attenuations; and higher optical depths ($\tau_V \mu \sim 3$) can boost this discrepancy as high as 0.4 dex. This is not simply a scatter about the CMLR, but is rather a true systematic. The effect is similar in $[Z] - \tau_V(1 - \mu)$ space.

To illustrate the potential effects of attenuation in pulling a single SFH away from a CMLR, consider the following scenario: at fixed fractional optical depth $\mu = 0.4$, a SFH with $t_{form} = \tau = 2$ Gyr changes in $g - r$ color and $\log \Upsilon_i^*$ by +0.094 and +0.14 when τ_V is changed from 0.0 to 1.0, a considerably steeper slope than the fiducial CMLR. Furthermore, the slope of the attenuation vector in $(g - r)$ – $\log \Upsilon_i^*$ space increases with μ , matching the slope of the CMLR at $\mu \sim 0.14$ (recall that μ affects the balance between attenuation of young stars and old). In Bell & de Jong (2001) and Bell et al. (2003), attenuation was

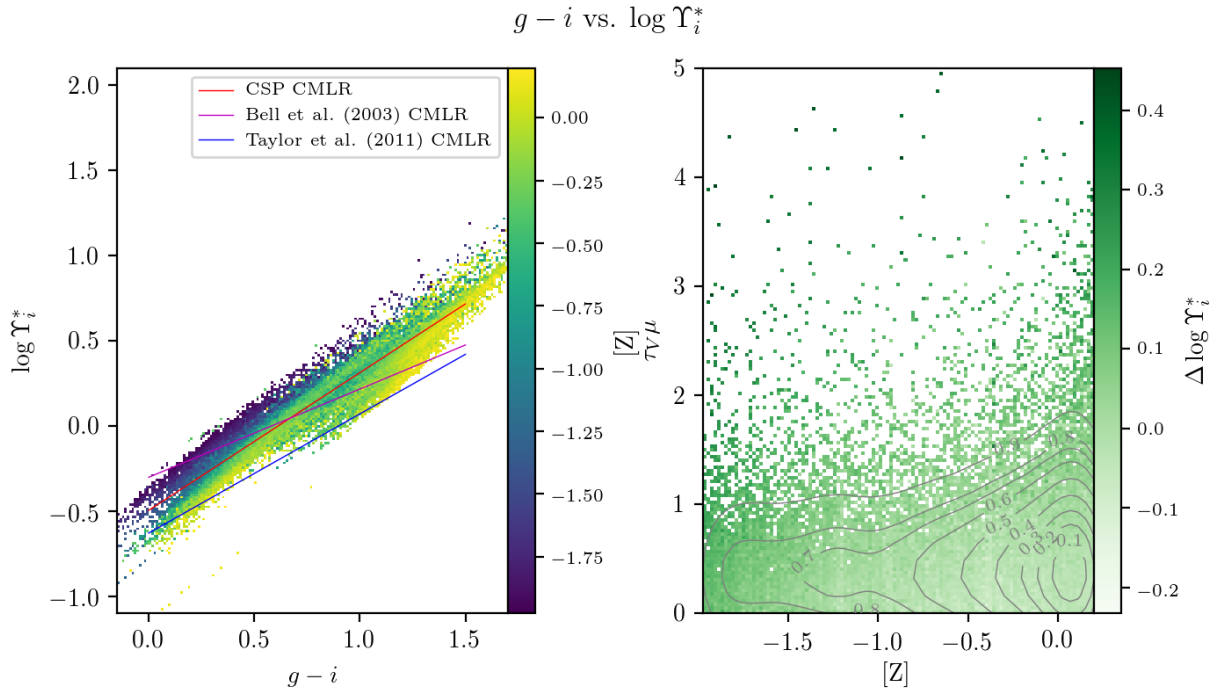


Figure 2.10 : As Figure 2.9, except calibrating $\log \Upsilon_i^*$ against $g - i$ color, plus Taylor et al. (2011) CMLR in the left-hand panel in *blue*. All mass normalizations are once again corrected to Kroupa (2001) IMF.

explicitly ignored, because the attenuation vector lay almost parallel in color–mass-to-light space to the adopted CMLR. Depending on the exact value of μ , this may not be true. So, for the SFH chosen above, the stellar mass-to-light ratio is under-estimated for most realistic values of μ and τ_V .

Also a concern is the effect of the stellar IMF on the relative mass normalization. Using 1000 separately-randomized SFHs for three of the five stellar IMFs built into **FSPS**⁵—[Salpeter \(1955\)](#), [Chabrier \(2003\)](#), and [Kroupa \(2001\)](#)—, we have separately-determined the Υ_i^* normalization and its overall dependence on $g - r$ color (see Table 2.3) for our training library. The effects of IMF on integrated colors are of course small (and likely attributable to differences in SFH randomization), but the overall mass normalizations differ quite strongly: [Kroupa \(2001\)](#) and [Chabrier \(2003\)](#) are offset respectively by -0.209 dex and -0.252 dex, with respect to [Salpeter \(1955\)](#).

In summary, CMLRs do not capture the full range of information contained in a galaxy’s SED; indeed, they can also be susceptible to degeneracies between age, metallicity, and attenuation. Specifically, even at infinite signal-to-noise, both CMLRs tested here suffer from intrinsic scatter above the 0.05 dex level in the very common stellar metallicity range of -0.5 – 0.2 and at diffuse ISM optical depths greater than 1.0. Deviations from a fiducial dust law can also induce changes in the effective stellar mass-to-light ratio which are *not*

⁵It was computationally less costly to randomize each IMF’s set of SFHs than it was to use the same SFHs using each of the three IMFs.

IMF	m	b	σ [dex]
Salpeter (1955)	1.145	-0.286	9.38×10^{-2}
Kroupa (2001)	1.147	-0.496	9.62×10^{-2}
Chabrier (2003)	1.155	-0.538	9.44×10^{-2}

Table 2.3 : Linear fit relating $g - r$ color to $\log \Upsilon_i^*$, and the magnitude of the scatter about the best-fit line (all a little less than 0.1 dex).

parallel to the CMLR, as had been previously suggested (Bell & de Jong 2001; Bell et al. 2003). There is much more information to glean from galaxy SEDs than can be encoded in optical colors.

2.4 Parameter Estimation in the PCA Framework

The goal of this analysis is to obtain estimates of physical quantities (especially resolved stellar mass) by reducing the dimensionality of observed spectra from a vector of length ~ 4000 to one of length ~ 6 , and the overall approach to the analysis is very close to C12: for some observed spectrum, we then find its best representation in terms of linear combinations of the principal component vectors, taking into account covariate noise arising from imperfect spectrophotometry. Finally, we evaluate how well each training spectrum matches the observed spectrum *in principal component space*, and assign weights to the training spectra accordingly. The weights are used to approximate probability density functions (PDFs) of interesting quantities such as stellar mass-to-light ratio (Υ^*). Table 2.4 provides a complete digest of the notation used in this section to describe the use of principal component analysis.

2.4.1 The PCA system

We first construct the PCA vector basis:

1. Pre-process all model spectra:
 - (a) Convolve with Gaussian kernel of width $\sigma \sim 65 \text{ km s}^{-1}$, to account for difference between C3K native resolution and MaNGA instrumental resolution⁷.

⁷The line-spread function specifies the (wavelength-dependent) manner in which a spectrum is blurred by a spectrograph. In the case of the MaNGA data, this amounts to between 1 and 3 pixels on the spectrograph, depending on the wavelength. Details for how to compute this can be found in Cappellari

Symbol	Description	Dimension ⁶
n	Number of CSPs in training library	-
n'	Number of spaxels analyzed in a single MaNGA datacube	-
l	Number of spectral channels in each CSP and observed spectrum	-
p	Number of quantities (such as stellar mass-to-light ratio) stored for each CSP	-
q	Number of principal components retained for final dimensionality reduction	-
D	Training data (already normalized)	(n, l)
D'_q	Training data, comprising only the first q PCs (subscript often omitted for clarity)	(n, l)
E	Eigenspectra obtained from the model library	(q, l)
A	Principal Component amplitudes obtained by projecting spectra onto the eigenspectra	(n, q)
R	Residual obtained by subtracting D'_q from D	(n, l)
K_{th}	Theoretical covariance matrix, obtained from R	(q, q)
$\{Y_i\}$	Set of physical parameters that produced the set of model spectra (also notated simply Y , when referring to a matrix with rows representing model spectra)	(n, p)
$C(Z)$	Linear regression coefficients (zeropoints) that link the values in $\{P\}$ to PC amplitudes A	$(q, p) ((p))$
O	Observed spectra, in flux-density units	(n', l)
a	Median value of observed spectra O or training data T , used to normalize data	(n')
M	Median spectrum, obtained by averaging all model spectra's values in a given spectral element	(l)
S	Unity-normalized and median-spectrum-subtracted spectra, $O/a - M$	(n', l)
O'_q	Observed spectra, comprising only the first q PCs (subscript often omitted for clarity)	(n', l)
K^{obs}	Observational covariance matrix, obtained from multiply-observed MaNGA objects and unique to a given spectrum	(n', l, l)
V	The variance of one spectrum, obtained directly from the reduced data products	(l, l)
$N_{obs}^{lhs}, N_{obs}^{rhs}$	Assumed noise propagated from exact de-redshifting of observed spectra into the fixed, rest-frame eigenspectra wavelength grid	
K^{PC}	PC covariance matrix for a given spectrum	(n', q, q)
D^{PC}	Linear combination of K^{PC} and $\{P\}$ to obtain the PC amplitudes A	(n', l)

- (b) Interpolate to a logarithmic wavelength grid from 3600–8800 Å, with $d \log \lambda = 1.0 \times 10^{-4}$, yielding final model spectra (D).
 - (c) Normalize spectra, dividing by their median values ⁸.
2. Compute and subtract from all model spectra the median spectrum of all models (M), yielding median-subtracted training spectra (T)
 3. Compute the eigen-decomposition of T using “covariance method”, retaining the first q vectors as “principal components” (E).
 4. Project T onto E , compute the residuals R , and compute the resulting covariance K_{th} .

Figure 2.11 shows the normalized mean spectrum and each of the first six eigenspectra. Comparison with a “broken-stick” model of marginal variance suggests that six is a suitable number (see Section 2.4.2 for more discussion). Conveniently, at this value of q , the remaining variance in the training data is well below typical random and spectrophotometric uncertainties, which means that the PC space should represent the complete view on the data within MaNGA’s observational constraints. While the physical interpretation of the eigenspectra is not straightforward (and “adding up” multiples of PCs is *not* equivalent to “adding up” stars to form a SSPs or SSPs to form a more complicated stellar population), we explore their correlations with physical properties in Section 2.4.3.

If a single spectrum (with l wavelength values) is a single point in l -dimensional space, then n spectra form a cloud in l -dimensional space. In the case of the generated model spectra, we can claim to have constructed a space where $n \sim 20,000$ and $l \sim 5,000$. PCA

(2017), as well as in Appendix A.

⁸Normalizing by the median (rather than the mean) makes very little difference for the training data, but is less sensitive to the occasional un-flagged emission line or small discontinuity in the observed data.

will then find the orthogonal basis set that maximizes the amount of information retained, utilizing $q < l$ dimensions. PCA can be reduced to a singular value decomposition (SVD), but in our case, where $n > l$, it is equivalent and most efficient to compute as an eigenvalue problem on the covariance matrix. In particular, the training data D has a dimension of (n, l) ⁹, and we wish to reduce it to a set of eigenvectors E (i.e., a subspace) of dimension (q, l) . The eigenvector that contains the most “information” (corresponding to the vector in l -dimensional space that captures the most variation in the data) is the eigenvector of

⁹We adopt the convention of a matrix with dimension (a, b) having a rows and b columns. For such a matrix A , we would select the value in row i and column j as $A_{i,j}$, all of row i as $A_{i, \cdot}$, and all of column j as $A_{\cdot, j}$. For cases where subscripts could be mistaken for indices, we substitute superscripts.

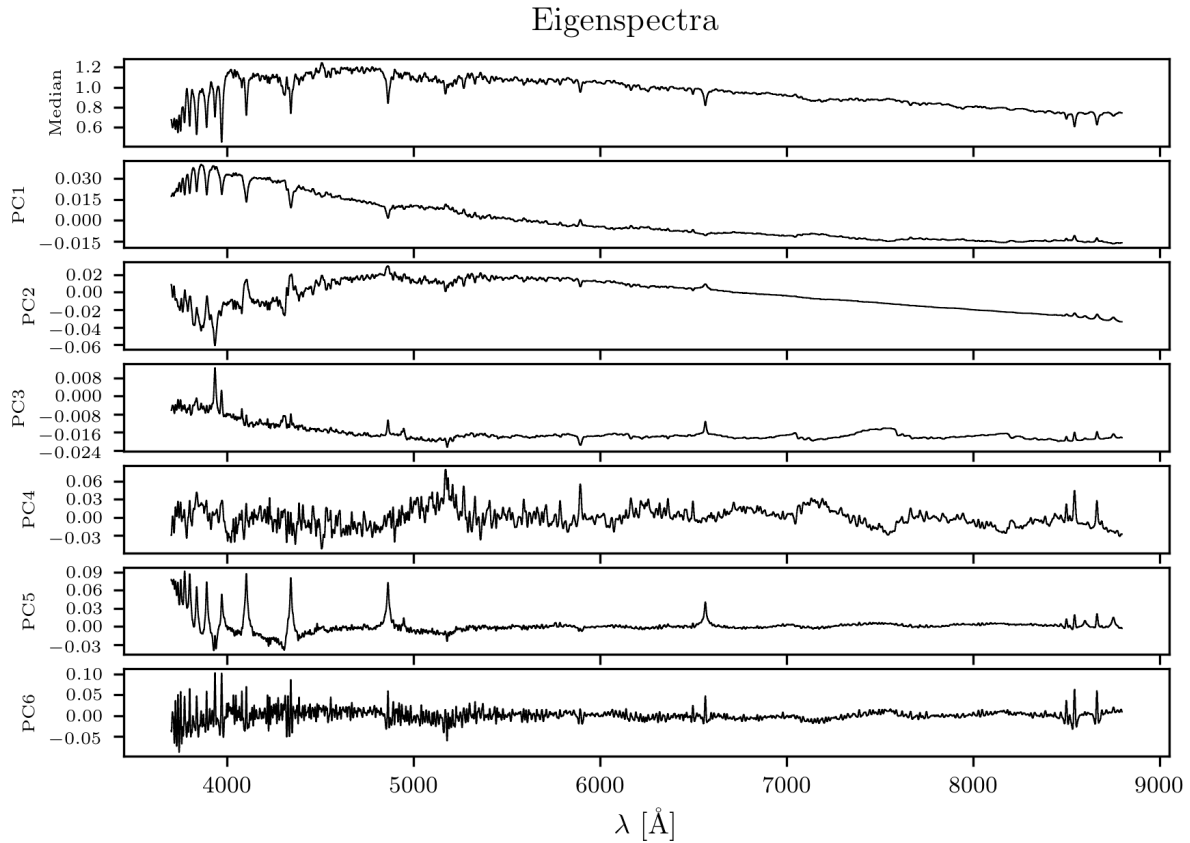


Figure 2.11 : Top panel: the normalized mean spectrum of the training data. Panels 2–7: principal component vectors 1–6 of the training data.

$C = \text{Cov}(D)$ with the largest eigenvalue.

To project all of the points in D onto E , take the dot product of D with the transpose of E , yielding a matrix of dimension (n, q) , whose i^{th} row is the weights of each eigenvector used to construct $D_{i,:}$. Thus,

$$A = D \cdot E^T \quad (2.1)$$

Therefore, in order to reconstruct all of the training data D in terms of their first q PCs (D'), we take the dot product of A and E

$$T' = A \cdot E \quad (2.2)$$

and define the residual

$$R = D - D' = D - (A \cdot E) \quad (2.3)$$

which is used to construct a theoretical covariance matrix $K_{th} = \text{Cov}(R)$, meant to account for all remaining variation in the models not captured by the first q eigenspectra, and is used in addition to observational and spectrophotometric uncertainties in Section 2.4.7 to compute weights on each model.

2.4.2 Validating number of PCs retained: eigenvalues and the scree plot

The i^{th} eigenvalue λ_i of a principal component system describes the fraction of the total variance in the system captured by PC i :

$$V_i^f = \frac{\lambda_i}{\sum_j \lambda_j} \quad (2.4)$$

This is often visualized as a “scree plot” (Fig. 2.12), in which a flattening of V^f is used to indicate lessened marginal gains in fit quality per additional PC retained. Jackson (1993) recommends a heuristic based on the “broken-stick” method, which assumes that

the variance is split randomly into N parts (that is, all spectral channels have uniform variance). In such a case, the i^{th} -largest fractional variance will be

$$U_i^f = \frac{1}{N} \sum_{j=i}^N \frac{1}{j} \quad (2.5)$$

The PC representation can be considered complete when U_i^f exceeds V_i^f (that is, when any improved fit quality can be ascribed entirely to adding a parameter to the fit). Fig. 2.12 shows that $q = 6$ is safely in this regime.

Furthermore, it is desirable to enforce a PCA solution that is general (i.e., the PCs should not lose substantial reliability on data not used to train the model). This can be thought of as the model simply memorizing the training data, and can be evaluated by examining fit quality on held-out (“validation”) data generated identically to the training data. Over-fitting could arise from the training SFHs themselves, or from the three subsampled parameters (σ , τ_V , and μ). Fig. 2.13 illustrates the root-mean-square (RMS) residual between the validation data and their PC representations.

The inclusion of noise in the observed spectra (but not in the CSPs used to construct the PCA model) means that lowering the “down-projection error” for observed spectra (described by theoretical spectral covariance matrix K^{th}) will not substantially improve the fidelity of their reconstructions. In other words, setting the number of principal components retained to 6 means that noisy data will limit the quality of the down-projections (see Section 2.4.8.2) for spectra with median signal-to-noise ratio above approximately 20.

2.4.2.1 Computational concerns

The dimensionality q of the chosen “reduced” space (i.e., the number of eigenspectra with which we seek to reproduce some general observed spectra of dimension l) has a few additional important consequences from the computational perspective:

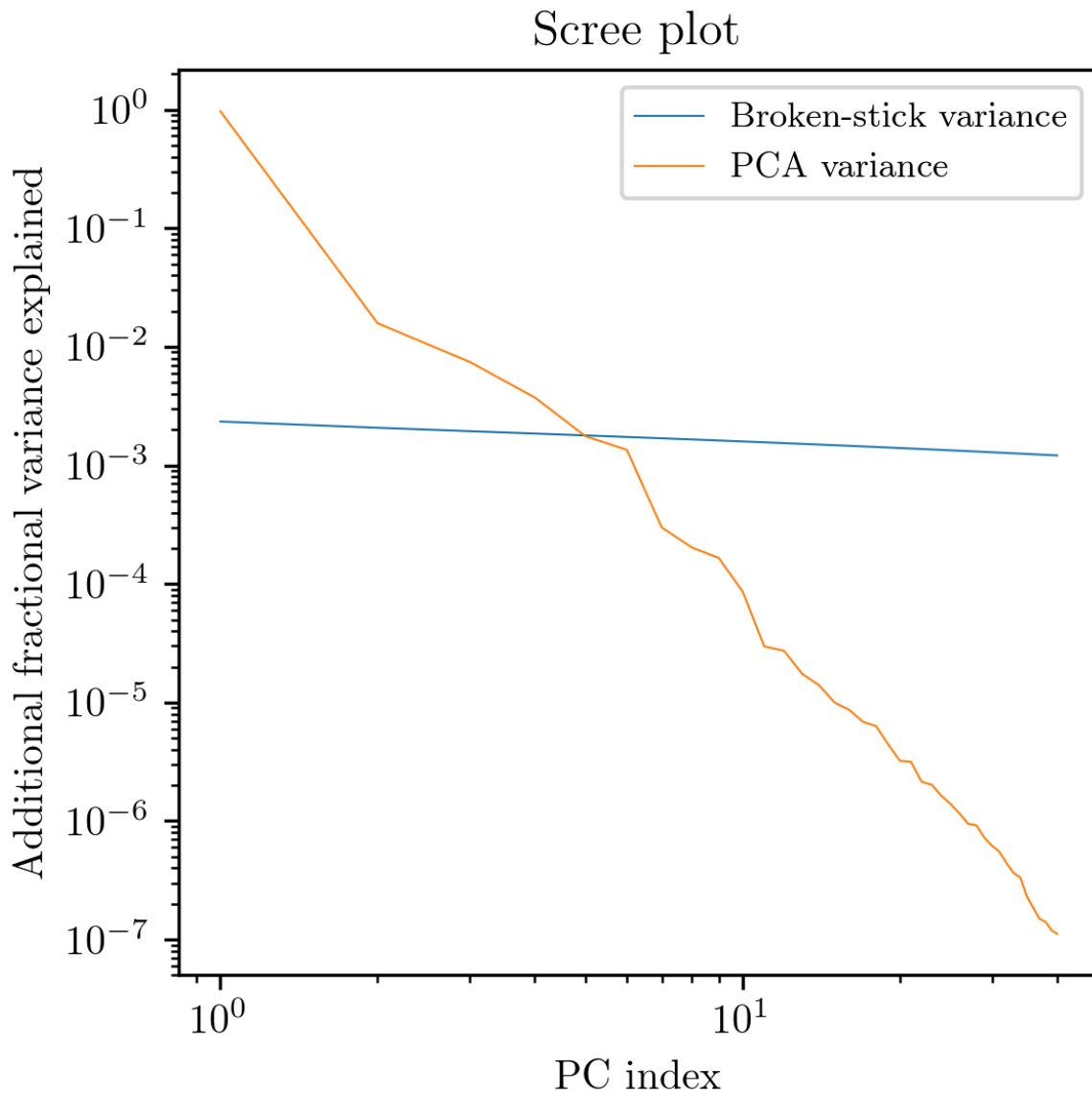


Figure 2.12 : In blue: training data variance described by each successive principal component; in black: the fractional variance expected from the broken-stick method (randomly-apportioned variance).

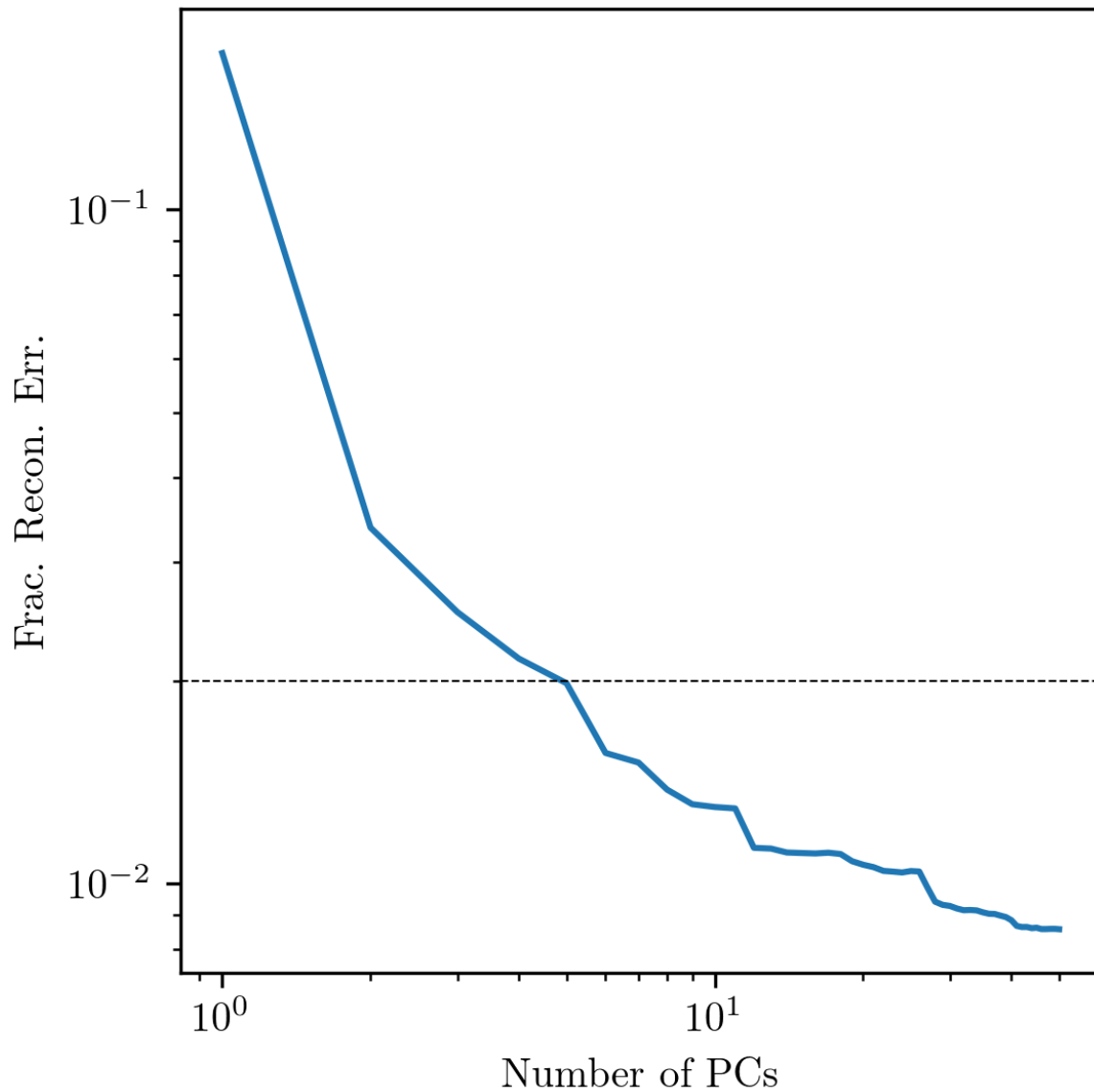


Figure 2.13 : In light blue, the dependence of RMS reconstruction residual on the number of PCs retained. Reconstruction is carried out on a sample of 4000 held-out (“validation”) spectra. The black dashed line denotes an RMS reconstruction error of 2%.

- Matrix multiplication of $A_{n \times m}$ and $B_{m \times p}$ generally is a $\mathcal{O}(m n p)$ operation, so minimizing the number of principal components retained will allow faster down-projection.
- Since the volume of a cube of d dimensions and side length $2r$ rises as $(2r)^d$; and the volume of a sphere of d dimensions and radius r rises as $\frac{2r^d \pi^{d/2}}{d \Gamma(d/2)}$, a sphere occupies a smaller fraction of the cube's volume as d increases. A consequence of this “curse of dimensionality” is observed when one arbitrarily increases the number of principal components retained, q : the distance between two points increases faster than the likelihood-weight can account for the increase, so model weights become extremely low. The likelihood scores used to compare each model to an observed spectrum only provide a *point estimate* of the model likelihood, so seeing many models with nonzero likelihood scores will give confidence that a particular spectrum is well-characterized in PC space.

2.4.3 Developing a physical intuition for principal components

As in C12, we wish to develop an intuition for the physics encoded in each PC. Though easily understandable relationships between physical quantities and principal component amplitudes are not guaranteed, they do tend to emerge. These relationships can be visualized by plotting each model’s PC amplitude against the set of parameters $\{P_i\}$ (see Fig. 2.14). For example, mass-to-light ratio in r , i , and z bands are most correlated with the first PC. This is of course compatible with the overall shape of that eigenspectrum (see pane 2 of Figure 2.11). Kong & Cheng (2001) similarly noted (by performing PCA on SSPs) that a young stellar population is correlated with large coefficients on principal component 1. However, some of the information about stellar mass-to-light ratio is contained in higher PCs (which have smaller coefficients, on average), meaning that using just PC1 (as that

study did) will never give better results than using all PCs. Another striking example is the correlation of velocity dispersion σ with principal components 3 and 6.

However, caution must be used when interpreting the eigenspectra directly: these intuitive interpretations are made under the assumption that the training spectra represent reality both in individual stars (not guaranteed, in the case of the fully-theoretical spectra used here); and in the adopted distributions of SFHs. That is, the training data and the PCA dimensionality-reduction must work in tandem.

2.4.4 The observational spectral covariance matrix

There is an additional source of uncertainty in MaNGA spectra, beyond that provided in the LOGCUBE data products. Specifically, the spectrophotometric flux-calibration of individual exposures, followed by the compositing of those exposures into a regularly-gridded datacube, induces small ($\sim 4\%$, according to Law et al. 2016), wavelength-dependent irregularities in individual spectra. In part, this is because the exposures are taken under a wide variety of airmasses & seeing conditions. The overall effect is that of a small covariance between spectral channels: C12 found that accounting for this covariance is necessary for obtaining reliable estimates of stellar mass-to-light ratios and other quantities. The covariance is described by a matrix K_{obs} , which can be calculated by comparing multiple independent sets of observations of a single object (C12, Equation 9):

$$K_{obs}(\lambda_1, \lambda_2) = \frac{1}{2N_{pair}} \sum_{j=1}^{N_{pair}} [(S_j^0(\lambda_1) - S_j^1(\lambda_1)) \times (S_j^0(\lambda_2) - S_j^1(\lambda_2))] \quad (2.6)$$

where each element $K_{obs}(\lambda_1, \lambda_2)$ denotes the covariance between observed-frame spectral elements λ_1 and λ_2 , and is calculated using the difference between two spectra (S_j^0 and S_j^1) of a single object j .

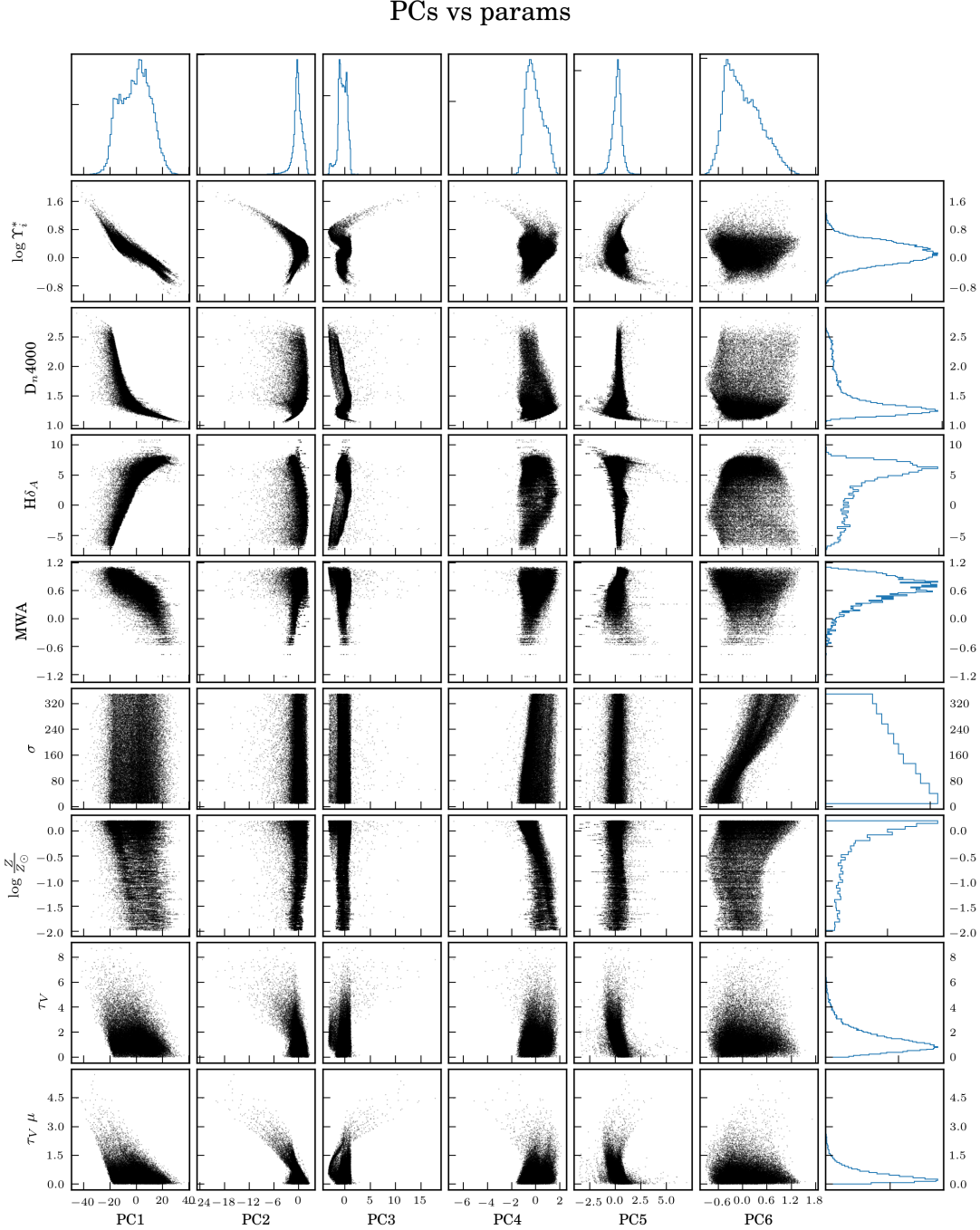


Figure 2.14 : Selected directly-modelled parameters (σ , $\log \frac{Z}{Z_\odot}$, τ_V , and $\tau_V \mu$) and derived parameters ($\log \Upsilon_i^*$, D_n4000 , $H\delta_A$, and log mass-weighted stellar age), versus principal component amplitudes. Each scatter-subplot plots the amplitude of the PC corresponding to its column (on the x-axis) against the parameter corresponding to its row (on the y-axis). The right-most column and top-most row hold histograms of PC amplitudes and parameter values, respectively.

In C12, the spectral covariance matrix was found using reobserved objects from the SDSS(-III)/BOSS project. Since BOSS and MaNGA use the same spectrograph, the spectral covariances will be similar; however, the hexabundle construction of the MaNGA IFUs results in more precise compensation for atmospheric dispersion, which commensurately improves spectrophotometric calibration (Yan et al. 2016b). Therefore, we will recalculate K_{obs} using multiply-observed MaNGA galaxies. Though the number of re-observed MaNGA galaxies is much lower than the number of re-observed BOSS sources, each MaNGA galaxy has hundreds or thousands of spectra that can be compared with their “sister” locations. The result is shown in Figure 2.15, and as expected contains less off-diagonal power than the BOSS covariance. While the covariance should be smooth (since its main contributor is the multiplicative flux-calibration vector), there are some sharper features which manifest in the RMS of ten-thousand random draws from K_{obs} (Figure 2.16): for instance, in the $\sim 7000 - 8000\text{\AA}$ range. While such features could perhaps be attributed to poorly-compensated sky emission or telluric absorption, this appears not to be the case: we have examined both K_{obs} itself and random draws from it, but found no consistent correspondence with typical telluric absorption or sky emission spectra.

K_{obs} can be equivalently thought of as a multivariate-normal probability distribution (with each spectral channel being represented by one row and column in the covariance matrix) centered around zero, describing the noise profile for an ensemble of MaNGA spectra. This view offers a pathway towards comparing the covariance of MaNGA spectra with that of BOSS spectra. We draw 10,000 samples each from the BOSS covariance matrix (which was computed in C12) and the MaNGA covariance matrix. At each wavelength, the RMS value (which can be taken as the average RMS value of the noise in that spectral channel) is computed. The results of that computation are shown in Figure 2.16. As a general rule, the BOSS covariance matrix (computed and used in C12) has greater

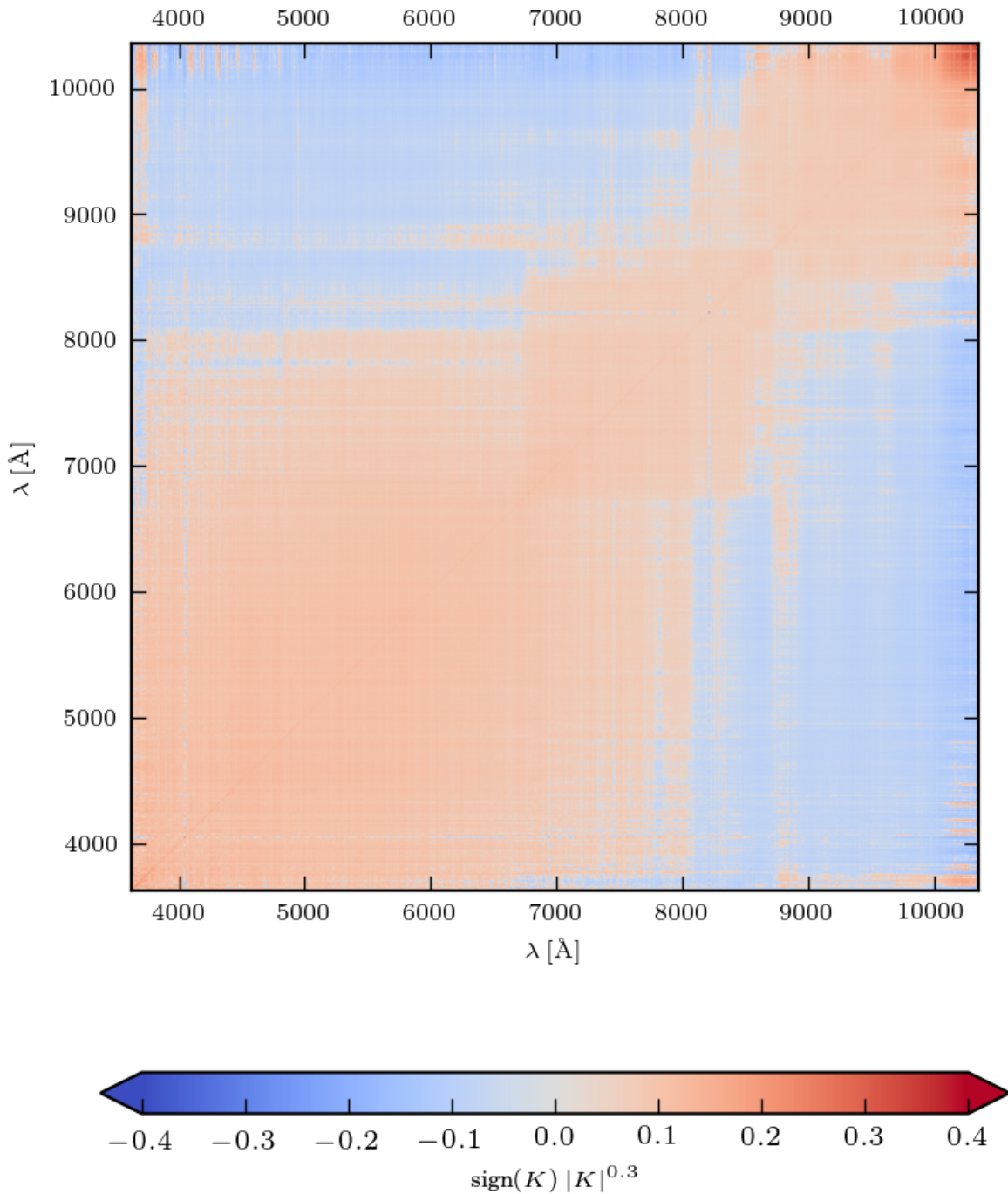


Figure 2.15 : MaNGA’s observational covariance matrix K_{obs} , which arises due to imperfect spectrophotometric flux-calibration of MaNGA spectra. See Figure 5 of C12 for comparison.

spectrophotometric uncertainty (generally by a factor of ~ 5 in the wavelength ranges employed in this work) than the MaNGA covariance matrix computed above.

K_{obs} will be used in Section 2.4.7 to obtain a PC amplitude covariance matrix and confidence bounds for parameters of interest.

2.4.5 Fitting the observations with eigenspectra

Each observed spectrum can now be fit as a linear combination of “eigenspectra” E , subject to a scaling (a) and an unknown (but constrained) noise vector (N), which comprises the incompleteness of the PCA decomposition and the imperfect spectrophotometry.

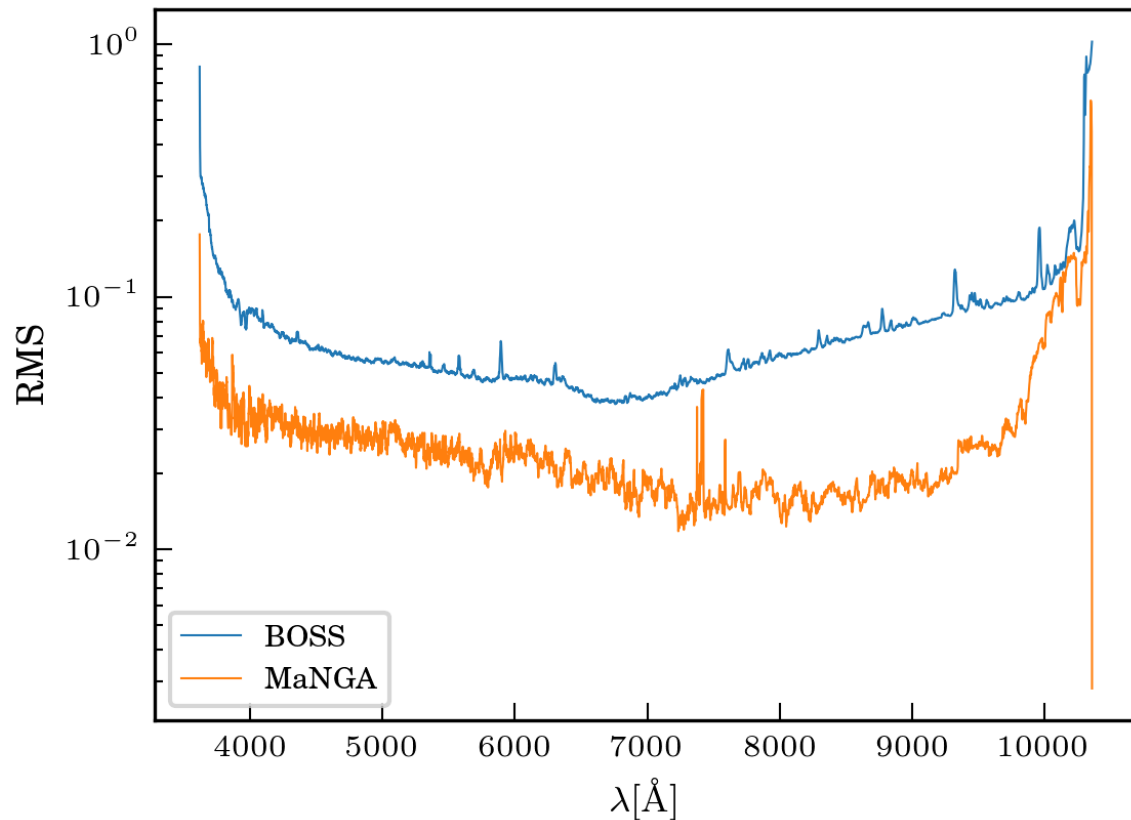


Figure 2.16 : In blue, the RMS value of 10,000 noise vectors drawn from the BOSS covariance matrix; and in orange, the RMS value of 10,000 noise vectors drawn from the MaNGA covariance matrix.

First, an observed spectrum is pre-processed:

1. Galactic extinction is removed, assuming an O'Donnell (1994) extinction law and $R_V = 3.1$, and using the $E(B - V)$ color excess provided in the header of the reduced data products (Schlegel et al. 1998). Both flux-density and its inverse-variance are corrected.
2. The spectrum is brought into the rest frame, combining the systemic velocity obtained from the NSA with spatially-resolved stellar velocity field obtained from the MaNGA DAP results. Both the flux-density and its inverse-variance are de-redshifted and drizzled into the rest frame using an adaptation of Carnall (2017)¹⁰.
3. The spectrum is normalized by its median value (a), and the median spectrum (M) of the PCA system is subtracted.
4. Spectral channels with likely contamination by emission lines are flagged for later replacement: any spectral channel within 1.5 times the line-width (velocity dispersion, as found in the MaNGA DAP) from the rest-frame line center is flagged. Which wavelength locations are masked is based on the equivalent width of the H α emission-line measured by the MaNGA DAP:
 - Always: H α through He; [OII]3726,28; [NeIII]3869; [OIII]4959,5007; [OI]6300; [NII]6548,84; [SII]6716,30; [SIII]9069; [SIII]9531

¹⁰It is preferable to obtain a rest-frame spectrum with the exact same wavelength pixelization as the eigenspectra. Two wavelength solutions f_l and f_r are extracted, corresponding to the two closest integer-pixel mappings between the eigenspectra's wavelength grid and the spectral cube's “exact” wavelength solution. f_l and f_r are combined with weights equal to the relative fraction that they subtend on the exact solution. The uncertainties in these two exact solutions are also propagated into a final, re-gridded solution. This approach was found to produce better fits to the observations than the integer-pixel solution, which tended to prefer a fit with broader absorption features.

- Where $\text{EW}(H\alpha) > 2 \text{ \AA}$: Balmer lines through H30
- Where $\text{EW}(H\alpha) > 10 \text{ \AA}$: Paschen series P8 through P18; HeI3819; HeI3889; HeI4026; HeI4388; HeI4471; HeII4686; HeI4922; HeI5015; HeI5047; HeI5876; HeI6678; HeI7065; HeI7281 [NeIII]3967; [SII]4069; [SII]4076; [OIII]4363; [FeIII]4658; [FeIII]4702; [FeIV]4704 [ArIV]4711; [ArIV]4740; [FeIII]4989; [NI]5197; [FeIII]5270; [ClIII]5518; [ClIII]5538; [NII]5755; [SIII]6312; [OI]6363; [ArIII]7135; [OII]7319; [OII]7330; [ArIII]7751; [ArIII]8036; [OI]8446; [ClII]8585; [NI]8683; [SIII]8829

Flagged spectral channels are replaced (i.e., item-imputed) as the inverse-variance-weighted rolling-mean of the unmasked subset of the nearest 101 pixels. This approach is almost identical to that employed in C12. Since this step is performed on the normalized, median-subtracted spectrum, the replacement does not universally decrease, for instance, the depth of absorption-lines in the spectrum. As we discuss below, the more rigorous way of performing this calculation would involve *re-computing* the geometric transformation that produces the PC amplitudes from the spectrum, an unacceptable loss in speed. Previous work has demonstrated that modestly-gappy data ($\sim 10\%$ of spectral channels masked) produces $\sim 2\%$ deviations (RMS) in principal-component amplitudes (Figure 5 of Connolly & Szalay 1999). Other possible frameworks for emission-line masking are discussed in Section 2.4.6.

5. If the spectrum is more than 30% masked by either data-quality flags or emission-line masks, the entire spectrum is presumed bad. Tests on further synthetic spectra (see Section 2.4.10 and Appendix B for more details about how such mock observations were prepared) suggest that in spectra *un-contaminated* by bad data, fits with and without flags do not substantially change either PC amplitudes (i.e., a group of similar noise realizations of the same synthetic spectra, at a single SNR, does not,

in a statistically-significant way, experience a change in its PC amplitudes) or the estimates of stellar mass-to-light ratio that emerge.

6. The spectrum $S = \frac{O}{a} - M$ is now ready to be decomposed using the eigenspectra obtained in Section 2.4.1.

Transforming the discretely-sampled spectrum by a fraction of a pixel also induces a small, off-diagonal covariance K_{obs}^{od} . The exact magnitude of the covariance depends on the position within a rest-frame spectral bin of the boundary between the two nearest integer-pixel solutions. The position of this boundary, f , lies in the range 0–1 (in units of the width of a log λ bin), and the off-diagonal terms are the variances of the left-hand-side and right-hand-size, weighted by f_{lhs} and $f_{rhs} = 1 - f_{lhs}$.

$$K_{obs}^{od} = f_{lhs}N_{obs}^{lhs} + (1 - f_{lhs})N_{obs}^{rhs} \quad (2.7)$$

which depends only weakly on the precise rest-frame pixel boundary, so we fix $f_{lhs} = f_{rhs} = 0.5$, where the result is maximized for the case of constant noise.

2.4.6 Towards optimal flagging and masking of Balmer emission-lines

The Balmer absorption features in stellar population spectra are among the most important age diagnostics; however, in all but the most quiescent, gas-free environments, these features will be contaminated by gaseous emission. As stated above, in this work, we elect to flag all spectral elements within 1.5 times the velocity-dispersion of H α . Those flagged spectral elements of the median-subtracted spectrum S are then replaced by the weighted mean of the nearest 101 spectral elements (hereafter notated as the “WM101” or fiducial method). On one hand, this relatively narrow flagging region might induce a bias in the PC amplitudes for spectra with bright, high-velocity-dispersion gaseous emission; on the other hand, it is not desirable to sacrifice the information contained in these important

spectral features. We address here two alternatives: work with emission line-subtracted spectra (as [Gallazzi et al. 2005](#) does—the “GC05” method), or explicitly exclude all flagged-and-replaced spectral channels (notated as the “M” method, because it is equivalent to replacing flagged spectral channels with the median of the PC system).

It is perhaps most tempting to work with spectra where emission lines have already been subtracted, since the cores of the Balmer absorption lines are now uncontaminated (“GC05”). However, this requires having first executed a round of full-spectral fitting (which necessarily adopts a stellar library). Indeed, concurrent work with MaNGA IFS data has shown that emission line measurements can be sensitive to the particular SSP library used for fitting the stellar continuum: [Belfiore et al. \(2019\)](#), Figure 9) indicates that as S/N rises beyond 10, changing spectral library from the hierarchically-clustered MILES library (MILES-HC, which is the DR15 fiducial) to MIUSCAT, M11-MILES, or BC03 induces a systematic uncertainty in emission-line flux comparable to the random uncertainties. In other words, the choice of stellar library is important.

One could also argue for the more conservative masking option, explicitly excluding all spectral channels suspected to be contaminated by emission-lines (“M” method). The case against that tactic is more subtle: first, the PC system used in this work is centered at zero, as a result of subtracting the median spectrum M of the CSP library from each of the CSP spectra. When one “eliminates” spectral channels thought to be unreliable, one implies that the values in those channels are identical to the corresponding value in M (i.e, there is no further information beyond what the median spectrum of the SFH training library provides); in reality, the values in the spectrum in such channels are likely better approximated by an average of their near neighbors.

2.4.6.1 Tension between flagged-and-replaced spectra and their fits?

We show here a further test, which uses the 25 most extremely star-forming (but non-AGN) galaxies, based on total integrated H α luminosity (from the MaNGA DAP). If the “WM101” method neglects effects from emission wings, then we should see deficiencies in the stellar continuum fits around the Balmer lines as the equivalent width of H α in emission increases. In other words, we want to know if unmasked emission wings cause a problem in our fiducial correction more than in the alternative “M” method. We correct the 25 high-SFR galaxies using both methods, and fit them using the PCA basis set. Finally, for both correction methods, we measure & compare equivalent width of four Balmer absorption lines (H α , H β , H γ , and H δ) in both the corrected-observations and the fits to them (Figure 2.17). If, as $\text{EW}_{\text{em}}(\text{H}\alpha)$ increases, the “fit” and “corrected-then-fit” spectra produce significantly different $\text{EW}_{\text{abs}}(\text{H}\alpha)$ values, then one would conclude that a strong Balmer emission line “biases” the eventual spectral fit.

The result of these comparisons is shown in Figure 2.17: each panel shows the difference in the equivalent widths of Balmer lines in absorption between the initial “corrected” spectra and the fits to those spectra (in the top panels, correction is performed with the “M” method; in the bottom panels, correction is performed with the “WM101” method; and left to right, columns refer to H α , H β , H γ , and H δ). The differences between these cases are very slight, but at the most basic level, regardless of correction paradigm, stronger Balmer absorption in the corrected spectra than in their fits tends to correlate with increased H α emission. However, replacement with M tends to produce a stronger Balmer absorption deficit in the fits, regardless of which line is considered; the “WM101” method behaves in a manner less dependent on $\text{EW}_{\text{em}}(\text{H}\alpha)$ in the case of H β & H δ (little to no improvement is seen in the H α and H γ cases). While it’s clear that “WM101” produces

some tension between individual spectra and their fits, this basic test indicates that the performance in the vicinity of some Balmer absorption lines is more consistent than the “M” method.

2.4.6.2 Evaluating Balmer-masking with synthetic observations of PCA best-fits

Here we produce and discuss an additional test of the two candidate replacement schemes: the fiducial (“WM101”) and the alternative (“M”). For each of 200 randomly-selected galaxies, we perform a normal PCA fit of each spaxel (projecting each individual, observed spectrum onto the principal components obtained from the training data—see Section 2.4.7). The obtained principal component amplitudes A are then used to reconstruct the best approximation of the observation, O_{true} , which we treat as the “known” spectrum. We also measure the equivalent width of the H β absorption feature (Worthey

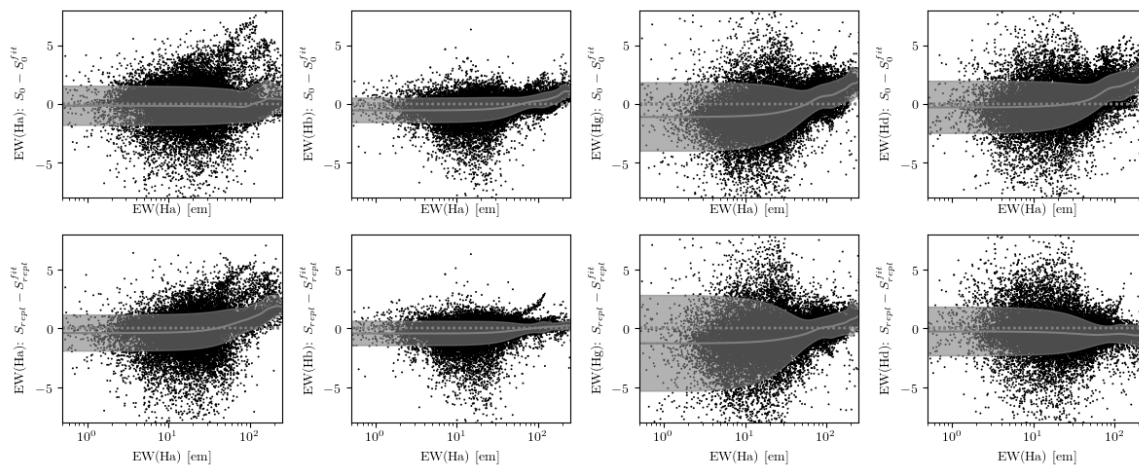


Figure 2.17 : Each panel shows the difference in EW of Balmer absorption (left to right: H α , H β , H γ , H δ) between the corrected and corrected-then-fit spectra: in the top row, “corrected” refers to flagged elements being replaced with the corresponding values in M (S_0 , equivalent to neglecting those spectral channels entirely); in the bottom row, “corrected” refers to flagged elements replaced with the rolling mean of their neighbors (S_{repl}). The solid, gray line denotes the rolling median at fixed $EW_{em}(H\alpha)$, and the gray band the dispersion at fixed $EW_{em}(H\alpha)$.

& Ottaviani 1997) for O_{true} . After applying instrumental noise to O_{true} (see Section 2.4.4 and Section 2.4.10 for more information about constructing synthetic observations), we fit O_{true} using each of the two correction methods, transform (as before) the resultant fit from PC space to spectral space (O_{fit}), and once again measure H β for each case.

Figure 2.18 shows the difference $d\text{EW} = \text{EW}_{\text{abs}}^{\text{H}\beta}(O_{\text{fit}}) - \text{EW}_{\text{abs}}^{\text{H}\beta}(O_{\text{true}})$ for the rolling-mean replacement (top row) and the zero-replacement (bottom row). $d\text{EW}$ is plotted against (from left to right) $\text{EW}_{\text{abs}}^{\text{H}\beta}(O_{\text{true}})$, median signal-to-noise ratio (SNR), and the equivalent width of the H α emission line as reported in the MaNGA DAP (spaxels with fractional uncertainty in H α emission equivalent width greater than $\frac{1}{3}$ are excluded). Broadly speaking, the two cases are very similar; but slight differences emerge in limiting cases. For instance, for the “M” method seems to produce more outliers with $d\text{EW} < 0\text{\AA}$ at high $\text{EW}_{\text{abs}}^{\text{H}\beta}(O_{\text{true}})$, and vice-versa at low $\text{EW}_{\text{abs}}^{\text{H}\beta}(O_{\text{true}})$ (but behaves on average the same).

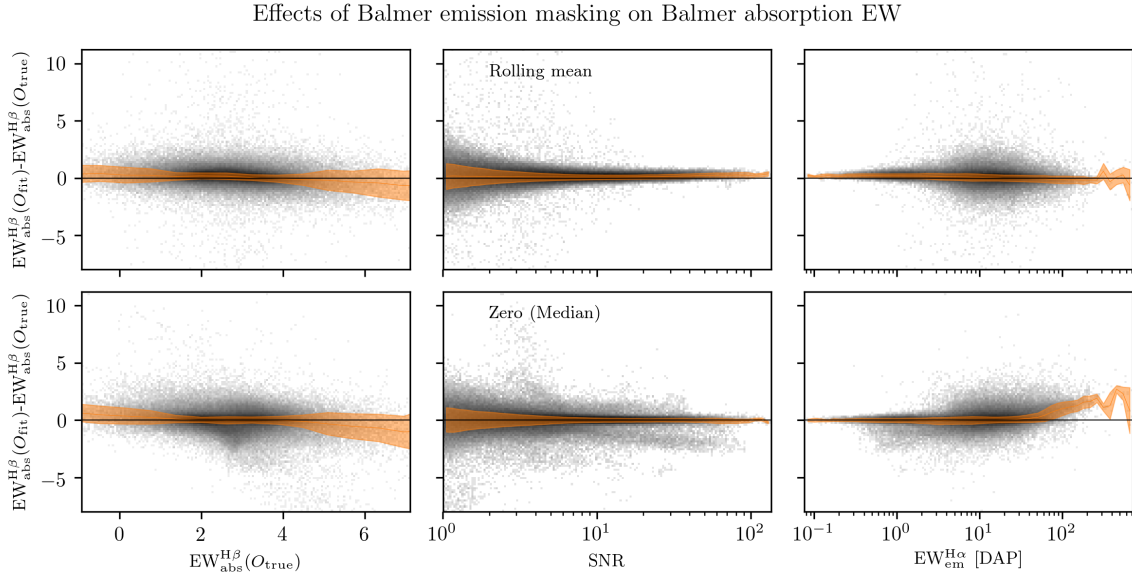


Figure 2.18 : $d\text{EW} = \text{EW}_{\text{abs}}^{\text{H}\beta}(O_{\text{fit}}) - \text{EW}_{\text{abs}}^{\text{H}\beta}(O_{\text{true}})$ versus (left to right) $\text{EW}_{\text{abs}}^{\text{H}\beta}(O_{\text{true}})$, median signal-to-noise ratio (SNR), and DAP equivalent width of the H α , using the fiducial (top row) and the alternative (bottom row) strategies. Pixels are colored according to the logarithm of the number of spectra within. On each panel is overlaid the rolling median of $d\text{EW}$ (red line) and the dispersion about the median calculated using the median absolute deviation (red band).

Though this effect is small, it suggests that Balmer depths can be somewhat moderated by replacement with the median spectrum M (which conceptually represents a medium-age stellar population).

Second, the “WM101” method exhibits some unbalance of outliers having $d\text{EW} \sim -1\text{\AA}$ at moderate-to-high signal-to-noise. That said, it has a locus at $d\text{EW} \sim 0.2\text{\AA}$ at similar signal-to-noise. Finally, though the “WM101” method is stable with respect to $\text{EW}_{\text{em}}^{\text{H}\alpha}[DAP]$, the “M” method becomes somewhat overzealous in its production of $d\text{EW} > 0\text{\AA}$ fits. The apparent “bulging” of the two distributions at moderate $\text{EW}_{\text{em}}^{\text{H}\alpha}[DAP]$ reflects that more spaxels reside in that neighborhood, rather than an intrinsic deficiency of the replacement schemas there. The effects we note here are subtle, and this test suggests that the two proposed replacement methods do not substantially differ except in the most extreme cases. Ultimately, the widths of $d\text{EW}$ are small. That said, because the “WM101” method behaves more uniformly with respect to $\text{EW}_{\text{abs}}^{\text{H}\beta}(O_{\text{true}})$ and $\text{EW}_{\text{em}}^{\text{H}\alpha}[DAP]$, we believe it is the slightly preferable choice.

2.4.6.3 Flag-and-replace stellar models

We briefly explore here the effects of the “WM101” method on the CSP model spectra themselves, and what influence that exerts on the eigenspectra. Since the Balmer absorption lines provide indications of stellar population age, smoothing over those features in the models should also suppress them in a resulting principal component basis set. Beginning with the set of CSPs described in Section 2.3, the “WM101” method outlined in Section 2.4.5 is used to “eliminate” the influence of all spectral channels within 120 kms^{-1} of all Balmer lines¹¹. After those adulterations, the model spectra are once again used to build a PC basis set.

¹¹This velocity window is used as an illustration for the case of a reasonably wide emission line.

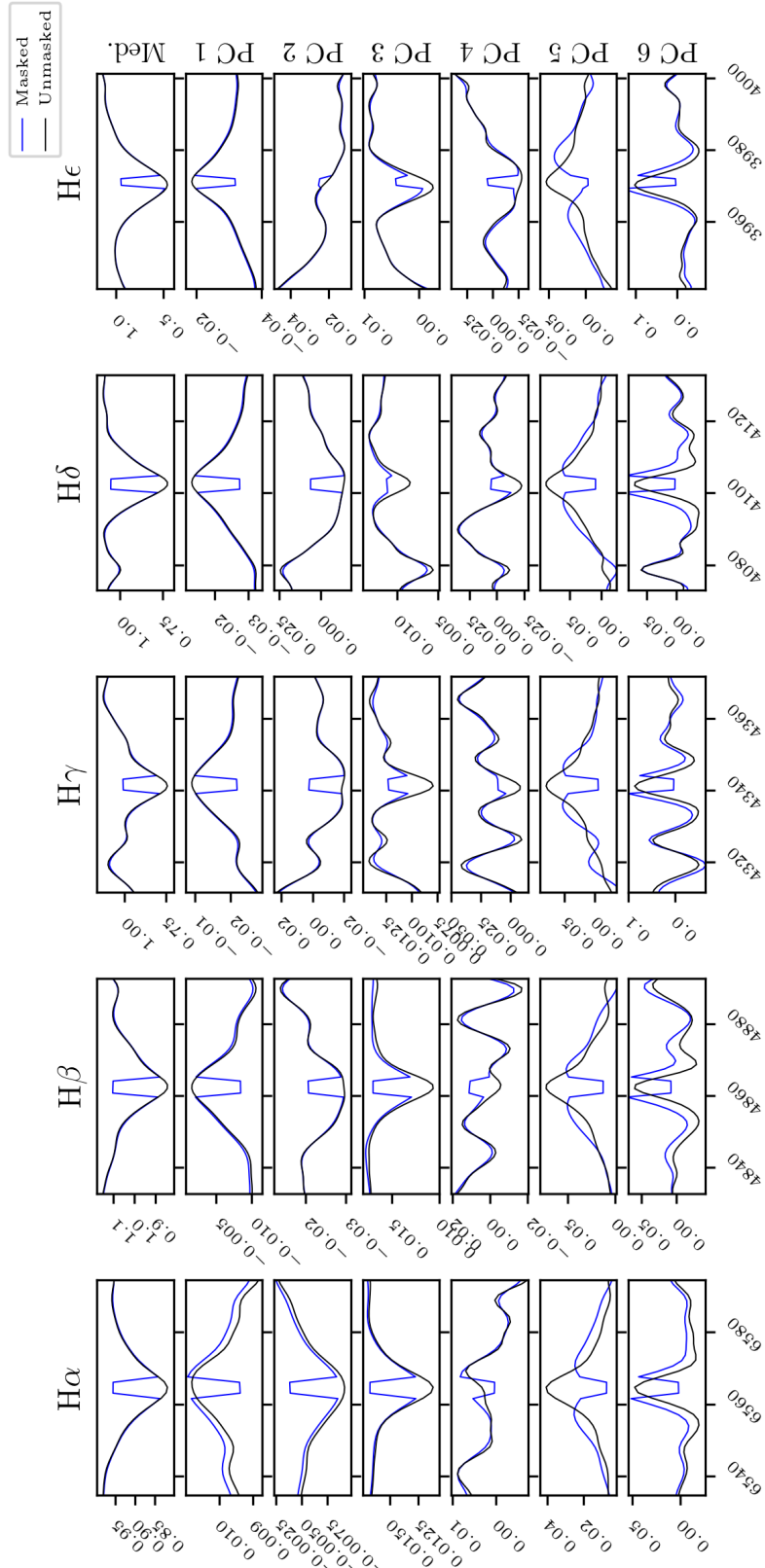


Figure 2.19 : A comparison in the vicinity of the first five Balmer absorption lines ($H\alpha$, $H\beta$, $H\gamma$, $H\delta$, and $H\epsilon$) of the principal component basis set resulting from flag-and-replacement (blue) and no flag-and-replacement (black). The overall spectral shape is largely preserved, especially in the lower principal components; and the masked regions exert an influence opposite to the absorption features. Each row of panels signifies a principal component vector (or, for the top row, the median spectrum), and each column

Figure 2.19 shows a comparison between the eigenspectra of our “normal” PC basis set with that resulting from “WM101” replacement of the *model spectra themselves* in the vicinity of Balmer line centers. The shapes of the eigenspectra (i.e., neglecting the core of the absorption line affected by the mask) are conserved best in PC1–PC4 (as mass-to-light ratio follows PC1 most closely, this is a very desirable behavior). Furthermore, examining the shapes of the absorption features, if the fiducial PC basis set “dips” in the core of the line, the flag-and-replaced version tends to “rise” in the handful of spectral channels within the replacement area; and if the fiducial “rises”, then the replaced area “dips”. Note that the eigenspectra’s masked spectral channels are *not* necessarily drawn towards zero, simply in the opposite direction as the manifestation of the Balmer absorption feature.

2.4.7 Estimating PC coefficients and uncertainties for observed spectra

We now discuss finding the values and the uncertainty of the principal component coefficients A . Observed galaxy spectra O previously had their missing data (where emission-line or data-quality masks are set) are then imputed by a rolling filter with a width of 101 pixels. If data cannot be imputed in this way, it is still possible to perform the calculation below by imputing missing values as zeros (introduces some bias), or by explicitly eliminating entries of columns of eigenspectra E and both rows and columns of spectral covariance K where data are flagged and replaced (much slower, as the projection matrix must be explicitly recalculated for each spectrum). Spectra O are then normalized by dividing by their median value a and subtracting the PCA median spectrum M , yielding a spectrum S .

The PC amplitudes A are the solution to the linear system $E A = S$, subject to covariate noise (assumed to be drawn from a multivariate-normal distribution with mean zero and covariance K). In particular, an individual observation S includes the

“true” spectrum S_0 ; plus contributions from the “theoretical” noise, N_{th} (which accounts for the imperfect PCA decomposition), the error due to imperfect spectrophotometry N_{obs} (discussed in Section 2.4.4), the small off-diagonal covariance K_{obs}^{od} resulting from the fractional-pixel rest-frame wavelength solution, and the photon-counting noise N_{cube} reported in the datacube itself:

$$\tilde{S} = S + a N_{th} + N_{obs} + N_{cube} \quad (2.8)$$

The noise vectors N_{th} and N_{obs} are assumed to be drawn from their respective covariance matrices K_{th} and K_{obs} , and N_{cube} is the noise profile associated with the measured and reported inverse-variance of the data. K_{th} was computed above as the covariance of the residual obtained in reconstructing the training data from the first q PCs. K_{obs} indicates the uncertainty manifested in the flux-calibration step of data reduction (see Section 2.4.4).

K_{obs} should be evaluated over the *observed* wavelength range appropriate to particular observations, rather than over the corresponding rest-frame wavelength range. This produces a slightly different covariance matrix from spaxel to spaxel even within the same spectral cube, and potentially a very different covariance matrix from object to object. This is due to the different observed-frame positions of the same rest wavelength, as recessional velocity changes; as well as the varying surface brightness within a galaxy’s physical extent. As K_{obs} is assumed to be smooth on small wavelength scales, we use the nearest-pixel solution for each spectrum. We add a small ($\alpha \sim 10^{-3}$) regularization term to the main-diagonal of K_{obs} : this functions as a “softening parameter”, which maintains a minimum dispersion of K_{PC} (only becoming important at high signal-to-noise). This small term allows for some marginal data-model mismatch (see Section 2.5)—but still allows for data-quality masks to be set in the case of PDFs which are an especially bad match for the prior (see Section 2.4.9 for more discussion of data-quality masks).

In order to solve the system $E \cdot A = S$, we define the orthogonal projection matrix

$$H = (E^T E)^{-1} E^T \quad (2.9)$$

where $(E^T E)^{-1}$ is found only once through Cholesky decomposition (one method of decomposing a Hermitian, positive-definite matrix into the product of a lower-triangular matrix and its conjugate transpose, [Press et al. 1986](#)) after regularizing on the main diagonal¹². Since H depends only on the eigen-decomposition of the training data, it is not affected by the specific noise realization of an observation, and need not be calculated repeatedly, unless masked data wish to be explicitly discounted, rather than replaced with a local median as outlined above. The maximum-likelihood PC weights are then given by

$$A = H \cdot S \quad (2.10)$$

and the principal component covariance matrix by

$$K_{PC} = H^T K H \quad (2.11)$$

The spectrum corresponding to the maximum-likelihood solution A is therefore the inner product $E \cdot A$, and an example comparison between an observed spectrum and its maximum-likelihood PC representation is shown in Figure [2.20](#), in the two top-right panels.

2.4.7.1 Effects of sky residuals

Since the spectral range considered here extends into the infrared wavelengths, it is important to consider the possible effects of badly-subtracted sky emission (properly-subtracted emission will have no effect apart from an increase in uncertainty). As of

¹²The effect of the regularization's strength on the residual between original and “reduced” spectrum is strongly subdominant to the effect of the dimensionality reduction itself, and the fit quality does not change noticeably over a wide range in regularization parameter $\alpha \sim [1 \times 10^{-6}, 1]$

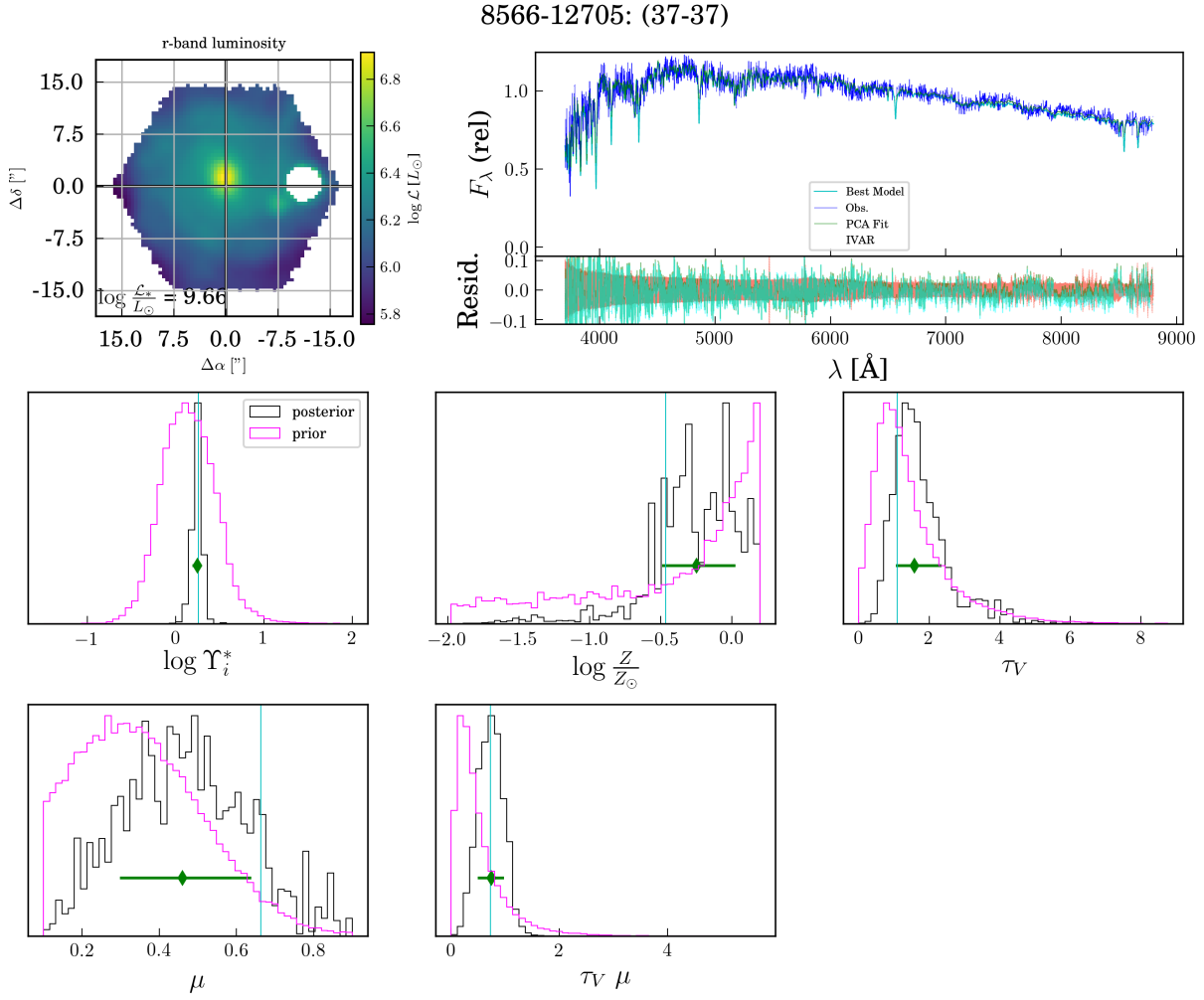


Figure 2.20 : The standard diagnostic figure produced for the center spaxel (coordinates 37, 37) of MaNGA galaxy 8566-12705. Top-left frame: map of the galaxy’s *i*-band luminosity (the “hole” in the map signifies where data have been masked due to either a foreground star or data-quality issues identified in the data reduction process). Top-right frame, top section: in *blue*, the observed, median-normalized spectrum $\frac{Q}{a}$; in *green*, the spectrum reconstructed from the first 6 principal components of the model library; in *cyan*, the highest-weighted model spectrum (flagged spectral channels are not displayed). Top-right frame, bottom section: in *green*, the residual of the PC fit (with respect to the original spectrum); in *cyan*, the residual of the best-fitting model (with respect to the original spectrum); flagged spectral channels are not displayed; in *salmon*, the average fractional residual of the PCA fit, approximately 5%, in this case (comparable to the typical spectrophotometric error budget of MaNGA spectra). Other frames: histograms of individual SPS input and derived parameters, with the full training model set (“prior”) in magenta, the distribution after weighting by model likelihoods (in black, see Equation 2.13), and the highest-likelihood model as the vertical, cyan line. The 50th percentile of the posterior is shown as a green diamond, and the 16th to 84th percentile range as a green, horizontal bar.

MPL-8, 28 “science” IFU frames have viewed just sky. These data provide a baseline for the types of sky residuals which might be present in typical science exposures.

First, we test how incomplete sky-subtraction affects the estimates of principal component amplitudes themselves. In Figure 2.21, we show the dependence of each of the first six principal components on sky residual RMS (relative to a given spectrum’s normalization—so, a smaller sky residual in absolute terms will have a more severe effect in a low-surface-brightness spaxel). The weight vector associated with each spectrum is neglected, to emulate the worst-case of entirely un-subtracted sky. Redshift is varied along the abscissas: one observed-frame sky spectrum can probe a variety of rest-frame wavelengths, depending on the source redshift. Generally, at low residual RMS and low redshift, the effects on principal component amplitudes are small (less than .1). However, the impact of sky residuals rises with source redshift, since the observed-frame spectrum samples a redder wavelength range where there are more bands of sky emission. Estimates of mass-to-light ratio rely mainly on the first PC, whose amplitude is generally around 10, which makes deviations of $\sim .1$ relatively unimportant, when compared to the overall uncertainty budget.

Second, we create additional synthetic data by randomly sampling the sky-only IFU frames (as in Appendix B), and adding them to the “mock” observations. This does not result in any noticeable change to the spectral fits, and the stellar mass-to-light ratios are consistent at .02 level, RMS.

2.4.8 Quantity estimates

In order to estimate a latent (i.e., unobserved) parameter or quantity of interest P_i corresponding to some observed data S in the lower-dimensional space defined by E , we find the likelihood W_a of each model (where a denotes an individual model) given S . We

begin by finding the weighted-magnitude of the difference between a given model's PC coefficients A_a and the PC down-projection of observations A_o , using the PC projection of the total spectral covariance matrix obtained above. That is, we calculate the Mahalanobis distance (Mahalanobis 1936) between model and observations, subject to a distance metric defined by the covariance matrix:

$$D_a^2 = (A_a - A_o) \cdot P_{PC} \cdot (A_a - A_o)^T \quad (2.12)$$

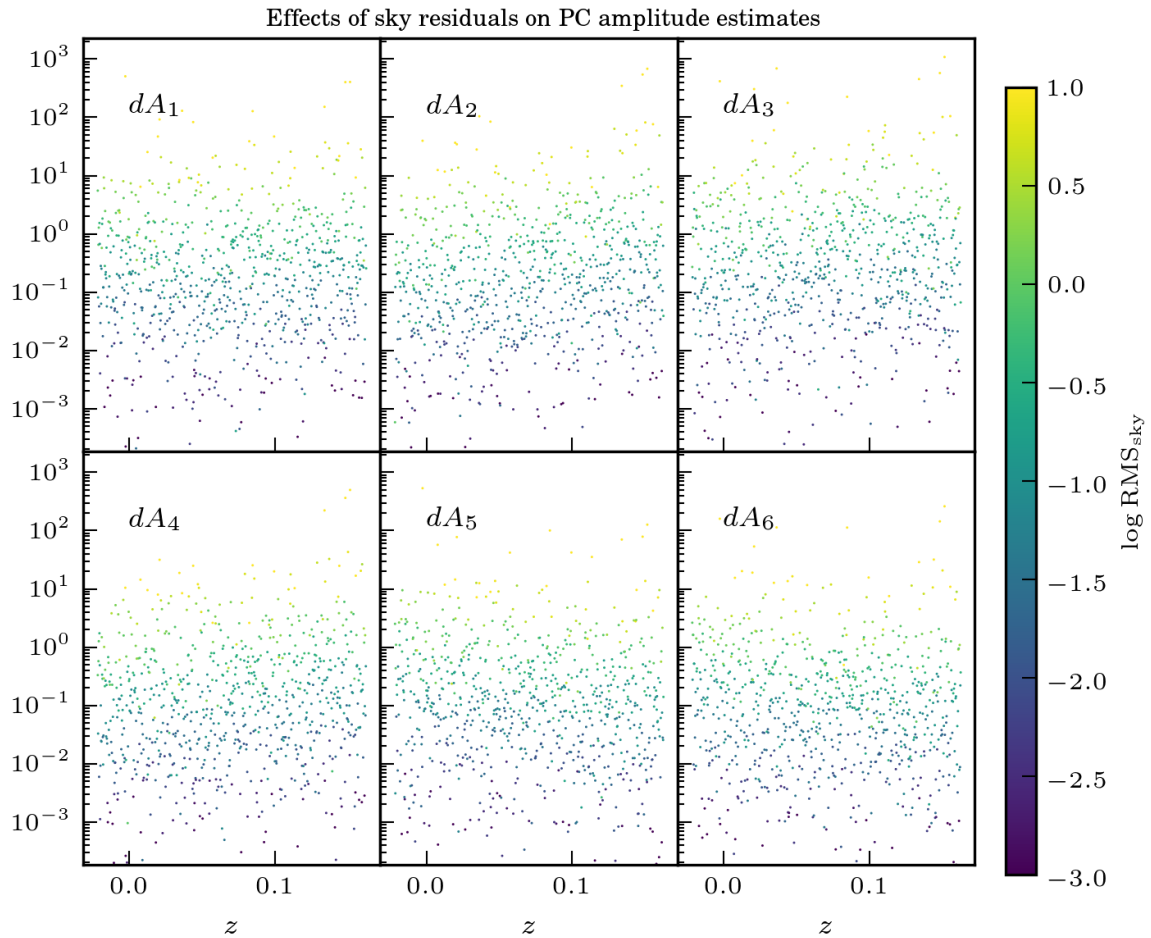


Figure 2.21 : In each subplot, the change in principle component amplitude dA_i (ordinate axis) induced by sky residuals at a level RMS_{sky} (color) relative to a normalized, observed spectrum, at some redshift (abscissa). At residual RMS below 10%, the effects on PC amplitudes are generally small (also 10%) or less. The PC amplitude perturbations very slightly increase with redshift.

where D_a^2 is the squared Mahalanobis distance between a model defined by PC coefficients A_a and the PC down-projection of observations A_o , subject to the PC covariance matrix K_{PC} and its inverse P_{PC} . The distance is immediately convertible to a model likelihood W_a (Giri 1977):

$$\log W_a = -\frac{1}{2}(\log |K_{PC}| - D_a^2 - q \log 2\pi) \quad (2.13)$$

The likelihood is used as a weight, and accounts for theoretical degeneracies associated with any spectral fitting process (e.g., age-metallicity); as well as the effects of observational noise and spectrophotometric error. In reality, most desktop computers are capable of computing Equation 2.12 simultaneously for all spaxels in a cube.

The lower panels of Figure 2.20 show example SPS-input and derived parameter distributions for the central spaxel of MaNGA galaxy 8566-12705. The magenta histograms show the distribution of training data used to build the PCA system and construct the parameter estimates, and the black histograms show the result of weighting by the individual model likelihoods yielded by Equation 2.13. The best-characterized quantities are stellar mass-to-light ratio and dust optical depth affecting old stars $\tau_V \mu$ (in general, τ_V alone is best estimated when young stars are present; otherwise, $\tau_V \mu$ can be estimated more robustly). In contrast, stellar metallicity is only weakly constrained, and (though not displayed here) parameters scaling the BHB and BSS are not at all well-constrained.

An estimate for some parameter Y_i can be obtained by computing W_a (by evaluating Equation 2.13) for all model spectra and a given observed spectrum, and then constructing a probability distribution based on those weights. Here, we quote the 16th, 50th, and 84th percentile values, with one-half the 16th to 84th percentile range as the “distribution width”. Below, we extensively evaluate the effectiveness of the PCA parameter estimation method in inferring stellar mass-to-light ratio, reddening, and stellar metallicity by using held-out “test” data generated in the same way as the training data and (Appendix B describes in

detail how the mock observations are created from synthetic spectra).

2.4.8.1 Validating number of models against reliability of quantity estimates

Separate from the issue of PC decomposition, the number of training spectra may also impact the quality of the parameter estimates, since the PC-coefficient space must be well-sampled in the vicinity of the best-fit spectrum in order to build reliable parameter PDFs. To illustrate this, we generate estimates of Υ_i for all spaxels in a single galaxy after randomly selecting a fraction of the training data to use in building the PDF. We then calculate the standard deviation of that distribution. Fig. 2.22 illustrates the interplay of median spectral signal-to-noise ratio and number of models, which together affect parameter estimate accuracy. In particular, there is very little improvement that results from increasing the number of models beyond 15,000. Fig. 2.22 also shows that even using large numbers of models, at high signal-to-noise, estimates of $\log \Upsilon_i^*$ begin to be affected by under-population of the PDF, at the .01 (absolute) level.

2.4.8.2 What limits our ability to infer quantities of interest?

The question of number of training models can be further elucidated by the following example: suppose that a quantity of interest, p , has some unknown, linear dependence B on principal component amplitudes A :

$$P = A \cdot B + \epsilon \quad (2.14)$$

where ϵ denotes a vector of white noise.

To illustrate this, we generate a vector B from a q -dimensional unit Gaussian, and simulate the effects of sampling this “placeholder quantity”’s PDF with a varying number of “placeholder models”, subject to covariate uncertainty in PC amplitude estimates. After

fixing B , we randomize N models (N is allowed to vary from 10^1 to 10^6) distributed according to a q -dimensional unit Gaussian modulated by the eigenvalues of the PCA system derived from the CSP training library. A separate, “correct” model PC amplitude vector and true quantity value p_0 are generated according to the same prescription. A PC amplitude covariance matrix K_{PC} drawn at random from actual fits to MaNGA spectra (see Sections 2.4.5 and 2.4.7) is used to sample the posterior probability density function (PDF) of Y (see Section 2.4.8), given an estimate of A which is exactly correct. The median

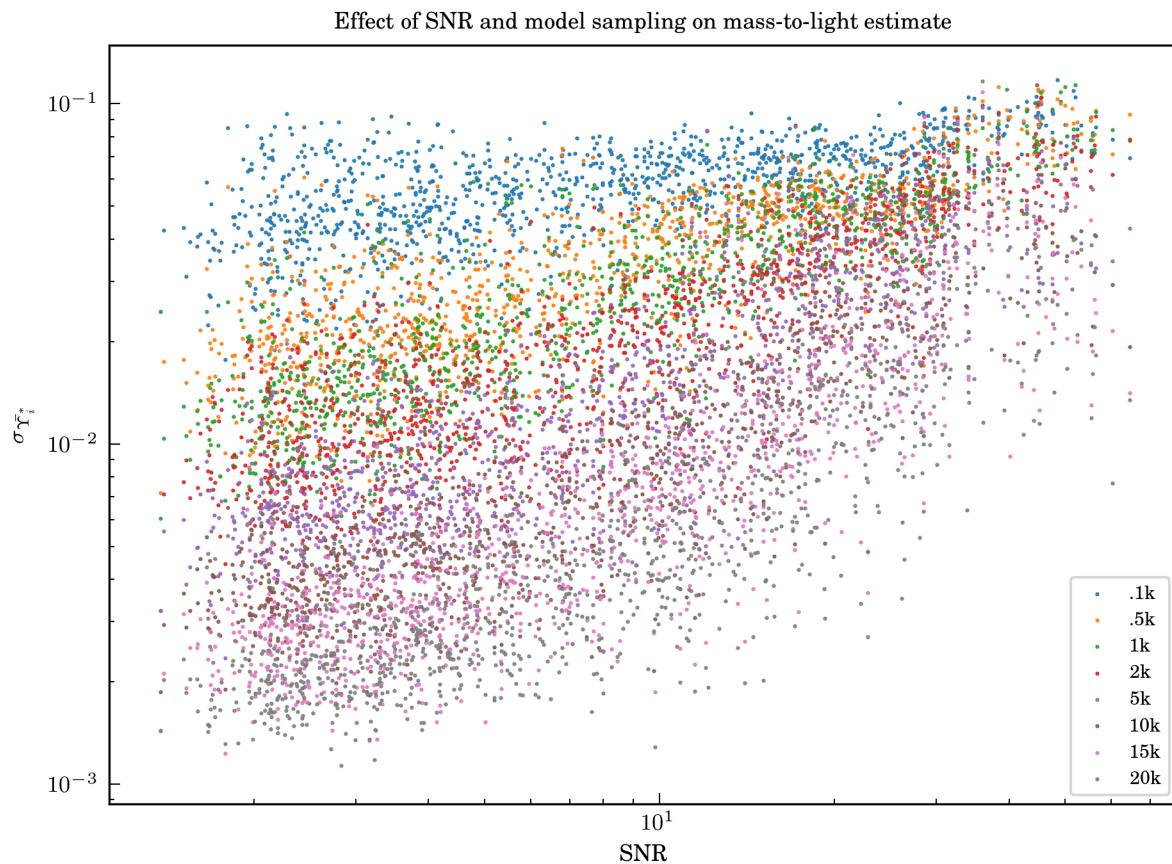


Figure 2.22 : Variability in mass-to-light estimate (50th percentile of marginalized posterior PDF) associated with changing the number of models used to populate the distribution. Each color point represents a single spectrum with the specified number of models. At low signal-to-noise and high model count, this effect is negligible; however, more models help mitigate PDF under-population at $S/N > 10$.

of this PDF, \tilde{p} , is taken as the fiducial estimate of p .

We proceed to evaluate how close \tilde{p} is to the true value, p_0 , normalizing the deviation $dp = \tilde{p} - p_0$ by the intrinsic width in the distribution of the quantity of interest in the set of placeholder models, σ_p . Under these assumptions, and setting $q = 6$, the critical number of models to achieve $\frac{dp}{\sigma_p} \lesssim .01$ is $N = 10^4$. Furthermore, as N increases, this quantity of merit decreases further, though the most poorly-behaved cases ($\frac{dp}{\sigma_p} \sim 1$) arise with vanishingly-low frequency at $N \gtrsim 10^3$.

However, this does not tell the whole story, since we cannot exactly estimate A for our observed spectra; an estimate of A is more realistically drawn from a distribution centered at A_0 with covariance K_{PC} (see Section 2.4.4 and Yan et al. 2016b). This erases many of the precision gains achieved at $N > 10^4$. In other words, imperfect spectrophotometry of the MaNGA data places a more stringent limit on the accuracy of quantity estimates.

Figure 2.23 shows the effect of varying N from 10^1 to 10^6 on the cumulative distribution of $\log \frac{\Delta p}{\sigma_p}$. While at $N < 10^3$, these trials also exhibit some unreliability ($\log \frac{dp}{\sigma_p} \gtrsim 0$), there is almost no marginal benefit to adopting $N \gtrsim 10^4$.

This test indicates that while increasing the number of models brings some improvement in estimate quality for a generic quantity of interest, the benefit is diminished when the imperfect estimation of PC amplitudes A (mediated by the spectrophotometric covariance of the data, via the PC covariance matrix K_{PC}) is accounted for. In order to realize meaningful benefits from increasing the number of CSP models, the spectrophotometry of the survey itself would have to improve by a significant margin.

2.4.9 Data-quality and masking

We implement very basic data-quality cuts, intended to locate and mark spectra which might produce misleading measurements. Though no whole galaxies are neglected

for data-quality concerns, spaxels with any of the following characteristics are presumed to have unreliable fits and parameter estimates:

- More than 30% of spectral pixels masked for any reason (combining the MaNGA DRP and emission-line flags)—see Section 2.4.5
- Median signal-to-noise ratio below 0.1.
- Uncertainty in stellar line-of-sight velocity greater than 500 km/s

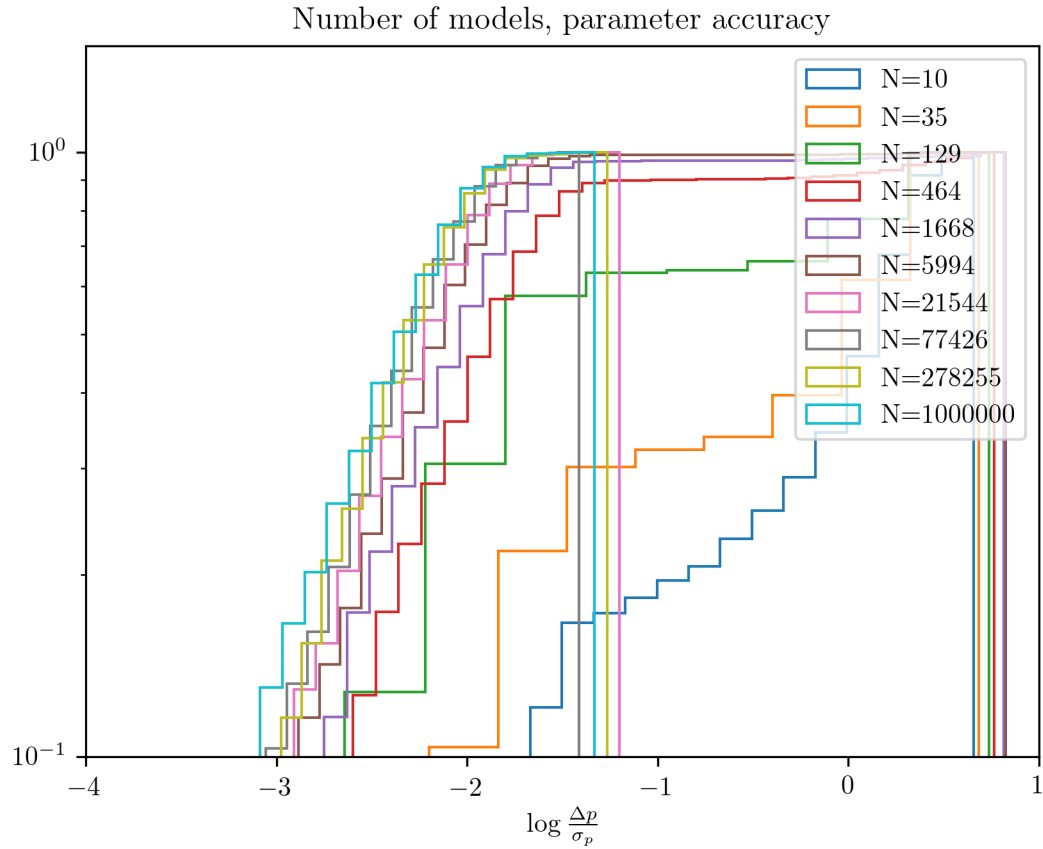


Figure 2.23 : The cumulative distribution of $\log \frac{\Delta p}{\sigma_p}$ for values of N between 10^1 and 10^6 , under the assumption of imperfect estimation of A . The model library used in this work has $N = 40000$, reliably within the locus of trials with low $\frac{dp}{\sigma_p}$.

- Poorly-sampled posterior PDF: where the highest-likelihood model fit to a given spectrum is W^* , if less than a fraction b of all models have likelihoods at least $d W^*$, it is concluded that not enough models sample the important region of PC space to robustly estimate stellar mass-to-light ratio and other stellar population characteristics. Subsequent analysis in this work uses $b = 10^{-4}$ and $d = 10^{-1}$ (see Appendix 2.4.8.1 for related discussion), but the associated data-product maps of Υ_i^* also have maps of the value of b for $d = 0.01, 0.05, 0.1, 0.25, 0.5, 0.9$. In general, this mask is generally applied at high signal-to-noise ratio, and in cases where an observed spectrum differs from a typical galaxy spectrum (e.g., a broad-line AGN)

The effects of imperfect sky-subtraction on synthetic spectra are discussed in Appendix 2.4.7.1: stellar mass-to-light ratio is mostly informed by the first principal component (which typically has an amplitude of ~ 10), and the deviations in that principal component induced by un-subtracted sky at the 10% (RMS)¹³ level is ≤ 0.1 , a 1% perturbation. Taking into account all principal components, the logarithmic change induced for a stellar mass-to-light ratio estimate is $\leq .02$.

2.4.10 Tests on held-out, synthetic data

We now address the reliability of the stellar mass-to-light ratio estimates obtained through PCA, by testing against synthetic data (referred to also as “mock observations”) intended to simulate real MaNGA observations. It is expected that reliability of $\log \Upsilon_i^*$ estimates will increase with signal-to-noise ratio, before plateauing at in the range $10 \leq \text{SNR} \leq 30$. At higher SNR, systematics related to the choice of model stellar atmospheres, SFHs, and other secondary factors will begin to adversely-influence the fit quality. Since

¹³In reality, this is a *very significant* degree of sky-contamination, since the flux-density of the sky contamination is strongly bimodal.

a relatively small amount of recent star-formation can yield a blue spectrum, but most of the mass is contained in low-mass stars, blue spectra may have less accurate mass-to-light estimates. $\log \Upsilon_i^*$ systematics with respect to stellar metallicity are possible for the same reason they are for pure CMLRs: in brief, stellar metallicity affects the evolution of single stars—changing, for example, main-sequence lifetimes at fixed initial mass, which significantly changes the integrated photometric properties (color and luminosity being the most salient) of the stellar population (see Choi et al. 2016, and related MESA/MIST works for a more thorough review). Finally, extreme attenuation could result in an under-estimate of $\log \Upsilon_i^*$, as in the CMLRs.

To evaluate the reliability of the $\log \Upsilon_i^*$ fits with respect to color, known stellar metallicity, and known attenuation, we use test data that were generated identically to the rest of the CSP training library (see Section 2.3), but were not used to find the PCA system or for the parameter inference described in Section 2.4.8. Appendix B contains a complete description of the transformation from the test data to “mock observations,” which are intended to emulate an actual observation of such a spectrum. The mock observations are then pre-processed identically to real observations, and analyzed using the PCA framework previously described. The overall philosophy of the following tests is to bin simultaneously by median signal-to-noise ratio and either $g - r$ color, [Z], or τ_V , to discover how those factors impact the reliability of inferred stellar mass-to-light ratios. We report in tabular format statistics of the stellar mass-to-light ratio estimates for both mock observations and real MaNGA galaxies. Table 2.5 shows which tables and figures give diagnostic information for which quantities of merit, and binning by which spaxel properties.

In the general case, for some parameter Y , the known value intrinsic to one SFH is

denoted Y_0 , and the estimate as \tilde{Y} . We then define the “deviation” between the two,

$$\Delta Y = \tilde{Y} - Y_0 \quad (2.15)$$

and consider the dependence of deviation in stellar mass-to-light ratio on color, known stellar metallicity, and known attenuation.

We similarly define the “uncertainty” of the distribution (σ_Y) as half the difference between the distribution’s 16th and 84th percentiles. Finally, we define a parameter’s “normalized deviation” to be the deviation divided by the distribution half-width, $\frac{\Delta Y}{\sigma_Y}$. Note the distinction between deviation (ΔY), which relies on knowledge of the true parameter value Y_0 in comparison to the estimated value \tilde{Y} ; and uncertainty (σ_Y), which is purely a description of the width of the posterior PDF of Y given some observed spectrum.

Using the mock observations for 473 galaxies (slightly less than 7% of MPL-8, and consisting of 537333 spaxels), we show in Figure 2.24 the deviation $\Delta \log \Upsilon_i^*$ after binning separately by median signal-to-noise ratio (high SNR in top panel) and $g - r$ color (colored lines within one panel). At moderate to high signal-to-noise ($\text{SNR} > 10$), the overall $\Delta \log \Upsilon_i^*$ profiles at fixed color do not change appreciably with increasing signal-to-noise. At lower signal-to-noise, the mode of red spectra moves to $\Delta \log \Upsilon_i^* < 0$ (the mass-to-light ratio is underestimated), and the mode of blue spectra moves to $\Delta \log \Upsilon_i^* > 0$ (the mass-to-light ratio is overestimated). The width of this distribution also decreases somewhat as

Data Type	Bin Type 1 (subplot)	Bin Type 2 (line color)	Quantity of Merit	Table	Figure
Mock	SNR	$g - r$	$\Delta \log \Upsilon_i^*$	2.6	2.24
Mock	SNR	$g - r$	$\sigma_{\log \Upsilon_i^*}$	2.7	2.25
Mock	SNR	$g - r$	$\frac{\Delta \log \Upsilon_i^*}{\sigma_{\log \Upsilon_i^*}}$	2.9	2.27
Mock	SNR	τ_V	$\Delta \log \Upsilon_i^*$	2.11	2.29
Mock	SNR	[Z]	$\Delta \log \Upsilon_i^*$	2.10	2.28
Obs.	SNR	$g - r$	$\sigma_{\log \Upsilon_i^*}$	2.8	2.26

Table 2.5 : Locations of figures & summary statistics for mock observations & real MaNGA data.

signal-to-noise increases to moderate value.

Next, we test the dependence of the quoted mass-to-light uncertainty ($\sigma_{\log \Upsilon_i^*}$) on optical ($g - r$) color, and the results are shown in Figure 2.25. Several effects manifest in this case, which we will address separately: first, at fixed signal-to-noise (within one panel), the moderate-color spectra have the lowest uncertainty, and the blue spectra have the highest, with red spectra falling somewhere in the middle. Naturally, the reddest spectra could be produced by either an intrinsically old stellar population or prevalent dust—in fact, [Bell et al. \(2003\)](#) estimated the impact of dust for pure CMLRs as 0.1–0.2 dex, somewhat higher than the (approximately 0.05 dex) offset we observe between moderate-color and red spectra. The bluest spectra are the most uncertain because though the majority of the light originates from young, blue stars, most of the mass resides in small, dim stars. In other words, there is the potential for the mass-carrying population to have its signal washed out by the younger, brighter one. We believe the positive (0.05–0.1 dex) offset of $\sigma_{\log \Upsilon_i^*}$ in blue spectra with respect to $\sigma_{\log \Upsilon_i^*}$ for intermediate- and red-color spectra at signal-to-noise ratios less than 10 is a manifestation of this effect.

In addition, at fixed color, an increase in signal-to-noise is not necessarily associated with a decrease in $\sigma_{\log \Upsilon_i^*}$. Rather, improvements seem to disappear (and possibly reverse at signal-to-noise greater than 20). In reality, there are several lower limits on $\sigma_{\log \Upsilon_i^*}$: the spectrophotometric uncertainty, which we model as independent of surface brightness, produces covariate noise at between the 1–3% level, and has a spectral signature similar to a changing mass-to-light ratio. The rising uncertainty at $S/N > 20$ could also be understood in terms of how densely-populated the model grid is with respect to the uncertainty on the data: by increasing the signal-to-noise of the data, the n -dimensional volume subtended by a noise vector N will decrease to the point where the parameter PDF is not well-sampled (this will be particularly problematic where a SFH’s PC representation lies near an “edge”).

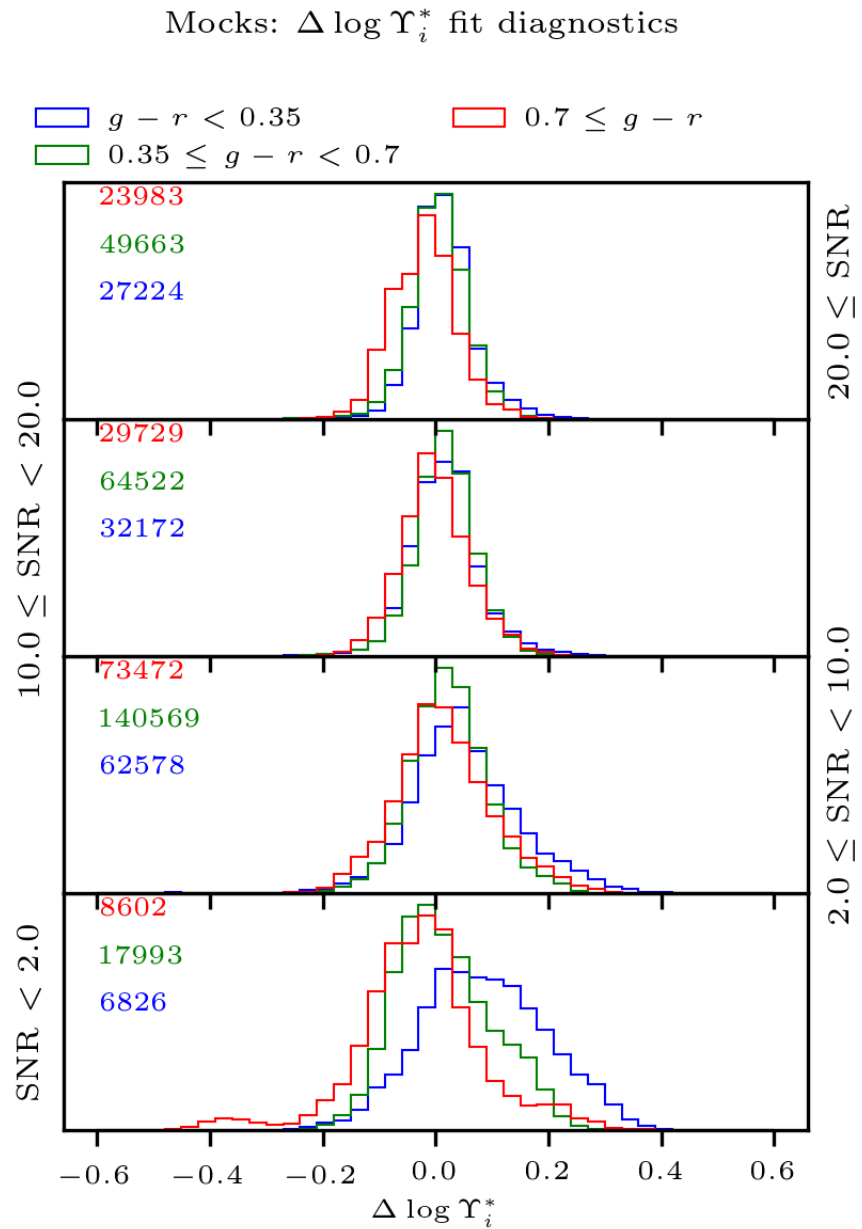


Figure 2.24 : Distributions of deviations of PCA-inferred stellar mass-to-light ratio ($\Delta \log \Upsilon_i^*$), binned into vertical subplots according to median signal-to-noise ratio, and then within each subplot according to $g - r$ color. Stellar mass-to-light ratio estimates become slightly more reliable with increasing signal-to-noise ratio, but do not improve significantly at SNR above 10, beyond $\Delta \log \Upsilon_i^* \sim 0.1$ dex.

Bin 1 (panel) range	Bin 2 (color) range	$P^{50}(\Delta \log \Upsilon_i^*)$	$P^{50}(\Delta \log \Upsilon_i^*) - P^{16}(\Delta \log \Upsilon_i^*)$	$P^{84}(\Delta \log \Upsilon_i^*) - P^{50}(\Delta \log \Upsilon_i^*)$
$[-\infty, 2.0]$	$[-\infty, 0.35]$	8.21×10^{-2}	1.04×10^{-1}	1.18×10^{-1}
$[-\infty, 2.0]$	$[0.35, 0.7]$	5.51×10^{-3}	7.40×10^{-2}	1.00×10^{-1}
$[-\infty, 2.0]$	$[0.7, \infty]$	-2.59×10^{-2}	9.04×10^{-2}	9.11×10^{-2}
$[2.0, 10.0]$	$[-\infty, 0.35]$	4.51×10^{-2}	7.84×10^{-2}	9.95×10^{-2}
$[2.0, 10.0]$	$[0.35, 0.7]$	2.15×10^{-2}	6.39×10^{-2}	6.71×10^{-2}
$[2.0, 10.0]$	$[0.7, \infty]$	1.03×10^{-2}	7.44×10^{-2}	8.89×10^{-2}
$[10.0, 20.0]$	$[-\infty, 0.35]$	1.47×10^{-2}	5.30×10^{-2}	5.51×10^{-2}
$[10.0, 20.0]$	$[0.35, 0.7]$	1.62×10^{-2}	4.90×10^{-2}	5.00×10^{-2}
$[10.0, 20.0]$	$[0.7, \infty]$	-1.89×10^{-3}	5.62×10^{-2}	5.91×10^{-2}
$[20.0, \infty]$	$[-\infty, 0.35]$	1.19×10^{-2}	4.12×10^{-2}	4.80×10^{-2}
$[20.0, \infty]$	$[0.35, 0.7]$	4.75×10^{-3}	4.52×10^{-2}	4.80×10^{-2}
$[20.0, \infty]$	$[0.7, \infty]$	-1.73×10^{-2}	6.16×10^{-2}	5.11×10^{-2}

Table 2.6 : Statistics of $\Delta \log \Upsilon_i^*$ for mock observations, separated by mean SNR and $g - r$ color: columns 3–5 respectively list the 50th percentile value, the difference between the 84th percentile value & the 50th percentile value, and the difference between the 50th percentile value & the 16th percentile value.

Bin 1 (panel) range	Bin 2 (color) range	$P^{50}(\sigma_{\log \Upsilon_i^*})$	$P^{50}(\sigma_{\log \Upsilon_i^*}) - P^{16}(\sigma_{\log \Upsilon_i^*})$	$P^{84}(\sigma_{\log \Upsilon_i^*}) - P^{50}(\sigma_{\log \Upsilon_i^*})$
$[-\infty, 2.0]$	$[-\infty, 0.35]$	2.25×10^{-1}	3.13×10^{-2}	3.25×10^{-2}
$[-\infty, 2.0]$	$[0.35, 0.7]$	1.88×10^{-1}	2.30×10^{-2}	3.02×10^{-2}
$[-\infty, 2.0]$	$[0.7, \infty]$	2.11×10^{-1}	2.47×10^{-2}	4.62×10^{-2}
$[2.0, 10.0]$	$[-\infty, 0.35]$	1.90×10^{-1}	6.80×10^{-2}	6.28×10^{-2}
$[2.0, 10.0]$	$[0.35, 0.7]$	1.46×10^{-1}	2.77×10^{-2}	3.99×10^{-2}
$[2.0, 10.0]$	$[0.7, \infty]$	1.73×10^{-1}	2.98×10^{-2}	2.28×10^{-2}
$[10.0, 20.0]$	$[-\infty, 0.35]$	1.21×10^{-1}	2.97×10^{-2}	9.19×10^{-2}
$[10.0, 20.0]$	$[0.35, 0.7]$	1.13×10^{-1}	1.98×10^{-2}	3.70×10^{-2}
$[10.0, 20.0]$	$[0.7, \infty]$	1.57×10^{-1}	4.10×10^{-2}	3.10×10^{-2}
$[20.0, \infty]$	$[-\infty, 0.35]$	1.01×10^{-1}	2.07×10^{-2}	7.48×10^{-2}
$[20.0, \infty]$	$[0.35, 0.7]$	1.05×10^{-1}	1.77×10^{-2}	3.01×10^{-2}
$[20.0, \infty]$	$[0.7, \infty]$	1.49×10^{-1}	4.02×10^{-2}	3.41×10^{-2}

Table 2.7 : Statistics of $\sigma_{\log \Upsilon_i^*}$ for mock observations, separated by mean SNR and $g - r$ color: columns 3–5 respectively list the 50th percentile value, the difference between the 84th percentile value & the 50th percentile value, and the difference between the 50th percentile value & the 16th percentile value.

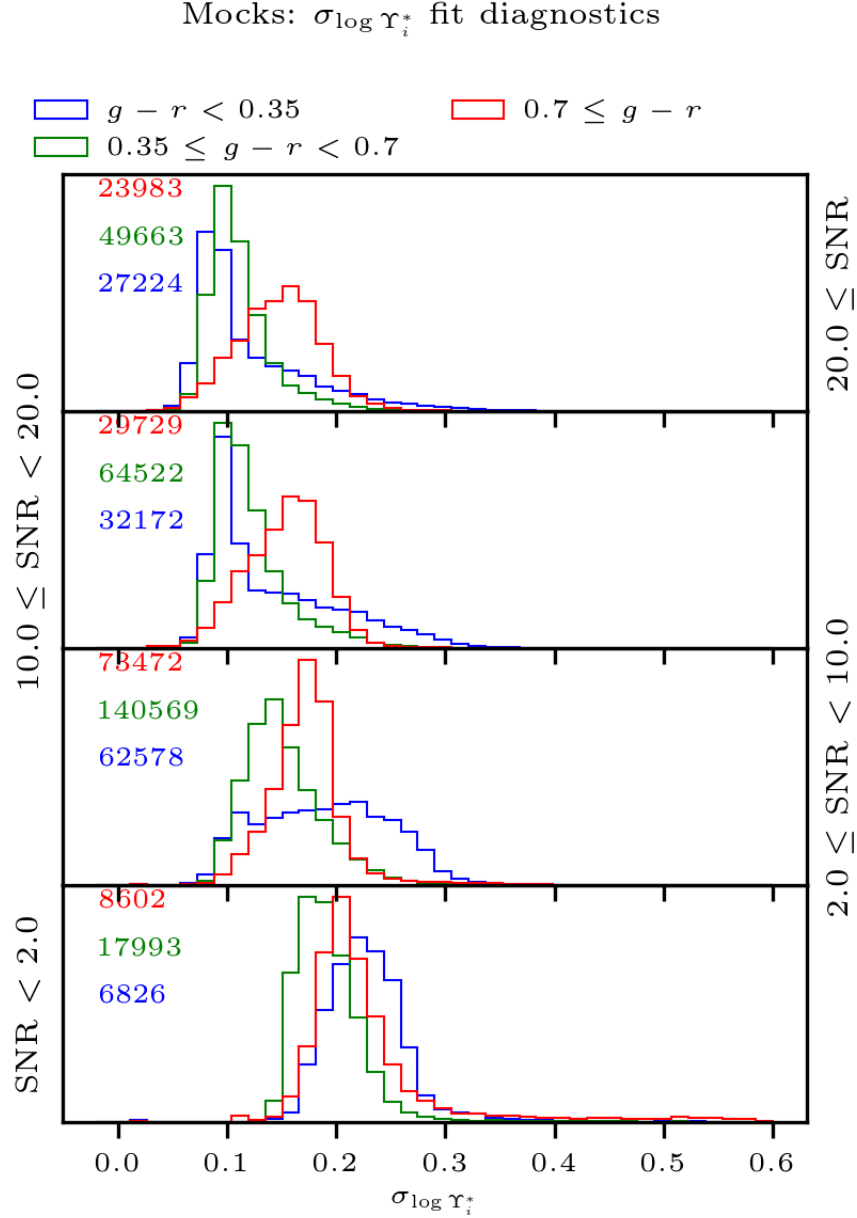
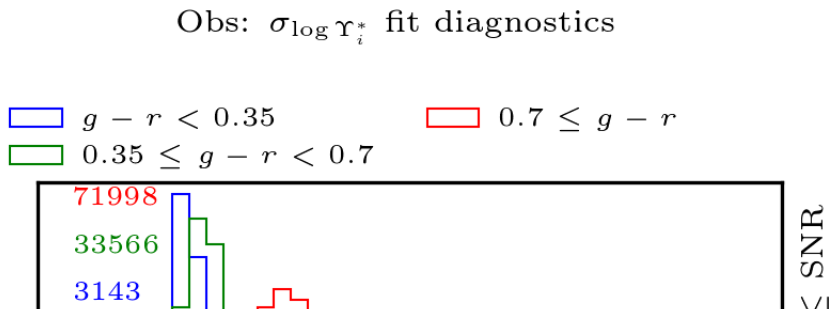


Figure 2.25 : Distributions of uncertainty in PCA-inferred stellar mass-to-light ratio ($\sigma_{\log \Upsilon_i^*}$) for mock observations of synthetic spectra, binned into vertical subplots according to median signal-to-noise ratio, and then within each subplot according to $g - r$ color. The overall uncertainty does decrease with median signal-to-noise ratio: this effect is strongest for blue spectra and weakest for red (at low signal-to-noise, an acceptable fit to a blue spectrum allows for a significant amount of mass from old stars—this degeneracy weakens as signal-to-noise ratio rises).



Interestingly, regardless of color or signal-to-noise, the RMS of the deviation (the width of the $\Delta \log \Upsilon_i^*$ distribution) is always of the same order as (and often a factor of up to two less than) the mean of the uncertainty ($\sigma_{\log \Upsilon_i^*}$). This means that on the whole, uncertainties in stellar mass-to-light ratio reflect the real statistical uncertainty. We examine this below by showing the distribution of $\frac{\Delta \log \Upsilon_i^*}{\sigma_{\log \Upsilon_i^*}}$.

For the sake of comparison, we display $\sigma_{\log \Upsilon_i^*}$ for the same sample of *real* galaxies (Figure 2.26). The distributions of these data are qualitatively similar to the case of the mock observations of synthetic spectra: regardless of color, stellar mass-to-light ratio uncertainty decreases as signal-to-noise ratio increases, but this effect is strongest for blue spectra and weakest for red. The most noticeable difference between fits to mock observations and real observations is at moderate signal-to-noise ratio: the mocks' distribution of uncertainty has a higher mode (0.25 dex, versus the observations' 0.15 dex). It is probable that this difference in behavior has to do with slight discrepancies in the distribution of training data with respect to real galaxies. The relative strengths of individual binned distributions are likewise determined by the details of the SFH library: for example, a larger proportion of observations at low signal-to-noise ratio are blue, since the lower surface-brightness outskirts of galaxies will have commensurately-lower signal-to-noise ratios. As a whole, though, the distributions of $\sigma_{\log \Upsilon_i^*}$ for mocks and real observations are broadly similar when the same signal-to-noise and color ranges are compared. We believe this indicates both that the mocks are a faithful reconstruction of MaNGA observations; and that the actual distribution of SFHs in MaNGA spaxels is sufficiently similar to the training data to infer unobserved properties such as stellar mass-to-light ratio.

We next consider the normalized deviations ($\frac{\Delta \log \Upsilon_i^*}{\sigma_{\log \Upsilon_i^*}}$) with respect to the mocks, which are important for evaluating whether the provided mass-to-light ratio uncertainties are accurate. Figure 2.27 illustrates the relatively steady accuracy of the $\log \Upsilon_i^*$ estimates

with respect to color and signal-to-noise (besides the effects on $\Delta \log \Upsilon_i^*$ already discussed).

In all cases but low-signal-to-noise, blue spectra, the $\frac{\Delta \log \Upsilon_i^*}{\sigma_{\log \Upsilon_i^*}}$ distributions are relatively symmetrical, and do not exhibit significant power at high absolute values (which would indicate unreliable uncertainties in some region of parameter-space). Most distributions compare favorably to the ideal case of the uncertainty roughly matching the deviation (blue, dotted curve). In summary, from the above tests on both synthetic and real observations, we conclude that the PCA parameter estimation implemented here for $\log \Upsilon_i^*$ achieves acceptable levels of accuracy and precision for use in estimating total stellar-mass.

In Section 2.3.3, we showed that our family of CSPs exhibit scatter about their

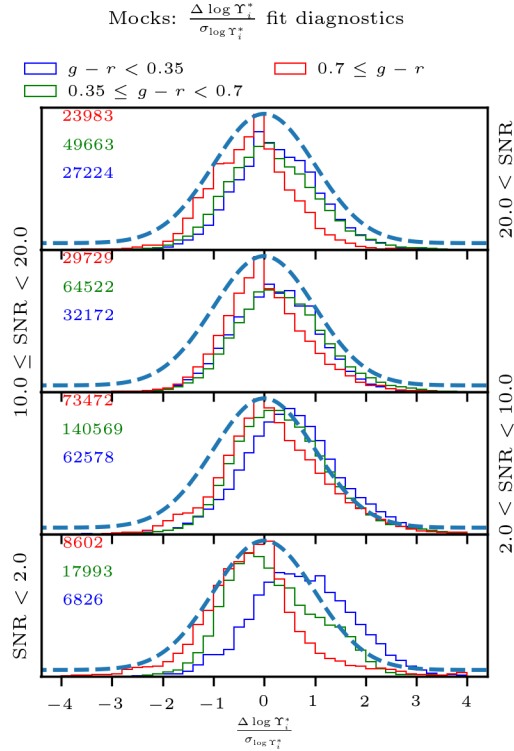


Figure 2.27 : As Figure 2.25, except with distributions of $\frac{\Delta \log \Upsilon_i^*}{\sigma_{\log \Upsilon_i^*}}$. Up to the small offset effects covariate with integrated color (see Figure 2.24), we find that the reported uncertainties in $\log \Upsilon_i^*$ faithfully reflect the real deviation between the inferred stellar mass-to-light ratio and its true value. Overplotted in blue-gray is a normal distribution with dispersion of unity, which should correspond to the nominal case of uncertainties that match well with the actual accuracy of an estimate.

Bin 1 (panel) range	Bin 2 (color) range	$P^{50}(\sigma_{\log \Upsilon_i^*})$	$P^{50}(\sigma_{\log \Upsilon_i^*}) - P^{16}(\sigma_{\log \Upsilon_i^*})$	$P^{84}(\sigma_{\log \Upsilon_i^*}) - P^{50}(\sigma_{\log \Upsilon_i^*})$
$[-\infty, 2.0]$	$[-\infty, 0.35]$	2.18×10^{-1}	2.81×10^{-2}	4.23×10^{-2}
$[-\infty, 2.0]$	$[0.35, 0.7]$	1.72×10^{-1}	2.04×10^{-2}	2.70×10^{-2}
$[-\infty, 2.0]$	$[0.7, \infty]$	1.91×10^{-1}	1.67×10^{-2}	1.99×10^{-2}
$[2.0, 10.0]$	$[-\infty, 0.35]$	1.67×10^{-1}	4.74×10^{-2}	6.03×10^{-2}
$[2.0, 10.0]$	$[0.35, 0.7]$	1.37×10^{-1}	2.43×10^{-2}	4.44×10^{-2}
$[2.0, 10.0]$	$[0.7, \infty]$	1.69×10^{-1}	2.55×10^{-2}	2.16×10^{-2}
$[10.0, 20.0]$	$[-\infty, 0.35]$	1.11×10^{-1}	2.15×10^{-2}	6.47×10^{-2}
$[10.0, 20.0]$	$[0.35, 0.7]$	1.14×10^{-1}	1.86×10^{-2}	3.68×10^{-2}
$[10.0, 20.0]$	$[0.7, \infty]$	1.69×10^{-1}	3.74×10^{-2}	2.62×10^{-2}
$[20.0, \infty]$	$[-\infty, 0.35]$	9.54×10^{-2}	1.69×10^{-2}	6.45×10^{-2}
$[20.0, \infty]$	$[0.35, 0.7]$	1.07×10^{-1}	2.18×10^{-2}	3.90×10^{-2}
$[20.0, \infty]$	$[0.7, \infty]$	1.65×10^{-1}	4.37×10^{-2}	3.46×10^{-2}

Table 2.8 : Statistics of $\sigma_{\log \Upsilon_i^*}$ for real MaNGA observations, separated by mean SNR and $g - r$ color: columns 3–5 respectively list the 50th percentile value, the difference between the 84th percentile value & the 50th percentile value, and the difference between the 50th percentile value & the 16th percentile value.

Bin 1 (panel) range	Bin 2 (color) range	$P^{50}(\frac{\Delta \log \Upsilon_i^*}{\sigma_{\log \Upsilon_i^*}})$	$P^{50}(\frac{\Delta \log \Upsilon_i^*}{\sigma_{\log \Upsilon_i^*}}) - P^{16}(\frac{\Delta \log \Upsilon_i^*}{\sigma_{\log \Upsilon_i^*}})$	$P^{84}(\frac{\Delta \log \Upsilon_i^*}{\sigma_{\log \Upsilon_i^*}}) - P^{50}(\frac{\Delta \log \Upsilon_i^*}{\sigma_{\log \Upsilon_i^*}})$
$[-\infty, 2.0]$	$[-\infty, 0.35]$	7.11×10^{-1}	9.11×10^{-1}	1.02×10^0
$[-\infty, 2.0]$	$[0.35, 0.7]$	5.79×10^{-2}	7.61×10^{-1}	1.12×10^0
$[-\infty, 2.0]$	$[0.7, \infty]$	-2.36×10^{-1}	8.42×10^{-1}	8.04×10^{-1}
$[2.0, 10.0]$	$[-\infty, 0.35]$	5.16×10^{-1}	8.98×10^{-1}	9.70×10^{-1}
$[2.0, 10.0]$	$[0.35, 0.7]$	3.00×10^{-1}	8.33×10^{-1}	9.56×10^{-1}
$[2.0, 10.0]$	$[0.7, \infty]$	1.19×10^{-1}	8.41×10^{-1}	1.09×10^0
$[10.0, 20.0]$	$[-\infty, 0.35]$	2.25×10^{-1}	8.29×10^{-1}	8.13×10^{-1}
$[10.0, 20.0]$	$[0.35, 0.7]$	2.88×10^{-1}	8.12×10^{-1}	9.01×10^{-1}
$[10.0, 20.0]$	$[0.7, \infty]$	-2.60×10^{-2}	7.03×10^{-1}	8.62×10^{-1}
$[20.0, \infty]$	$[-\infty, 0.35]$	2.15×10^{-1}	7.67×10^{-1}	8.43×10^{-1}
$[20.0, \infty]$	$[0.35, 0.7]$	9.37×10^{-2}	8.03×10^{-1}	9.31×10^{-1}
$[20.0, \infty]$	$[0.7, \infty]$	-2.38×10^{-1}	7.90×10^{-1}	7.39×10^{-1}

Table 2.9 : Statistics of $\frac{\Delta \log \Upsilon_i^*}{\sigma_{\log \Upsilon_i^*}}$ for mock observations, separated by mean SNR and $g - r$ color: columns 3–5 respectively list the 50th percentile value, the difference between the 84th percentile value & the 50th percentile value, and the difference between the 50th percentile value & the 16th percentile value.

best-fit CMLR which correlates in its magnitude with extreme stellar metallicity and attenuation. Here, we test the precision and accuracy of our $\log \Upsilon_i^*$ estimates. When using stellar population absorption indices, heuristics like the “3/2 rule” describe the covariance between mean stellar age and metallicity (Worley et al. 1994)¹⁴. Similarly to what was observed with CMLRs, significant dust attenuation applied to an otherwise-young stellar population could conceivably effect an overestimate of its mass-to-light ratio. Figures 2.28 and 2.29 respectively bin $\Delta \log \Upsilon_i^*$ by median signal-to-noise ratio and either τ_V or $[Z]$ for mock observations.

In Figure 2.28, we see that regardless of metallicity, reliability of $\log \Upsilon_i^*$ estimates

¹⁴The 3/2 rule is an observation stating that an increase (decrease) of a stellar population’s age by a factor of three is almost indistinguishable from an increase (decrease) in metallicity by a factor of two.

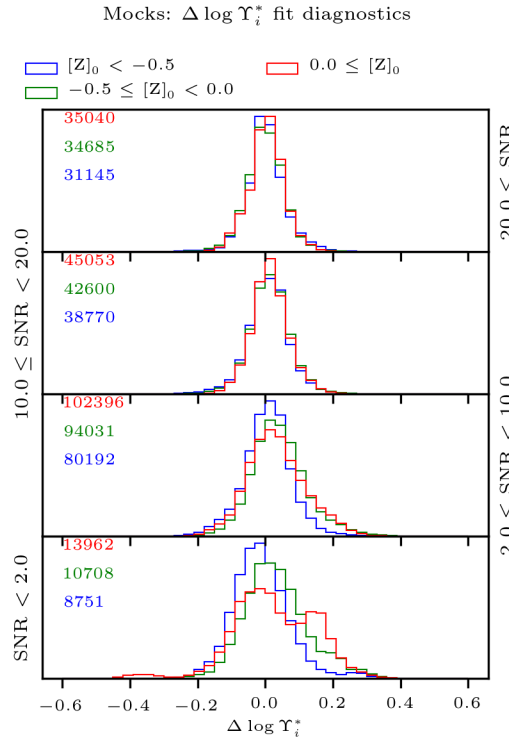


Figure 2.28 : As Figure 2.24, except binning with respect to known $[Z]$ rather than $g - r$ color. Other than at low signal-to-noise ratio and high metallicity (where deviations may reach 0.3 dex), there are minimal systematics in inferred $\log \Upsilon_i^*$ with respect to $[Z]$.

increase with signal-to-noise, and converge to $\Delta \log \Upsilon_i^* \sim 0.1$ at $S/N \sim 20$. At high stellar metallicity and low signal-to-noise ratio, the distribution of $\Delta \log \Upsilon_i^*$ becomes significantly skewed (with the long tail at positive $\Delta \log \Upsilon_i^*$, indicating an overestimate generally less than 0.15 dex). Though this deviation is not reflected in the associated uncertainties (i.e., $\frac{\Delta \log \Upsilon_i^*}{\sigma_{\log \Upsilon_i^*}}$ is high), it ceases at higher SNR. At lower metallicity, the typical deviation between known and estimated mass-to-light ratio remains unimodal across the entire SNR regime.

In Figure 2.29, we see that high signal-to-noise spectra yield more or less equally-reliable estimates of $\log \Upsilon_i^*$, regardless of attenuation. As signal-to-noise decreases, spectra with intermediate attenuation tend to skew towards underestimating $\log \Upsilon_i^*$, while the distribution for high-attenuation spectra becomes much wider, in a way which is not

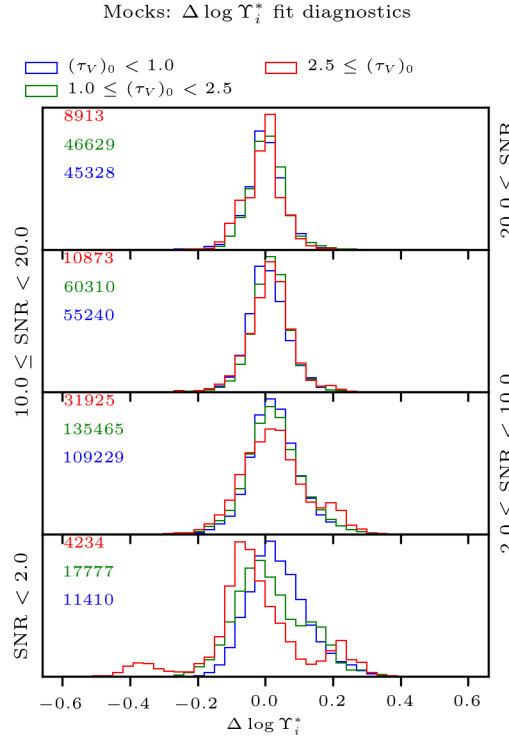


Figure 2.29 : As Figure 2.24, except binning with respect to known τ_V rather than $g - r$ color. As before, at high signal-to-noise, performance of the $\log \Upsilon_i^*$ estimate does not change strongly with attenuation; however, at lower signal-to-noise, high-attenuation spectra may have their stellar mass-to-light ratio overestimated by up to about 0.3 dex. Such cases are expected to be rare in the MaNGA data.

Bin 1 (panel) range	Bin 2 (color) range	$P^{50}(\Delta \log \Upsilon_i^*)$	$P^{50}(\Delta \log \Upsilon_i^*) - P^{16}(\Delta \log \Upsilon_i^*)$	$P^{84}(\Delta \log \Upsilon_i^*) - P^{16}(\Delta \log \Upsilon_i^*)$
[-∞, 2.0]	[-∞, -0.5]	-1.69×10^{-2}	7.03×10^{-2}	8.01×10^{-2}
[-∞, 2.0]	[-0.5, 0.0]	2.47×10^{-2}	8.08×10^{-2}	9.81×10^{-2}
[-∞, 2.0]	[0.0, ∞]	1.74×10^{-2}	9.91×10^{-2}	1.31×10^{-1}
[2.0, 10.0]	[-∞, -0.5]	8.10×10^{-3}	6.63×10^{-2}	5.91×10^{-2}
[2.0, 10.0]	[-0.5, 0.0]	3.56×10^{-2}	6.92×10^{-2}	7.91×10^{-2}
[2.0, 10.0]	[0.0, ∞]	2.70×10^{-2}	7.58×10^{-2}	9.21×10^{-2}
[10.0, 20.0]	[-∞, -0.5]	8.30×10^{-3}	5.48×10^{-2}	5.31×10^{-2}
[10.0, 20.0]	[-0.5, 0.0]	1.36×10^{-2}	5.46×10^{-2}	5.51×10^{-2}
[10.0, 20.0]	[0.0, ∞]	1.35×10^{-2}	4.99×10^{-2}	5.21×10^{-2}
[20.0, ∞]	[-∞, -0.5]	6.53×10^{-6}	4.73×10^{-2}	5.21×10^{-2}
[20.0, ∞]	[-0.5, 0.0]	2.05×10^{-6}	4.99×10^{-2}	5.01×10^{-2}
[20.0, ∞]	[0.0, ∞]	5.05×10^{-3}	5.14×10^{-2}	4.61×10^{-2}

Table 2.10 : Statistics of $\Delta \log \Upsilon_i^*$ for mock observations, separated by mean SNR and known stellar metallicity: columns 3–5 respectively list the 50th percentile value, the difference between the 84th percentile value & the 50th percentile value, and the difference between the 50th percentile value & the 16th percentile value.

Bin 1 (panel) range	Bin 2 (color) range	$P^{50}(\frac{\Delta \log \Upsilon_i^*}{\sigma_{\log \Upsilon_i^*}})$	$P^{50}(\frac{\Delta \log \Upsilon_i^*}{\sigma_{\log \Upsilon_i^*}}) - P^{16}(\frac{\Delta \log \Upsilon_i^*}{\sigma_{\log \Upsilon_i^*}})$	$P^{84}(\frac{\Delta \log \Upsilon_i^*}{\sigma_{\log \Upsilon_i^*}}) - P^{16}(\frac{\Delta \log \Upsilon_i^*}{\sigma_{\log \Upsilon_i^*}})$
[-∞, 2.0]	[-∞, 1.0]	2.95×10^{-2}	7.48×10^{-2}	9.21×10^{-2}
[-∞, 2.0]	[1.0, 2.5]	3.61×10^{-3}	8.48×10^{-2}	1.32×10^{-1}
[-∞, 2.0]	[2.5, ∞]	-4.19×10^{-2}	7.65×10^{-2}	1.33×10^{-1}
[2.0, 10.0]	[-∞, 1.0]	2.46×10^{-2}	6.45×10^{-2}	7.43×10^{-2}
[2.0, 10.0]	[1.0, 2.5]	2.27×10^{-2}	7.12×10^{-2}	8.05×10^{-2}
[2.0, 10.0]	[2.5, ∞]	2.23×10^{-2}	8.56×10^{-2}	1.03×10^{-1}
[10.0, 20.0]	[-∞, 1.0]	4.94×10^{-3}	5.15×10^{-2}	5.82×10^{-2}
[10.0, 20.0]	[1.0, 2.5]	1.66×10^{-2}	5.12×10^{-2}	5.02×10^{-2}
[10.0, 20.0]	[2.5, ∞]	1.86×10^{-2}	6.27×10^{-2}	5.30×10^{-2}
[20.0, ∞]	[-∞, 1.0]	-3.60×10^{-7}	4.81×10^{-2}	5.15×10^{-2}
[20.0, ∞]	[1.0, 2.5]	4.13×10^{-3}	4.95×10^{-2}	4.76×10^{-2}
[20.0, ∞]	[2.5, ∞]	9.44×10^{-7}	6.50×10^{-2}	4.50×10^{-2}

Table 2.11 : Statistics of $\Delta \log \Upsilon_i^*$ for mock observations, separated by mean SNR and τ_V : columns 3–5 respectively list the 50th percentile value, the difference between the 84th percentile value & the 50th percentile value, and the difference between the 50th percentile value & the 16th percentile value.

reflected in the parameter uncertainty ($\sigma_{\log \Upsilon_i^*}$). Such spectra are expected to have little impact, though (by virtue of their high attenuation, such spectra have lower surface-brightness and contribute little to an estimate of a galaxy’s total stellar mass).

In summary, while the underlying attenuation and stellar metallicity of a mock SFH does certainly impact the stellar mass-to-light ratio yielded by the PCA parameter estimation, the effects are relatively small for non-extreme cases. When 473 *observed* galaxies are binned simultaneously by $\tau_V \mu$ and [Z], the vast majority have $\tau_V \mu < 1.0$ and $-0.5 < [Z] < 0.1$, supporting the claim that the training data are more widely-distributed in parameter space than actual MaNGA galaxies are. That is, even with the extremely permissive priors on attenuation and stellar metallicity, the vast majority of fits to observations lie in the region of [Z]– $\tau_V \mu$ space for which estimates of $\log \Upsilon_i^*$ behave the best. Similar figures illustrating $\Delta \log \Upsilon_i^*$ and $\frac{\Delta \log \Upsilon_i^*}{\sigma_{\log \Upsilon_i^*}}$ in bins of signal-to-noise ratio and either [Z] or $\tau_V \mu$ have been omitted for brevity’s sake, and do not cause concern.

2.5 Resolved stellar mass-to-light ratios: Discussion and Conclusion

In this work, we construct a set of 4000 synthetic SFHs (subsampled 10 times in [Z], τ_V , μ , and σ), perform PCA on the resulting optical spectra, and use the resulting, lower-dimensional space to fit IFS observations from the SDSS-IV/MaNGA survey. Using those fits, we estimate resolved, *i*-band stellar mass-to-light ratios for galaxies in MPL-8, with uncertainties which take into account model-dependent and age-metallicity degeneracies, as well as a spectrophotometric covariance estimated from multiply-observed galaxies. The parameter-estimation strategy chosen performs well when tested on synthetic, test data generated identically to the training data, at median signal-to-noise ratios between 2 and 20 (see Figures 2.24, 2.25, and 2.27). We note that deviations in this intermediate-signal-

to-noise regime generally lie at the ~ 0.1 dex level or smaller, and are mostly uncorrelated with stellar metallicity and foreground attenuation. At higher and lower median signal-to-noise, extreme values of these two parameters correlate with mis-estimates of Υ_i^* at the ~ 0.2 dex level.

We include here sample maps of resolved stellar mass-to-light ratio for a sample of three early-type galaxies (Figure 2.30) and four late-type galaxies (Figure 2.31), including uncertainties & data-quality masks, accompanied by a cutout image of the galaxy from legacy imaging. The maps of resolved stellar mass-to-light ratio are spatially smooth, suggesting that the PC down-projection of two nearby spaxels indeed reflects the PSF of the data induced by the dithering and wavelength-rectification processes: The process of assembling individual science exposures (each at one of three positions on a galaxy’s face, and subject to some distinct differential atmospheric refraction, attenuation by the atmosphere, etc.) detailed in Law et al. (2016, Section 9.2) induces a spatial covariance between nearby spaxels. Therefore, one might expect that two spaxels that are nearby to one another might have similar estimates of mass-to-light ratio, beyond the degree to which the underlying stellar populations are similar. We do in fact qualitatively observe this smooth variation in the resolved stellar mass-to-light ratio.

2.5.1 Remaining spectral-fitting systematics and degeneracies

The use of a synthetic stellar library represents the most uncertain systematic in this work. Perhaps most importantly, the one-dimensional stellar atmospheres adopted for this work are fixed in abundance of α elements. In reality, $\frac{\alpha}{\text{Fe}}$ is known to differ from the solar value in the central regions of early-type galaxies (Worley et al. 1992; Matteucci 1994; Thomas et al. 1999). These are among the brightest spaxels in the survey. Indeed, such regions are occasionally observed to have poorly-determined estimates of $\log \Upsilon_i^*$ (Section

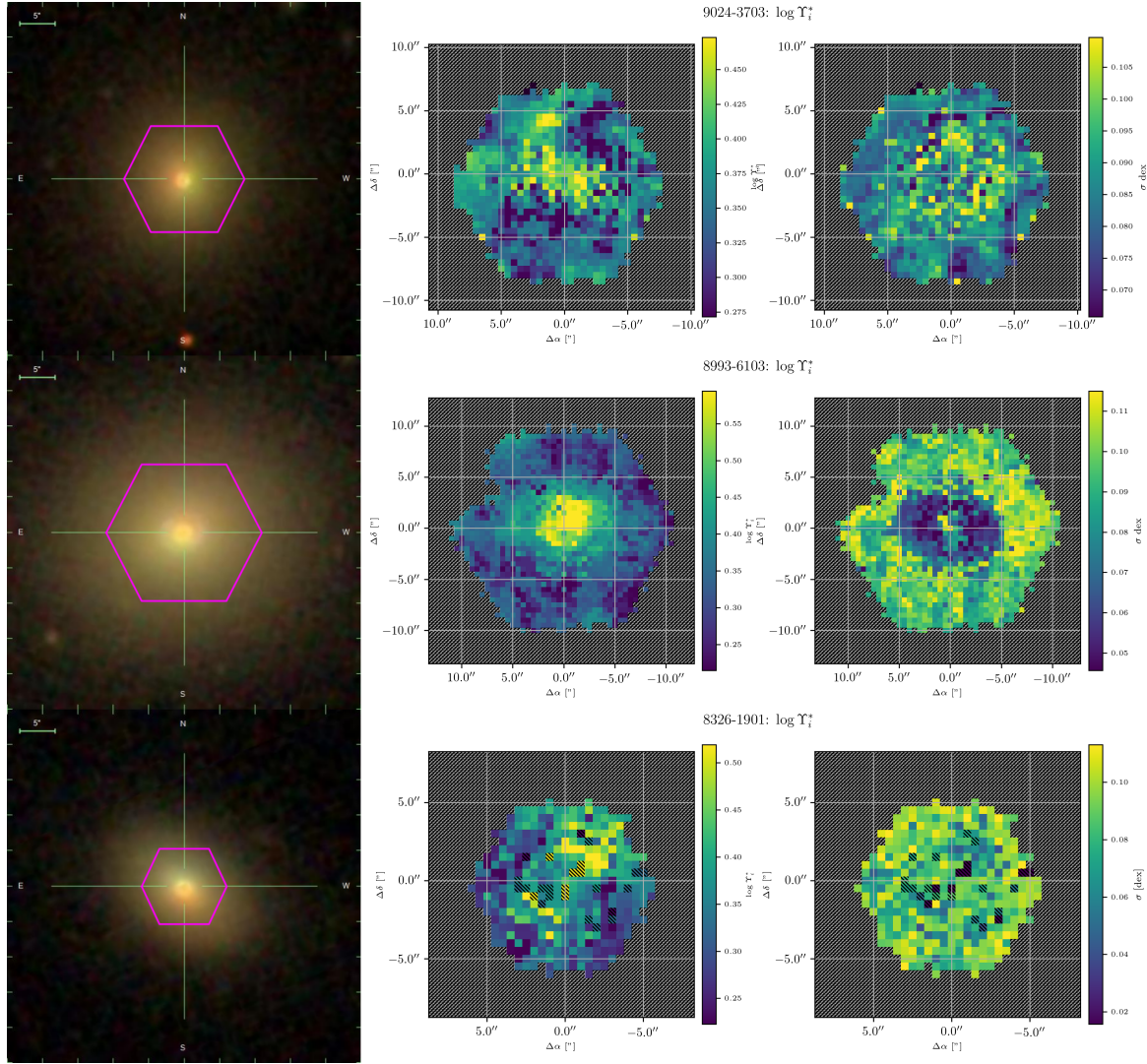


Figure 2.30 : A selection of three early-type galaxies: In the left-hand column, the SDSS cutout with a purple hexagon denoting the approximate spatial grasp of the IFU. In the middle column, an image of the resolved estimate of *i*-band stellar mass-to-light ratio, taken as the 50th percentile of the posterior PDF for a given spaxel. In the right-hand panel, a map of the adopted uncertainty in stellar mass-to-light ratio, taken as half the difference between the 16th and 84th percentiles of the posterior PDF. Spaxels with hatching top-left to bottom-right have poorly-sampled PDFs, and spaxels with hatching top-right to bottom-left have no data. Spaxels filled with dots had a numerical failure in the PC down-projection, which prevented an estimate from being made (very rare).

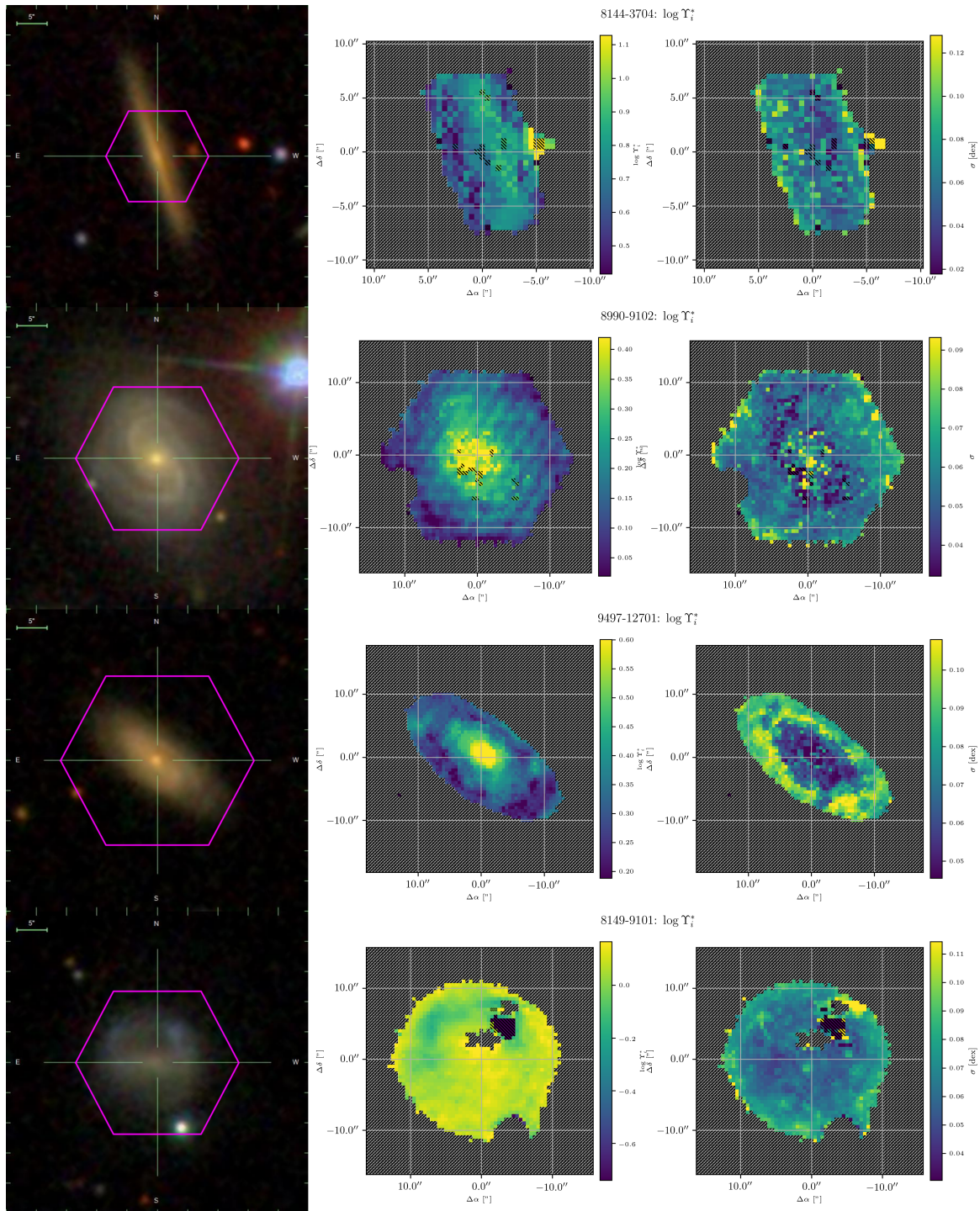


Figure 2.31 : As Figure 2.30, but a selection of four late-type galaxies. 8114-3704 is seen edge-on & exhibits a dust lane, 8990-9102 is star-forming and is seen nearly face-on, 9497-12701 is moderately-inclined and has a low SFR, and 8149-9101 is a low-mass dwarf galaxy with ongoing star-formation.

[2.4.9](#)). Fortunately, the MaStar project is now undertaking bright-time observations of stars using the BOSS spectrograph, the same instrument as is used for MaNGA galaxies. A resolution- and wavelength-range-matched sample of about 10,000 stars with a wide variety of stellar parameters will represent an important value-added deliverable of MaNGA, as well as a useful input to SPS codes. Secondarily, strong constraints on the prevalence and impact of non-standard stellar evolution scenarios (such as blue stragglers and blue horizontal branch) will inform future choices of SPS inputs.

2.5.2 Public Data and Future Work

The resolved estimates of stellar mass-to-light ratio treated in detail in this work will be included in the next public data release of SDSS-IV as a value-added catalog (VAC). In [MaNGA-PCA Paper II](#) (next in this series), we:

- Further evaluate the resolved stellar mass-to-light estimates of MaNGA galaxies by transforming them to maps of stellar mass surface density and comparing to radial averages of dynamical mass surface density from the DiskMass Survey ([Bershady et al. 2010](#)).
- Devise a method of aperture-correcting estimates of resolved stellar mass in order to obtain estimates of total galaxy stellar mass, which will also be released to the community.
- Compare the PCA-derived estimates of total galaxy stellar mass to those from integrated photometry.
- Evaluate the factors contributing to a mass deficit in IFU-summed spectra, relative to summing stellar masses in individual spaxels.

Also provided will be light-weight python scripting utilities to assist in accessing the resolved mass-to-light maps. Resolved maps of additional parameters (such as dust, SFH burst diagnostics, and stellar metallicity) may be released as part of future scientific analyses (they may also be obtained from the authors, upon request).

A The MaNGA Instrumental Line-Spread Function

The line-spread function of a spectrograph will introduce an additional “blur” in the spectral dimension, beyond that produced by astrophysical velocity dispersion. Additionally, the width of the (presumed-Gaussian) resolution element varies across the instrument by nearly a factor of two. This has the potential to severely hamper the quality and reliability of the SFH fits. For example, assuming a constant kernel width across the full MaNGA wavelength range will:

- Artificially increase measured velocity dispersions. This effect will be a pervasive and systematic bias, and will not simply increase the width of the velocity dispersion PDF.
- Potentially introduce other systematics related to how certain absorption lines reflect different stellar populations.

A more subtle effect results from the process of de-redshifting a spectrum into the rest frame. The width of the (observed-frame) LSF, in pixels, will be modified by a factor of $\frac{1}{1+z}$, such that higher-redshift galaxies will seem to experience less instrumental blurring in the rest-frame. If all observed galaxies were assumed to have a redshift of zero, then this would be a *sim10%* effect; however, by assuming a fiducial redshift of .04, this effect becomes less important, on average. A slight redshift bias may persist, which could be solved by producing many (redshift-dependent) PCA solutions. In practice, repeated (expensive) LSF

convolutions and SVD operations defeats the speed gains of the PCA parameter fitting, and so a single fiducial redshift is deemed sufficient.

B Constructing synthetic observations using held-out test data

Here we address PCA’s ability to recover properties of synthetic spectra, derived from known SFHs and stellar properties. We use held-out test data generated identically to the CSP model library to construct synthetic datacubes, with similar statistical properties to observed MaNGA galaxies, as described in Appendix B. The process is as follows:

1. Obtain a full-resolution model spectrum, along with the properties used to generate it (“truth”)
2. Read in MaNGA DRP and DAP products, which will be used to generate the remaining galaxy properties such as cosmological redshift and velocity field, without having to model them explicitly.
3. Convolve model spectrum with fiducial instrument dispersion (interpolated to the correct wavelength grid), after adjusting for the cosmological redshift of the source (Cappellari 2017)
4. Redshift the model according to the velocity field from the DAP products (making a high-resolution cube in the observed frame)
5. Scale each spaxel according to the total r -band flux map from the DRP products
6. Down-sample the observed-frame model spectra onto the MaNGA instrument’s wavelength grid
7. Add noise according to the inverse-variance arrays from the DRP products
8. Mask additional spaxels where velocity field is not well-defined

9. Write out synthetic DRP & DAP datacubes and “ground-truth” values for the parameters PCA will estimate.

The PCA parameter estimation method is then used in the same manner as on the science data. One example is shown below in Figure 2.32

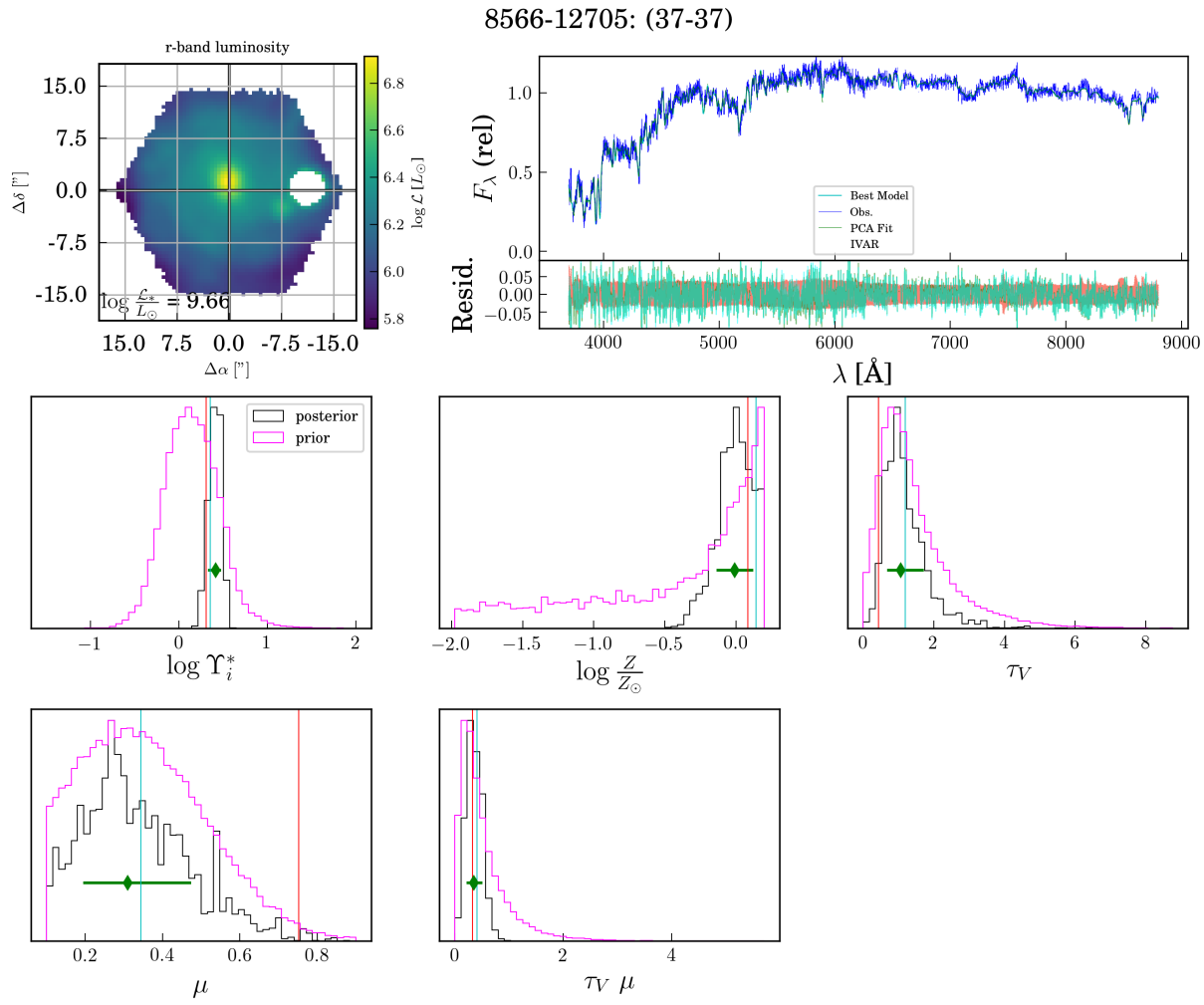


Figure 2.32 : Full diagnostic figure for synthetic data based on the test galaxy 8566-12705. Same format as Figure 2.20, with the addition of a vertical, red line on the parameter histograms denoting the actual value of the parameter.

C Statement of Work

Here are briefly outlined the contributions of all listed authors for this publication, in order of their listing in the journal article.

- **Zachary J. Pace:** Led development of the SFH modelling, the PC downprojection, the tests of inference accuracy, the software pipeline (including rollout at the University of Utah); also led the writing of this manuscript.
- **Christy Tremonti:** Provided input on the SFH model set, and suggested tests of the methodology; proofreading and revisions.
- **Yanmei Chen:** Advised the lead author during summer appointment as NSF EASPSI Fellow at Nanjing University (Nanjing, China) during Summer 2016.
- **Adam Schaefer:** Aided in devising tests of the methodology; proofreading and revisions.
- **Matthew Bershady:** Aided in understanding the stellar models, particularly the role of the Calcium triplet; proofreading and revisions.
- **Remaining authors** (Kyle Westfall, Médéric Boquien, Kate Rowlands, Brett Andrews, Joel Brownstein, Niv Drory, David Wake): Proofreading and revisions; inclusion as Sloan Digital Sky Surveys Architects due to contributions to hardware, administration, survey science or software.

References

- Aguado, D. S., Ahumada, R., Almeida, A., et al. 2019, ApJS, 240, 23
 Aniyan, S., Freeman, K. C., Gerhard, O. E., Arnaboldi, M., & Flynn, C. 2016, MNRAS, 456, 1484

- Aniyan, S., Freeman, K. C., Arnaboldi, M., et al. 2018, ArXiv e-prints, arXiv:1802.00465
- Asplund, M., Grevesse, N., Sauval, A. J., & Scott, P. 2009, *ARA&A*, 47, 481
- Baldry, I. K., Balogh, M. L., Bower, R. G., et al. 2006, *MNRAS*, 373, 469
- Balogh, M. L., Baldry, I. K., Nichol, R., et al. 2004, *ApJ*, 615, L101
- Balogh, M. L., Morris, S. L., Yee, H. K. C., Carlberg, R. G., & Ellingson, E. 1999, *ApJ*, 527, 54
- Balogh, M. L., Navarro, J. F., & Morris, S. L. 2000, *ApJ*, 540, 113
- Barbuy, B., Erdelyi-Mendes, M., & Milone, A. 1992, *A&AS*, 93, 235
- Behroozi, P. S., Wechsler, R. H., & Conroy, C. 2013, *ApJ*, 770, 57
- Belfiore, F., Westfall, K. B., Schaefer, A., et al. 2019, ArXiv e-prints, arXiv:1901.00866
- Bell, E. F., & de Jong, R. S. 2001, *ApJ*, 550, 212
- Bell, E. F., McIntosh, D. H., Katz, N., & Weinberg, M. D. 2003, *ApJS*, 149, 289
- Bernardi, M., Sheth, R. K., Dominguez-Sanchez, H., et al. 2017, ArXiv e-prints, arXiv:1712.05414
- Bershady, M. A., Verheijen, M. A. W., Swaters, R. A., et al. 2010, *ApJ*, 716, 198
- Blanton, M. R., Kazin, E., Muna, D., Weaver, B. A., & Price-Whelan, A. 2011, *AJ*, 142, 31
- Blanton, M. R., & Roweis, S. 2007, *AJ*, 133, 734
- Blanton, M. R., Bershady, M. A., Abolfathi, B., et al. 2017, *AJ*, 154, 28
- Brinchmann, J., Charlot, S., White, S. D. M., et al. 2004, *MNRAS*, 351, 1151
- Bruzual, G., & Charlot, S. 2003, *MNRAS*, 344, 1000
- Bruzual A., G. 1983, *ApJ*, 273, 105
- Budavári, T., Wild, V., Szalay, A. S., Dobos, L., & Yip, C.-W. 2009, *MNRAS*, 394, 1496
- Bundy, K., Bershady, M. A., & Law, D. R. e. a. 2015, *ApJ*, 798, 7
- Burgarella, D., Buat, V., & Iglesias-Páramo, J. 2005, *MNRAS*, 360, 1413
- Cabanac, R. A., de Lapparent, V., & Hickson, P. 2002, *A&A*, 389, 1090
- Cappellari, M. 2017, *MNRAS*, 466, 798
- Cappellari, M., & Emsellem, E. 2004, *PASP*, 116, 138

- Carnall, A. C. 2017, ArXiv e-prints, arXiv:1705.05165
- Chabrier, G. 2003, PASP, 115, 763
- Charlot, S., & Fall, S. M. 2000, ApJ, 539, 718
- Chen, Y.-M., Kauffmann, G., Tremonti, C. A., et al. 2012, MNRAS, 421, 314
- Chevallard, J., & Charlot, S. 2016, MNRAS, 462, 1415
- Choi, J., Dotter, A., Conroy, C., et al. 2016, ApJ, 823, 102
- Cid Fernandes, R., Mateus, A., Sodré, L., Stasińska, G., & Gomes, J. M. 2005, MNRAS, 358, 363
- Connolly, A. J., & Szalay, A. S. 1999, AJ, 117, 2052
- Conroy, C., Castelli, F., & Kurucz, R. in prep.
- Conroy, C., & Gunn, J. E. 2010, ApJ, 712, 833
- Conroy, C., Gunn, J. E., & White, M. 2009, ApJ, 699, 486
- Conroy, C., White, M., & Gunn, J. E. 2010, ApJ, 708, 58
- da Cunha, E., & Charlot, S. 2011, MAGPHYS: Multi-wavelength Analysis of Galaxy Physical Properties, Astrophysics Source Code Library, ascl:1106.010
- da Cunha, E., Charlot, S., & Elbaz, D. 2008, MNRAS, 388, 1595
- Dale, D. A., Helou, G., Contursi, A., Silbermann, N. A., & Kolhatkar, S. 2001, ApJ, 549, 215
- Dawson, K. S., Schlegel, D. J., Ahn, C. P., et al. 2013, AJ, 145, 10
- Di Matteo, P., Bournaud, F., Martig, M., et al. 2008, A&A, 492, 31
- Doi, M., Tanaka, M., Fukugita, M., et al. 2010, AJ, 139, 1628
- Dorman, B., O'Connell, R. W., & Rood, R. T. 1995, ApJ, 442, 105
- Drory, N., MacDonald, N., Bershady, M. A., et al. 2015, AJ, 149, 77
- Fioc, M., & Rocca-Volmerange, B. 1997, A&A, 326, 950
- Foreman-Mackey, D., Sick, J., & Johnson, B. 2014, python-fsps: Python bindings to FSPPS (v0.1.1), doi:10.5281/zenodo.12157
- Fossati, M., Mendel, J. T., Boselli, A., et al. 2018, A&A, 614, A57
- Fukugita, M., Ichikawa, T., Gunn, J. E., et al. 1996, AJ, 111, 1748
- Gallazzi, A., & Bell, E. F. 2009, ApJS, 185, 253

- Gallazzi, A., Brinchmann, J., Charlot, S., & White, S. D. M. 2008, MNRAS, 383, 1439
- Gallazzi, A., Charlot, S., Brinchmann, J., & White, S. D. M. 2006, MNRAS, 370, 1106
- Gallazzi, A., Charlot, S., Brinchmann, J., White, S. D. M., & Tremonti, C. A. 2005, MNRAS, 362, 41
- Gelman, A., & Hennig, C. 2015, ArXiv e-prints, arXiv:1508.05453
- Giovannoli, E., Buat, V., Noll, S., Burgarella, D., & Magnelli, B. 2011, A&A, 525, A150
- Giri, N. C. 1977, in Multivariate Statistical Inference, ed. N. C. Giri, Probability and Mathematical Statistics: A Series of Monographs and Textbooks (Academic Press), 49 – 71
- Gosnell, N. M., Mathieu, R. D., Geller, A. M., et al. 2014, ApJ, 783, L8
- Gunn, J. E., Siegmund, W. A., Mannery, E. J., et al. 2006, AJ, 131, 2332
- Jackson, D. A. 1993, Ecology, 74, 2204
- Jolliffe, I. T. 1986, Principal component analysis (Springer)
- Kauffmann, G., Heckman, T. M., White, S. D. M., et al. 2003, MNRAS, 341, 33
- Kong, X., & Cheng, F. Z. 2001, MNRAS, 323, 1035
- Kriek, M., van Dokkum, P. G., Franx, M., Illingworth, G. D., & Magee, D. K. 2009, ApJ, 705, L71
- Kriek, M., van Dokkum, P. G., Franx, M., et al. 2006, ApJ, 649, L71
- Kroupa, P. 2001, MNRAS, 322, 231
- Kuntschner, H. 2004, A&A, 426, 737
- Law, D. R., Yan, R., Bershady, M. A., et al. 2015, AJ, 150, 19
- Law, D. R., Cherinka, B., Yan, R., et al. 2016, AJ, 152, 83
- Leja, J., Johnson, B. D., Conroy, C., van Dokkum, P. G., & Byler, N. 2017, ApJ, 837, 170
- Madau, P., & Dickinson, M. 2014, ARA&A, 52, 415
- Mahalanobis, P. C. 1936, Proceedings of the National Institute of Sciences of India, 2
- Maraston, C., Daddi, E., Renzini, A., et al. 2006, ApJ, 652, 85
- Maraston, C., Greggio, L., Renzini, A., et al. 2003, A&A, 400, 823
- Maraston, C., Strömbäck, G., Thomas, D., Wake, D. A., & Nichol, R. C. 2009, MNRAS, 394, L107

- Marigo, P., Girardi, L., Bressan, A., et al. 2008, *A&A*, 482, 883
- Martinsson, T. P. K., Verheijen, M. A. W., Westfall, K. B., et al. 2013, *A&A*, 557, A131
- Matteucci, F. 1994, *A&A*, 288, 57
- Matteucci, F. 2016, in *Journal of Physics Conference Series*, Vol. 703, *Journal of Physics Conference Series*, 012004
- McGaugh, S. S., & de Blok, W. J. G. 1997, *ApJ*, 481, 689
- McGaugh, S. S., & Schombert, J. M. 2014, *AJ*, 148, 77
- Ocvirk, P., Pichon, C., Lançon, A., & Thiébaut, E. 2006, *MNRAS*, 365, 74
- O'Donnell, J. E. 1994, *ApJ*, 422, 158
- Pace, Z. J., Tremonti, C., Chen, Y., et al. 2019, *ApJ*
- Pacifci, C., Charlot, S., Blaizot, J., & Brinchmann, J. 2012, *MNRAS*, 421, 2002
- Pacifci, C., Kassin, S. A., Weiner, B., Charlot, S., & Gardner, J. P. 2013, *ApJ*, 762, L15
- Piotto, G., De Angeli, F., King, I. R., et al. 2004, *ApJ*, 604, L109
- Press, W. H., Flannery, B. P., & Teukolsky, S. A. 1986, *Numerical recipes. The art of scientific computing*
- Salpeter, E. E. 1955, *ApJ*, 121, 161
- Sánchez, S. F., Pérez, E., Sánchez-Blázquez, P., et al. 2016a, *RMxAA*, 52, 21
- . 2016b, *RMxAA*, 52, 171
- Santucci, R. M., Placco, V. M., Rossi, S., et al. 2015, *ApJ*, 801, 116
- Schlegel, D. J., Finkbeiner, D. P., & Davis, M. 1998, *ApJ*, 500, 525
- Serra, P., Amblard, A., Temi, P., et al. 2011, *ApJ*, 740, 22
- Shapley, A. E., Steidel, C. C., Erb, D. K., et al. 2005, *ApJ*, 626, 698
- Sil'chenko, O. K. 2006, *ApJ*, 641, 229
- Simha, V., Weinberg, D. H., Conroy, C., et al. 2014, *ArXiv e-prints*, arXiv:1404.0402
- Simpson, D. P., Rue, H., Martins, T. G., Riebler, A., & Sørbye, S. H. 2014, *ArXiv e-prints*, arXiv:1403.4630
- Smee, S. A., Gunn, J. E., Uomoto, A., et al. 2013, *AJ*, 146, 32
- Somerville, R. S., Behroozi, P., Pandya, V., et al. 2018, *MNRAS*, 473, 2714

- Spiniello, C., Trager, S., Koopmans, L. V. E., & Conroy, C. 2014, MNRAS, 438, 1483
- Spiniello, C., Trager, S. C., Koopmans, L. V. E., & Chen, Y. P. 2012, ApJ, 753, L32
- Stasińska, G. 2007, ArXiv e-prints, arXiv:0704.0348
- Suzuki, N. 2006, ApJS, 163, 110
- Taylor, E. N., Hopkins, A. M., Baldry, I. K., et al. 2011, MNRAS, 418, 1587
- Terlevich, E., Diaz, A. I., & Terlevich, R. 1989, Ap&SS, 157, 15
- Thomas, D., Greggio, L., & Bender, R. 1999, MNRAS, 302, 537
- Thomas, D., Maraston, C., Bender, R., & Mendes de Oliveira, C. 2005, ApJ, 621, 673
- Thomas, D., Maraston, C., & Korn, A. 2004, MNRAS, 351, L19
- Thomas, R., Le Fèvre, O., Scuderi, M., et al. 2017, A&A, 602, A35
- Tinker, J. L., Brownstein, J. R., Guo, H., et al. 2017, ApJ, 839, 121
- Tinsley, B. M. 1972, A&A, 20, 383
- . 1973, ApJ, 186, 35
- Tojeiro, R., Heavens, A. F., Jimenez, R., & Panter, B. 2007, MNRAS, 381, 1252
- Tremonti, C. A., Heckman, T. M., Kauffmann, G., et al. 2004, ApJ, 613, 898
- Usher, C., Beckwith, T., Bellstedt, S., et al. 2018, MNRAS, arXiv:1809.07650
- Vazdekis, A., Cenarro, A. J., Gorgas, J., Cardiel, N., & Peletier, R. F. 2003, MNRAS, 340, 1317
- Vazdekis, A., Koleva, M., Ricciardelli, E., Röck, B., & Falcón-Barroso, J. 2016, MNRAS, 463, 3409
- Vazdekis, A., Sánchez-Blázquez, P., & Falcón-Barroso, J. e. a. 2010, MNRAS, 404, 1639
- Wake, D. A., Bundy, K., Diamond-Stanic, A. M., et al. 2017, AJ, 154, 86
- Westfall, K. B., Cappellari, M., Bershady, M. A., et al. 2019, arXiv e-prints, arXiv:1901.00856
- Wild, V., Kauffmann, G., Heckman, T., et al. 2007, MNRAS, 381, 543
- Wilkinson, D. M., Maraston, C., Thomas, D., et al. 2015, MNRAS, 449, 328
- Worthington, G., Faber, S. M., & Gonzalez, J. J. 1992, ApJ, 398, 69
- Worthington, G., Faber, S. M., Gonzalez, J. J., & Burstein, D. 1994, ApJS, 94, 687

- Worthey, G., & Ottaviani, D. L. 1997, ApJS, 111, 377
- Yan, R., Bundy, K., Law, D. R., et al. 2016a, AJ, 152, 197
- Yan, R., Tremonti, C., Bershady, M. A., et al. 2016b, AJ, 151, 8
- Yang, X., Mo, H. J., & van den Bosch, F. C. 2003, MNRAS, 339, 1057
- Yip, C. W., Connolly, A. J., Vanden Berk, D. E., et al. 2004, AJ, 128, 2603
- York, D. G., Adelman, J., Anderson, Jr., J. E., et al. 2000, AJ, 120, 1579

Chapter 3

Resolved and Integrated Stellar Masses in the SDSS-IV/MaNGA Survey, Paper II: Applications of PCA-based stellar mass estimates

*A version of this chapter has previously appeared
in the Astrophysical Journal
Pace, et al. 2019, ApJ, 883, 83
and is notated P19b throughout this dissertation*

Abstract

A galaxy's stellar mass is one of its most fundamental properties, but it remains challenging to measure reliably. With the advent of very large optical spectroscopic surveys, efficient methods that can make use of low signal-to-noise spectra are needed. With this in mind, we created a new software package for estimating effective stellar mass-to-light ratios Υ^* that uses principal component analysis (PCA) basis set to optimize the comparison between observed spectra and a large library of stellar population synthesis models. In Pace et al. (2019a), we showed that with a set of six PCA basis vectors we could faithfully represent most optical spectra from the Mapping Nearby Galaxies at APO (MaNGA) survey; and we tested the accuracy of our M/L estimates using synthetic spectra. Here, we explore sources of systematic error in our mass measurements by comparing our new measurements to data from the literature. We compare our stellar mass surface density estimates to kinematics-derived dynamical mass surface density measurements from the DiskMass Survey and find some tension between the two which could be resolved if the disk scale-heights used in the kinematic analysis were overestimated by a factor of ~ 1.5 . We formulate an aperture-corrected stellar mass catalog for the MaNGA survey, and compare to previous stellar mass estimates based on multi-band optical photometry, finding typical discrepancies of 0.1 dex. Using the spatially resolved MaNGA data, we evaluate the impact of estimating total stellar masses from spatially unresolved spectra, and we explore how the biases that result from unresolved spectra depend upon the galaxy's dust extinction and star formation rate. Finally, we describe a SDSS Value-Added Catalog which will include both spatially resolved and total (aperture-corrected) stellar masses for MaNGA galaxies.

3.1 Introduction

A galaxy's total stellar mass is a helpful indicator of its overall evolutionary state: more massive galaxies tend to reside in older, more massive dark matter haloes (Gallazzi et al. 2005, 2006), and they tend to have exhausted or expelled the majority of their cold gas in previous generations of star-formation star formation (Kauffmann et al. 2003a; Balogh et al. 2004; Baldry et al. 2006). Similarly, more massive galaxies have stellar populations and gas which are relatively metal-enriched (Gallazzi et al. 2005, 2006). In contrast, low-mass galaxies are still forming stars from their high mass fraction of cold gas (McGaugh & de Blok 1997), and continue to enrich their interstellar medium (ISM) from a relatively pristine chemical state (Tremonti et al. 2004).

It is possible to roughly quantify a galaxy's total stellar mass by measuring its stellar mass-to-light ratio Υ^* and then multiplying by the galaxy's luminosity. Two main classes of methods have been employed to make this calculation. The DiskMass Survey (DMS, Bershady et al. 2010a), for instance, measured stellar and gas kinematics for 30 face-on disk galaxies in the local universe, and combined them with estimates of typical disk scale-heights to calculate dynamical mass surface density in several radial bins for each galaxy. Such dynamical measurements are limited, though, by potential systematics in the adopted disk scale-heights and assumptions about the stellar velocity dispersions (Aniyan et al. 2016, 2018).

An alternative is to compare the light emitted by stars in a galaxy to stellar population synthesis models (Tinsley 1972, 1973). This involves wedging theory of stellar evolution to a stellar initial mass function (IMF), a star-formation history, and either theoretical model stellar atmospheres or empirical libraries of stellar photometry or spectroscopy. In general,

one can either attempt to match an observed spectral-energy distribution (SED) directly to a star-formation histories (SFH), or use a library of SFHs to quantify, for example, a relationship between an optical color and a stellar mass-to-light ratio Bell & de Jong (2001); Bell et al. (2003). Related approaches for optical spectra (Kauffmann et al. 2003a) rely on measuring stellar spectral indices, such as the 4000-Å break (D_n4000) or the equivalent-width of the H- δ absorption feature ($H\delta_A$). The process of reconstructing the exact SFH that produces an optical spectrum, though, is fraught with degeneracies: broadly speaking, mean stellar age, stellar metallicity, and attenuation due to dust are extremely covariate. Thus, recent efforts have concentrated on reducing the intractability of this problem.

In Pace et al. (2019, hereafter MaNGA-PCA Paper 1), we applied a relatively innovative approach to inferring a stellar mass-to-light ratio from an optical spectrum, which used a library of ~ 40000 SFHs and the associated optical spectra to construct a more computationally-friendly fitting framework, following the method of Chen et al. (2012, , hereafter C12). Using principal component analysis (PCA), we computed a set of six basis vectors which were able to faithfully represent most optical spectra from the MaNGA survey¹. By projecting each observed spectrum down on the basis set of the principal component vectors, and adopting covariate observational uncertainties, we better account for theoretical degeneracies in stellar population synthesis, and obtain estimates of stellar mass-to-light ratio usable at a variety of signal-to-noise ratios, metallicities, and foreground dust attenuations.

Galaxies are not single points of light, though. Stellar populations vary on spatial scales comparable to the sizes of individual HII regions, and undertaking observations

¹These six “eigenspectra” do not themselves directly represent physical quantities; rather, when combined, they can serve to emulate spectra of stellar populations, and so are taken to encode more abstractly quantities of interest (such as stellar mass-to-light ratio, stellar metallicity, or dust attenuation).

that sample only at kiloparsec (or coarser) resolution therefore mix together light from locations in a galaxy that have very different properties and physical conditions. Thus, some information will necessarily be lost. For example, several studies have found that measurements based on integrated color-mass-to-light relations (CMLRs) tend to underestimate the total stellar mass (by 25–40%, depending on specific star-formation rate) because dusty regions contribute very little to the integrated colors (Zibetti et al. 2009; Sorba & Sawicki 2015; Martínez-García et al. 2017). Explanations for this phenomenon run the gamut from simple variation in intrinsic luminosity of stellar populations across a galaxy’s face (the “outshining hypothesis”) to the spatial variation of dust inducing a simultaneous reduction in total luminosity and increase in effective stellar mass-to-light ratio. Furthermore, the same mechanism need not dominate when transforming between different spatial scales (sub-kiloparsec to several-kiloparsec, or kiloparsec to galaxy-wide).

In this work, we build further on the resolved estimates of stellar mass-to-light ratio and resolved estimates of stellar mass obtained in MaNGA-PCA Paper I: In Section 3.2, we briefly summarize the SDSS-IV/MaNGA survey and the data products upon which our analysis depends. In Section 3.3, we compare PCA-derived estimates of resolved stellar mass surface-density (SMSD) to those of dynamical mass surface density (DMSD) from the DiskMass Survey. In Section 3.4, we obtain a catalog of total galaxy stellar mass after testing two aperture-correction methods designed to account for stellar mass outside the spatial sampling area of the MaNGA instrument. In Section 3.4.3, we examine the effects of spatially-coadding all spectral pixels on the total galaxy stellar mass obtained. Finally, in Section 3.5, we briefly summarize our results and outline the future release of a SDSS value-added catalog (VAC) of total galaxy stellar-masses.

3.2 Data

This work further analyzes principal component analysis (PCA) fits from Pace et al. (2019) to integral-field spectroscopic data from the MaNGA survey (Bundy et al. 2015), part of SDSS-IV (Blanton et al. 2017). MaNGA is an integral-field survey which targets upwards of 10,000 nearby galaxies ($0.01 < z < 0.15$). The NASA-Sloan Atlas (NSA, Blanton et al. 2011) provides the majority of the targets for the MaNGA survey. Two-thirds of targets are drawn from the “Primary+” sample, which have spatial coverage to at least $1.5 R_e$; and the remaining one-third from the “Secondary” sample, which have spatial coverage to $2.5 R_e$. In order to obtain an approximately-flat distribution in galaxy $\log M^*$ (Wake et al. 2017), MaNGA targets are selected uniformly in i -band absolute magnitude (Fukugita et al. 1996; Doi et al. 2010). Within a particular redshift range, the MaNGA sample is also selected to be volume-limited. Absolute magnitudes, tabulated in the DRPALL catalog file, have been calculated using K-corrections computed with the `kcorrect v4_2` software package (Blanton & Roweis 2007), which assumed a Chabrier (2003) stellar initial mass function and Bruzual & Charlot (2003) SSPs.

MaNGA observations employ the BOSS spectrograph (Smee et al. 2013; Dawson et al. 2013), an instrument on the SDSS 2.5-meter telescope at Apache Point Observatory (Gunn et al. 2006). The spectrograph covers the optical–near-IR wavelength range (3600 to 10300 Å) at a spectral resolution $R \sim 2000$. Galaxies are spatially-sampled by coupling the BOSS spectrograph’s fiber feed to closely-packed hexabundles of fiber-optic cables, called integral-field units (IFUs), which each have between 19 and 127 fibers (Drory et al. 2015). Each fiber subtends 2” on the sky. Like previous SDSS surveys, hexabundles are affixed to the focal plane using a plugplate, and are exposed simultaneously (York et al. 2000). Sky subtraction relies on 92 single fibers spread across the focal plane. Twelve seven-fiber

“mini-bundles” (six per half-plate) simultaneously observe standard stars, and are used for spectrophotometric flux calibration (Yan et al. 2016b).

MaNGA data are provided in both row-stacked spectra (RSS) and datacube (LINCUBE & LOGCUBE) formats. RSS exposures are rectified into a datacube using a modified Shepard’s algorithm, such that the size of the spatial element (spaxel) is $0.5''$ by $0.5''$ (Law et al. 2016). The LOGCUBE products have logarithmic wavelength spacing ($d \log \lambda = 10^{-4}$, $d \ln \lambda \approx 2.3 \times 10^{-4}$)². The dithering approach ensures that 99% of the face of the target object is exposed to within 1.2 % of the target depth (Law et al. 2015). Sets of three exposures are accumulated until a threshold signal to noise ratio is achieved (Yan et al. 2016a). The typical point-spread function of a MaNGA datacube has a FWHM of $2.5''$ (Law et al. 2015). The MaNGA Data Analysis Pipeline (DAP, Westfall et al. 2019) measures stellar kinematics, emission-line strengths, and stellar spectral indices for individual spaxels. The PCA analysis undertaken in [MaNGA-PCA Paper I](#), the results of which we employ here relies on the DAP products to establish a velocity field and deredshift individual spectra into the rest-frame.

This work builds on [MaNGA-PCA Paper I](#), which inferred stellar mass-to-light ratio using a PCA-based spectral-fitting and parameter estimation method similar to earlier work from the SDSS-III/BOSS survey (C12). This analysis relied upon a set of composite stellar populations (CSPs), whose optical spectra were used to construct a lower-dimensional spectral-fitting basis set. The spectral-fitting paradigm adopted in [MaNGA-PCA Paper I](#) takes into better account uncertainties in stellar population synthesis (such as the age-metallicity degeneracy), along with covariate uncertainty accounting for imperfect spectrophotometry. [MaNGA-PCA Paper I](#) analyzed 1773 galaxies drawn randomly from MaNGA Product Launch 8 (MPL-8), a set of 6779 observations of galaxies taken between

²In this work, the notation log denotes a base-10 logarithm, and ln denotes a base-e logarithm.

March 2014 and June 2018, and returned resolved estimates & their uncertainties for quantities of interest such as i -band effective stellar mass-to-light ratio, $\log \Upsilon_i^*$. [MaNGA-PCA Paper I](#) established the quality of the $\log \Upsilon_i^*$ estimates by vetting them against synthetic observations of held-out test models: PCA-based estimates of $\log \Upsilon_i^*$ were found to have on average very modest ($\lesssim 0.1$ dex) systematics over a wide range of optical colors, stellar metallicites, and foreground dust attenuations. The estimates of uncertainty for $\log \Upsilon_i^*$ were also found to be realistic.

3.3 Resolved stellar-mass surface densities: comparison to results from dynamics

While estimates of stellar mass-to-light ratio based on SPS do have systematics (e.g., relating to the prevalence and strength of starbursts—see [MaNGA-PCA Paper I](#)), those systematics differ in important ways from those affecting dynamical measurements of stellar-mass. Speaking generally, the measured quantity in dynamical studies is the dynamical mass surface density (DMSD), which is proportional to the square of the ratio between vertical velocity dispersion σ_z and disk scale-height h_z ([Bershady et al. 2010a](#)). Measuring σ_z requires either a perfectly face-on galaxy (rare) or a decomposition of the line-of-sight velocity distribution (LOSVD) for a moderately-inclined galaxy. For moderately-inclined disks, LOSVD decomposition generally relies on a rotation curve from cold or warm gas (HI or H α), which arise most often in galaxies with a mixture of young and old stellar populations (the younger being dynamically colder). Furthermore, as [Aniyan et al. \(2018\)](#) notes, σ_z and h_z must reflect the same stellar population. [Aniyan et al. \(2016\)](#) concluded that a factor-of-two underestimate of DMSD could arise if the two kinematical populations are conflated into one.

With these considerations in mind, it would be helpful to evaluate the two methods of

mass determination in direct contrast. MaNGA, for instance, has observed three galaxies also part of the DiskMass Survey (DMS, [Bershady et al. 2010a](#)): DMS measured dynamical mass surface density in several radial bins for UGC3997 (8566-12705), UGC4107 (8567-12701), and UGC4368 (8939-12704). For all of these galaxies, the gas fraction by mass is small, and the dark matter distribution contributes minimally to the vertical velocity structure. In other words, the stellar mass should strongly dominate the dynamical mass. Therefore, SMSD estimated from SPS should be just slightly less than the DMSD estimated from kinematics. For a given galaxy, comparing the two radial profiles can provide some intuition for the extent to which the above systematics are important.

In the DiskMass Survey ([Bershady et al. 2010a](#)), the dynamical mass surface density Σ^{dyn} is determined according to the vertical velocity-dispersion σ_z , disk scale-length h_R , and disk scale-height h_z :

$$\Sigma^{\text{dyn}} \propto \frac{\sigma_z^2}{h_z} \quad (3.1)$$

Using the PCA fitting method described in [MaNGA-PCA Paper I](#), we have made resolved estimates of the stellar mass of the three galaxies in both the DiskMass and MaNGA observed samples. We transformed the resolved stellar mass into stellar mass surface density Σ^* by noting the solid angle and the surface area at the fiducial redshift subtended by each MaNGA spaxel, and then deprojecting to face-on using inclinations derived in [Martinsson et al. \(2013b\)](#), a modest ($\sim 20\%$) correction. Though inclinations are provided in MaNGA for these galaxies, we have elected to use the DMS values, to better ensure like radii are compared to like radii. We have elected to show the derived stellar (dynamical) mass surface density for the PCA (DMS) data, since Σ^* is independent of Hubble parameter h for PCA/SPS (both area and luminosity have a h^{-2} dependence). The h -corrections to the DMS dynamical-masses are small (~ 0.02 dex), but have been made. Figure 3.1 compares the radially-averaged total-dynamical and resolved SPS estimates of

mass surface density, and we reproduce in Table 3.1 the relevant rows of Martinsson et al. (2013a, Table 4), which summarizes the kinematic decompositions of the two galaxies.

Given that the mass in stars heavily dominates the velocity structure of all of these galaxies, one would expect the dynamical-mass surface density (DMSD) would equal or only slightly exceed the stellar-mass surface density (SMSD), because of the mass contributed by gas, a bulge, or the dark matter halo—so, why are the dynamical and SPS estimates of mass-density systematically discrepant? This comparison is an apt illustration of the distinct systematics of stellar population synthesis and disk kinematic fitting.

Aniyan et al. (2016, 2018) respectively address issues with matching appropriate values of h_z for a given measurement of σ_z (i.e., the adopted scale-height must be that of a similar dynamical tracer), and the contribution of a dark matter halo to the stellar σ_z . Assuming disks are maximal places upper limits on the disk mass surface-density (and hence, upper limits on stellar mass-to-light ratio and lower limits on disk thickness). That is, accounting for dark matter in the dynamical models tends to lower the estimate of disk maximality (Hessman 2017). Lower limits on disk mass surface density (hence, lower limits on stellar mass-to-light ratio and upper limits on disk thickness) are reasonably bounded by

UGC (1)	plateifu (2)	$\mathcal{F}_b^{2.2h_R}$ (DMS) (3)	\hat{f}_{h_z} (4)	$\mathcal{F}_b^{2.2h_R}(\hat{f}_{h_z})$ (5)
3997	8566-12705	0.48	0.90 ± 0.12	0.46
4107	8567-12701	0.56	1.83 ± 0.15	0.76
4368	8939-12704	0.72	1.68 ± 0.10	0.93

Table 3.1 : Summary of comparisons between DMSD and SMSD, and the effect of a changing disk scale height on the estimated baryon fraction: column (3) ($\mathcal{F}_b^{2.2h_R}$) is the fractional contribution of the stellar disk to the rotation curve at 2.2 disk scale-lengths reported in Martinsson et al. (2013a). Columns (4) and (5) give \hat{f}_{h_z} (the value of f_{h_z} which gives the best galaxy-wide match between Σ_{dyn} and Σ^*), and the associated value of $\mathcal{F}_b^{2.2h_R}$.

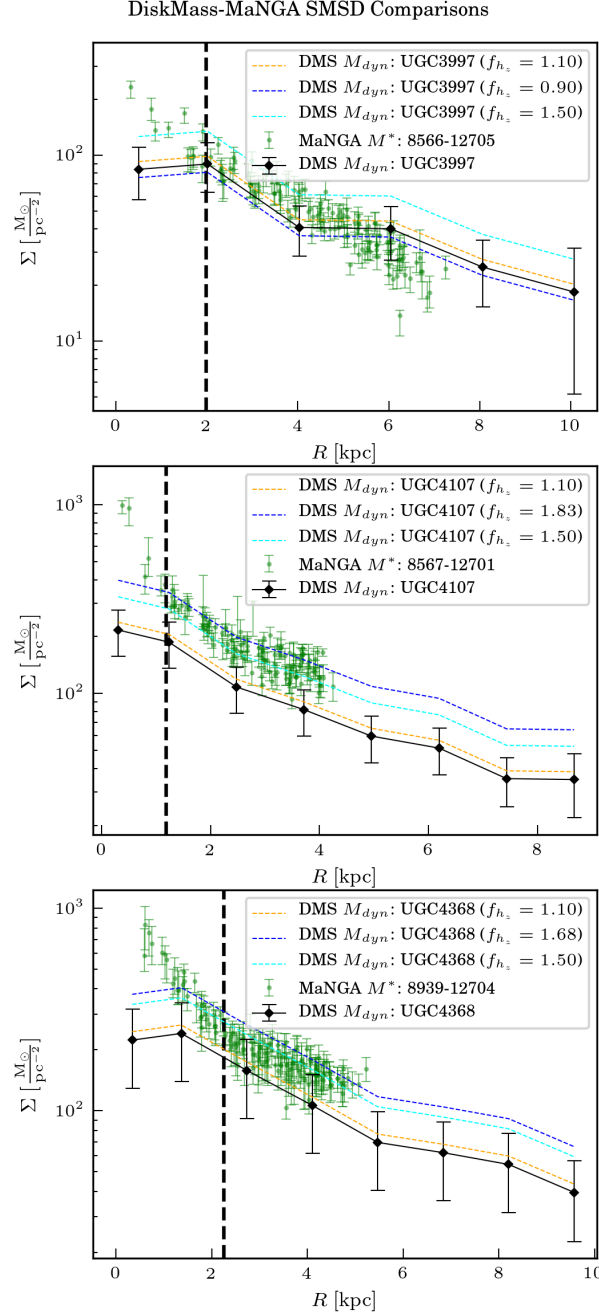


Figure 3.1 : Comparison between PCA-measured stellar mass surface density (green circles) to the dynamical-mass surface-densities (DMSDs) from the DiskMass Survey (black diamonds connected by black, solid line, corrected to our fiducial h_z) for three galaxies: 8566-12705 (UGC3997), 8567-12701 (UGC4107), and 8939-12704 (UGC4368). For each galaxy, the radius of the bulge is shown as a vertical black dashed line: bulges differ from disks in their density profile, dynamics, and stellar populations, so the same kinematical relationships do not apply (Martinsson et al. 2013a). We also show the values of Σ_{dyn} which would result from three different corrections to h_z (i.e., assuming three values of f_{h_z}): in orange, the DMSD assuming $f_{h_z} = 1.1$; in cyan, assuming $f_{h_z} = 1.5$, and in blue, assuming f_{h_z} equal to the value which produces the best agreement between the DMSD and SMSD. The best-fit value of f_{h_z} , as well as the associated value of $\mathcal{F}_b^{2.2h_R}$, is given for each of the three galaxies in the legend and in Table 3.1.

the DMS measurements: the scale height of the stellar dynamical tracer is not larger than the observed broad-band disk thickness, and dark matter corrections are modest (Westfall et al. 2011; Swaters et al. 2014). However, since DMS measurements indicate that disks are substantially sub-maximal, there is room to consider adjustments to the adopted disk thickness to bring dynamical values closer in line with our SPS estimates. At issue is not the scaling relation adopted in Bershady et al. (2010b) since edge-on dynamical measurements where scale heights are directly accessible give similar results (Bershady et al. 2011). As (Aniyan et al. 2016) posit, though, the scale height relevant for the stellar dynamical tracer could be systematically smaller than the measured broadband values.

As an illustration of the effects of scaling h_z , we have considered a galaxy-wide overestimate of h_z by a factor f_{h_z} . In such a case, the stellar-mass surface density implied by a dynamical-mass surface density and baryon fraction (neglecting contributions from gas) is given by

$$\Sigma^* \approx \Sigma_{dyn} f_{h_z} \quad (3.2)$$

We first bin PCA-derived measurements of SMSD in radial bins which correspond to the DMS radial bins. We exclude radial bins interior to the bulge radius, and optimize to obtain the factor (f_{h_z}) most consistent with the galaxy-wide offset between SMSD and DMSD. We list this best-fit value in Table 3.1, Column 4, along with the implied baryon-fraction associated with this change in f_{h_z} ($\mathcal{F}_b^{2.2h_R}(f_{h_z}) \approx \mathcal{F}_b^{2.2h_R} \sqrt{f_{h_z}}$: Table 3.1, Column 5). The uncertainty in f_{h_z} is largely dictated by the intrinsic dispersion of SMSD in a given radial bin. Allowing for the possibility that the PCA masses are systematically high by about 0.1 dex could provide some relief from large values of f_{h_z} , but does not make dynamics and SPS consistent. This allowance also worsens the mismatch for UGC3997 (8566-12705), which already has $f_{h_z} < 1$. A more complete analysis, though, must re-propagate the dynamical effects of the gas, which has a different scale-height and must be considered separately

(though UGC3997 and UGC4107 have such low gas mass surface densities in comparison to stellar that the additional correction should be quite small).

This brief exercise does not paint a clear picture of whether h_z is significantly underestimated: for the case of UGC3997—by far the lowest-surface-brightness of the three—, f_{h_z} is implied to be less than unity³, while for the remaining two galaxies, the favored values of f_{h_z} are 1.83 and 1.68, somewhat less than the factor of two that Aniyan et al. (2016) favors. While claims regarding specific values of f_{h_z} are outside the scope of this paper, clearly modest corrections to h_z bring Σ_{dyn} into qualitative agreement with our SPS-derived values of Σ^* .

In MaNGA-PCA Paper I, we treated in some detail the systematics in stellar population fitting, and justified our various choices in parametrizing the SFH training data. However, we further expound here regarding two important and outstanding issues. First, our relatively burst-poor SFHs may be systematically too heavy (Gallazzi & Bell 2009). If h_z were more closely-constrained at the values found by the DiskMass Survey, allowing more stochastic variations in instantaneous SFR might be justified. Regardless, the above comparisons also justifies more detailed treatments of disk dynamics with dark matter (Hessman 2017) and more accurate measurements of disk thickness and vertical mass-to-light ratio gradients (Schechtman-Rook & Bershady 2013, 2014; Eigenbrot & Bershady 2018).

Second, these results rely on the assumption of a radially-uniform IMF, which is seen to change both from galaxy to galaxy (for a JAM-SPS modelling comparison, see Li et al.

³In fact, for UGC3997, the inferred Σ_{dyn} and Σ^* profiles are quite different in slope, which implies that there might be another latent effect at play. A flared disk (i.e., one whose scale height increases with radius) is strongly disfavored, because its SMSD profile would have a steeper slope with respect to a given SMSD profile. This is the opposite effect from what we see for UGC3997.

2017) and within a single galaxy (Martín-Navarro et al. 2015; La Barbera et al. 2016). As Li et al. (2017) reports, a bottom-heavy (-light) IMF in the inner (outer) galaxy will bring about a more negative stellar mass-to-light ratio gradient as compared to dynamics. We see no evidence for such a discrepancy in Figure 3.1, but the three particular galaxies examined here are likely not the best candidates for a search for such a trend; galaxies more widely sampled in radii may shed further light on this matter.

More careful integration of resolved SPS with Jeans and Schwarzschild modelling may in the future permit direct comparison between stellar and dynamical masses for elliptical galaxies (Li et al. 2019). A simple comparison between the projected (plane-of-sky) SMSD and DMSD is not by itself informative for several reasons: first, the majority of such studies assume a radially-constant stellar mass-to-light ratio, which is at minimum inconsistent with this work’s assumptions; second, the integration of the (three-dimensional) posterior dark matter density profile along lines-of-sight requires adopting a cutoff radius for the dark matter halo (Zhu priv. comm.), a radius which will be larger than the field of view subtended by a MaNGA IFU, since galaxies are only sampled to $2.5 R_e$ Wake et al. (2017); and third, while the volume-density profile will be dominated in the centers of ellipticals by the stars, it will appear in projection that all parts of an elliptical galaxy are dark matter-dominated, due to the long “column” of dark matter-dominated galaxy outskirts along each line-of-sight. For this reason, we do not ourselves make any comparisons using elliptical galaxies.

3.4 A catalog of aperture-corrected total galaxy stellar masses

In addition to resolved stellar mass maps, we provide very approximate aperture-corrections to estimate total galaxy stellar mass. The basic task is to calculate the approximate amount of stellar luminosity outside the grasp of the IFU, and multiply it

by a reasonable guess for the stellar mass-to-light ratio. This involves accounting for both regions outside the IFU proper and regions with known bad data quality. The latter case is handled first, for which cases the adopted mass-to-light ratio is the median of the eight nearest unmasked spaxels' values.

The limited spatial coverage of the MaNGA IFU at radii larger than $1.5 R_e$ ($2.5 R_e$) in the Primary+ (Secondary) Sample will cause the outskirts of galaxies to remain unsampled. [González Delgado et al. \(2014\)](#) proposed a simple solution for CALIFA data, where additional mass is added by adopting the average mass-to-light ratio between 1.5 and $2.5 R_e$ as a fiducial mass-to-light ratio of the galaxy outskirts: since stellar mass-to-light ratio is observed to not change significantly in the outermost regions of disks, this seems a reasonable choice.

In order to choose the aperture-correction method, we first evaluate how much of the galaxy's luminosity falls outside the MaNGA IFU. In Figure 3.2, we separate galaxies by sample (Primary+ and Secondary), and plot the flux deficit between the IFU-summed PCA-reconstructed stellar continuum bandpass flux and the K-corrected bandpass flux from the NASA-Sloan Atlas ([Blanton & Roweis 2007](#)). 80% of galaxies lose less than 22% of their integrated, i -band flux to aperture effects, and the vast majority of those are in the Primary+ sample. Many such galaxies have a foreground star just outside the IFU, which (if improperly isolated in the photometry) might bias the flux fraction outside the IFU to a higher value.

Ultimately, we must choose a constant mass-to-light ratio for the galaxy outskirts, and we consider two methods:

1. “**CMLR method**”: compute a color or the missing flux, and convert it into a stellar mass-to-light ratio using a CMLR (such as the one found in [Pace et al. 2019](#)).

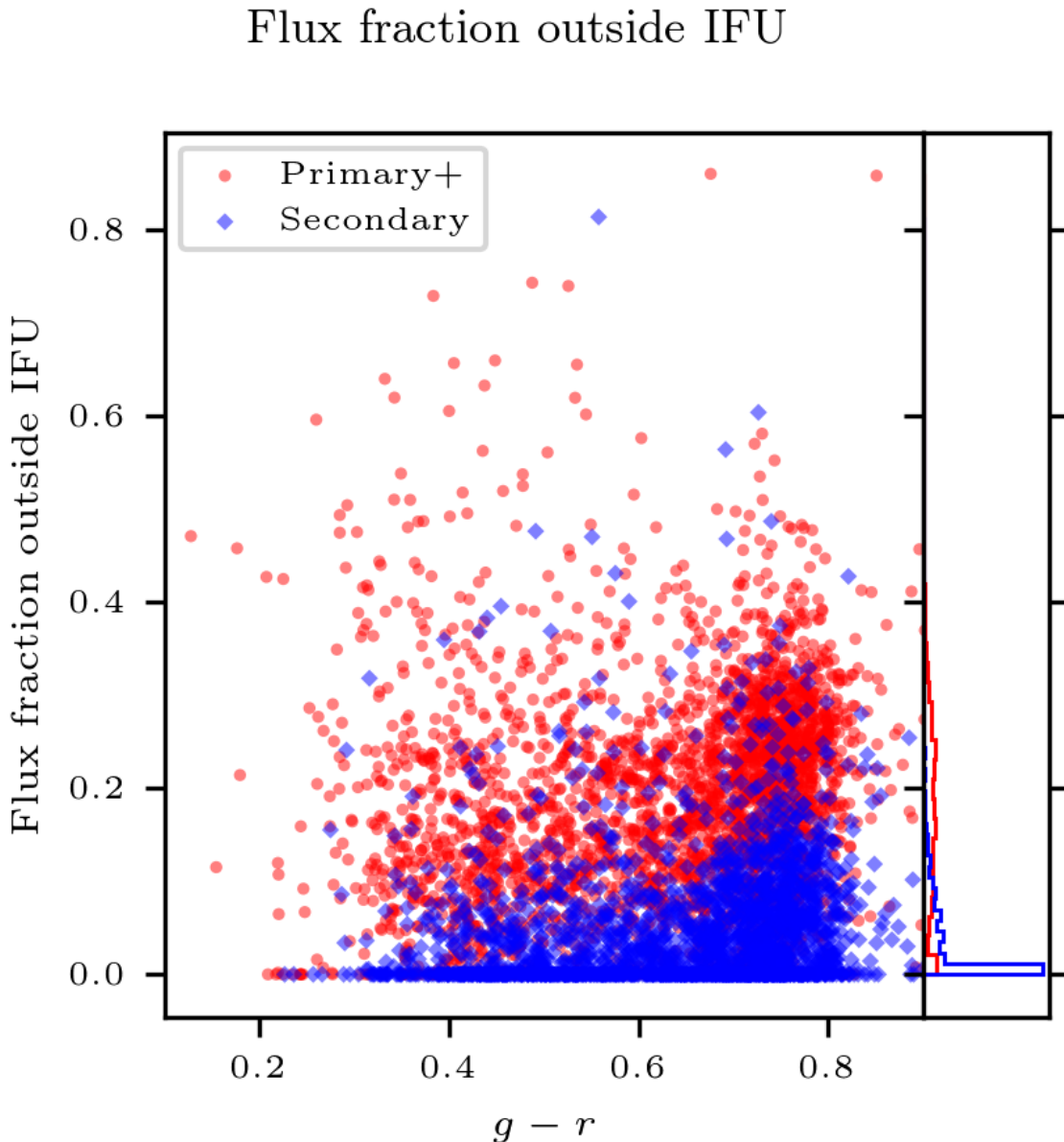


Figure 3.2 : The fraction of i -band flux falling outside the grasp of the MaNGA IFU, plotted against $g - r$ color, and separated by whether the galaxy is in the Primary+ (red circle) or Secondary (blue diamond) sample. In the right panel is shown the distribution of flux fraction outside the IFU, separated by the sample designation (Primary+ or Secondary).

2. “**Ring method**”: adopt as the stellar mass-to-light ratio for the aperture-correction the median value in a ring in the outermost accessible part of the galaxy. For high-inclination galaxies ($\frac{b}{a} < 0.5$), we average over spaxels within 30 degrees of the major axis, and in the outermost $0.5 R_e$ of the galaxy with well-determined stellar mass-to-light ratios. By restricting our sampling to along or nearby the major axis, we better ensure that we are averaging over like radii (in contrast, including spaxels along the minor axis probes a range of radii even along a single line of sight). For galaxies with $\frac{b}{a} > 0.5$, we average over the same $0.5 R_e$ ellipse, but with no restrictions on azimuthal angle relative to the major axis.

Though the difference between the two methods has little discernable systematic on average, for an individual galaxy, $\frac{\Upsilon_{\text{CMLR}}^*}{\Upsilon_{\text{ring}}^*}$ exhibits some extreme values at extreme colors of residual flux. Granted, these seem to primarily be galaxies with little residual flux at all (see Figure 3.3), and those cases ought to be quite susceptible to measurement uncertainties.

Figure 3.3 shows the dependence of the difference between “ring” and “CMLR” stellar-mass aperture-correction on optical ($g - r$) color and sample (the Primary Sample has coverage out to at least $1.5 R_e$, and the Secondary out to at least $2.5 R_e$). Point size illustrates the flux fraction outside the IFU (as in Figure 3.2). The secondary sample seems to experience greater scatter in inferred stellar mass-to-light for the galaxy outskirts, but this results in very small luminosity-scalings for these corrections. In other words, when bandpass fluxes derived from MaNGA spectroscopy are very close to (but still less than) the catalog flux, a small discrepancy in one photometric band (relative to another) will produce an extreme color, which would imply an extreme mass-to-light ratio.

Given the potential for color-correlated systematics seen above, we also evaluate the impact this has on total galaxy stellar mass: after all, if the flux outside the IFU

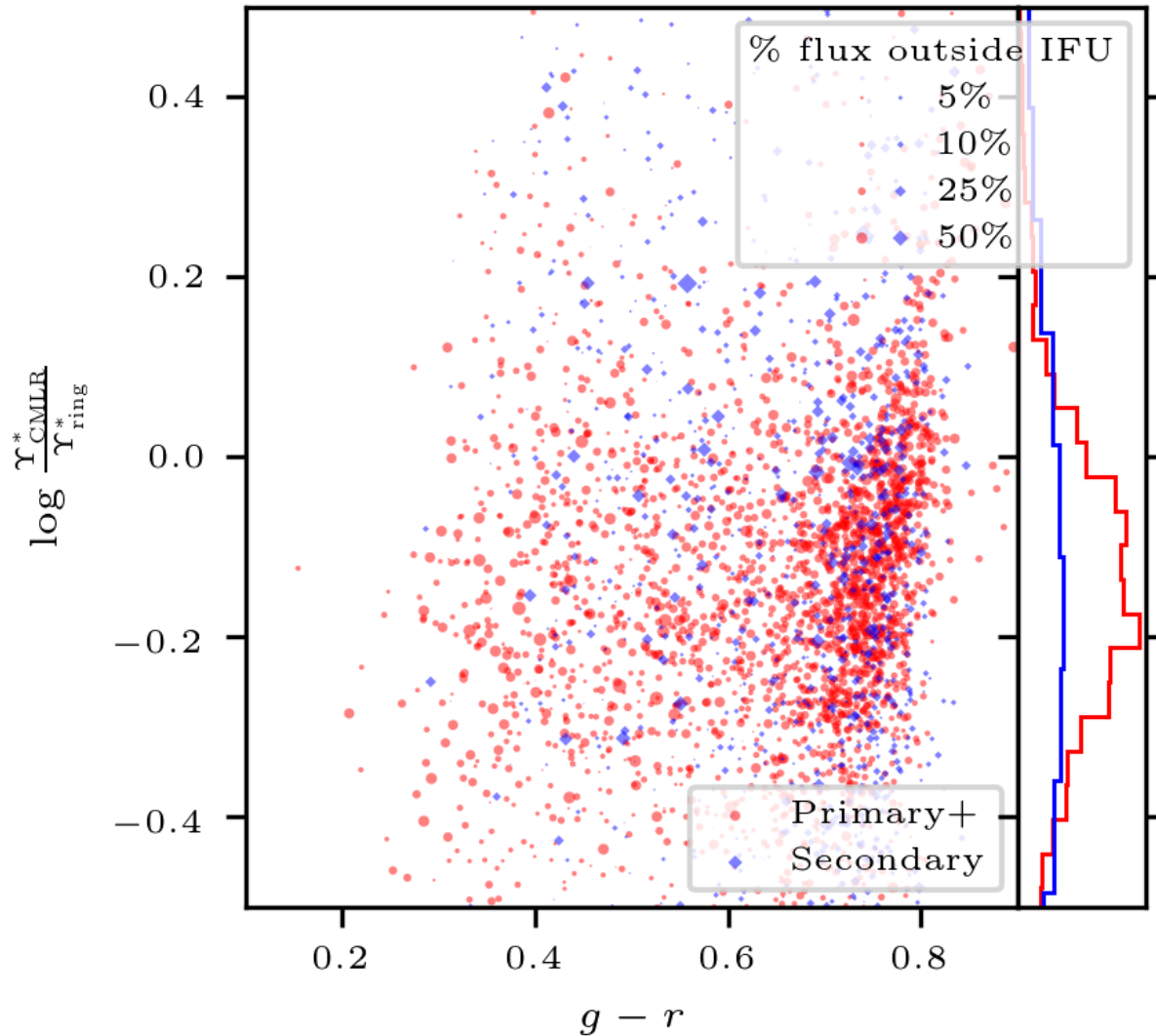
$\Upsilon_{\text{CMLR}}^* \text{ vs } \Upsilon_{\text{ring}}^*$


Figure 3.3 : The difference in inferred stellar mass-to-light ratio for the galaxy outskirts between the ring method and the CMLR calibration. Point color and shape are the same as Figure 3.2, and points are sized according to the fraction of total luminosity outside the IFU. Galaxies whose reconstructed-*i*-band flux equals or exceeds the K-corrected NSA *i*-band flux are not displayed. Shown in the right panel is the distribution of $\log \frac{\Upsilon_{\text{CMLR}}^*}{\Upsilon_{\text{ring}}^*}$, separated by sample (Primary or Secondary).

is very small, a disagreement in inferred mass-to-light ratio is unimportant. Indeed, Figure 3.4 shows that the difference in the *total stellar mass* induced by changing the aperture-correction method is much less than 0.1 dex. However, the locus of points at a fixed color indicates that the “ring” method does produce very slightly higher masses. Furthermore, as expected, the Primary sample (being sampled to a smaller radius, on average) is aperture-corrected more severely, so the differences between the two methods is more prominent. In addition, we find that neither method produces noticeably more extreme color-correlated systematics with respect to previous photometrically-obtained stellar masses (see Section 3.4.2).

We recommend adopting the “CMLR” method: while we expect that the resulting mass-to-light ratios have systematics at the 0.1 dex level or below, this approach implicitly compensates for radial mass-to-light ratio gradients (Tortora et al. 2010, 2011; Boardman et al. 2017) by varying the fiducial stellar mass-to-light ratio based on the actual “missing flux”. Therefore, we avoid (for example) chronically overestimating the mass in the outer regions of a galaxy with a negative stellar mass-to-light ratio gradient. That said, one could make the case for adopting the “ring” correction for the Secondary sample, since the discrepancy in total mass should be reduced relative to the Primary sample, assuming a negative mass-to-light ratio gradient. Put another way, any adopted aperture-corrections are only as good as the imaging and spectroscopically-synthesized photometry used to estimate the bandpass flux deficits. In our catalog of aperture-corrections, we will include both potential mass aperture-corrections, with the caveat the the “CMLR” method is likely safer in the general case.

Impact of aperture-correction on M^{tot}

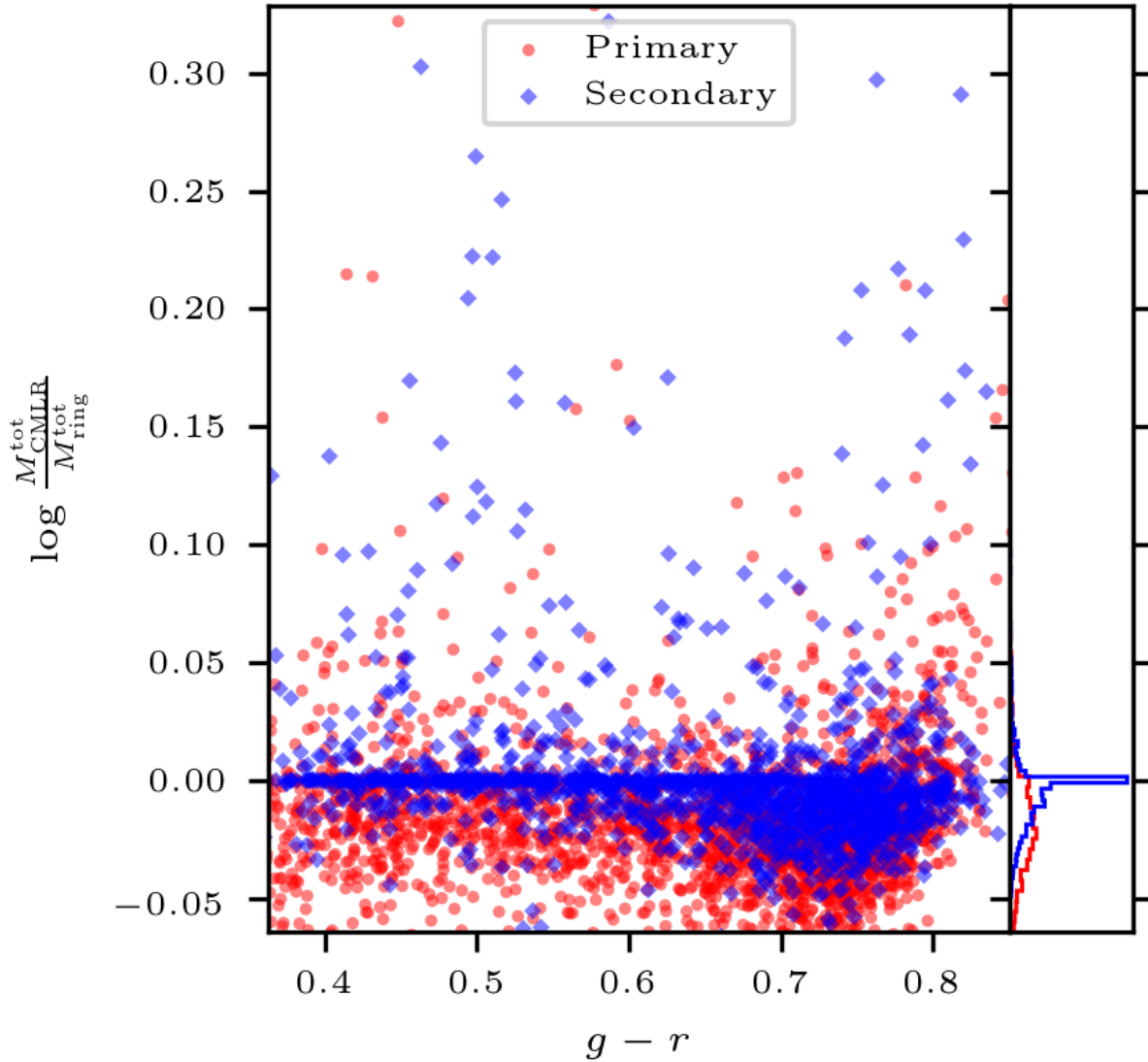


Figure 3.4 : The difference in *total stellar mass* induced by a choice of stellar mass-to-light ratio for the outskirts (ring model or CMLR), versus $g - r$ color. Points are colored according to their sample, as Figure 3.2. Galaxies fully covered by the IFU (i.e., with no missing i -band flux) have their values of $\log \frac{M_{\text{CMLR}}^{\text{tot}}}{M_{\text{ring}}^{\text{tot}}}$ set to zero. In the right panel is the distribution of $\log \frac{M_{\text{CMLR}}^{\text{tot}}}{M_{\text{ring}}^{\text{tot}}}$, separated by sample (Primary or Secondary).

3.4.1 Tests of aperture-correction against resolved photometry

The above comparisons between the two proposed aperture-correction methods indicate that in most cases, it is preferable to adopt a fiducial mass-to-light ratio for the regions of the galaxy outside the IFU based on the color of the residual flux in the g and r bands and a CMLR. It would be desirable, however, to check the stellar masses which would result from applying a CMLR to resolved photometry of MaNGA galaxies against the spectroscopically-derived values. This test will shed light on the possibility of bias in the aperture-corrections. To that end, we exploit the legacy multi-band pre-imaging which exists for all MaNGA galaxies (York et al. 2000).

Figure 3.5 offers (for a single galaxy) a comparison between the stellar masses & stellar mass-to-light ratios resulting from the PCA analysis, and those emerging from simply applying a fiducial CMLR (from [MaNGA-PCA Paper I](#)) to individual pixels from the SDSS-I preimaging cutouts (York et al. 2000). In the case shown (and in most cases), the cumulatively-radially-summed mass yielded by combining single preimaging pixels with a CMLR gives an unphysically-high mass. Since the CMLR gives the logarithm of the stellar mass-to-light ratio, low signal-to-noise pixels which are anomalously red produce anomalously-high stellar mass-to-light ratios (and thus, huge masses); but anomalously-blue pixels produce next to no mass at all (but not negative mass). The net effect is for total mass to increase radially without bound. As a counterpoint to this, we show a similar cumulative mass profile which results from coadding nearby preimaging pixels to reach some target signal-to-noise ratio in the i -band, and alleviating this issue. At the same time, the overall slope of the radial mass-to-light ratio profile is preserved relative to the PCA. Also shown are the aperture-corrections resulting from the “CMLR” and “ring” methods.

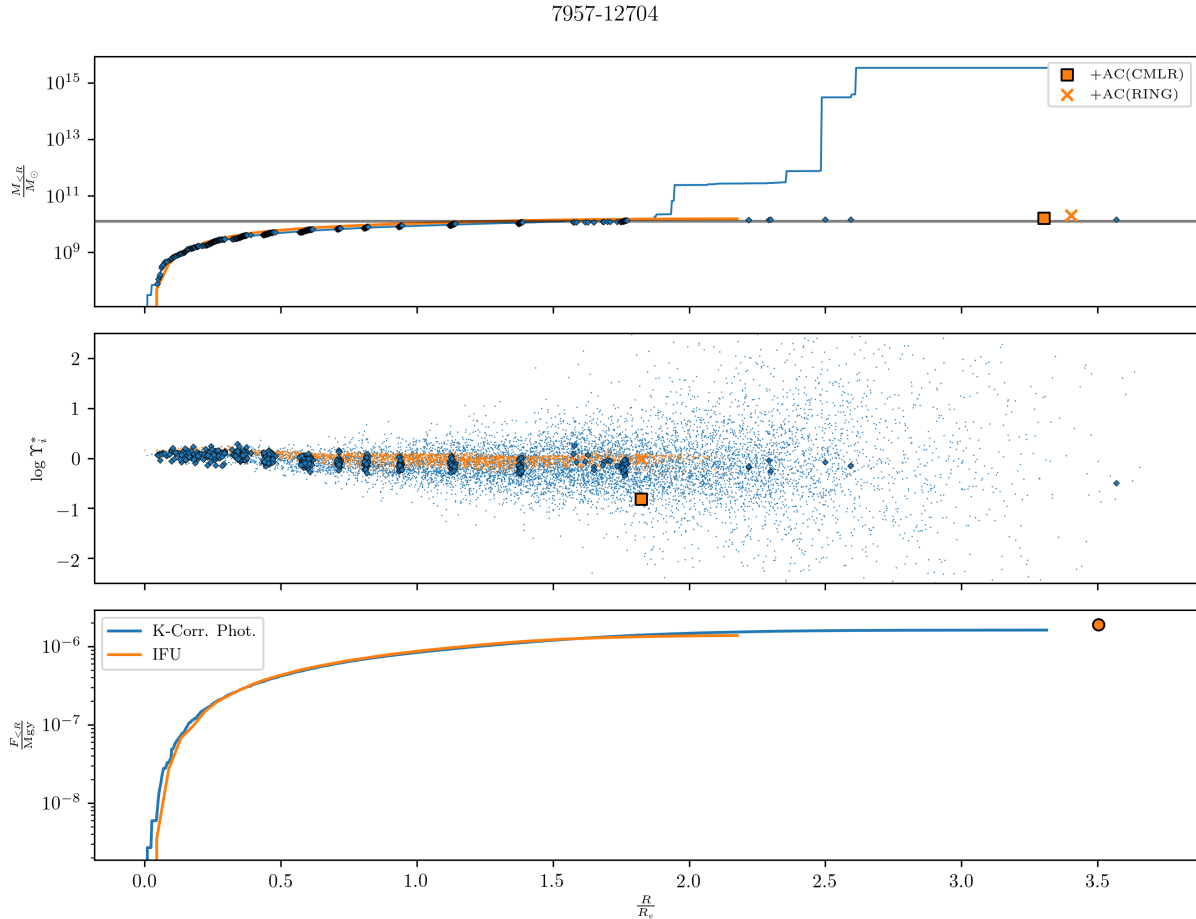


Figure 3.5 : An example spectroscopic-photometric aperture “curve-of-growth” comparison figure. *Top panel:* Cumulative stellar-mass enclosed within ellipses of increasing radius (units of R_e), found using photometry and a CMLR (blue line) with spectroscopic PCA methods (orange line). For the photometry, low signal-to-noise (found at high radii) biases mass-to-light high and introduces bias (the blue curve increases without bound). Blue diamonds show cumulative masses from radially- and azimuthally-binned photometry with the fiducial CMLR. The orange ■ and X refer to the total stellar-mass of the galaxy after aperture-correction with respectively the “CMLR” and “ring” methods. The horizontal, black, dashed line denotes the stellar-mass from the NSA. *Middle panel:* radial plot of i -band mass-to-light ratio: blue dots denote pixels from preimaging, orange dots spaxels from the MaNGA datacube, and blue diamonds denote radially-azimuthally binned photometry; and the single, orange ■ and X denote the mass-to-light ratio that would respectively result from the “CMLR” and “ring” aperture-corrections. *Bottom panel:* As top panel, but radially-summed fluxes.

In the case shown, and indeed for most galaxies, the adopted mass-to-light ratio for the “ring” aperture-correction (orange X in Figure 3.5) is sizably greater than the “CMLR” value (orange ■). Once again, we believe this has *some* basis in reality, because optical colors do overall trend blueward with increasing radius inside a galaxy (i.e., negative stellar mass-to-light ratios). That said, in many cases, the difference between the two mass-to-light ratios is larger than might be expected.

In all cases, the flux enclosed within small annuli is larger for the preimaging data than for the photometry reconstructed from the MaNGA spaxels: this is because the preimaging pixels are a factor of several smaller than the MaNGA spaxels (so, flux from the preimaging will be counted at a smaller radius than flux from the MaNGA datacube). The effect becomes insignificant at higher radii, because galaxy surface brightness gradients get less steep with radius. Additionally, in some rare cases (less than 5% of the time), the total enclosed flux at the largest radius in the IFU is smaller than the enclosed flux for the photometry by approximately 10% at the same radius. This does not seem to depend on redshift or color, nor does it seem to correspond with the presence of foreground stars.

Knowing what we do about galaxy stellar mass-to-light ratio gradients, it is reasonable to conclude that the “ring” method likely provides a relatively strong upper-limit on the stellar mass outside the IFU, especially for galaxies in the Primary sample. As shown in Figure 3.4, the logarithmic mass differential induced by changing the aperture-correction method is not as large in the Secondary sample as in the Primary sample, though the effect is small (less than 0.1 dex) across the board. Galaxies sampled to a higher effective radius on average will have in their outermost spaxels a lower mass-to-light ratio. Furthermore, though the individual photometric residuals used by the CMLR might be more uncertain, the overall correction will also be smaller on average. Ultimately, for the Secondary sample,

both aperture-corrections are likely equally usable.

3.4.2 Integrated masses: comparison to NASA-Sloan Atlas & JHU-MPA Catalog

As a point of comparison with the systematics we have uncovered and discussed so far, we also attempt to characterize the differences between the IFU-summed and aperture-corrected stellar masses from PCA and those obtained by analyzing photometric data from SDSS (York et al. 2000): we consider simultaneously the NASA-Sloan Atlas, which fits a set of SFH templates to elliptical-Petrosian photometric fits, in order to obtain K-corrected rest-frame magnitudes and stellar-masses (Blanton et al. 2011; Blanton & Roweis 2017), and the JHU-MPA catalog, which uses *ugriz* photometry to estimate dust attenuation, mass-to-light ratio, and broadband, K-corrected luminosities (Kauffmann et al. 2003a; Salim et al. 2007; Aihara et al. 2011).

In Figure 3.6, we compare the PCA-derived stellar mass estimates from this work to those reported in the NSA and the JHU-MPA catalog (both catalogs have been corrected to $h = .693$, and to a Kroupa IMF). We note that the PCA masses are almost universally the highest, exceeding both libraries by approximately 0.1–0.15 dex at red colors (this discrepancy increases for the JHU-MPA catalog at bluer colors, to a maximum of 0.3–0.4 dex). Scatter about the mean deviation is approximately 0.2 dex across all colors, and 0.1 dex at fixed color. Possible responsible effects include stellar libraries (even in old SSPs, $\log \Upsilon_i^*$ can vary systematically by ~ 0.05 dex) and simple differences in SFHs. To wit, the SFHs employed in this work are much more continuous than those adopted in previous work: the majority of the training data used in Blanton & Roweis (2007) were SSPs, and Kauffmann et al. (2003a) permitted a burst on average once per 2 Gyr after formation. Finally, it should perhaps be encouraging that at the redder colors ($0.5 \leq (g - r) \leq 0.8$)

corresponding to intermediate-age stellar populations, the mass discrepancies lessen.

The systematics shown above are not unique to PCA mass measurements, and will likely be found between any combination of measurements, be they photometric or spectroscopic. For example, $\log \frac{M_{\text{JHU/MPA}}^*}{M_{\text{NSA}}^*}$ varies from -0.2 dex at $g - r \sim 0.3$ to 0.2 dex at $g - r \sim 0.8$. Furthermore, even changing the method of measuring photometry can induce systematics, as well: The NSA measures magnitudes in two different ways, fitting a Sérsic profile and fitting an elliptical-Petrosian aperture. We elected to compare to masses derived from elliptical-Petrosian photometric estimates, because they are less prone to catastrophically poor fits (see [Wake et al. 2017](#), for more discussion). That said, elliptical-Petrosian fits are bluer by $\Delta(g - r) .046 \pm .088$ for the full MaNGA sample, which induces a 0.1 dex difference in the NSA stellar masses.

Even if these discrepancies do indicate a real overestimate of stellar-mass by the PCA technique, the overall conclusions reached by comparing to the DiskMass dynamical masses do not change: the implied scale-height correction would decrease in magnitude, but would not be consistent with unity. Furthermore, this brings about the *opposite* problem in the case of UGC3997, whose best-fit correction factor f_{h_z} is *less than one* using the fiducial stellar masses (so, simply applying the 0.1 dex systematic as a further “correction factor” would bring the two measurements *more out of line*.) However, as noted above, the difference in slope between the masses from SPS and dynamics implies that some other effect is at play.

3.4.3 Are stellar masses derived from galaxy-coadded spectroscopy reliable?

We also aim to test the scenario explored by [Zibetti et al. \(2009\)](#), where integrated galaxy colors were found to produce systematically low mass-to-light ratios, due to the effects of attenuation being incompletely captured. Any observations at coarser spatial

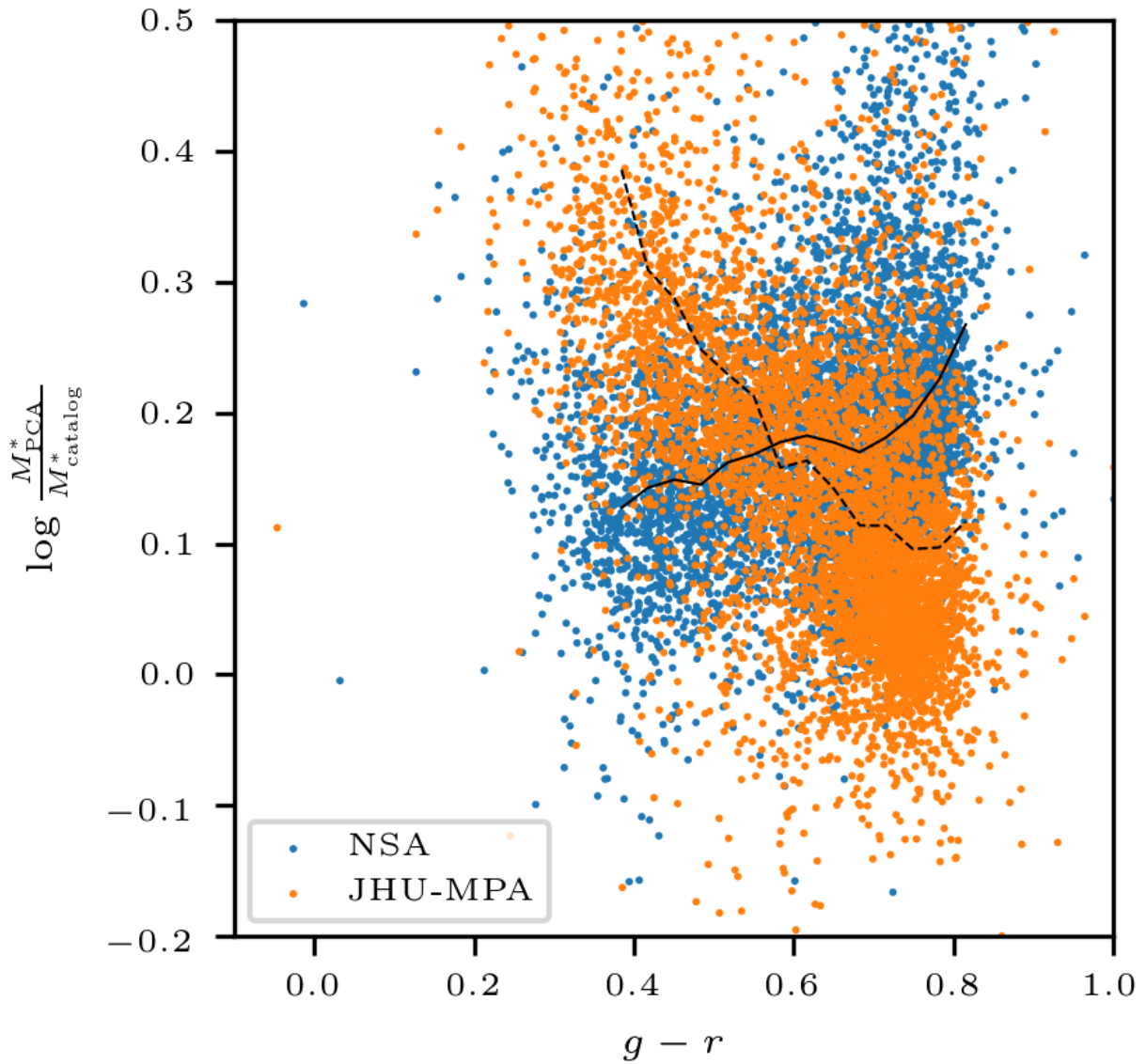


Figure 3.6 : For 1773 galaxies, the difference between the stellar masses from this study's PCA analysis and those from the NSA (blue points, and a locally-weighted regression as a solid, black line); and the difference between the stellar masses from this study's PCA analysis and those from the JHU-MPA galaxy catalog (orange points, and a locally-weighted regression as a dashed, black line). Both NSA and JHU-MPA masses have been corrected to a Kroupa IMF.

resolution than resolved stellar populations could, in principle, suffer from similar biases.

Here, we evaluate whether a spectrum for an entire galaxy (which will be dominated by light from young or relatively unattenuated stellar populations) will predict the same total galaxy stellar mass as a galaxy-coadded spectrum. In other words, we test the importance of implicit luminosity-weighting for spectra. To do so, we begin with a resolved map of a galaxy’s stellar mass: we compare the sum over all resolved masses with the stellar mass obtained by flux-weighting the corresponding, spatially-resolved mass-to-light ratios⁴, and multiplying by the total luminosity in the IFU. We first attempt to explain the difference between the spaxel-summed mass (M^*) and the mass obtained from the luminosity-weighted mass-to-light ratios (M_{LW}) by measuring how unequal the inferred dust attenuation is across the sampled area of the galaxy (represented by the standard-deviation of the distribution of local-stellar-mass-weighted optical depth, σ_{τ_V} —Figure 3.7). As more inclined galaxies are expected to exhibit more-strongly-attenuated lines-of-sight from our perspective, we also show a similar plot colored by elliptical axis ratio (Figure 3.8).

We note that $\bar{\tau}_V$ correlates, as expected, with major-minor axis ratio $\frac{b}{a}$ (a proxy for inclination), with a power-law exponent of ~ 0.40 and a scatter of ~ 0.12 dex (Figure 3.9). This indicates that the PCA-based estimates of optical depth provide a reasonable indication of the influence of dust. The scatter at fixed axis ratio is considerable, though (~ 0.12 dex), which hints that simply adopting the axis ratio as a proxy for attenuation could neglect important galaxy-to-galaxy differences.

But, there could be additional important factors at play besides simply attenuation:

⁴Spaxels with fitting errors, bad PDF population, or problematic spectroscopic data are excluded. In Section 3.4, such spaxels were replaced by the median of their neighbors, but here we eliminate them altogether, so that all spaxels with good data are considered only once.

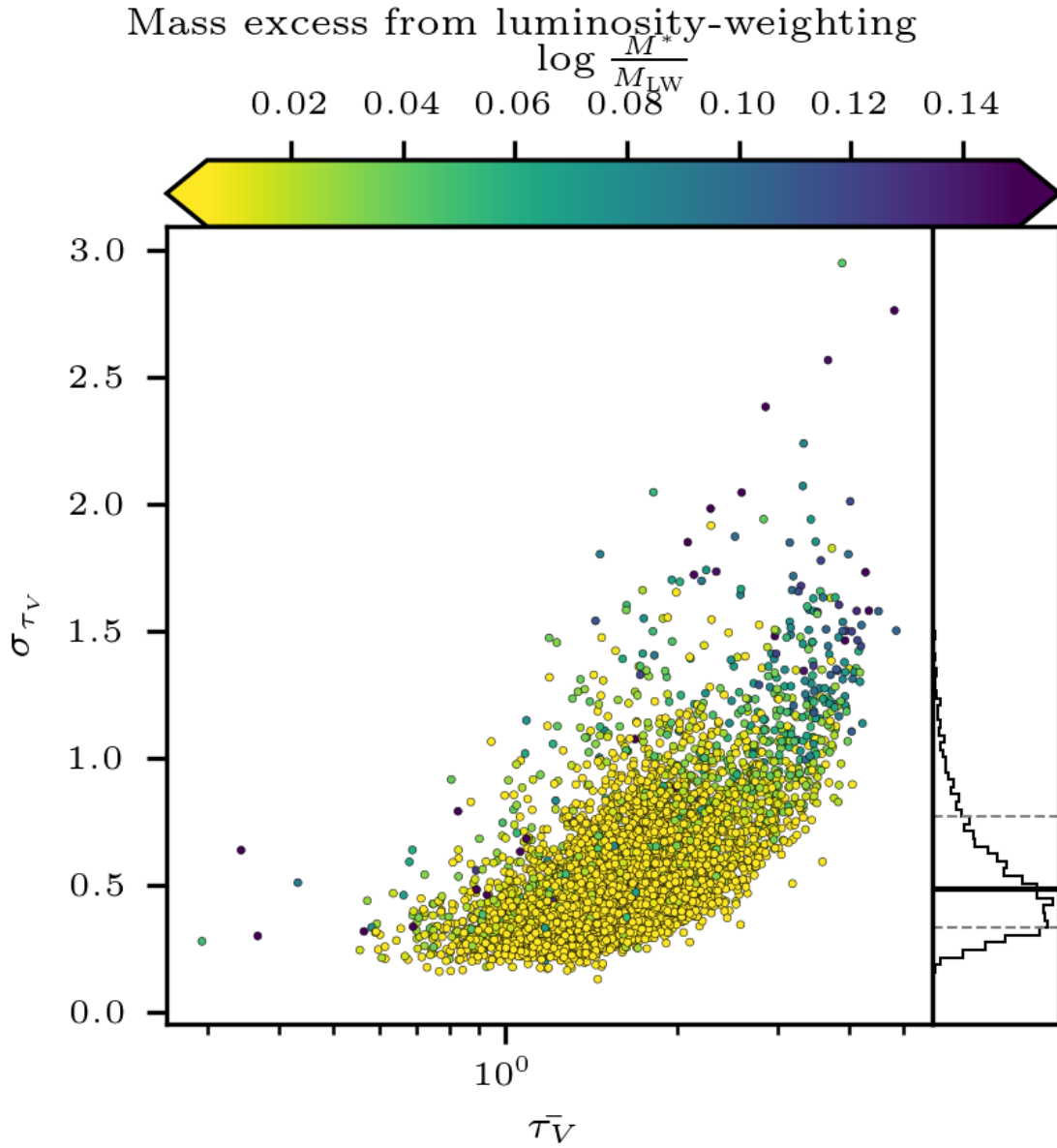


Figure 3.7 : The logarithmic mass-deficit $\log \frac{M^*}{M_{\text{LW}}^*}$ induced by luminosity-weighting the spaxel-resolved stellar mass-to-light ratios (point color), plotted with respect to spaxel-stellar-mass-weighted dispersion in inferred V -band optical depth σ_{τ_V} and average inferred spaxel-stellar-mass-weighted V -band optical depth $\bar{\tau}_V$. The distribution of σ_{τ_V} is shown in the right-hand panel, and the 16th, 50th, and 84th percentiles are shown as horizontal lines (dashed, solid, and dashed, respectively). The galaxies with the highest mass deficit have the highest degree of dispersion in local-stellar-mass-weighted τ_V , even at fixed average τ_V .

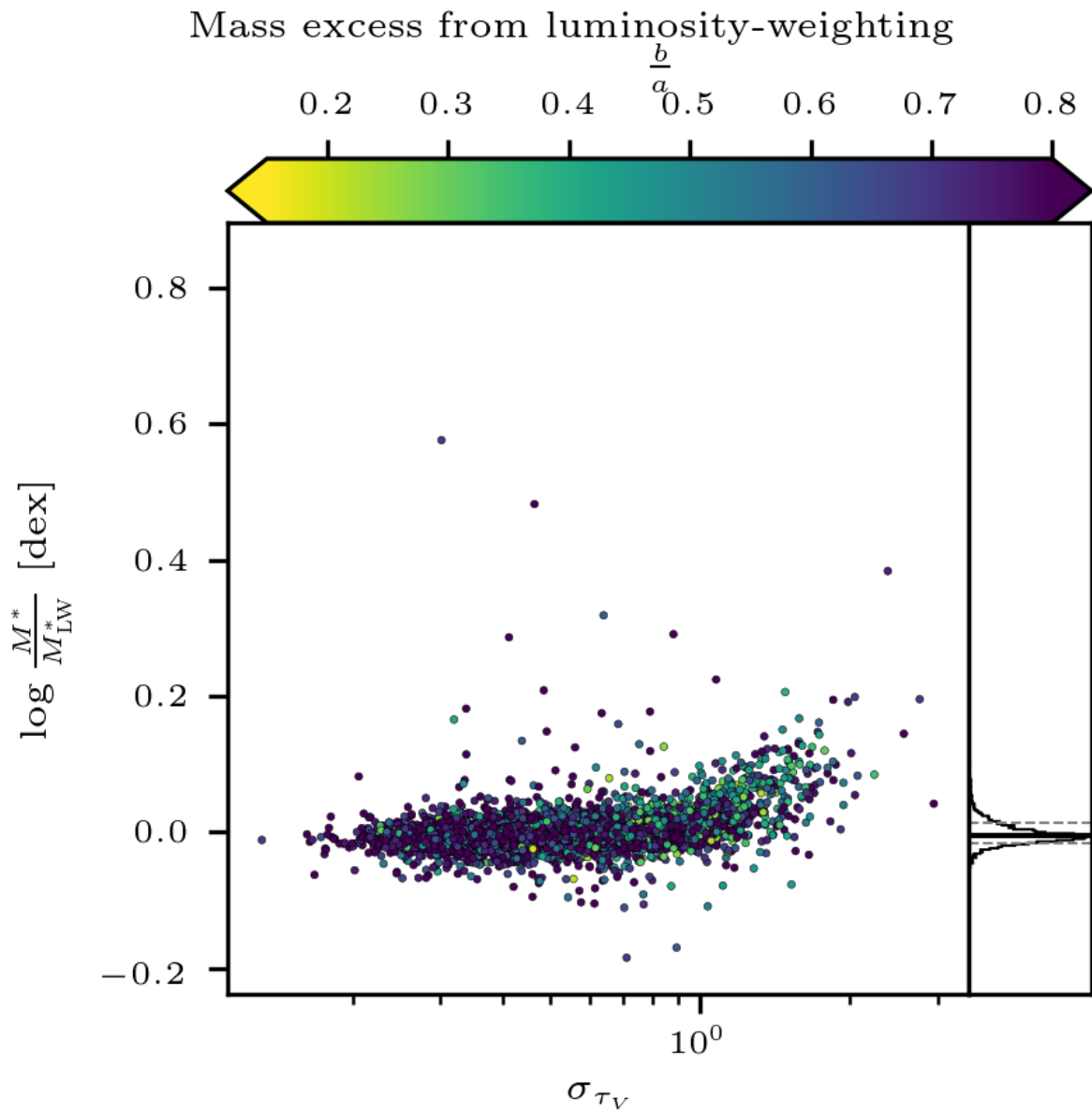


Figure 3.8 : The logarithmic luminosity-weighting-induced mass deficit plotted against σ_{τ_V} , and colored by NSA axis ratio. In the right-hand panel is shown the distribution of $\log \frac{M^*}{M_{\text{LW}}^*}$.

Effect of axis ratio on inferred dust properties

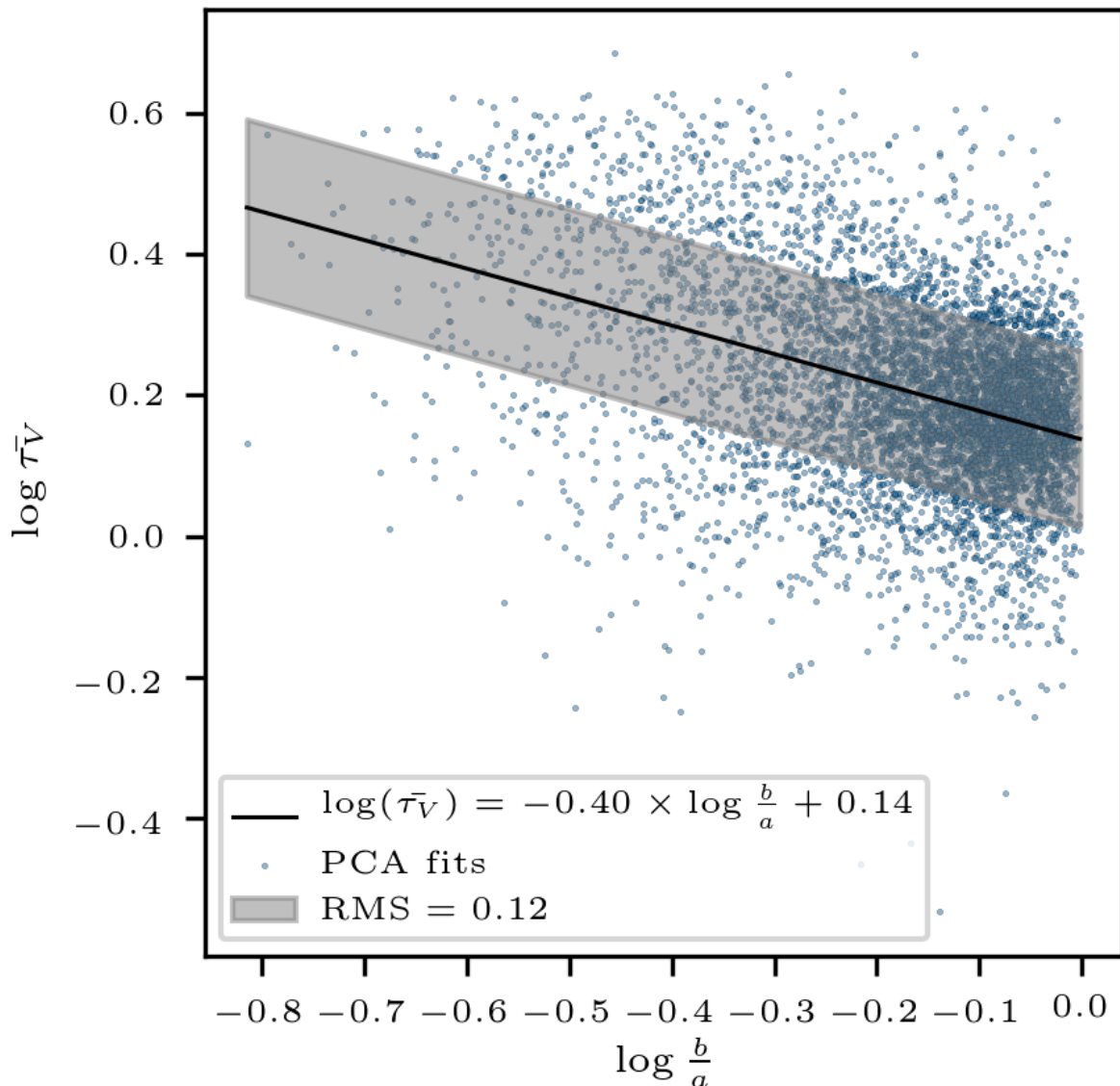


Figure 3.9 : The correlation of spaxel-stellar-mass-weighted attenuation $\bar{\tau}_V$ on elliptical-Petrosian axis ratio $\frac{b}{a}$, both on a log scale. Blue points are individual galaxies analyzed using PCA, the black line is the least-squares fit, and the gray band is the RMS of the residuals.

Sorba & Sawicki (2015) noted that, in the case of photometric stellar-mass estimates, $\log M^* - \log M_{\text{LW}}^*$ was largest in galaxies with large values of sSFR, supporting the “outshining” hypothesis. We find the total SFR in the innermost R_e by selecting spaxels with emission-line ratios indicating ionization dominated by recent star-formation—i.e., lying below both Kauffmann et al. (2003b) and Kewley et al. (2001) limits—, co-adding their (dust-corrected) H α luminosities, and assuming the Calzetti (2013) SFR-H α calibration. H α luminosity has been corrected for dust attenuation to first-order, by adopting the stellar-mass-weighted mean attenuation as a fiducial V-band optical depth, and augmenting the H α luminosity by a factor of $f_{\text{corr}} = \exp\left(\bar{\tau}_V \left(\frac{6564\text{\AA}}{5500\text{\AA}}\right)^{-1.3}\right)$ (Charlot & Fall 2000). We define a parameter $\eta_{R < R_e}$, intended to capture the majority of a galaxy’s recent star formation, which divides the SFR surface density in the innermost 1 R_e by the total, aperture-corrected stellar mass⁵:

$$\eta_{R < R_e} = \frac{\Sigma_{R < R_e}^{\text{SFR}}}{M_{\text{tot}}^*} f_{\text{corr}} \quad (3.3)$$

and we experiment in Figure 3.10 with obtaining a tighter correlation than is seen in Figure 3.7 by replacing $\bar{\tau}_V$ with $\eta_{R < R_e}$.

Though there are high-mass-deficit galaxies at low-to-intermediate σ_{τ_V} with high η , such points do not seem to be more extreme in their central SFR than low-mass-deficit counterparts at similar σ_{τ_V} . This provides some indication that strong central star formation is a subdominant effect to non-uniform attenuation when luminosity-weighting is concerned. In other words, the simple “outshining” scenario may present less of a problem for spectroscopic measurements of stellar mass. At any rate, both dust and mean-stellar-age considerations are somewhat less important than the (~ 0.1 dex) effects which can emerge from the choice of aperture-correction (see Section 3.4).

⁵We normalize by the total stellar mass to account for trends in star-formation rate surface density with total galaxy stellar mass.

We attempt here an illustration of the relative importance of σ_{τ_V} , $\bar{\tau}_V$, and $\eta_{R < R_e}$ for luminosity-weighted stellar mass, in order to summarize our findings: we use a multivariate ordinary least-squares fit of $\log \frac{M^*}{M_{\text{LW}}^*}$ versus $\bar{\tau}_V$, σ_{τ_V} , and $\log \eta_{R < R_e}$. We use the model

$$\log \frac{M^*}{M_{\text{LW}}^*} \sim \alpha + \beta_0 \bar{\tau}_V + \beta_1 \sigma_{\tau_V} + \beta_2 \log \eta_{R < R_e} \quad (3.4)$$

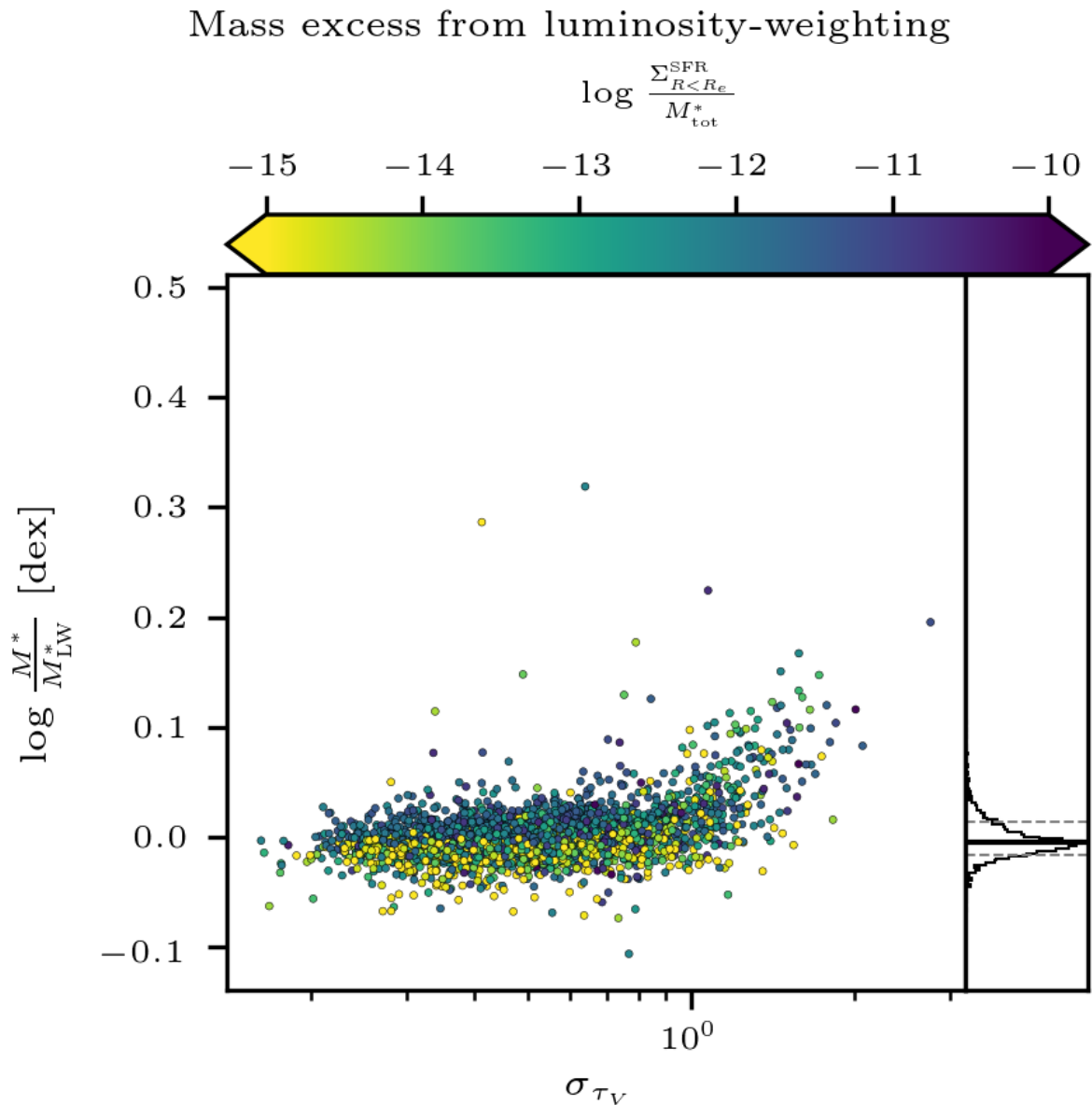


Figure 3.10 : As Figure 3.7, except colored by $\eta_{R < R_e} = \log \frac{\Sigma_{R < R_e}^{\text{SFR}}}{M_{\text{tot}}^*} f_{\text{corr}}$, the specific star formation rate surface density within $1 R_e$.

and attempt to find values for α , β_0 , β_1 , and β_2 , the former of which sets a zeropoint for the luminosity-weighting-induced variation in stellar mass-to-light ratio in our sample, and the latter three of which respectively modulate the effects of average dust attenuation, differential dust attenuation, and specific star-formation rate surface density. In Table 3.2, we summarize the OLS fit: of the three factors considered, σ_{τ_V} exhibits the strongest effects on luminosity-weighted, as indicated by the confidence interval for β_1 clearly excluding zero and the extremely low p-value. However, simply high, but uniform attenuation *does not* induce an apparent mass-deficit after luminosity-weighting. Lastly, the regression indicates that $\log \eta_{R < R_e}$ can exert some effect, though small (an order of magnitude less severe than unequal attenuation). While we caution the reader against ascribing too much meaning to this regression (we do not include uncertainties on $\bar{\tau}_V$, σ_{τ_V} , or $\log \eta_{R < R_e}$), it does provide us some insight that unequal attenuation is likely the dominant factor governing what modulates the effects of luminosity-weighting on stellar mass-to-light ratio at kiloparsec scales; and that an extremely large amount of recent star-formation could constitute a secondary influence. As this sample also contains a fair degree of contamination by galaxies with AGNs, foreground stars, or overlapping galaxies, such cases could be isolated in the future using visual classification.

Finally, we produce a list of the twenty worst-offending differences between IFU-summed and luminosity-weighted stellar masses (Table 3.3), and show images of each

Variable	Quantity modulated	CI (2.5–97.5)	p
α	zeropoint	$[1.38 \times 10^{-2}, 2.61 \times 10^{-2}]$	$< 10^{-8}$
β_0	$\bar{\tau}_V$	$[-4.49 \times 10^{-3}, -1.38 \times 10^{-3}]$	2.24×10^{-4}
β_1	σ_{τ_V}	$[4.65 \times 10^{-2}, 5.34 \times 10^{-2}]$	$< 10^{-8}$
β_2	$\log \eta_{R < R_e}$	$[2.83 \times 10^{-3}, 3.69 \times 10^{-3}]$	$< 10^{-8}$

Table 3.2 : Summary of the OLS fit of $\log \frac{M^*}{M_{\text{LW}}^*}$ versus $\bar{\tau}_V$, σ_{τ_V} , and $\log \eta_{R < R_e}$. For each of the “slope parameters” β and the “zeropoint” α , we give approximate confidence intervals and p-values.

(Figure 3.11). We exclude galaxies whose centers are contaminated by broad-line AGN emission: the vast majority of broad-line AGN have poor PCA fits; but the rare spaxel that is not flagged can cause trouble when compared to the rest of the galaxy, and areas with fainter (but still broad) AGN emission also normally have poor PCA fits.

3.5 Discussion and Conclusions

In this work, we build upon [MaNGA-PCA Paper I](#) in this series, which used a library of 40000 spectra of composite stellar populations to construct a reduced-dimensionality space for fitting moderate signal-to-noise optical spectra of nearby galaxies; and as a

MaNGA plateifu	$\log \frac{M^*}{M_{\text{LW}}^*}$ [dex]	Description
8158-3703	0.576	low-surface-brightness dwarf galaxy
8139-12702	0.319	two galaxies in IFU
8999-3702	0.287	possible poor stellar continuum fit, stellar velocity field
8566-1901	0.224	two foreground stars
8249-12702	0.206	two galaxies in IFU, different redshifts
9869-12704	0.199	foreground star
8942-6102	0.192	two foreground stars
8080-12702	0.167	edge-on galaxy with prominent dust lane
8995-9102	0.166	star-forming dwarf galaxy
10504-9101	0.161	moderately-inclined disk with inner dust lane
9889-1902	0.159	barred spiral galaxy with strong star-formation
8253-12703	0.151	nearly edge-on disk with prominent dust lane
8145-6102	0.148	several foreground stars
9880-12703	0.145	possible background galaxy
8619-12705	0.143	star-forming dwarf galaxy with red, background galaxy
8988-6102	0.141	moderately-inclined disk with star-forming outskirts and dusty interior
8440-12705	0.133	edge-on galaxy with prominent dust lane
8618-3702	0.130	possible foreground star(s)
9039-9101	0.130	two star-forming galaxies, foreground star
9029-12701	0.127	edge-on disk with prominent dust lane

Table 3.3 : The twenty galaxies with the largest difference between M^* and M_{LW}^* .

complement to [MaNGA-PCA Paper I](#), investigate the systematics of resolved stellar mass surface density (with respect to kinematically-measured dynamical mass surface density), total (aperture-corrected) galaxy stellar mass (with respect to photometric estimates), and flux-weighted stellar mass-to-light ratios.

We use three MPL-8 galaxies also observed as part of the DiskMass Survey ([Bershady et al. 2010a](#)) as a testbed for evaluating the systematics of kinematic and spectroscopic estimates of dynamical and stellar mass surface-density. We find that the resolved, inclination-corrected stellar mass surface-density obtained by a simple transformation

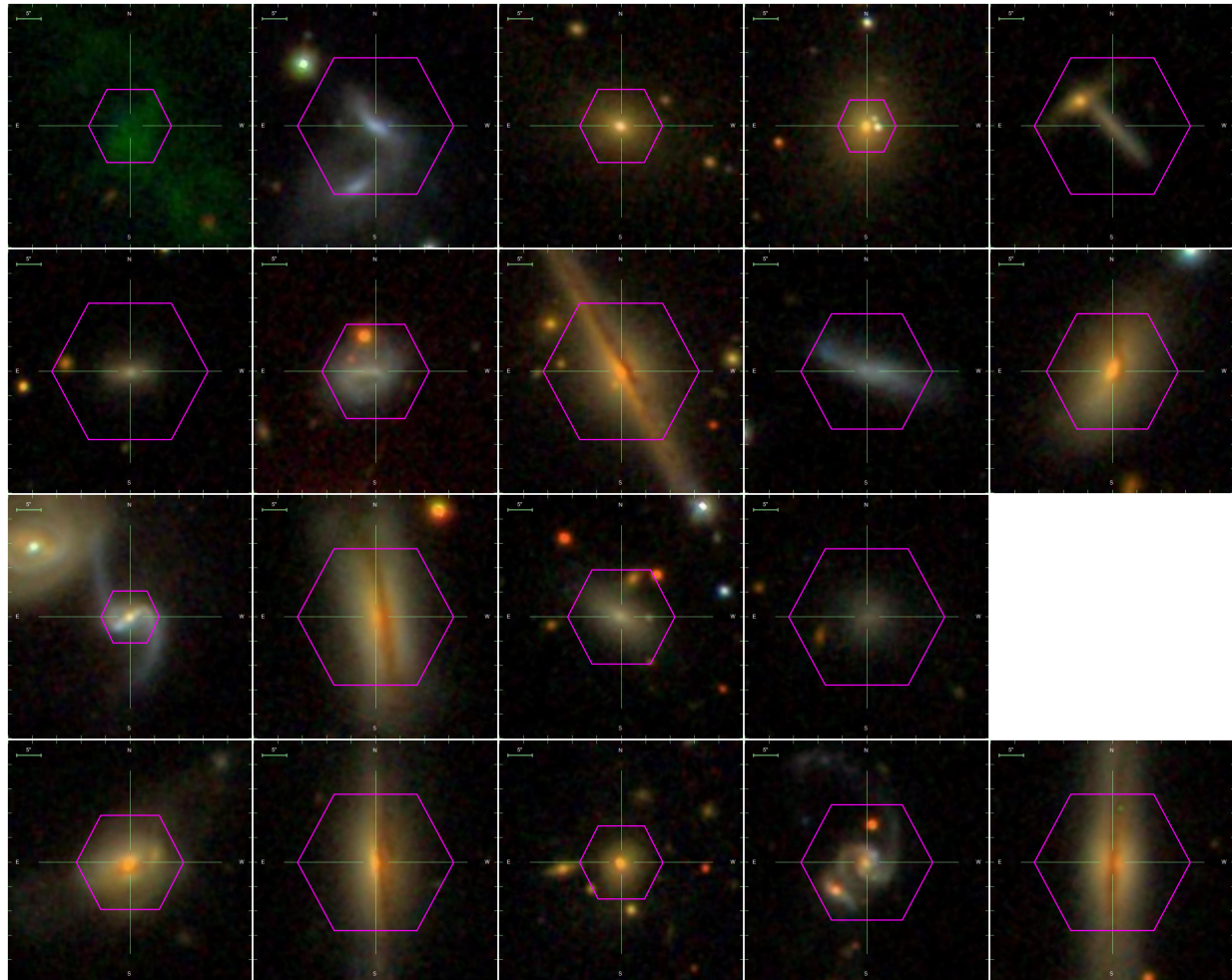


Figure 3.11 : The twenty galaxies with the largest difference between M^* and M_{LW}^* . If read left-to-right and top-to-bottom, galaxies are in the same order as Table 3.3. Galaxies with unavailable three-band image cutouts have been omitted.

between PCA-derived Υ_i^* and M^* in most cases exceeds the estimates of dynamical mass surface density. Given that by definition, the dynamical mass includes stars, gas, and dark matter, this discrepancy indicates appreciable systematics in one or both methods. For the two higher-surface-brightness cases, better agreement between dynamical and SPS measurements could be obtained in two cases by postulating that the disk scale-height was overestimated by a factor of ~ 1.5 . If, though, photometric mass estimates discussed in Section 3.4.2 were taken as truth (i.e., if the mass estimates here are anomalously heavy by that margin), the scale-height correction could be reduced to approximately a factor of 1.3.

3.5.1 Galaxy total stellar-mass: aperture-correction and luminosity-weighting

In order to estimate total galaxy stellar-mass (including that lying outside the grasp of the IFU), we test two rudimentary methods of aperture-correction: the “ring” method applies a fiducial mass-to-light ratio equal to the median of the outermost-sampled $0.5R_e$ to the difference between the NSA K-corrected i -band flux and the summed flux from the entire IFU; the favored “CMLR” method uses the missing flux in the g and r bands to place the remainder of the galaxy on a CMLR. Furthermore, we note that the flux fraction lying outside the IFU is correlated with MaNGA subsample (on average, the Primary+ subsample is exposed out to a smaller galactocentric radius, so the aperture-correction is larger, and in the case of a negative gradient in stellar mass-to-light ratio, the difference between “ring” and “CMLR” corrections will be increased). We adopt the “CMLR” method, since we believe it treats the Primary+ and Secondary samples more equally, and is less susceptible to over-correction.

We also examine the question of whether co-adding an entire IFU’s spectra yields a different estimate of average stellar mass-to-light ratio. The intrinsic luminosity-

weighting has been attributed to “outshining” (where young, bright, blue spectra—having intrinsically low mass-to-light ratio—“wash out” the older spectra which sample most of the mass), as well as to the effects of dust. Both scenarios are simply a consequence of luminosity-weighting a mass-related property. We find that for MaNGA IFS data, galaxies with dust lanes or which are viewed edge-on experience the strongest mass-deficits between luminosity-weighted and IFU-summed stellar masses. It is plausible that a different IFS survey with different spatial-sampling characteristics or catalog selection function may experience a different balance of “outshining” and dust-induced effects. This study is not alone in noting the deleterious effects of spatial binning on the robustness of spectral fits: in tests of the fidelity of full-spectral fitting, [Ibarra-Medel et al. \(2019\)](#) find that synthetic observations of hydrodynamic simulations of Milky Way-like galaxies with a MaNGA-like instrument, under MaNGA-like observing conditions, and with a spatial binning scheme (intended to increase signal-to-noise ratio) can produce a total mass deficit of up to 0.15 dex. This deficit worsens as inclination increases and a galaxy becomes edge-on: in the extreme, at $i \sim 90^\circ$, the light is dominated by the stellar populations at the lowest line-of-sight-integrated optical depth—so, only the outermost ring of stars is seen.

Given the observation that spatial coadding produces biases at the 0.05–0.1 dex level on $\log \Upsilon_i^*$, it may be prudent to re-evaluate the circumstances under which spectra are automatically coadded. It has become common practice to add together spatially adjacent spectra having low signal-to-noise ratios using adaptive binning techniques like Voronoi binning ([Cappellari & Copin 2003](#)), in order to achieve uncertainties better suited to stellar population analysis. By binning indiscriminate to the properties of the spectra themselves, though, one might group regions in a galaxy that are intrinsically very different. In the case of, for instance, a disk galaxy with star-forming spiral arms and an older bulge or thick disk (having respectively low and moderate-to-high stellar mass-to-light ratios), one spatial

bin might include contributions from both a star-forming arm (intrinsically bright) and the nearby bulge or older, thick disk (generally dimmer), potentially biasing an estimate of $\log \Upsilon_i^*$ low. A more reliable approach would preferentially continue to accumulate bins along paths where spectra are similar. One pathway to this might rely on principal component decomposition of observed spectra, followed by agglomeration of nearby spectra that are both nearby and similar in PC space.

3.5.2 Public Data

In addition to the soon-to-be-released resolved maps of $\log \Upsilon_i^*$ described in [MaNGA-PCA Paper I](#), we will also release in tabular format estimates of total galaxy stellar-mass as a value-added catalog (VAC) in SDSS Data Release 16 (DR16). Included will be IFU-coadded stellar masses, stellar masses interior to 1 and 2 R_e (where appropriate), and aperture-corrections using the “ring” and (recommended) “CMLR” methods described above.

A Statement of Work

Here are briefly outlined the contributions of all listed authors for this publication, in order of their listing in the journal article.

- **Zachary J. Pace:** Devised and led the comparison to DiskMass; led the software pipeline implementation (including rollout at the University of Utah); also led the writing of this manuscript.
- **Christy Tremonti:** Provided input on aperture-correction, and suggested tests against the archival photometry; proofreading and revisions.
- **Yanmei Chen:** Advised the lead author during summer appointment as NSF

EASPSI Fellow at Nanjing University (Nanjing, China) during Summer 2016.

- **Adam Schaefer:** Aided with caomparisons to photometry; guided discussion of luminosity-weighting, particularly the mass-deficit's relationship to SFR; proofreading and revisions.
- **Matthew Bershady:** Aided in interpreting the comparisons between the MaNGA resolved stellar mass-to-light ratio measurements and the DiskMass dynamical mass surface density measurements; proofreading and revisions.
- **Remaining authors** (Kyle Westfall, Médéric Boqien, Kate Rowlands, Brett Andrews, Joel Brownstein, Niv Drory, David Wake): Proofreading and revisions; inclusion as Sloan Digital Sky Surveys Architects due to contributions to hardware, administration, survey science or software.

References

- Aihara, H., Allende Prieto, C., An, D., et al. 2011, ApJS, 193, 29
- Aniyan, S., Freeman, K. C., Gerhard, O. E., Arnaboldi, M., & Flynn, C. 2016, MNRAS, 456, 1484
- Aniyan, S., Freeman, K. C., Arnaboldi, M., et al. 2018, ArXiv e-prints, arXiv:1802.00465
- Baldry, I. K., Balogh, M. L., Bower, R. G., et al. 2006, MNRAS, 373, 469
- Balogh, M. L., Baldry, I. K., Nichol, R., et al. 2004, ApJ, 615, L101
- Bell, E. F., & de Jong, R. S. 2001, ApJ, 550, 212
- Bell, E. F., McIntosh, D. H., Katz, N., & Weinberg, M. D. 2003, ApJS, 149, 289
- Bershady, M. A., Martinsson, T. P. K., Verheijen, M. A. W., et al. 2011, ApJ, 739, L47
- Bershady, M. A., Verheijen, M. A. W., Swaters, R. A., et al. 2010a, ApJ, 716, 198
- Bershady, M. A., Verheijen, M. A. W., Westfall, K. B., et al. 2010b, ApJ, 716, 234
- Blanton, M. R., Kazin, E., Muna, D., Weaver, B. A., & Price-Whelan, A. 2011, AJ, 142, 31

- Blanton, M. R., & Roweis, S. 2007, AJ, 133, 734
- . 2017, kcorrect: Calculate K-corrections between observed and desired bandpasses, Astrophysics Source Code Library, ascl:1701.010
- Blanton, M. R., Bershady, M. A., Abolfathi, B., et al. 2017, AJ, 154, 28
- Boardman, N. F., Weijmans, A.-M., van den Bosch, R., et al. 2017, MNRAS, 471, 4005
- Bruzual, G., & Charlot, S. 2003, MNRAS, 344, 1000
- Bundy, K., Bershady, M. A., & Law, D. R. e. a. 2015, ApJ, 798, 7
- Calzetti, D. 2013, Star Formation Rate Indicators, ed. J. Falcón-Barroso & J. H. Knapen, 419
- Cappellari, M., & Copin, Y. 2003, MNRAS, 342, 345
- Chabrier, G. 2003, PASP, 115, 763
- Charlot, S., & Fall, S. M. 2000, ApJ, 539, 718
- Chen, Y.-M., Kauffmann, G., Tremonti, C. A., et al. 2012, MNRAS, 421, 314
- Dawson, K. S., Schlegel, D. J., Ahn, C. P., et al. 2013, AJ, 145, 10
- Doi, M., Tanaka, M., Fukugita, M., et al. 2010, AJ, 139, 1628
- Drory, N., MacDonald, N., Bershady, M. A., et al. 2015, AJ, 149, 77
- Eigenbrot, A., & Bershady, M. A. 2018, ApJ, 853, 114
- Fukugita, M., Ichikawa, T., Gunn, J. E., et al. 1996, AJ, 111, 1748
- Gallazzi, A., & Bell, E. F. 2009, ApJS, 185, 253
- Gallazzi, A., Charlot, S., Brinchmann, J., & White, S. D. M. 2006, MNRAS, 370, 1106
- Gallazzi, A., Charlot, S., Brinchmann, J., White, S. D. M., & Tremonti, C. A. 2005, MNRAS, 362, 41
- González Delgado, R. M., Pérez, E., Cid Fernandes, R., et al. 2014, A&A, 562, A47
- Gunn, J. E., Siegmund, W. A., Mannery, E. J., et al. 2006, AJ, 131, 2332
- Hessman, F. V. 2017, MNRAS, 469, 1147
- Ibarra-Medel, H. J., Avila-Reese, V., Sánchez, S. F., González-Samaniego, A., & Rodríguez-Puebla, A. 2019, MNRAS, 483, 4525
- Kauffmann, G., Heckman, T. M., White, S. D. M., et al. 2003a, MNRAS, 341, 33
- Kauffmann, G., Heckman, T. M., Tremonti, C., et al. 2003b, MNRAS, 346, 1055

- Kewley, L. J., Dopita, M. A., Sutherland, R. S., Heisler, C. A., & Trevena, J. 2001, ApJ, 556, 121
- La Barbera, F., Vazdekis, A., Ferreras, I., et al. 2016, MNRAS, 457, 1468
- Law, D. R., Yan, R., Bershady, M. A., et al. 2015, AJ, 150, 19
- Law, D. R., Cherinka, B., Yan, R., et al. 2016, AJ, 152, 83
- Li, H., Ge, J., Mao, S., et al. 2017, ApJ, 838, 77
- Li, R., Li, H., Shao, S., et al. 2019, arXiv e-prints, arXiv:1903.09282
- Martín-Navarro, I., La Barbera, F., Vazdekis, A., Falcón-Barroso, J., & Ferreras, I. 2015, MNRAS, 447, 1033
- Martínez-García, E. E., González-Lópezlira, R. A., Gladis Magris, C., & Bruzual, A. G. 2017, ApJ, 835, 93
- Martinsson, T. P. K., Verheijen, M. A. W., Westfall, K. B., et al. 2013a, A&A, 557, A131
- . 2013b, A&A, 557, A130
- McGaugh, S. S., & de Blok, W. J. G. 1997, ApJ, 481, 689
- Pace, Z. J., Tremonti, C., Chen, Y., et al. 2019, ApJ
- Salim, S., Rich, R. M., Charlot, S., et al. 2007, ApJS, 173, 267
- Schechtman-Rook, A., & Bershady, M. A. 2013, ApJ, 773, 45
- . 2014, ApJ, 795, 136
- Smee, S. A., Gunn, J. E., Uomoto, A., et al. 2013, AJ, 146, 32
- Sorba, R., & Sawicki, M. 2015, MNRAS, 452, 235
- Swaters, R. A., Bershady, M. A., Martinsson, T. P. K., et al. 2014, ApJ, 797, L28
- Tinsley, B. M. 1972, A&A, 20, 383
- . 1973, ApJ, 186, 35
- Tortora, C., Napolitano, N. R., Cardone, V. F., et al. 2010, MNRAS, 407, 144
- Tortora, C., Napolitano, N. R., Romanowsky, A. J., et al. 2011, MNRAS, 418, 1557
- Tremonti, C. A., Heckman, T. M., Kauffmann, G., et al. 2004, ApJ, 613, 898
- Wake, D. A., Bundy, K., Diamond-Stanic, A. M., et al. 2017, AJ, 154, 86
- Westfall, K. B., Bershady, M. A., & Verheijen, M. A. W. 2011, ApJS, 193, 21

- Westfall, K. B., Cappellari, M., Bershady, M. A., et al. 2019, arXiv e-prints, arXiv:1901.00856
- Yan, R., Bundy, K., Law, D. R., et al. 2016a, AJ, 152, 197
- Yan, R., Tremonti, C., Bershady, M. A., et al. 2016b, AJ, 151, 8
- York, D. G., Adelman, J., Anderson, Jr., J. E., et al. 2000, AJ, 120, 1579
- Zibetti, S., Charlot, S., & Rix, H.-W. 2009, MNRAS, 400, 1181

Chapter 4

SDSS-IV/MaNGA: Can impulsive gaseous inflows explain steep oxygen abundance profiles & anomalously-low-metallicity regions?

*A version of this chapter has been submitted
to the Astrophysical Journal
Pace, et al. 2020, ApJ, vol, page
and is notated P20 throughout this dissertation*

Abstract

Gaseous inflows are necessary suppliers of galaxies' star-forming fuel, but are difficult to characterize at the survey scale. We use integral-field spectroscopic measurements of gas-phase metallicity and single-dish radio measurements of total atomic gas mass to estimate the magnitude and frequency of gaseous inflows incident on star-forming galaxies. We reveal a mutual correlation between steep oxygen abundance profiles between $0.25 - 1.5 R_e$, increased variability of metallicity between $1.25 - 1.75 R_e$, and elevated HI content at fixed total galaxy stellar mass. Employing a simple but intuitive inflow model, we find that galaxies with total stellar mass less than $10^{10.7} M_\odot$ have local oxygen abundance profiles consistent with reinvigoration by inflows. Approximately 10-25% of low-mass galaxies possess signatures of recent accretion, with estimated typical enhancements of approximately 10-90% in local gas mass surface density. Higher-mass galaxies have limited evidence for such inflows. The large diversity of HI mass implies that inflow-associated gas ought to reside far from the star-forming disk. We therefore propose that a combination of high HI mass, steep metallicity profile between $0.25 - 1.5 R_e$, and wide metallicity distribution function between $1.25 - 1.75 R_e$ be employed to target possible hosts of inflowing gas for high-resolution radio follow-up.

4.1 Introduction

Galaxies must exchange gas with their immediate environments: the continuous consumption of gaseous reservoirs through star formation implies a need for replenishment (Kennicutt & Evans 2012). For example, to sustain the Milky Way’s current star formation rate (SFR) of $\sim 1.5 M_{\odot} \text{yr}^{-1}$ over the past 8 Gyr (a factor of several greater than the depletion time, the reciprocal of the star formation efficiency), gas capable of forming stars should be introduced at a similar rate (Snaith et al. 2015; Licquia & Newman 2015). This is also true near the peak of the cosmic star formation history, $z = 0 - 2$ (Tacconi et al. 2013), indicating that refueling is important across cosmic time. Furthermore, the empirical relationship between galaxies’ star formation and gas content implies that the resupplying process is integral to galaxies’ evolution through time (Kennicutt 1998). This need for additional fuel is exacerbated by star-formation-driven outflows: winds from massive stars and supernovae are capable of launching outflows into galaxy haloes at rates greater than the SFR itself (Heckman et al. 1990; Rubin et al. 2014; Chisholm et al. 2018), further depleting available gas reservoirs. Finally, cosmological simulations seem to demand inflows in order to reproduce galaxies’ SFRs and buildup of stellar mass over cosmic time: the inflowing gas present in simulations can reach the disks of galaxies with $M^* < 10^{10.3} M_{\odot}$ without being shock-heated, implying that it will be detectable as HI (Kereš et al. 2005; Dekel & Birnboim 2006).

While outflows from galaxy disks are well-studied phenomena in the extragalactic environment, inflows have proven more elusive to direct detection at the survey scale. High-column-density, inflowing structures such as high-velocity clouds (HVCs—Wakker 2004) are ubiquitous in the Milky Way’s immediate vicinity, and similar structures ought to exist

in other haloes, as well. However, direct detection of HI in extragalactic HVC analogs is not practical, since the radio array configurations with sufficient spatial resolution lack the sensitivity to detect low-column-density structures. Furthermore, it is difficult to establish an unassailable link between gas in the vicinity of galaxies and the star formation in the galaxy itself: after all, cold gas is pervasive in galaxy haloes regardless of level of star formation activity (e.g., [Bieging 1978](#); [Sanders 1980](#); [Zhang et al. 2019](#)). Projection effects, unknown ionization state, obscuration on the far side of a dusty disk, and the paucity of metals all contribute to challenges in observing potential gaseous inflows. Targeted studies of individual galaxies have produced interesting examples of low-metallicity star formation indicative of ongoing accretion ([Howk et al. 2018a,b](#); [Sánchez Almeida et al. 2014](#)); but larger samples across a wider range of galaxy properties, conditions, and environments are needed. The difficult aspects of this open question must be addressed: to quantify the impact of inflowing gas is to ground one branch of the baryon cycle.

Since direct measurements of inflow are presently impractical at the survey scale, we must seek out its secondary effects, specifically on galaxies’ chemistry: a galaxy’s gas content is tied to the abundance of heavy elements in its interstellar medium (ISM), and therefore also to the buildup of stellar populations over cosmic time. Models of galaxy chemical evolution see gas mass fraction, gas-phase metallicity¹, and stellar mass as manifestations of galaxies’ active transformation of gas into stars, with heavier elements released back into the ISM during the final stages of massive stars’ lives ([Tinsley 1972, 1973](#); [Vincenzo et al. 2016](#)). The observational evidence for this interplay is abundant in statistical samples of star-forming galaxies, with central metallicity increasing with stellar-mass ([Tremonti et al. 2004](#)), and gas fraction decreasing as stars and metals accumulate

¹Throughout this work, we use the terms “oxygen abundance”, “gas-phase metallicity”, and simply “metallicity” interchangeably.

(Hughes et al. 2013). It appears necessary to have some combination of gaseous inflows and outflows to explain the chemical abundances of old stars in the Milky Way (Spitoni et al. 2019) and gas-phase abundances in other galaxies (?).

Because inflows may be brief and localized, rather than smooth in space and time, they may produce detectable chemical signatures in the disk. In general, a star-forming galaxy’s metallicity decreases as galactocentric radius increases (Oey & Kennicutt 1993; Zaritsky et al. 1994; Sánchez et al. 2014; Belfiore et al. 2017; Poetrodjojo et al. 2018; Sanchez 2019). Reports differ regarding whether the slope of a galaxy’s oxygen abundance profile (the metallicity gradient) correlates with its total stellar mass (Sánchez et al. 2014; Belfiore et al. 2017; Zinchenko et al. 2019; Mingozi et al. 2020). It has been argued that characteristic metallicity gradients emerge from inside-out galaxy formation (Prantzos & Boissier 2000); but, they may simply emerge from the gaseous reservoirs’ evolution *at a local scale* (Moran et al. 2012; Zhu et al. 2017; Barrera-Ballesteros et al. 2018; Sánchez Almeida & Sánchez-Menguiano 2019; Bluck et al. 2019).

While common and statistically well-characterized on average, metallicity gradients are not perfectly uniform: chemical abundance does appear to vary azimuthally as well as radially, despite the rapid timescale (within one galactic rotation period) on which metals ejected from massive stars are thought to mix with the surrounding ISM (Petit et al. 2015). In the Milky Way, for instance, abundance gradients measured at different azimuth angles have been found to differ by ± 0.03 dex kpc $^{-1}$ (Balser et al. 2015); but it is not clear whether this behavior extends to all star-forming galaxies as a population (for a diversity of views, see Kreckel et al. 2016; Sánchez-Menguiano et al. 2016; Vogt et al. 2017; Ho et al. 2017, 2018). Recently, Kreckel et al. (2019) have reported typical metallicity dispersions of 0.03 – 0.05 dex at fixed radius in a sample of galaxies observed with VLT/MUSE. Furthermore, deviations from single gradients in individual galaxies have been observed—

albeit in somewhat smaller samples—with breaks in the radial metallicity profiles separating the disks’ innermost regions, intermediate radii, and outskirts (Sánchez-Menguiano et al. 2018). Simultaneously, integral-field surveys such as MaNGA have yielded reports of anomalously-low-metallicity (ALM) regions, atypically-metal-poor areas at \sim kpc scales: Hwang et al. (2019) finds a sizable ALM sample (defined as having oxygen abundance at least 0.14 dex below the mean metallicity for all MaNGA spaxels at the same stellar mass surface density and total galaxy stellar mass) in the MaNGA sample. About 25% of local star-forming galaxies reportedly exhibit these characteristics, preferring galaxies below $10^{10} M_{\odot}$ and morphologically-disturbed galaxies; and about 10% of all MaNGA star-forming spaxels have the “ALM” designation. The suggested explanation is the rapid, impulsive (“bursty”) accretion of gas from the halo which fuels star formation.

Despite the recent evidence that has emerged for localized inflows onto star-forming disks, the details remain indistinct. Cosmic filaments, the source for inflowing gas in cosmological simulations, are many times the size of galaxies’ star-forming disks (Martin et al. 2019); and some questions remain about whether their associated inflows could effect a sustained and detectable depression of metallicity. The duty cycle of inflows (i.e., the fraction of time that the average gas reservoir actively accretes gas) is also relatively ill-constrained. However, to establish the definitive link between ALM gas and the actual inflow, the local gas reservoir should be characterized—an important deficiency in the current generation of observations. At present, the best indication of local gas supplies at the survey scale is global (single-dish) HI measurements. In addition, given the relatively short mixing timescale of heavy elements in the ISM, the width of the metallicity distribution function at fixed radius (or within a narrow radial range) could be employed as a tracer of newly-introduced gas with non-ambient metallicity. This work will address such opportunities.

This study seeks to link the diversity of radial metallicity profiles & the width of the metallicity distribution function at fixed radius with galaxies' atomic gas reservoirs, by exploring the mutual correlations between radial oxygen abundance slope, oxygen abundance dispersion, total HI mass, and total stellar mass; and employs a conceptual model of local dilution to estimate plausible enhancements to star-forming gas reservoirs at the local (kpc) scale. In Section 4.2, we describe the MaNGA resolved spectroscopy and three related value-added catalogs (VACs) which provide measurements of total galaxy stellar-mass, measurements of disk effective radius, and total HI mass. In Section 4.3, we describe the strong-line metallicity calibration used; measure radial metallicity profiles with a metallicity decrement (a replacement for the more traditional gradient); measure azimuthal metallicity variations using the width of the metallicity distribution in a narrow annulus; and delineate the sample selection. In Section 4.4, we report the trends between HI mass, metallicity decrement, metallicity distribution width, and total stellar mass. In Section 4.5, we describe the local dilution of star-forming gas reservoirs with an intuitive model. In Section 4.6, we summarize our results & their implications. Throughout this work, we adopt the nine-year WMAP cosmology (Hinshaw et al. 2013), and a Kroupa (2001) stellar initial mass function (IMF).

4.2 Data

This work uses integral-field spectroscopic (IFS) data from the MaNGA survey (Bundy et al. 2015), part of SDSS-IV (Blanton et al. 2017). MaNGA will observe more than 10,000 nearby galaxies ($0.01 < z < 0.15$) from the NASA-Sloan Atlas (NSA, Blanton et al. 2011), with an approximately-uniform distribution in *i*-band absolute magnitude, resulting in a roughly-flat distribution in $\log M^*$, and is approximately volume-limited within a given redshift range (Wake et al. 2017). Two-thirds of observed galaxies are

drawn from the “Primary+” sample (coverage to at least $1.5 R_e$); and the remainder come from the “Secondary” sample (covered to at least $2.5 R_e$). The spectroscopic data used in this study come from MaNGA Product Launch 8 (MPL-8), an internally-released dataset nearly identical to SDSS Data Release 16 (Ahumada et al. 2019), and containing 6779 galaxies.

MaNGA spectroscopic observations cover the wavelength range of 3600 to 10300 Å with $d \log \lambda \sim 10^{-4}$ ($R \sim 2000$), and use the BOSS spectrograph (Smee et al. 2013; Dawson et al. 2013), an instrument at the SDSS 2.5-meter telescope at Apache Point Observatory (Gunn et al. 2006). To achieve uniform spatial sampling, the spectrograph is coupled to closely-packed fiber hexabundles, each containing between 19 and 127 fibers (Drory et al. 2015). Sky-subtraction and spectrophotometric calibration are accomplished using single fibers and smaller hexabundles (Law et al. 2016; Yan et al. 2016b). All hexabundles and sky fibers are inserted into a plugplate affixed to the focal plane (York et al. 2000). Sets of three “dithered” pointings compose the MaNGA observations, and to form the datacubes (CUBE products), these observations are rectified to a spatial grid in the plane of the sky, with spaxel size 0.5” by 0.5” and seeing-induced PSF having an *i*-band FWHM $\sim 2.5''$ (Law et al. 2015; Yan et al. 2016a; Law et al. 2016). The MaNGA Data Analysis Pipeline (DAP, Westfall et al. 2019) measures stellar kinematics, emission-line fluxes (Belfiore et al. 2019), and stellar spectral indices for individual spaxels.

This work builds on the results of two MaNGA Value-Added Catalogs (VACS). First, we use estimates of total galaxy stellar-masses from the MaNGA-PCA project, which used an orthogonal spectral basis set trained on realistic SFHs to obtain robust resolved galaxy stellar masses (Pace et al. 2019a); the resolved masses were then aperture-corrected to form a catalog of total stellar-masses (Pace et al. 2019b). These stellar masses are likely much more reliable than those included in the MaNGA targeting catalog, since galaxy-

averaged light is more apt to “miss” stellar-mass in dusty environments and other low-flux regions (Zibetti et al. 2009; Sorba & Sawicki 2015; Pace et al. 2019b). Second, the MaNGA PyMorph DR15 photometric catalog provides parameters obtained from Sérsic and Sérsic-Exponential fits to MaNGA galaxies’ plane-of-sky surface-brightness profiles (Fischer et al. 2019). This allows radial abundance trends to be computed with respect to the disk (a more fundamental unit of chemical evolution), rather than the disk plus the bulge.

Finally, we include single-dish atomic hydrogen (HI) mass measurements and upper-limits: the GASS (Catinella et al. 2010) and ALFALFA (Haynes et al. 2018) surveys form the small archival portion of the HI measurements. The majority of measurements come from the HI-MaNGA project (Masters et al. 2019; Goddy et al. 2020; Stark & Masters in prep.), an observational campaign carried out with the Green Bank Telescope. This program targets MaNGA galaxies at $cz < 15,000 \text{ kms}^{-1}$, but regardless of their morphology, with an intended depth of 1.5 mJy at 10 kms^{-1} (after spectral smoothing), resulting in a stellar-mass distribution of targets peaking at $M^* \sim 10^{9.8} M_\odot$ (see Figure 1 of Masters et al. 2019). GBT HI observations were translated into HI mass estimates, and in the case of non-detections, mass upper-limits were estimated using the observational noise and assuming a rotation-curve with of 200 km s^{-1} . In total, 3413 MaNGA galaxies have measured HI masses or upper-limits.

4.3 Abundance calibrations and radial decrements

We measure gas-phase metallicities of individual MaNGA spaxels using the ratios between the fluxes of strong nebular emission lines, since the “direct” (T_e) method requires much deeper spectroscopy at the high expected metallicities of MaNGA spaxels. We rely on one of the strong-line calibrations of Pilyugin & Grebel (2016, hereafter, PG16), which matches several strong-line ratios to T_e abundances over a reference sample of 313 HII

regions. Specifically, we use the R2 calibration, referred to hereafter as PG16-R2. The three strong-line ratios used to define the calibration in PG16 are defined as follows:

- $R_2 = \frac{F([OII]_{3727}) + F([OII]_{3729})}{F(H\beta)}$
- $R_3 = \frac{F([OIII]_{4959}) + F([OIII]_{5007})}{F(H\beta)}$
- $N_2 = \frac{F([NII]_{6548}) + F([NII]_{6584})}{F(H\beta)}$

Generally, the strong-line ratios R_2 & R_3 (as well as their sum, generally notated R_{23}), are double-valued; that is, a single value can indicate one of two values of oxygen abundance. In the PG16-R2 calibration, this degeneracy between “upper” and “lower” branches is broken using the N_2 ratio (previous work has cautioned against using nitrogen-based line ratios to determine oxygen abundance, because the abundance ratio of N/O is variable, even at fixed oxygen abundance—but adopting it for the coarse task of deciding the R_{23} branch is safer). The accuracy of the resulting oxygen abundance estimate is $\lesssim 0.1$ dex over the range $7.0 \leq 12 + \log \frac{O}{H} \leq 9.0$, and Schaefer et al. (2019a) has found the PG16-R2 calibration to be less susceptible to N/O variations than other strong-line calibrations. Since variations in excitation (ionization parameter) can impact reliability of abundance estimates, this calibration adjusts for this effect using the ratio between R_2 & R_3 . (Pilyugin et al. 2018) concluded that for MaNGA spectra, the PG16-R2 calibration does not suffer from the same excitation-dependent deficiencies that purely N_2 -dependent calibrations do.

The metallicity for a particular spaxel is estimated according to a Monte Carlo randomization of attenuation-corrected emission-lines. The first four Balmer emission lines ($H\alpha$, $H\beta$, $H\gamma$, $H\delta$) are used to estimate the attenuation law, assuming a Charlot & Fall (2000) two-component dust model. The best-fitting dust parameters τ_V and μ (along

with their covariances) are found through Levenberg-Marquardt optimization. The line-specific attenuation correction-factors are then randomized according to the covariance matrix of the best-fit parameters, with 1000 draws total. The observed emission-line fluxes are likewise independently resampled 1000 times according to their reported uncertainties, and multiplied with the resampled dust-corrections. The combination of these draws for all emission lines is used to approximate the distribution of possible strong-line ratios R_2 , R_3 , and N_2 , which themselves are used to approximate draws from the distribution of oxygen abundance. This process is repeated for each spaxel in the field of view. The median of those 1000 draws from the oxygen abundance distribution is taken as the fiducial oxygen abundance for a spaxel, $(O/H)^*$; with the median absolute deviation of that distribution is taken as a measure of the dispersion. Both are logarithmic quantities.

4.3.1 Radial decrement definition

Since the star-forming disk is the main engine driving galaxy chemical evolution, the most useful radial unit is a *disk effective radius* (R_e^d) rather than a *total effective radius* (R_e^t). We use the bulge-disk decompositions from the MaNGA PyMorph photometric catalog (Fischer et al. 2019) to assign a radial coordinate to all spaxels based on the measured disk effective radius (hereafter, the shorthand R_e refers to a disk effective radius, unless otherwise specified). In practice, radial oxygen abundance trends fitted to ensembles of individual spaxels tend to be dictated strongly by the measurements in the outermost $\sim 0.5R_e$, since the number of spaxels within a radial interval rises in proportion to the distance from the center of the galaxy. For the case of an abundance gradient with non-constant slope, the central abundance would also be improperly estimated. In Belfiore et al. (2017), metallicity measurements were binned in intervals of $0.1 R_e$ and an unweighted least-squares fit made, thereby standardizing the contribution at various radii to the gradient

fit. Instead, we define a radial metallicity “decrement” between two widely-spaced annuli, as $\Delta_{in}^{out} = (O/H)_{in}^* - (O/H)_{out}^*$; in other words, a positive decrement indicates that oxygen abundance decreases radially.

The bounds for the radial bins are chosen to minimize the adverse effects of blurring by the PSF. We exclude spaxels along or close to the minor axes of inclined galaxies, where the PSF-induced smoothing in the data will “smear out” radial variations most severely: galaxies with observed minor-to-major axis ratios under 0.33 are excluded entirely, since dust-correction becomes extremely problematic at inclinations greater than 75 deg (Pellegrini et al. 2019). At axis ratios greater than 0.75, it is difficult to accurately determine a galaxy’s axis ratio, and so all spaxels are included. In the intermediate range ($0.33 < b/a < 0.75$), the azimuthal angle from the major axis determines the acceptance or rejection of a spaxel, with the angle rising linearly from 20 degrees at $b/a = 0.33$ to 90 degrees (i.e., no restriction) at $b/a = 0.75$.

Though we might desire to maximize the number of radial bins available, there is limited utility to reducing bin width smaller than the PSF size. Furthermore, a larger radial interval allows more spaxels to be aggregated. Most important for our purposes is the observation that both the MaNGA Primary and Secondary samples are relatively clean from PSF-induced contamination at radial separations greater than $0.5 R_e$. We elect to use radial bins with widths of $0.5 R_e$, and spaced apart by $0.75 R_e$ (see Figure 4.1). In this work, we consider bin limits of $[0.0, 0.5] R_e$ (radial bin 0) and $[1.25, 1.75] R_e$ (radial bin 1).

4.3.2 Sample & Data quality

Our base sample of galaxies is the PyMorph VAC (4266 galaxies), almost all of which have total stellar masses from the MaNGA-PCA VAC. Of these, 1152 (2080) have H I mass estimates (upper-limits) from either targeted GBT follow-up (Masters et al. 2019; Goddy

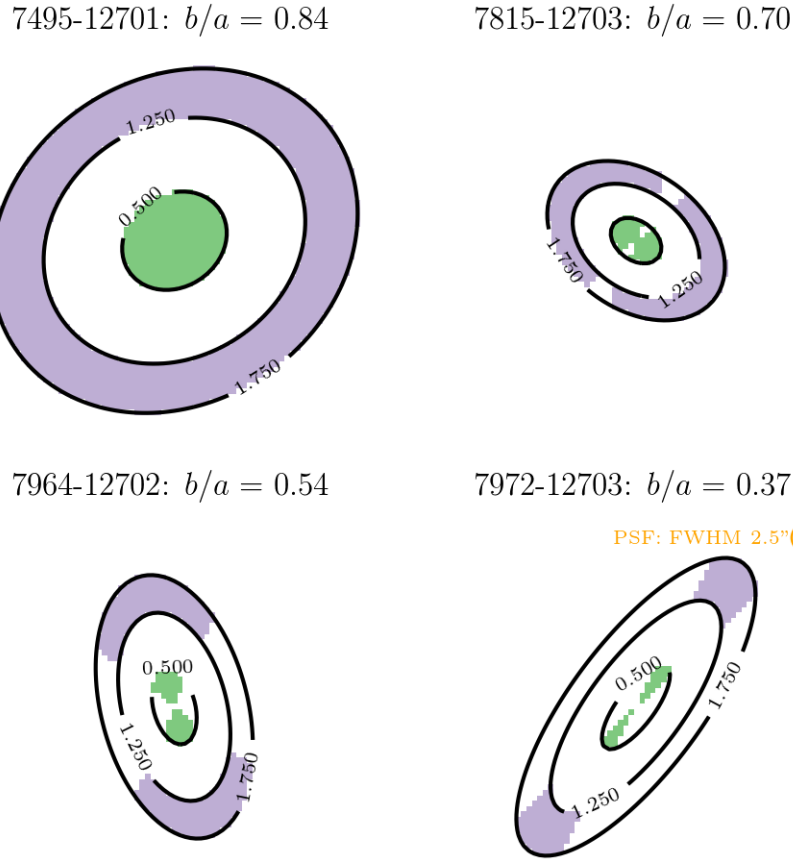


Figure 4.1 : The radial binning scheme described above, applied to four MaNGA galaxies with decreasing disk aspect-ratios. Pixels are colored according to their use in radial bins: light green indicates radial bin 0 ($0.0 - 0.5 R_e$), and lavender indicates radial bin 1 ($1.25 - 1.75 R_e$). Pixels colored white indicate locations not included in any bin, due to either radial coordinate or azimuthal angle away from the major axis. These restrictions are applied in addition to those on data-quality (see Section 4.3.2). Contours are in units of R_e , and are labeled at the outer boundary of bin 0, as well as the inner & outer boundaries of bin 1. The spatial resolution element (FWHM) is visualized as an orange circle in the bottom-right panel: as inclination increases, the PSF samples an increasing diversity of galaxy radii along the minor axis.

et al. 2020), ALFALFA (Haynes et al. 2018), or GASS/GASS-low (Catinella et al. 2010), accessed in that descending order of priority.

We adopt the following constraints on individual spaxels within galaxies, all of which must be met in order for the spaxel to be included in the radial fits and decrement calculation. These cuts are applied in addition to the radial and azimuthal restrictions described above.

- Signal-to-noise cuts: We require $S/N(H\alpha) > 5$, $S/N(H\beta) > 3$, $S/N([O\ III]) > 3$, and $S/N([N\ II]) > 3$, since these lines form the basis for the selection of star-formation-dominated spaxels.
- Excitation cuts: We require spaxels to lie in the star-formation-dominated portion of the $[N\ II]/H\alpha$ -versus- $[O\ III]/H\beta$ excitation diagram, i.e., below the Kauffmann et al. (2003) and Kewley et al. (2001) demarcation lines.
- Diffuse ionized gas (DIG) rejection: Lacerda et al. (2018) finds that when $EW(H\alpha)$ is less than 3Å, DIG dominates the emission spectrum. We select only spaxels with $EW(H\alpha) \geq 3\text{\AA}$.
- Restrictions on resampled oxygen abundances: The Monte Carlo-resampled distribution of the oxygen abundance (obtained from the line-ratio calibration) must have a median absolute deviation (MAD) < 0.3 dex, and must lie in the range [7.0, 9.0] (where the PG16-R2 calibration is well-characterized).

In order for an individual galaxy to be included for the purposes of radial metallicity trends, there must be at least 8 (10) unmasked spaxels in radial bin 0 (radial bin 1). With these thresholds set, we are left with 252 (110) galaxies having H I masses (upper-limits).

A further 273 galaxies passing all spectroscopic data-quality criteria above (bullet-points), but which were not targeted in the HI follow-up, are included separately.

4.4 Abundance decrement trends

Star-forming galaxies have been shown to possess similar metallicity gradients across a range of total stellar masses (Sánchez et al. 2014; Belfiore et al. 2017; Mingozi et al. 2020), with some evidence that gradients steepen with increasing galaxy stellar mass (Belfiore et al. 2017; Poetrodjojo et al. 2018; Mingozi et al. 2020). Figure 4.2 illustrates that despite broadly consistent radial metallicity decrements across a range of galaxy stellar masses, there is also great diversity at fixed mass. Likewise, a wide range of HI mass fractions exist at similar stellar mass. Before exploring the origin of the dispersion in measured decrement at fixed stellar mass, and its relation to HI, we consider how our decrements compare to previous measurements of abundance gradient.

4.4.1 Decrements vs. gradients

The relationship between a radial decrement and a gradient is intuitive: after adopting endpoints of $0.25 R_e^t$ and $1.75 R_e^t$ (the midpoints of the inner and outer radial intervals), the median measured metallicity gradients obtained in Mingozi et al. (2020, a recent study using MaNGA data) can be transformed into decrements, for comparison to this work (Figure 4.2, light purple points with errorbars). At low stellar mass ($\log M^*[M_\odot] < 10$), the median radial gradient from Mingozi et al. (2020) is well within the range of individual decrements measured in this work. It is crucial to note that the Mingozi et al. (2020) points represent constraints on the *median radial abundance trend* at fixed mass, rather than the

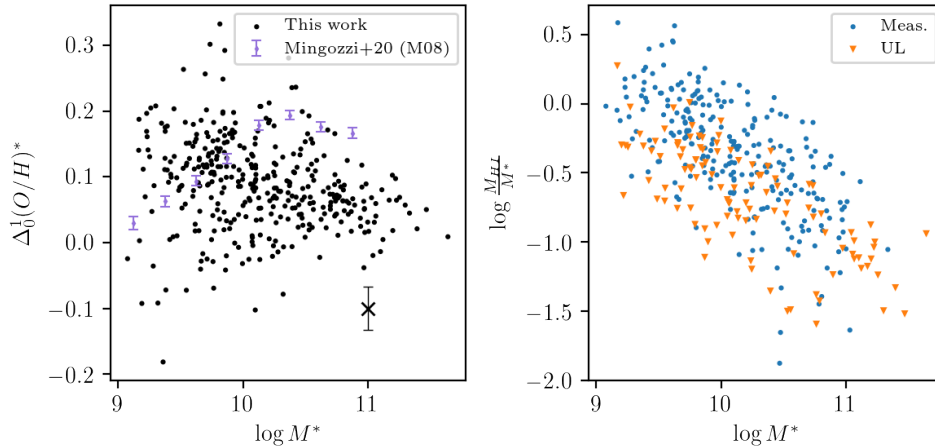


Figure 4.2 : The relationships between total galaxy stellar mass, radial abundance decrement ($\Delta(O/H)^* = (12 + \log \frac{O}{H})_{\text{inner}} - (12 + \log \frac{O}{H})_{\text{outer}}$) between the first two radial bins, and $\frac{M_{\text{HI}}}{M^*}$. A positive decrement indicates a radially-decreasing gas-phase metallicity profile. In the left-hand panel, stellar mass is shown on the abscissa and $\Delta(O/H)^*$ on the ordinate (a representative uncertainty for $\Delta(O/H)^*$ is also shown). We also show the mass-dependent radial decrements arising from the median radial gradients calculated in [Mingozzi et al. \(2020\)](#), assuming a uniform gradient from $0.25 - 1.5 R_e^t$ (note the radial unit of *total effective radii*). In the right-hand panel, we show the logarithm of the ratio between stellar mass and HI mass (positive detections are blue circles, upper-limits are orange, downward-facing triangles). While there is of course a broad trend of decreasing $\frac{M_{\text{HI}}}{M^*}$ with M^* , the scatter about that trend is significant (likely $\gtrsim 0.3$ dex, or a factor of several). Similarly, the scatter in $\Delta(O/H)^*$ at fixed stellar mass becomes most significant at $\log M^*[\text{M}_\odot] \lesssim 10.5$.

*true distribution of metallicity gradients*². The transformed gradients of (Mingozzi et al. 2020) do differ from this works’ results at higher stellar mass ($\log M^*[M_\odot] \geq 10$). Some combination of the following effects are likely responsible:

- Mingozzi et al. (2020) uses a similar, but not identical R_{23} strong-line metallicity calibration defined in Maiolino et al. (2008, Table 4), which relies on “direct” T_e metallicities at $(O/H)^* < 8.4$ and photoionization models at higher abundance. Belfiore et al. (2017) has shown that changing the strong-line metallicity calibration affects gradients and their trends with mass, so similar differences are expected here.
- The gradients of Mingozzi et al. (2020) were found in *total effective radius* (R_e^t) coordinates (rather than the *disk effective radius* coordinates used for this work’s empirically-measured gradients). This means galaxies with prominent bulges will produce gradients that are too steep.
- Mingozzi et al. (2020) fit the radial gradients only between $0.5 - 2.0 R_e^t$, excluding nearly the full breadth of the innermost radial annulus adopted in this work, in order to sidestep non-linear radial profiles (in particular, the well-known flattening of the abundance profile inward of $1.0 R_e$).

4.4.2 Radial metallicity trends and HI

Does HI content exert an influence over $\Delta(O/H)^*$ beyond its correlation with stellar mass? Figure 4.3 shows evidence of a positive correlation between HI mass fraction and radial gas-phase metallicity decrement, when galaxies are separated by their total stellar

²The Mingozzi et al. (2020) median gradients were found by first aggregating individual galaxies’ spaxels into radial bins, and then fitting all galaxies in a stellar mass bin with one linear regression against galactocentric radius

mass into four bins. The bins are set as the 16th, 50th, and 84th percentiles of the stellar-mass distribution of galaxies with either an HI mass measurement or upper-limit: 10^{9.6}, 10^{10.1}, and 10^{10.7} M_⊙. The correlation manifests for galaxies with measured HI masses as well as upper-limits.

Since a steep decrement could emerge from a high central value, rather than a low outer value, a positive correlation between central metallicity and HI mass might feasibly bring about the observed correlation between strong decrement and HI mass fraction. In practice, though, galaxies with the largest HI fractions at fixed stellar mass also have *lower-than-typical gas-phase metallicities* in their inner 0.5 R_e. This is consistent with the standard picture of galaxy chemical evolution (Tinsley 1972, 1973), and qualitatively similar to other observed relations between gas fraction and oxygen abundance (Hughes et al. 2013). Thus, we conclude that the correlation is not an emergent result of differing galaxy-to-galaxy abundance zeropoints.

The correlation we observe between a steep radial metallicity profile and a large HI mass is reminiscent of a result noted in a sample of DustPedia galaxies with archival MUSE integral-field spectroscopic observations (De Vis et al. 2019). The DustPedia parent sample has a great breadth of photometric measurements (25 bands from UV to submillimeter); but there are only 75 galaxies with integral-field spectroscopic observations (from the MUSE archive), albeit with finer spatial sampling than MaNGA reaches. Radial metallicity trends are measured in De Vis et al. (2019) with a linear fit, and are a true gradient over the entire galaxy, though with respect to r₂₅ (the radius of the m_B = 25 isophote). Though converting between gradients in the units of r₂₅ (DustPedia) and the decrements in the units of disk effective radii (this study) is not straightforward, we note with interest that there is some basis for a Δ(O/H)*-HI correlation in the literature.

Since gas-phase metallicity is a manifestation of a galaxy’s (or a region’s) chemical

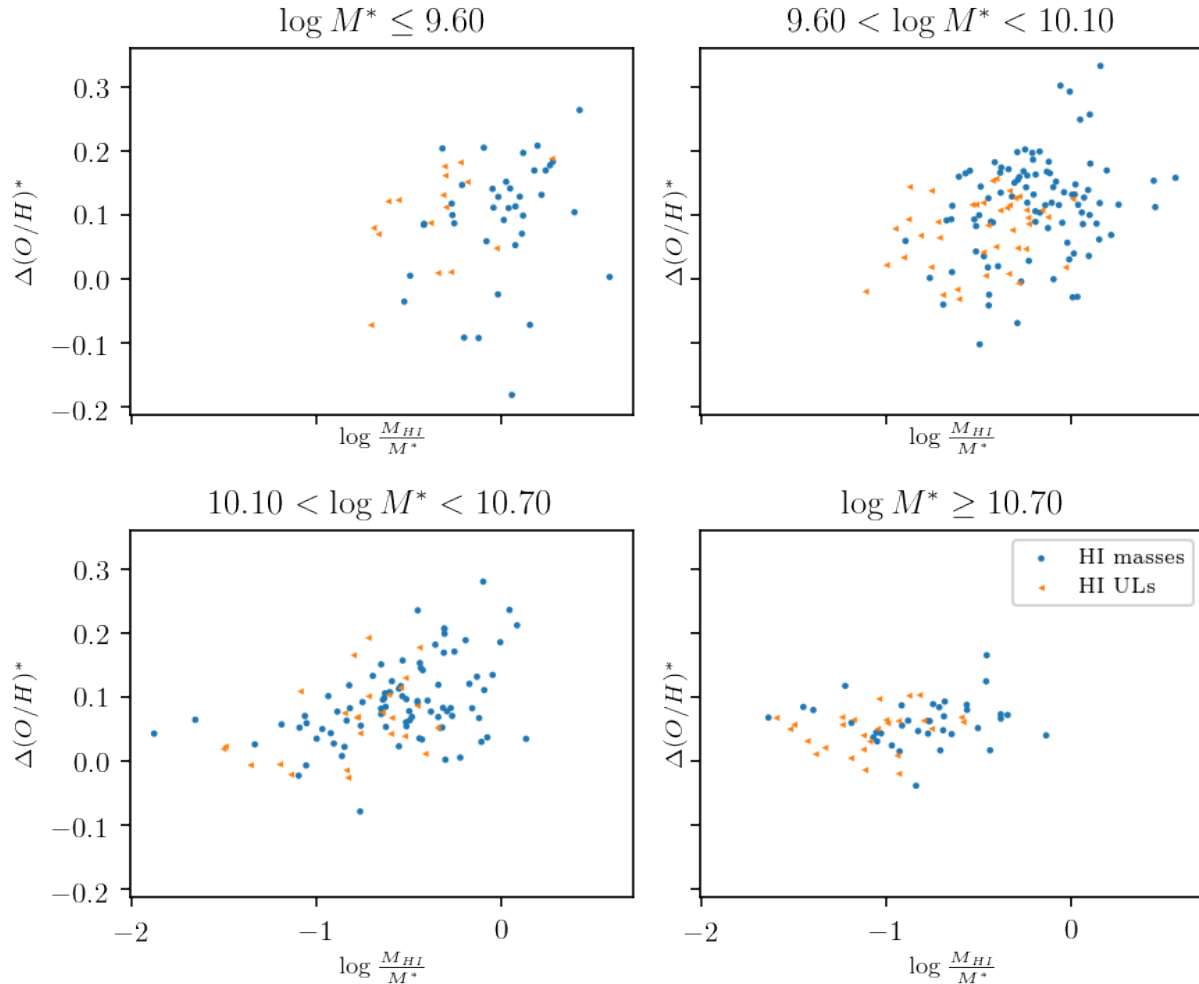


Figure 4.3 : The radial oxygen abundance decrement between $0.0 - 0.5 R_e$ & $1.25 - 1.75 R_e$ ($\Delta(O/H)^*$) is shown on the abscissa, with respect to the HI mass normalized by the stellar mass ($\log M_{HI}/M^*$). Positive HI detections are shown as blue squares, and upper-limits as orange triangles: at fixed total stellar mass, the atomic gas mass upper-limits probe a lower gas-fraction branch of the galaxy population. There is a moderate correlation between HI mass fraction and oxygen abundance decrement strength at fixed galaxy total stellar mass, present most prominently at $M^* < 10^{10.7} M_\odot$.

evolution, an abnormal metallicity decrement could indicate that an inflow has disturbed the galaxy’s abundance profile: such a galaxy might be in an abnormal or non-steady state, with oxygen abundance varying azimuthally as well as radially. We therefore now consider the width of the gas-phase metallicity distribution within the outer radial bin ($1.25 - 1.75 R_e$), $\tilde{\sigma}(O/H)^*$, defined as the median absolute deviation distribution of spaxel oxygen abundances within that radial interval. Since $\tilde{\sigma}(O/H)^*$ signifies heterogeneity in chemical enrichment within the outermost radial bin, it is a fair proxy for azimuthal variations in gas-phase metallicity at fixed radius. Figure 4.4 shows the relationship between $\tilde{\sigma}(O/H)^*$ and $\Delta(O/H)^*$ in the same four stellar-mass bins used in Figure 4.3; and Figure 4.5 shows the relationship between $\log M_{HI}/M^*$ and $\tilde{\sigma}(O/H)^*$. There is indeed a positive correlation between a strong radial decrement and large metallicity dispersion within a single radial bin; and also between gas-richness & $\tilde{\sigma}(O/H)^*$. This implies a close relationship between gas content and non-uniform chemical evolution across a single galaxy.

Table 4.1 catalogs the Kendall’s τ rank correlation coefficients between $\Delta(O/H)^*$, $\tilde{\sigma}(O/H)^*$, and $\frac{M_{HI}}{M^*}$. Since the HI fractions include some upper-limits, they cannot be strictly rank-ordered, and so a modified version of Kendall’s τ is used, which accounts for censored data (Akritas et al. 1995; Akritas & Siebert 1996; Helsel et al. 2005). As with Figures 4.3, 4.4, and 4.5, the correlations are measured in four bins of total stellar mass. The final three rows of Table 4.1 show the correlation between $\Delta(O/H)^*$ and $\tilde{\sigma}(O/H)^*$ for subsamples of the data with HI mass measurements, upper limits, and no data at all.

The correlations between $\tilde{\sigma}(O/H)^*$ and $\Delta(O/H)^*$ exist across all bins of total stellar mass, but those involving HI are both strongest and most statistically robust in the intermediate two bins ($9.6 \leq \log M^*[M_\odot] < 10.7$). At the extremes of stellar-mass ($\log M^*[M_\odot] \leq 9.6$ and $\log M^*[M_\odot] \geq 10.7$), the data cannot establish a correlation with a significance better than 5%. The lowest-mass bin has very few galaxies, and unlike at

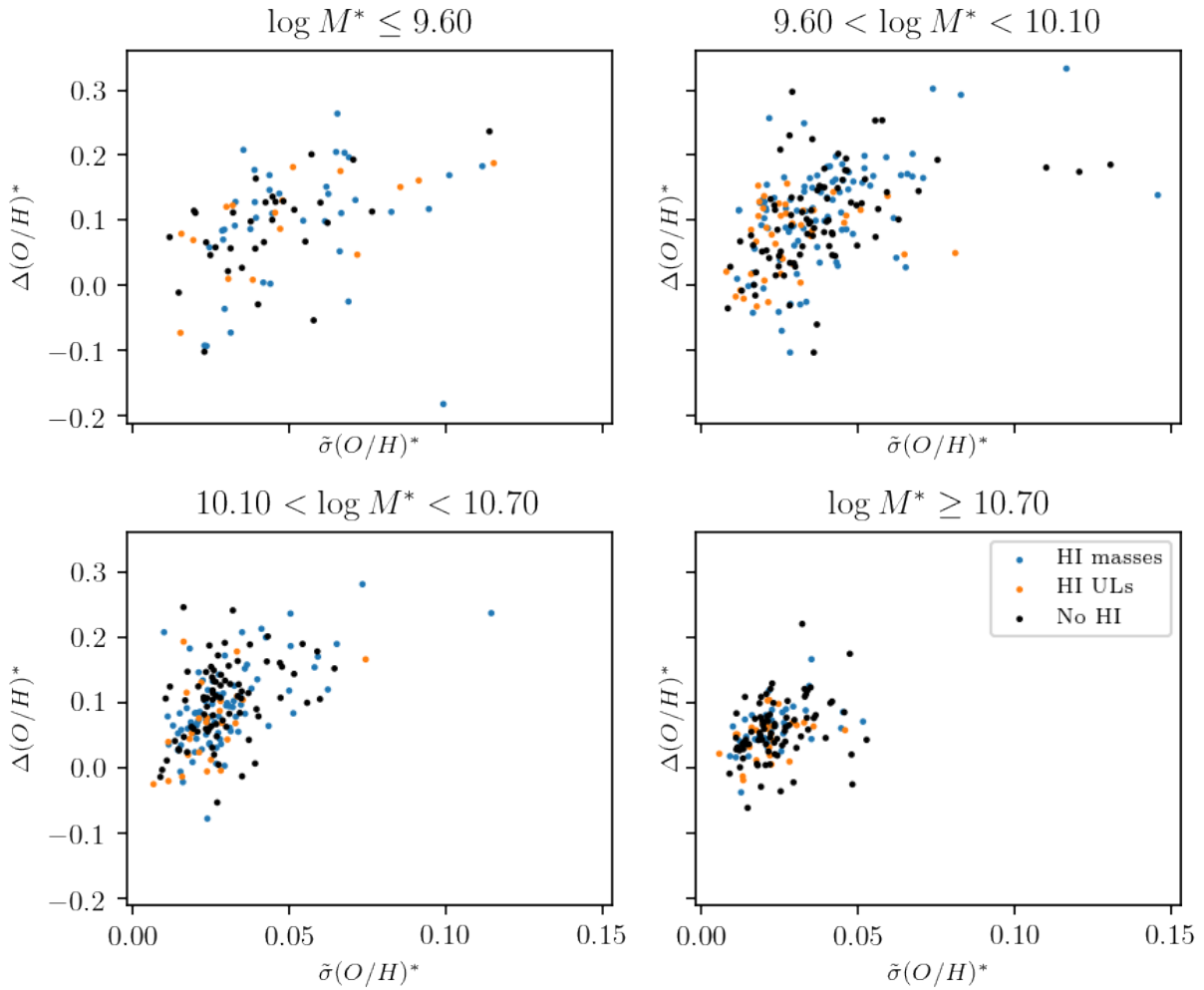


Figure 4.4 : As Figure 4.3, but relating dispersion of gas-phase metallicity at fixed radius (abscissa) with the strength of metallicity decrement (ordinate), when galaxies are separated by their total stellar mass. Within individual stellar-mass bins, there is a visual correlation between $\tilde{\sigma}(O/H)^*$ and $\Delta(O/H)^*$ (see Table 4.1 for Kendall's τ correlation coefficients accounting for upper-limits). This is true for galaxies with measured HI masses (blue), HI upper-limits (orange), and with no measured HI at all (black). The correlation is most striking in the three lower-mass bins, and is marginal for $M^* > 10^{10.7} M_\odot$.

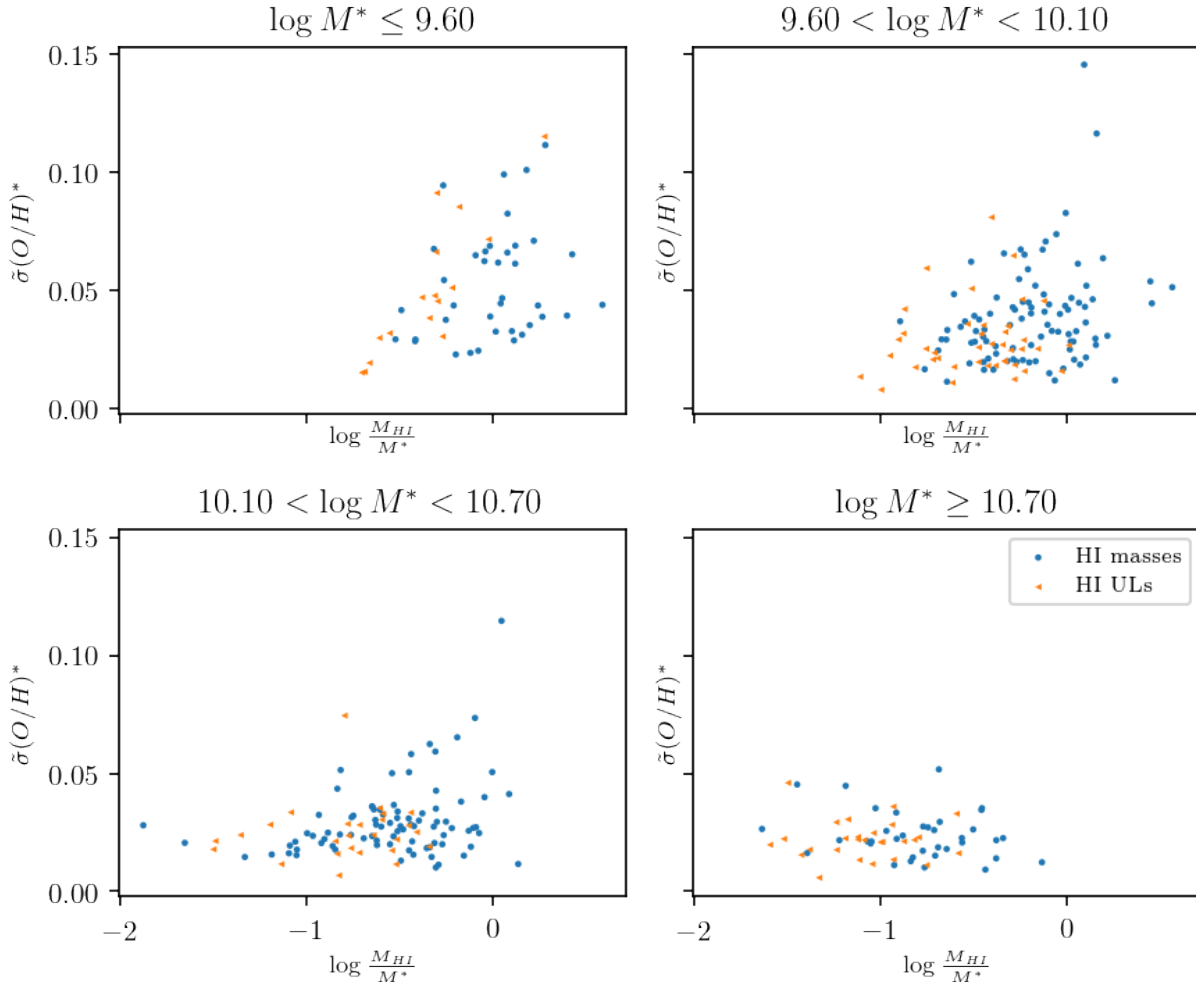


Figure 4.5 : As Figures 4.3 & 4.4, but relating dispersion of gas-phase metallicity at fixed radius (abscissa) and $\log \frac{M_{HI}}{M^*}$. Positive HI detections are shown as blue circles, and upper-limits as left-facing, orange triangles. As with $\Delta(O/H)^*$, there is a visual correlation between $\log \frac{M_{HI}}{M^*}$ and $\tilde{\sigma}(O/H)^*$. Like in Figure 4.3 the correlation shown here largely vanishes at $\log M^* [\text{M}_\odot] > 10.7$.

high mass, the correlations between $\Delta(O/H)^*$ and $\tilde{\sigma}(O/H)^*$ appear consistent with the intermediate-mass bins. In the intermediate mass bins (where the correlations between HI and chemical signatures are significant), the correlations between $\Delta(O/H)^*$ and $\tilde{\sigma}(O/H)^*$ are strongest for galaxies with HI detected: this may signify that the effect at play acts on the most HI-rich galaxies at fixed stellar mass. Therefore, we must conclude that the correlation between $\Delta(O/H)^*$, $\tilde{\sigma}(O/H)^*$, and $\frac{M_{\text{HI}}}{M^*}$ is truly tripartite.

The largest components of the MaNGA Main Sample, called “Primary” and “Secondary”, have different distributions in total stellar-mass, redshift, and angular size. This means that at fixed mass the Secondary Sample (higher redshift) will experience PSF-induced blurring at a larger physical scale than will the Primary Sample (lower redshift). Depending on the fundamental scale of the metallicity variations in galaxies, an observer’s ability to detect gradients and more local metallicity variations may vary with redshift,

(1) Correlation	(2) H I	(3) $\log M^*[\text{M}_\odot] \leq 9.6$ CC (p)	(4) $9.6 \leq \log M^*[\text{M}_\odot] < 10.1$ CC (p)	(5) $10.1 \leq \log M^*[\text{M}_\odot] < 10.7$ CC (p)
$\frac{M_{\text{HI}}}{M^*} - \Delta(O/H)^*$	obs.	0.160 (8.70e-2)	0.200 (6.15e-4)	0.275 (1.61e-5)
$\frac{M_{\text{HI}}}{M^*} - \tilde{\sigma}(O/H)^*$	obs.	0.177 (5.85e-2)	0.209 (3.37e-4)	0.162 (1.08e-2)
$\tilde{\sigma}(O/H)^* - \Delta(O/H)^*$	obs.	0.368 (6.24e-7)	0.350 (2.60e-14)	0.346 (1.16e-12)
$\tilde{\sigma}(O/H)^* - \Delta(O/H)^*$	det.	0.311 (6.13e-3)	0.354 (6.08e-7)	0.402 (4.18e-8)
$\tilde{\sigma}(O/H)^* - \Delta(O/H)^*$	UL	0.533 (4.56e-3)	0.234 (3.19e-2)	0.335 (1.72e-2)
$\tilde{\sigma}(O/H)^* - \Delta(O/H)^*$	None	0.354 (5.31e-3)	0.392 (2.18e-7)	0.268 (4.71e-4)

Table 4.1 : Correlation coefficients (p-values) between $\Delta(O/H)^*$, $\tilde{\sigma}(O/H)^*$, and $\frac{M_{\text{HI}}}{M^*}$, separated by total galaxy stellar-mass. **Column (1)** indicates the two quantities correlated, **column (2)** whether only the subsample with HI observations (obs.), detections (det.), or upper-limits (UL) were used (“None” indicates all galaxies were included—even non-HI-targets), and **columns (3)-(6)** which bin of total stellar mass is being aggregated. In (3)-(6), the Kendall’s τ rank correlation coefficient is listed, with the p-value in parentheses.

possibly giving rise to different distributions of $\Delta(O/H)^*$ and $\tilde{\sigma}(O/H)^*$ between Samples³. To test this effect, we calculate the correlation between $\Delta(O/H)^*$ and $\tilde{\sigma}(O/H)^*$ in bins of mass *and* separated by Primary or Secondary Sample. For $\log M^*[M_\odot] < 9.6$, the Primary Sample (56 galaxies) strongly dominates in number over the Secondary (8 galaxies), and in the Secondary Sample we are unable to establish a correlation at 5% significance; at $\log M^*[M_\odot] \geq 10.7$, a significant correlation only manifests in the Primary Sample. Though we do not show them, the $\Delta(O/H)^*$ - $\tilde{\sigma}(O/H)^*$ correlations are very similar in magnitude between Primary & Secondary Samples in the intermediate mass bins. We are satisfied, though, that the observed effects are not completely confined to either Primary or Secondary Sample—that is, that redshift effects are not dominant.

The trends noted here do not manifest as a result of contamination of the GBT beam by a secondary, nearby source: after eliminating galaxies with a companion within one beam HWHM (as cataloged in the MaNGA-GEMA VAC—[Argudo-Fernández et al. 2015](#)), the observed trends persist. The observed abundance dispersions in this MaNGA sample have a mode qualitatively in line with those found in a sample of PHANGS galaxies ([Kreckel et al. 2019](#)): the PHANGS study relied on the sulfur-based PG16-S2 calibration, but the two have been shown to be nearly identical ([Pilyugin & Grebel 2016](#)).

4.5 Inflow model: does it explain the metallicities?

We consider now whether an inflow falling onto galaxy outskirts could give rise to the chemical inhomogeneities we observe there. In this scenario, the low-metallicity inflow would mix with and “dilute” the ambient ISM, decreasing the measured metallicity. Since strong decrements and high HI fractions are also associated with an increased metallicity

³This effect ought to be strongest at low mass, where the Primary Sample targets are a factor of several closer than Secondary Sample targets ([Wake et al. 2017](#))

dispersion at fixed radius, it is clear that the inflow is not incident on the entire galaxy, or at least is not equally well-mixed with the ambient ISM. That is, the inflow covering fraction f_c as it manifests chemically is somewhat less than unity. Adopting a simplistic model of dilution, where the ambient metallicity at some radius is diluted locally by an additive factor d_{in} , the observed local metallicity will be given by

$$(O/H)_{obs}^{\dagger} = \frac{(O/H)_{amb}^{\dagger} + (O/H)_{in}^{\dagger} d_{in}}{1 + d_{in}} \quad (4.1)$$

where $(O/H)_{amb}^{\dagger}$ and $(O/H)_{in}^{\dagger}$ are the oxygen abundance by number, in linear units, in the ambient ISM (before the inflow) and the inflowing gas. In other words, $(O/H)^{\dagger} = 10^{(O/H)^{*}-12}$. By arithmetic rearrangement, we obtain

$$d_{in} = \frac{(O/H)_{amb}^{\dagger} - (O/H)_{obs}^{\dagger}}{(O/H)_{amb}^{\dagger} - (O/H)_{in}^{\dagger}} \quad (4.2)$$

a positive, finite quantity under the restriction $(O/H)_{amb}^{\dagger} > (O/H)_{in}^{\dagger}$.

Using this rough, but intuitive approximation, we next aim to constrain the permitted values of the inflow dilution factor d_{in} as a function of total stellar mass. To determine the ambient metallicity, we seek to separate out galaxies with substantially-higher $\tilde{\sigma}(O/H)^*$ than typical for a particular mass range. Within a given stellar-mass bin, we decompose the observed distribution of $\tilde{\sigma}(O/H)_1^*$ into two components, according to a Dirichlet-process Gaussian mixture model (DPGMM) as implemented in `scikit-learn` (Pedregosa et al. 2011) (see Figure 4.6). The component with the smaller metallicity dispersion is taken as the fiducial, undiluted sample, used to characterize the ambient metallicity; and the component with the larger mean metallicity dispersion is taken as a comparison sample with unknown dilution characteristics. We elect to decompose on $\tilde{\sigma}(O/H)_1^*$ because it allows easier population-statistics to be made with HI mass fraction and metallicity decrements within the fiducial and comparison samples.

Each stellar mass bin is bootstrap-resampled (80% of points retained) a total of 500 times, resulting in a unique reclassification. The resampling procedure produces relatively consistent component characteristics, indicating that the component diagnosis is relatively stable; and with the exception of the highest-mass bin ($\log M^*[M_\odot] > 10.7$), the presence of two components is strongly favored. From the differing behavior of galaxies with $\log M^*[M_\odot] \geq 10.7$, we may conclude that diluting inflows are relatively rare in their incidence at these masses. In the remaining, lower-mass bins ($\log M^*[M_\odot] < 10.7$), the decomposition indicates that 10%-25% of galaxies host a diluting inflow at any given time. This is similar to the $\sim 25\%$ estimate of Hwang et al. (2019).

In addition, within each bin of stellar mass, there is no discernable bias in total stellar mass between the fiducial ($\text{low-}\tilde{\sigma}(O/H)^*$) and comparison ($\text{high-}\tilde{\sigma}(O/H)^*$) populations. There are, however, differences in $\Delta(O/H)^*$ and $\frac{M_{\text{HI}}}{M^*}$ between populations. For example, we note that the high- $\tilde{\sigma}(O/H)^*$ populations have median HI mass fraction ($\frac{M_{\text{HI}}}{M^*}$) between 0.05 dex and 0.25 dex larger than the low- $\tilde{\sigma}(O/H)^*$ populations (considering only galaxies with positive HI detections). In the low- and intermediate-mass bins, there is also a difference (0.05–0.2 dex) between the low- and high- $\tilde{\sigma}(O/H)^*$ populations' distributions of $\Delta(O/H)^*$ (Figure 4.6, right-hand panel). These results are reminiscent of the trends found in Section 4.4.

Within each stellar mass bin, the comparison (high- $\tilde{\sigma}(O/H)^*$) sample's median oxygen abundance in radial bin 1 ($((O/H)_{\text{comp},1}^*)$) is taken as the observed, post-inflow metallicity ($((O/H)_{\text{obs}}^*)$). A range of possible pre-inflow metallicities ($((O/H)_{\text{in}}^*)$) are used, with the following limits

- The median oxygen abundance in radial bin 1 of the fiducial sample ($((O/H)_{\text{fid},1}^*)$)
- The average of $((O/H)_{\text{comp},1}^*)$ and $((O/H)_{\text{fid},1}^*)$

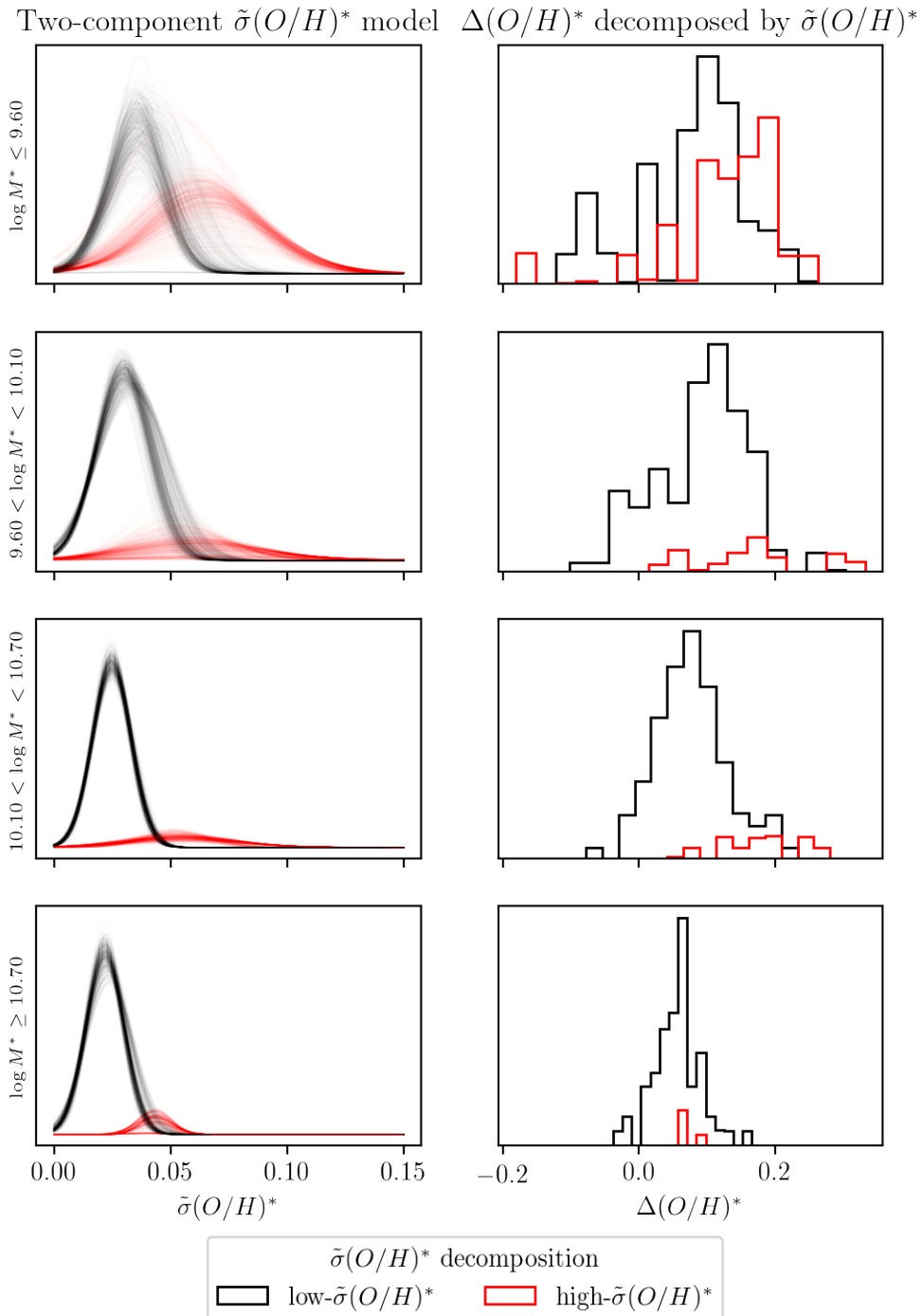


Figure 4.6 : Decompositions of the M^* -separated sample of galaxies on the basis of their metallicity dispersion in the interval $1.25 - 1.75 R_e$. All galaxies with well-measured decrements are used, regardless of HI observation or detection. Each row shows the decomposition results for one bin of total galaxy stellar mass. In the left-hand column are shown five-hundred two-component decompositions of $\tilde{\sigma}(O/H)^*$, under a bootstrap-resampling approach (80% of points retained). The black (red) curves show the best-fit

The metallicity of the accreted gas is set to one of two values obtained through a gas-regulator-model analysis of the same type as Schaefer et al. (2019b), but using the PG16-R2 metallicity calibrator: a value of 7.24 ($\sim 1/30 Z_{\odot}$) corresponds to the mean accreted metallicity of satellites of low-mass ($\log M^*[M_{\odot}] < 10$) galaxies; and a value of 7.52 ($\sim 1/15 Z_{\odot}$) corresponds to the mean accreted metallicity of satellites of high-mass ($\log M^*[M_{\odot}] > 10.5$) galaxies. While these metallicities by definition pertain to accretion by low-mass galaxies ($9 < \log M^*[M_{\odot}] < 10$), and are therefore most appropriate to the two lowest-mass bins, they are realistic order-of-magnitude estimates. An alternative would be to adopt for higher-mass galaxies the typical metallicities of Milky Way high-velocity clouds (HVCs), which are somewhat sub-solar (Wakker 2004), though not universally external in origin (Fox et al. 2016). We do not show results for typical HVC metallicities, since the model is relatively insensitive to inflow metallicity.

d_{in} is computed for each combination of $(O/H)_{amb}^*$ and $(O/H)_{in}^*$. The results are shown in Figure 4.7. We find that according to this picture of dilution by lower-metallicity gaseous inflows, local star-forming gas reservoirs encounter inflows with between 10% and 90% of ambient gas surface-density. The most massive, star-forming galaxies ($> 10^{10.7} M_{\odot}$) seem to be somewhat distinct in that any inflow is constrained to be relatively small in magnitude compared with their existing local gas reservoirs; at high stellar mass, the multi-component decomposition of $\tilde{\sigma}(O/H)^*$ does not heavily favor a high- $\tilde{\sigma}(O/H)^*$ population, so this result is much less certain. In contrast, our simple model permits lower-mass galaxies to experience significant inflows (10 – 100%) relative to their existing local gas reservoirs.

The assumed ambient metallicity can be thought of as a reflection of how commonly inflows are incident at local scales upon a star-forming disk: if most regions are subject to more constant refueling (i.e. dilution), then the ambient metallicity is implied to be higher. That is, when only the most metal-rich tail of the metallicity distribution reflects

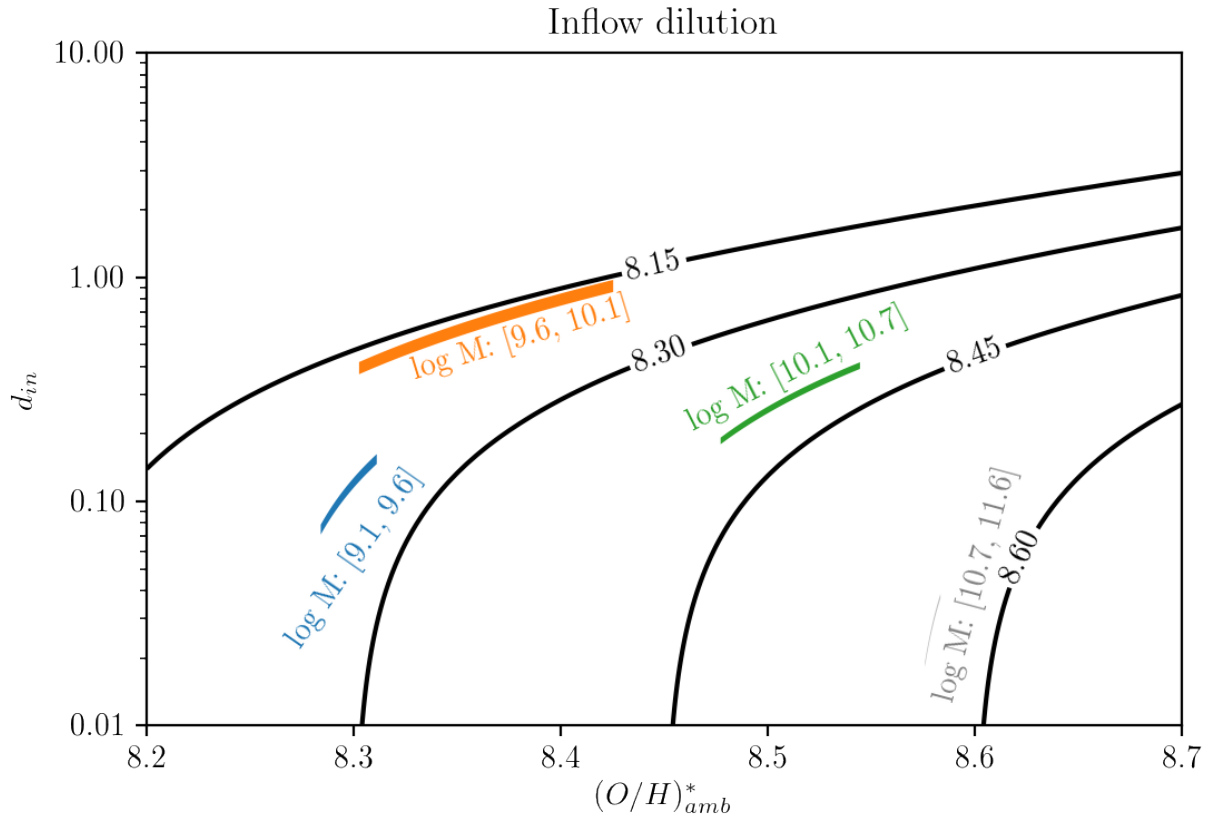


Figure 4.7 : A toy model of inflow’s effect locally on observed metallicity, assuming a range of ambient & observed (pre-inflow & post-inflow) metallicities, along with a range of inflow metallicities taken from a best-fit equilibrium model. A covariate range of local dilution factor and ambient metallicity (dependent on the choice of inflow metallicity) is shown for each of the four mass bins: the three lowest-mass bins are shown in color, since the two-component GMM used to estimate their pre- & post-inflow metallicities is fairly well-characterized; the highest-mass bin is shown in gray, since the two-component decomposition is not reliable. Overlaid are contours representing the corresponding, average observed gas-phase metallicity for a given combination of $(O/H)_{amb}^*$ and d_{in} .

the galaxy’s recent star formation free from inflows, the local dilution must be stronger on average. This implies a large inflow covering fraction, so we evaluate the higher inflow dilution factors as somewhat less likely, given the large observed metallicity dispersion at fixed radius.

4.5.1 Total H I, dust, and extended UV disks in the accretion-dilution model

Under the toy model described above, in which the ambient ISM of galaxies is diluted by lower-metallicity gas with extragalactic origin, there should be a correspondence between the degrees of dilution and local HI-enhancement. In Section 4.5, we computed that at total stellar masses of approximately $10^{9.6} - 10^{10.1} M_{\odot}$ and accreted-gas metallicities of 7.24, local dilution factors are implied to be approximately 50%, with a covering fraction somewhat less than one. Within individual stellar-mass bins, the higher- $\tilde{\sigma}(O/H)_1^*$ population has a larger HI mass fraction on average. This difference is most pronounced at intermediate mass: in the range $10^{9.6} - 10^{10.1} M_{\odot}$, high-metallicity-dispersion galaxies have $\log \frac{M_{HI}}{M^*}$ enhanced by 0.25 dex, and for the range $10^{10.1} - 10^{10.7} M_{\odot}$, the enhancement is 0.2 dex. Conversely, in the lower- and higher-mass bins, the enhancements are at most 0.1 dex.

To evaluate the possible inflow-induced enhancements in HI mass associated with the metallicity dilutions, we adopt a plausible, if simplistic description of a galaxy’s HI radial mass profile: an exponential disk with an inner core (representing a transition to predominantly molecular gas) and an outer cutoff. Interior to an atomic-to-molecular transition radius r_t , the atomic gas mass surface density is constant; between r_t and a cutoff radius r_c , the radial profile is an exponential, with a scale-length of r_t ; and exterior to r_c , there is no gas.

As an illustrative example, we consider the case of a hypothetical low-mass galaxy, with $M^* \sim 10^{9.85} M_{\odot}$ and $\log \frac{M_{HI}}{M^*} \sim -0.2$ (the median of the low- $\tilde{\sigma}(O/H)^*$ population

for that stellar-mass bin). Following roughly a set of HI mass-size relations (Verheijen & Sancisi 2001; Wang et al. 2016; Martinsson et al. 2016, , as collated and expanded in Blue Bird et al. 2020), we estimate a physical HI disk cutoff radius of $\sim 20\text{kpc}$ (or roughly $8R_e$). We rely on previous calibrations of bandpass-specific scale-lengths with respect to r_{25} to estimate the dimensionless ratio $\frac{\langle h_{\Sigma_{tot_gas}}/r_{25} \rangle}{\langle h_{0.7\mu m}/r_{25} \rangle} \approx 1.6$ (see Casasola et al. 2017, Table 7). In units of R_e , this ratio is adopted as r_t .

We will briefly use this model profile as a fiducial for a galaxy without an inflow, and evaluate possible inflow-related enhancements to it. Guided by our dilution model, we assume that a gaseous inflow provides a 50% enhancement to local star-forming gas reservoirs, with a covering fraction of 50%. Under this fiducial model, the mass fraction contained in the radial interval $[1.25 R_e, 1.75 R_e]$ is approximately 6%. Consequently, an inflow with the characteristics described above would affect a minuscule ($\sim 1\%$, or < 0.01 dex) enhancement in the *global* gas mass. This admittedly-limiting case is substantially less than typical differences between HI fractions in low- and high- $\tilde{\sigma}(O/H)^*$ populations (0.05 - 0.25 dex). In contrast, an inflow affecting all radii between $1.25R_e$ and r_c would enhance a galaxy's global HI mass by ~ 0.1 dex (assuming the same covering fraction and local gas enhancement). This is more plausible, but still less than the 0.25 dex the population comparison suggests. As the assumed outer extent of the inflow grows to exceed r_c , the enhancement in total gas mass becomes insensitive to r_c ; in order to reach the large HI fractions of the high- $\tilde{\sigma}(O/H)^*$ population, the inflow's radial profile must become shallower (i.e., the scale-length must increase). For example, an inflow profile incident only on $r > 1.25 R_e$, with a 50% local mass enhancement at $1.25 R_e$, $r_t = 2 R_e$ (a shallower slope than the fiducial), and $r_c = 16 R_e$ (a larger cutoff radius than the fiducial) achieves a global gas mass enhancement of nearly 0.2 dex. Modulating the inflow covering fraction with respect to radius is qualitatively similar to adopting a longer inflow scale-length: if

this were the case, metallicity profiles would steepen when measured at larger radius, but $\tilde{\sigma}(O/H)^*$ would lessen (as the metallicity distribution function at fixed radius becomes unimodal). These examples illustrate that if an inflow is responsible for the abundance trends found in this work, there ought to be a *significant* gaseous component at large galactocentric radius.

An extended gaseous tail could also form stars, albeit with lower efficiency (Rafelski et al. 2016). Indeed, a star-forming “plume” has been reported around M101 (Mihos et al. 2013), as well as associated with MaNGA ALM-region candidates (Hwang et al. 2019). That said, no statistical enhancement of NUV-to-*r*-band Petrosian radius ratio (which might signal low-efficiency star formation in the inflowing gas) is found in high- $\tilde{\sigma}(O/H)^*$ galaxies compared to peer galaxies at similar mass.

Inflows, if present, may also have a dust component, since their metallicity is strongly constrained to be nonzero. So, for an inflow with large enough mass and dust-to-gas ratio, the stellar populations may appear to have a greater attenuating dust foreground with respect to the typical galaxy without an inflow. To investigate this possibility, we adopt the importance-sampling inference method of Pace et al. (2019a), and use a representative library of 40,000 synthetic “training” SFHs and their spectra to infer the foreground V-band optical depth arising from a two-component dust model (Charlot & Fall 2000). However, we find that in the radial interval $1.25 - 1.75 R_e$, the inferred V-band optical depth (arising from both the diffuse and dense dust components) is not noticeably enhanced in galaxies inferred to belong to the high- $\tilde{\sigma}(O/H)^*$ population, at fixed stellar mass. This lack of visible foreground dust enhancement could be explained by a few factors: first, the number of high- $\tilde{\sigma}(O/H)^*$ galaxies in each mass bin is small by construction. Second, the geometry of the inflow with respect to the line of sight is unknown, and an inflow may not produce an attenuation signature along all lines of sight. Finally, at the expected inflow metallicities,

the dust-to-gas ratio is likely a factor of several smaller than at ambient metallicities (Kahre et al. 2018). Thus, the local dilution observed may not produce a detectable signature at all.

4.6 Discussion and Conclusions

Galaxies are widely understood to exchange gas with their surroundings. In this work, we relate the abundance patterns present within individual MaNGA star-forming galaxies to their total atomic gas content. We find

- Galaxies with high HI masses relative to their total stellar-masses tend to possess strong gas-phase metallicity decrements between their innermost star-forming regions ($0.0 - 0.5 R_e$) and those at slightly larger radii ($1.25 - 1.75 R_e$). This is similar to an effect noted in a sample of DustPedia galaxies (De Vis et al. 2019).
- Those same galaxies also tend to have relatively wide distributions (> 0.05 dex) of gas-phase metallicity in the radial interval $1.25 - 1.75 R_e$, compared with both peer galaxies of similar mass and a separate sample of star-forming galaxies at higher spatial resolution, but with metallicities obtained using the same strong-line calibration (Kreckel et al. 2019).
- These effects are limited to relatively low-mass galaxies: galaxies with $M^* > 10^{10.7} M_\odot$ seem to lack both strong metallicity decrements and large metallicity dispersions within the interval $1.25 - 1.75 R_e$. This indicates that inflows occur less frequently, or have a smaller overall impact. At low stellar mass, the correlations involving HI are not statistically significant at the 5% level. There are fewer galaxies overall in the lowest-mass bin, and unlike the highest-mass bin, the magnitude of the correlations between $\Delta(O/H)^*$ and $\tilde{\sigma}(O/H)^*$ do not diminish at low mass. More HI observations

of low-mass galaxies may result in more robust correlations with HI.

- Galaxies with abnormally-large metallicity dispersion between 1.5 and 2.5 R_e have on average 0.05 – 0.25 dex more HI when normalized by total stellar mass.

We attempt to explain the combination of effects by invoking azimuthally-asymmetric, low- (but not zero-) -metallicity inflows with a strong atomic component. Indeed, Pezzulli & Fraternali (2016) used an analytic chemical-evolution framework to predict that inward flows of gas produce steeper-than-normal metallicity gradients. The gas-rich inflows explored in this work are observationally distinct from those brought about by galaxy mergers, which have been shown to *flatten* abundance gradients, rather than steepen them (Rupke et al. 2010). Since enhanced radial metallicity decrements are also associated in our sample with increases in the *metallicity dispersion at fixed radius*, we conclude that any inflow ought to have a significant covering fraction—at least 10%, in order to noticeably widen the metallicity distribution in one radial interval; but less than 100%, a case in which $\Delta(O/H)^*$ would rise, but $\tilde{\sigma}(O/H)^*$ would not. Under our basic model, the plausible range of accreted ISM metallicities implies a range of inflow dilution factors (the margin by which a *local* gas reservoir’s mass is enhanced) of 20%-100%. Though a higher-metallicity inflow universally implies a larger inflow for the same pre-inflow ambient and post-inflow observed metallicity, this effect becomes all but negligible at higher stellar masses (higher ambient metallicities).

As discussed by Schaefer et al. (2019b), the presence of a nearby massive halo is associated with accreted gas that is more enriched. This means that even within one mass bin, the metallicity of accreted gas could vary by a factor of several. In other words, the same enhanced metallicity decrement would require a smaller inflow by mass for a satellite of a low-mass galaxy than for a satellite of a high-mass galaxy. Once MaNGA

observations and HI follow-up are complete, it may be possible to modulate the assumed inflow metallicity based on environment. Additionally, galaxy mass itself may impact the inflows it experiences: Muratov et al. (2017) finds that a high-mass halo ($M^* \sim 10^{10.8} M_\odot$) rarely sustains inflows that reach its interior ($< 0.25 R_{vir}$); whereas at lower halo mass ($M^* \sim 10^{9.3} M_\odot$), inflows have a duty cycle of about 50%! This agrees qualitatively with the observed dearth of evidence for inflows in the highest-mass bin in this work.

Though the dilution factors obtained according to this simple model imply moderate enhancements in local gas supply, there ought to be a connection to the reservoir of gas supplying the entire galaxy. With the assumed inflow metallicities, the HI mass associated with the dilution effect in strictly the radial interval $1.25 - 1.75 R_e$ is substantially smaller than the average difference in HI fractions between the high-metallicity-dispersion and low-metallicity-dispersion populations. Preserving the connection between local and global gas supply seems to require a gaseous component with relatively large radial scale-length. The GBT observations (having a FWHM of 8.8') are capable of detecting HI residing far away from the star-forming disk, and any diluting inflows incident upon a galaxy's disk could be understood as a small fraction of gaseous disk that extends outward to $10R_e$ or beyond (Bigiel & Blitz 2012).

Alternative explanations to the diluting-inflow hypothesis include intra-galaxy modulation of star formation efficiency (SFE): Schaefer et al. (2019a) reports radial variations in SFE of nearly an order of magnitude, but the degree of variance within single galaxies and at constant radius is at present unexplored (see also Bigiel et al. 2008). Galaxy regions with lower SFE may have lower metallicity than peer regions at similar radius. In order to explain the diversity of HI mass fraction at fixed stellar mass, the SFE would have to be coherently depressed across the entire galaxy for a significant portion of the age of the universe, which we consider an unlikely scenario.

Like in Hwang et al. (2019), this study finds evidence for gaseous inflows affecting a sizeable fraction of star-forming galaxies in the nearby universe ($\sim 25\%$), as reflected in the presence of anomalously-low-metallicity, star-forming gas. While Hwang et al. (2019) defines ALM gas according to a joint regression of metallicity against M^* and Σ^* (essentially, a global-local model), this study aims to detect the simple presence of ALM gas on a galaxy-by-galaxy basis in a galactocentric annulus between $1.25 \& 1.75 R_e$ according to an elevated dispersion of the metallicity distribution function within that annulus, along with a steep metallicity decrement relative to the central value. This

(1) plateifu	(2) mangaid	(3) M_{HI} (or U.L.)	(4) HI meas. type	(5) $\log M^*[M_\odot]$	(6) z	(7) $\frac{M_{HI}}{M^*}$	(8) $\tilde{\sigma}(O/H)^*$
9501-6101	1-384726	9.899	0	9.807	0.03924	0.09194	0.146
8452-12701	1-167678	nan	2	9.948	0.04017	nan	0.131
8323-12704	1-405813	nan	2	9.688	0.03819	nan	0.121
8156-12703	1-38894	9.974	0	9.815	0.04192	0.159	0.117
7495-9101	12-129610	9.443	1	9.168	0.03235	0.275	0.115
9506-12704	1-299793	10.469	0	10.424	0.04884	0.0455	0.115
9485-9102	1-121994	nan	2	8.980	0.01918	nan	0.114
8146-9101	1-556506	9.819	0	9.538	0.02393	0.281	0.112
8259-9101	1-257822	9.409	0	9.230	0.01980	0.180	0.101
8936-6104	1-152828	9.419	0	9.361	0.01570	0.0584	0.0993

Table 4.2 : A segment of the machine-readable table aggregating total galaxy stellar masses, chemical variations, and HI masses/upper-limits (where available). **Columns (1) & (2)** provide a galaxy’s MaNGA-ID and plate-ifu designations, **column (3)** the HI mass or upper-limit (“nan” if not in the HI follow-up campaign), **column (4)** the HI measurement type (0 signifies a measurement, 1 an upper-limit, and 2 not targeted), **column (5)** the total galaxy stellar mass (Pace et al. 2019b), **column (6)** the optical redshift, **column (7)** the ratio of the HI mass to the stellar mass ($\frac{M_{HI}}{M^*}$), **column (8)** the metallicity dispersion in the radial interval $1.25 - 1.75 R_e$ ($\tilde{\sigma}(O/H)^*$), and **column (9)** the measured metallicity decrement ($\Delta(O/H)^*$).

work also employs a different, likely more robust strong-line metallicity indicator (the PG16-R2 indicator from Pilyugin & Grebel 2016); and takes extensive steps to minimize the contamination of gaseous emission-line signatures across radial scales, excluding a great many spaxels near galaxies’ minor axes. We uncover a mutual link between a strong radial metallicity decrement (between the radial intervals $0 - 0.5 R_e$ & $1.25 - 1.75 R_e$), elevated dispersion of the metallicity distribution function at $1.25 - 1.75 R_e$, and total galaxy HI content; indicating a link between ALM gas and a galaxy’s total gas reservoir. The elevated metallicity decrement itself is a symptom of a radial gas flow found in simple, analytic models of galaxy chemical evolution (Pezzulli & Fraternali 2016). The correlations between $\Delta(O/H)^*$, $\tilde{\sigma}(O/H)^*$, and HI mass manifest at fixed total galaxy stellar-mass, up to a mass of $10^{10.7} M_\odot$, signaling that relatively low-mass galaxies constitute interesting laboratories for uncovering accretion signatures. We suggest targeting for high-resolution HI follow-up galaxies with wide metallicity distribution functions at fixed radius, pronounced metallicity gradients (or decrements), and large HI mass fractions for their stellar mass. A table is provided to aid in choosing targets for HI follow-up: a full version is included in machine-readable format, and we show a sample in Table 4.2. Resolved radio observations targeted according to chemistry may reveal coincident low-metallicity, star-formation-driven line emission & cold gas enhancement, indicating active accretion from an external gas reservoir.

References

- Ahumada, R., Allende Prieto, C., Almeida, A., et al. 2019, arXiv e-prints, arXiv:1912.02905
- Akritas, M. G., Murphy, S. A., & LaValley, M. P. 1995, Journ. Amer. Statistical Assoc., 90, 170
- Akritas, M. G., & Siebert, J. 1996, MNRAS, 278, 919
- Argudo-Fernández, M., Verley, S., Bergond, G., et al. 2015, A&A, 578, A110
- Balser, D. S., Wenger, T. V., Anderson, L. D., & Bania, T. M. 2015, ApJ, 806, 199

- Barrera-Ballesteros, J. K., Heckman, T., Sánchez, S. F., et al. 2018, ApJ, 852, 74
- Belfiore, F., Maiolino, R., Tremonti, C., et al. 2017, MNRAS, 469, 151
- Belfiore, F., Westfall, K. B., Schaefer, A., et al. 2019, AJ, 158, 160
- Bieging, J. H. 1978, A&A, 64, 23
- Bigiel, F., & Blitz, L. 2012, ApJ, 756, 183
- Bigiel, F., Leroy, A., Walter, F., et al. 2008, AJ, 136, 2846
- Blanton, M. R., Kazin, E., Muna, D., Weaver, B. A., & Price-Whelan, A. 2011, AJ, 142, 31
- Blanton, M. R., Bershady, M. A., Abolfathi, B., et al. 2017, AJ, 154, 28
- Bluck, A. F. L., Maiolino, R., Sánchez, S. F., et al. 2019, MNRAS, 2839
- Blue Bird, J., Davis, J., Luber, N., et al. 2020, MNRAS, 492, 153
- Bundy, K., Bershady, M. A., & Law, D. R. e. a. 2015, ApJ, 798, 7
- Casasola, V., Cassarà, L. P., Bianchi, S., et al. 2017, A&A, 605, A18
- Catinella, B., Schiminovich, D., Kauffmann, G., et al. 2010, MNRAS, 403, 683
- Charlot, S., & Fall, S. M. 2000, ApJ, 539, 718
- Chisholm, J., Tremonti, C., & Leitherer, C. 2018, MNRAS, 481, 1690
- Dawson, K. S., Schlegel, D. J., Ahn, C. P., et al. 2013, AJ, 145, 10
- De Vis, P., Jones, A., Viaene, S., et al. 2019, A&A, 623, A5
- Dekel, A., & Birnboim, Y. 2006, MNRAS, 368, 2
- Drory, N., MacDonald, N., Bershady, M. A., et al. 2015, AJ, 149, 77
- Fischer, J. L., Domínguez Sánchez, H., & Bernardi, M. 2019, MNRAS, 483, 2057
- Fox, A. J., Lehner, N., Lockman, F. J., et al. 2016, ApJ, 816, L11
- Goddy, J., Stark, D. V., & Masters, K. L. 2020, Research Notes of the AAS, 4, 3
- Gunn, J. E., Siegmund, W. A., Mannery, E. J., et al. 2006, AJ, 131, 2332
- Haynes, M. P., Giovanelli, R., Kent, B. R., et al. 2018, ApJ, 861, 49
- Heckman, T. M., Armus, L., & Miley, G. K. 1990, ApJS, 74, 833
- Helsel, D. R., et al. 2005, Nondetects and data analysis. Statistics for censored environmental data. (Wiley-Interscience)

- Hinshaw, G., Larson, D., Komatsu, E., et al. 2013, *ApJS*, 208, 19
- Ho, I. T., Seibert, M., Meidt, S. E., et al. 2017, *ApJ*, 846, 39
- Ho, I. T., Meidt, S. E., Kudritzki, R.-P., et al. 2018, *A&A*, 618, A64
- Howk, J. C., Rueff, K. M., Lehner, N., et al. 2018a, *ApJ*, 856, 166
- . 2018b, *ApJ*, 856, 167
- Hughes, T. M., Cortese, L., Boselli, A., Gavazzi, G., & Davies, J. I. 2013, *A&A*, 550, A115
- Hwang, H.-C., Barrera-Ballesteros, J. K., Heckman, T. M., et al. 2019, *ApJ*, 872, 144
- Kahre, L., Walterbos, R. A., Kim, H., et al. 2018, *ApJ*, 855, 133
- Kauffmann, G., Heckman, T. M., Tremonti, C., et al. 2003, *MNRAS*, 346, 1055
- Kennicutt, Robert C., J. 1998, *ApJ*, 498, 541
- Kennicutt, R. C., & Evans, N. J. 2012, *ARA&A*, 50, 531
- Kereš, D., Katz, N., Weinberg, D. H., & Davé, R. 2005, *MNRAS*, 363, 2
- Kewley, L. J., Dopita, M. A., Sutherland, R. S., Heisler, C. A., & Trevena, J. 2001, *ApJ*, 556, 121
- Kreckel, K., Blanc, G. A., Schinnerer, E., et al. 2016, *ApJ*, 827, 103
- Kreckel, K., Ho, I. T., Blanc, G. A., et al. 2019, *ApJ*, 887, 80
- Kroupa, P. 2001, *MNRAS*, 322, 231
- Lacerda, E. A. D., Cid Fernandes, R., Couto, G. S., et al. 2018, *MNRAS*, 474, 3727
- Law, D. R., Yan, R., Bershady, M. A., et al. 2015, *AJ*, 150, 19
- Law, D. R., Cherinka, B., Yan, R., et al. 2016, *AJ*, 152, 83
- Licquia, T. C., & Newman, J. A. 2015, *ApJ*, 806, 96
- Maiolino, R., Nagao, T., Grazian, A., et al. 2008, *A&A*, 488, 463
- Martin, D. C., O'Sullivan, D., Matuszewski, M., et al. 2019, *Nature Astronomy*, 3, 822
- Martinsson, T. P. K., Verheijen, M. A. W., Bershady, M. A., et al. 2016, *A&A*, 585, A99
- Masters, K. L., Stark, D. V., Pace, Z. J., et al. 2019, *MNRAS*, 488, 3396
- Mihos, J. C., Harding, P., Spengler, C. E., Rudick, C. S., & Feldmeier, J. J. 2013, *ApJ*, 762, 82
- Mingozzi, M., Belfiore, F., Cresci, G., et al. 2020, arXiv e-prints, arXiv:2002.05744

- Moran, S. M., Heckman, T. M., Kauffmann, G., et al. 2012, ApJ, 745, 66
- Muratov, A. L., Kereš, D., Faucher-Giguère, C.-A., et al. 2017, MNRAS, 468, 4170
- Oey, M. S., & Kennicutt, R. C., J. 1993, ApJ, 411, 137
- Pace, Z. J., Tremonti, C., Chen, Y., et al. 2019a, ApJ
- . 2019b, ApJ
- Pedregosa, F., Varoquaux, G., & Gramfort, A. e. a. 2011, Journal of Machine Learning Research, 12, 2825
- Pellegrini, E. W., Reissl, S., Rahner, D., et al. 2019, arXiv e-prints, arXiv:1905.04158
- Petit, A. C., Krumholz, M. R., Goldbaum, N. J., & Forbes, J. C. 2015, MNRAS, 449, 2588
- Pezzulli, G., & Fraternali, F. 2016, MNRAS, 455, 2308
- Pilyugin, L. S., & Grebel, E. K. 2016, MNRAS, 457, 3678
- Pilyugin, L. S., Grebel, E. K., Zinchenko, I. A., et al. 2018, A&A, 613, A1
- Poetrodjojo, H., Groves, B., Kewley, L. J., et al. 2018, MNRAS, 479, 5235
- Prantzos, N., & Boissier, S. 2000, MNRAS, 313, 338
- Rafelski, M., Gardner, J. P., Fumagalli, M., et al. 2016, ApJ, 825, 87
- Rubin, K. H. R., Prochaska, J. X., Koo, D. C., et al. 2014, ApJ, 794, 156
- Rupke, D. S. N., Kewley, L. J., & Chien, L. H. 2010, ApJ, 723, 1255
- Sanchez, S. F. 2019, arXiv e-prints, arXiv:1911.06925
- Sánchez, S. F., Rosales-Ortega, F. F., Iglesias-Páramo, J., et al. 2014, A&A, 563, A49
- Sánchez Almeida, J., Morales-Luis, A. B., Muñoz-Tuñón, C., et al. 2014, ApJ, 783, 45
- Sánchez Almeida, J., & Sánchez-Menguiano, L. 2019, ApJ, 878, L6
- Sánchez-Menguiano, L., Sánchez, S. F., Kawata, D., et al. 2016, ApJ, 830, L40
- Sánchez-Menguiano, L., Sánchez, S. F., Pérez, I., et al. 2018, A&A, 609, A119
- Sanders, R. H. 1980, ApJ, 242, 931
- Schaefer, A. L., Tremonti, C., Belfiore, F., et al. 2019a, arXiv e-prints, arXiv:1911.00581
- Schaefer, A. L., Tremonti, C., Pace, Z., et al. 2019b, ApJ, 884, 156
- Smee, S. A., Gunn, J. E., Uomoto, A., et al. 2013, AJ, 146, 32

- Snaith, O., Haywood, M., Di Matteo, P., et al. 2015, A&A, 578, A87
- Sorba, R., & Sawicki, M. 2015, MNRAS, 452, 235
- Spitoni, E., Silva Aguirre, V., Matteucci, F., Calura, F., & Grisoni, V. 2019, A&A, 623, A60
- Stark, D. V., & Masters, K. L. in prep.
- Tacconi, L. J., Neri, R., Genzel, R., et al. 2013, ApJ, 768, 74
- Tinsley, B. M. 1972, A&A, 20, 383
- . 1973, ApJ, 186, 35
- Tremonti, C. A., Heckman, T. M., Kauffmann, G., et al. 2004, ApJ, 613, 898
- Verheijen, M. A. W., & Sancisi, R. 2001, A&A, 370, 765
- Vincenzo, F., Matteucci, F., Belfiore, F., & Maiolino, R. 2016, MNRAS, 455, 4183
- Vogt, F. P. A., Pérez, E., Dopita, M. A., Verdes-Montenegro, L., & Borthakur, S. 2017, A&A, 601, A61
- Wake, D. A., Bundy, K., Diamond-Stanic, A. M., et al. 2017, AJ, 154, 86
- Wakker, B. P. 2004, Astrophysics and Space Science Library, Vol. 312, HVC/IVC Maps and HVC Distribution Functions, ed. H. van Woerden, B. P. Wakker, U. J. Schwarz, & K. S. de Boer, 25
- Wang, J., Koribalski, B. S., Serra, P., et al. 2016, MNRAS, 460, 2143
- Westfall, K. B., Cappellari, M., Bershady, M. A., et al. 2019, arXiv e-prints, arXiv:1901.00856
- Yan, R., Bundy, K., Law, D. R., et al. 2016a, AJ, 152, 197
- Yan, R., Tremonti, C., Bershady, M. A., et al. 2016b, AJ, 151, 8
- York, D. G., Adelman, J., Anderson, Jr., J. E., et al. 2000, AJ, 120, 1579
- Zaritsky, D., Kennicutt, Robert C., J., & Huchra, J. P. 1994, ApJ, 420, 87
- Zhang, C., Peng, Y., Ho, L. C., et al. 2019, ApJ, 884, L52
- Zhu, G. B., Barrera-Ballesteros, J. K., Heckman, T. M., et al. 2017, MNRAS, 468, 4494
- Zibetti, S., Charlot, S., & Rix, H.-W. 2009, MNRAS, 400, 1181
- Zinchenko, I. A., Just, A., Pilyugin, L. S., & Lara-Lopez, M. A. 2019, A&A, 623, A7

Chapter 5

Discussion, Summary, and Conclusions

The chemical evolution of galaxies arises due to a confluence of dark matter halo collapse, star-formation, gas expulsion, and likely rejuvenation of star-forming gaseous reservoirs. The result is exquisite correlations between properties of halos, the galaxies embedded within them, and even individual regions within those galaxies. The works above have sought to measure the properties (particularly the mass) of the stars, the quantity of metals in the ISM, and their mutual relationship with the gaseous reservoir.